Summer 1993

Boundary Layer influences on the Subsonic Near-Wake of a Family of Three-Dimensional Bluff Bodies

Charles Willliam Alcorn
Old Dominion University

BOUNDARY LAYER INFLUENCES ON THE SUBSONIC NEAR-WAKE OF A FAMILY OF THREE-DIMENSIONAL BLUFF BODIES

Charles William Alcorn

B.S.M.E. August 1986, Old Dominion University

M.S.M.E. August 1988, Old Dominion University

Diploma, Aerospace Engineering July 1989, von Kármán Institute

A Dissertation submitted to the Faculty of Old Dominion University in Partial Fulfillment of the Requirement for the Degree of

DOCTOR OF PHILOSOPHY

MECHANICAL ENGINEERING

OLD DOMINION UNIVERSITY

AUGUST 1993

Approved by:

Colin P. Britcher (Director)	Robert L. Ash
Richard W. Barnwell	Oktay Baysal
David A. Dress	A. Sidney Roberts, Jr.

ABSTRACT

BOUNDARY LAYER INFLUENCES ON THE SUBSONIC NEAR-WAKE OF A FAMILY OF THREE-DIMENSIONAL BLUFF BODIES

Charles William Alcorn
Old Dominion University, 1993
Director: Dr. Colin P. Britcher

A study is reported on subsonic bluff body near-wake flows. It has been determined that one family of bluff bodies, namely slanted-base ogive cylinders, can experience either a closed recirculating near-wake, or a longitudinal vortex near-wake depending on the base slant-angle and the Reynolds number. This suggests a dependence of near-wake parameters on the state of the boundary layer ahead of separation. This report addresses the influence of the boundary layer on the near-wake of slanted-base bluff bodies. Experiments were conducted in two facilities, the 6-inch Magnetic Suspension and Balance System (MSBS) at NASA Langley Research Center and the Old Dominion University low-speed wind tunnel. Interference-free drag measurements in the 6-inch MSBS validated previous drag results. Measurements in the ODU facility were made to determine base pressures, wake stagnation point locations, and boundary layer velocity profiles. Furthermore, spectral and cross-spectral analyses of the fluctuating streamwise velocity in the near-wake were performed to determine frequencies and coherence of large-scale structures. It was determined that despite variations in the boundary layer state, base pressures and wake stagnation point locations correlate with the Reynolds number based on the boundary layer momentum thickness as the independent variable. Variations in the frequency and coherence of large-scale structures were shown to exist with fixed boundary layer transition. A two-dimensional representation of a slanted-base configuration was studied analytically using classical theories and computationally using an existing finite element package. This study confirmed that the sudden changeover in wake structure is a result of flow reattachment onto the slanted-base.

ACKNOWLEDGMENTS

The author gratefully acknowledges the support and guidance of Dr. Colin P. Britcher, Advisor for this research. The author also acknowledges the support of the Institute for Computational and Applied Mechanics (ICAM), Professor S. N. Tiwari, Director. Further acknowledgments are extended to Timothy Schott for his technical support at the NASA Langley 6-inch MSBS, and to Jerry and Bill for help in fabricating the wind tunnel models.

TABLE OF CONTENTS

		PAGE
LIST OF TABLES		v
LIST OF FIGURES		vi
NOMENCLATURE		xi
Chapter 1	INTRODUCTION	1
1.1	Bluff Body Flows	1
1.2	Flow Model: Bluff Body Near-Wake	2
1.3	Dissertation Objective	4
Chapter 2	STEADY NEAR-WAKE STRUCTURE	6
2.1	Boundary Layer Influences: Backward Facing Step	6
2.2	Boundary Layer Influences: Axisymmetric Bluff Bodies	7
2.3	Boundary Layer Influences: Slanted-Base Bluff Bodies	9
2.4	Objectives: Boundary Layer Influences	11
Chapter 3	LARGE-SCALE WAKE STRUCTURES	22
3.1	Bluff Body Flows	22
3.2	Spectral Analysis	24
3.2.1	Spectral Analysis: Predominant Frequency	25
3.2.2	Cross-Spectral Analysis: Coherence	26
3.3	Objectives: Large-Scale Structures	29
Chapter 4	STEADY NEAR-WAKE ANALYSIS	41
4.1	Vortex Formation	41
4.2	Parameters Influencing Reattachment	43

4.3	Prediction of Reattachment: Theory of Nash	45
4.4	Prediction of Reattachment: Theory of Stratford	50
4.4.1	Previous Reattachment Predictions: Airfoils	54
4.4.2	Reattachment Predictions: Slanted-Base Bluff Bodies	55
Chapter 5	**TURBULENCE ANALYSIS**	65
5.1	Spectral Analysis: Power Spectrum	66
5.2	Cross-Spectral Analysis: Coherence	67
5.3	Two-Dimensional Analysis of Unsteady Bluff Wake Parameters	71
Chapter 6	**EXPERIMENTAL DETAILS**	78
6.1	NASA Langley 6-inch MSBS	78
6.1.1	Wind Tunnel Models	79
6.1.2	Drag Calibration	80
6.1.3	Flow Visualization	80
6.2	ODU 4-foot by 3-foot Low-Speed Facility	81
6.2.1	Wind Tunnel Model	82
6.2.2	Base Pressure Measurements	82
6.2.3	Wake Stagnation Point Measurements	83
6.2.4	Boundary Layer Measurements	84
6.2.5	Predominant Frequency Measurements	84
6.2.6	Coherence Measurements	85
Chapter 7	**STEADY FLOW RESULTS**	93
7.1	Benchmark Tests: 6-Inch MSBS	93
7.1.1	Drag Coefficients	93
7.1.2	Flow Visualization	94
7.2	Detailed Near-Wake Study: ODU Facility	95
7.2.1	Base Pressure Coefficients	95

7.2.1.1 Reynolds Number Effect: 0°, 40°, and 45° Bases 96
7.2.1.2 Reynolds Number Effect: 50° Base 97
7.2.2 Wake Stagnation Point 98
7.2.2.1 Base Slant-Angle Effect 98
7.2.2.2 Reynolds Number Effect 99
7.2.3 Boundary Layer Measurements 100
7.2.4 Near-Wake Similarity 101
7.2.4.1 Base Pressure 101
7.2.4.2 Wake Stagnation Point 102
Chapter 8 **LARGE-SCALE STRUCTURES: RESULTS** 119
8.1 Predominant Frequency Measurements 119
8.2 Coherence Measurements 121
8.2.1 Coherence at Low Frequency 122
8.2.2 Coherence at the Predominant Frequency 123
8.2.3 Coherence at High Frequency 124
8.3 Comparisons to Semi-Empirical Strouhal Numbers 125
CONCLUSIONS 137
REFERENCES 142
Appendix A Wind Tunnel Test Section Calibrations 149
Appendix B Data Acquisition Program for Pressure Measurements .. 151
Appendix C Drawings of Slanted-Base Bluff Body Model (ODU) 155
Appendix D Governing Equations: Bluff Body Flows 163
Appendix E Finite Element (FIDAP) Predictions 165

LIST OF TABLES

TABLE		PAGE
8.1	Wake Location with respect to Momentum Thickness...	122
8.2	Comparison of Predicted and Measured Strouhal Numbers	126

LIST OF FIGURES

FIGURE PAGE

CHAPTER 1

1.1 Components of a Bluff Body Near-Wake 5

CHAPTER 2

2.1 Designation of Flow Zones for a Backward Facing Step Flow.... 13

2.2 Effect of Boundary Layer State on Flow Reattachment: Backward Facing Step 13

2.3 Comparison of Flow Reattachment Locations: Backward Facing Step 14

2.4 Effect of Boundary Layer State on Base Pressure (Supersonic) .. 14

2.5 Effect of Momentum Thickness on Wake Stagnation Point Location (Porteiro) 15

2.6 Effect of Momentum Thickness on Base Pressure 15

2.7 Static Pressure Distribution through the Near-Wake..... 16

2.8 Effect of Pressure Gradient on Reattachment Point Location ... 16

2.9 Road Vehicle Slanted Base Configurations 17

2.10 Wake Flow Pattern for Various Road Vehicle Configurations ... 17

2.11 Influence of Rear-Window Angle on Vehicle Drag: VW Golf 18

2.12 Slanted-Base Ogive Cylinder Configuration 18

2.13 Influence of Slant-Angle on Drag Coefficient: Slanted-Base Ogive Cylinder..... 19

2.14 Free-Transition Drag Results: 45° Base 19

2.15 Comparison of Free- and Fixed-Transition Drag Results: Slanted-Base Ogive Cylinder 20

2.16 Base Pressure Measurements: 50° Base 20

2.17 Free- and Fixed-Transition Drag Results: 45° Base 21

CHAPTER 3

3.1 Boundary Layer Separation in the Wake of a Circular Cylinder . 31

3.2 Kármán Vortex Street in the Wake of a Circular Cylinder 31

3.3 Coherent Structures in Free Turbulent Shear Flows 32

3.4 Ring Vortices in the Wake of a Circular Jet 33

3.5 Effect of Boundary Layer State on Ring Vortex Development ... 33

3.6 Organized Structures in the Wake of a Cylinder Aligned with the Flow 34

3.7 Organized Structures in the Wake of a Sphere 35

3.8 Organized Structures in a Plane Mixing Layer 35

3.9 Spectrum in the Wake of a 60° Cone 36

3.10 Power Spectrum in the Wake of a Circular Disk 36

3.11 Predominant Frequencies in the Wake of Slanted-Base Ogive Cylinders 37

3.12 Coordinate System for Cross-Spectra Measurements 37

3.13 Coherence Measurements in the Wake of a Circular Disk (Roberts) 38

3.14 Coherence Measurements at Constant Frequency (Roberts) 38

3.15 Coherence Measurements at Constant Frequency (Xia) 39

3.16 Coherence Measurements at Constant Frequency (Fuchs) 39

3.17 Summary of Azimuthal Constituents in the Wake of a Circular Disk 40

CHAPTER 4

4.1 Flow Reattachment on Slanted-Base 57

4.2 3-D Slanted-Base Bluff Body 57

4.3 Flow Model for Vortex Formation 58

4.4 Criterion for a Turbulent or Laminar Free Shear Layer 58

4.5 Transition in a Free Shear Layer 59

4.6 Boundary Layer Displacement Thickness, δ^* 60

4.7 Reynolds Number Influence on Displacement Thickness 60

4.8 Flow Model for Flow Reattachment: Theory of Nash 61

4.9 Effect of Recovery Pressure, P_r, on Wake Stagnation Point 61

4.10 Effect of Base Slant Angle on Wake Stagnation Point 62

4.11 Reattachment Predictions for a Wortmann Airfoil: Theory of Stratford 62

4.12 Surface Pressure Distribution for an Ogive Cylinder Model 63

4.13 Limiting Pressure Distribution for Various Centerbody Trip Locations: $Re_D = 60{,}000$ 63

4.14 Limiting Pressure Distribution as a Function of $Re_D \left(\frac{x}{L} = 1\right)$ 64

4.15 Summary of Limiting Pressure Distribution 64

CHAPTER 5

5.1 Coordinate System for Coherence Measurements 75

5.2 Representation of m=1 and m=2 Azimuthal Constituents 76

5.3 Streamlines in a Stable Vortex Street 77

5.4 Geometric Model for St_D Variations with Base Drag 77

CHAPTER 6

6.1 NASA LaRC 6" Magnetic Suspension and Balance System 87

6.2 Slanted-Base Wind Tunnel Models: 6" MSBS..... 88

6.3 6" MSBS Drag Calibration 88

6.4 ODU Low-Speed Wind Tunnel 89

6.5 Experimental Set-Up: Pressure Measurements 89

6.6 ODU Wind Tunnel Model 90

6.7 Location of Base Pressure Taps..... 90

6.8 Probe for Measuring Wake Stagnation Point Location 91

6.9 Probe for Measuring Boundary Layer Velocity Profile..... 91

6.10 Experimental Set-Up: Predominant Frequency Measurements... 92

6.11 Experimental Set-Up: Coherence Measurements 92

CHAPTER 7

7.1 Boundary Layer Trip Locations: 6-Inch MSBS Model 103

7.2 Drag Coefficients for 0° Base Model 103

7.3 Drag Coefficients for 0° and 45° Base Models: Free Transition ... 104

7.4 Drag Coefficients for 45° Base Model: Fixed Transition..... 104

7.5 Smoke Flow Visualization: $Re_D < 60{,}000$ 105

7.6 Smoke Flow Visualization: $Re_D > 60{,}000$ 105

7.7 Base Pressure Distributions: $Re_D = 165{,}000$..... 106

7.8 Liquid Crystal Flow Visualization: 50° Base 107

7.9 Base Pressure Distribution along Vertical Centerline 108

7.10 Base Pressure Distribution along Horizontal Centerline 108

7.11 Base Drag Coefficients: $Re_D = 60{,}000$ 109

7.12 Base Pressure Variations for Lower Slanted-Base Angles 109

7.13 Base Pressure Variations for Lower Slanted-Base Angles 110

7.14 Base Drag Variations for 0° and 40° Bases 110
7.15 Base Pressure Coefficients: 50° Base 111
7.16 Variations in Vortex Center with Reynolds Number 112
7.17 Variations in Vortex Center for Fixed Transition 112
7.18 Variations in Vortex Center for 50° Base: Liquid Crystals..... 113
7.19 Base Drag Variations for 45° and 50° Bases 113
7.20 Base Drag for 50° Base: Fixed and Free Transition 114
7.21 Wake Stagnation Point Locations ($Re_D = 60{,}000$) 114
7.22 Variation in Wake Stagnation Point Location with Re_D 115
7.23 Boundary Layer Velocity Profiles: $Re_D = 110{,}000$ 116
7.24 Boundary Layer Momentum Thicknesses: Re_D=110,000 116
7.25 Base Pressure Coefficients vs. Re_θ : 0° and 45° Bases 117
7.26 Base Pressure Coefficients vs. Re_θ : 50° Base 117
7.27 Wake Stagnation Point Locations vs. Re_θ 118

CHAPTER 8

8.1 Power Spectra: 0° and 45° Bases (Free Transition, $Re_D = 110{,}000$) ... 127
8.2 Peak Frequency vs. Base Slant Angle 127
8.3 Strouhal Number Variations with Reynolds Number..... 128
8.4 Coherence Variations with Strouhal Number0° Base 129
8.5 Coherence Variations at $St_D = 0.04St_{D_{PRED}}$ 134
8.6 Azimuthal Constituents at $St_D = 0.04St_{D_{PRED}}$ 134
8.7 Coherence Variations at the Predominant Frequency 135
8.8 Azimuthal Constituents at the Predominant Frequency 135
8.9 Coherence Variations at $St_D = 2.0St_{D_{PRED}}$ 136
8.10 Azimuthal Constituents at $St_D = 2.0St_{D_{PRED}}$ 136

NOMENCLATURE

a	Longitudinal Vortex Spacing
b	Vertical Vortex Spacing
C_D	Drag Coefficient
C_{D_B}	Base Drag Coefficient
C_{D_S}	Vortex Street Drag Coefficient
C_p	Pressure Coefficient
C_ω	Real Part of Coherence
D	Model Diameter
D_B	Base Drag
E	Wavenumber
f	Wake Frequency
h	Height of Backward Facing Step
$\vec{k}$	Wave Vector
L	Model Length
L_B	Base Extension Length
L_r	Reattachment Length
M_e	Mach Number at Edge of Boundary Layer
m	Azimuthal Constituent
n	Empirical Power Law Constant
$P(\omega)$	Power Spectrum
$P_1(\omega)$	Power Spectrum of Signal No. 1

$P_{2(\omega)}$	Power Spectrum of Signal No. 2
$P_{(\vec{\xi}, \omega)}$	Cross Spectrum
P_A	Static Pressure at Test Section Entrance
P_B	Test Section Static Pressure at Model Location
p_b	Base Pressure
p_o	Freestream Static Pressure
p_r	Pressure at Reattachment
Q_{TS}	Test Section Dynamic Pressure
Q_ω	Imaginary Part of Coherence
$R_{(\tau)}$	Time Correlation
$R_{(\vec{\xi}, \tau)}$	Space-Time Correlation
Re_C	Reynolds Number Base on Chord Length
Re_D	Reynolds Number Base on Model Diameter
Re_L	Reynolds Number Base on Model Length
r	Radial Position in Wake
S_L	Lower Separated Stream
St_D	Strouhal Number Based on Model Diameter
$St_{D_{PRED}}$	Predominant Strouhal Number Based on Model Diameter
S_U	Upper Separated Stream
U_e	Velocity at Edge of Boundary Layer
U_M	Vortex Velocity Relative to Model
U_n	Flow Component Normal to Separation Line
U_S	Streamwise Vortex Velocity
U_t	Flow Component Tangent to Base
U_β	Azimuthal Vortex Velocity
U_∞	Freestream Velocity
u'	Fluctuating Streamwise Velocity Component

t	time
x	Axial Position
x_{BL}	Axial Location of Boundary Layer Measurements
x_r	Axial Wake Stagnation Point Location
$x_{L_{EQ}}$	Equivalent Laminar Flat Plate Boundary Layer Length
$x_{T_{EQ}}$	Equivalent Turbulent Flat Plate Boundary Layer Length
X_{TR}	Axial Location of Transition
Y_1	Height of Test Section
α	Empirical Mixing Constant
β	Azimuthal Angle in Wake
ΔP_{CONT}	Pressure Drop Across Contraction
δ	Boundary Layer Thickness
δ^*	Boundary Layer Displacement Thickness
η	Wake Deflection Angle
Γ	Coherence
γ	Ratio of Specific Heats
ν	Kinematic Viscosity
ϕ	Vortex Swirl Angle
ρ	Density $\left(\frac{kg}{m^3}\right)$
ρ_B	Density in Base Region
ρ_R	Density at Reattachment
Ψ	Streamline
Ψ_{DA}	Boundary of Dead Air Region
Ψ_M	Median Streamline
Ψ_O	External Streamline
Ψ_r	Reattachment Streamline
Ψ_S	Separation Streamline

ψ	Base Slant Angle
λ_B	Density Ratio with respect to Base
λ_R	Density Ratio with respect to Reattachment
τ	Time Delay
θ	Boundary Layer Momentum Thickness
$\vec{\xi}$	Spatial Vector

Chapter 1 INTRODUCTION

A wake is formed behind a solid body placed in a moving fluid as the flow separates from the surface. There is no direct effect of solid boundaries on the development of the flow in the wake, therefore, wakes are categorized as a type of free turbulent flow. Examples of simple wake flows are the flow downstream of an infinitely thin plate or the flow behind a very slender cylinder in axial flow. In either case the fluid in the wall-bounded regions join at the trailing edge, and the problem can be analyzed using an extension of the upstream boundary layer equations [1]. A much more difficult configuration to analyze, which is encountered more frequently in practical flow problems, is the flow past a body of finite thickness, such as a bluff body [1, 2].

1.1 *Bluff Body Flows*

The importance of bluff body flows is seen in aircraft fuselage designs, as well as, road vehicle, projectile, and missile configurations. It is frequently necessary in many aerodynamic designs to incorporate a blunt aftbody region, as compared to a streamlined tapering afterbody, to reduce weight. Furthermore, blunt-based configurations satisfy another design criterion for transport vehicles: the maximum utilization of the enclosed vehicle volume. Bluff body wakes are of particular interest as low pressures can develop in this region, resulting in base drag that can be a significant portion of the total body drag. Flight performance and fuel consumption are greatly affected by this aspect of bluff body flows.

The majority of research into subsonic near-wake flows pertains to simple two-dimensional configurations. Many practical engineering problems, such as heat exchanger flows, can be analyzed in two-dimensions, however, many wake flows require a three-dimensional analysis. Aircraft fuselages, road vehicles, projectiles, etc., are examples of bluff body configurations that require an axisymmetric or a three-dimensional treatment. In comparison to two-dimensional wake flows, subsonic three-dimensional bluff body wake flows have received little attention.

1.2 *Flow Model: Bluff Body Near-Wake*

To understand the importance of bluff body base drag, it is necessary to examine the flow in the near-wake region. A simple flow model for the subsonic near-wake of an axisymmetric or two-dimensional bluff body is given in Fig. 1.1 [3]. It is assumed that the flow is steady and that the boundary layer approaching the base region has grown for some distance. Downstream of separation a free shear layer develops, which has its origins in the upstream boundary layer. The free shear layer divides the external quasi-inviscid flow from the fluid in the base region [4]. The free shear layer is characterized by large transverse velocity gradients, and therefore high shear stresses.

Downstream of separation, fluid from the base region is scavenged by the free shear layer and is transported downstream. This mixing process results in a reduced pressure in the base region and tends to draw the free shear layer towards the base axis [5]. Thus, the static pressure outside the mixing region is not equivalent to that upstream of the base due to the curvature of the external streamlines. It is generally assumed that just downstream of separation, the curvature of the external streamlines can be neglected so that a constant pressure mixing region is present. Thus, the conditions just before separation represent the

initial conditions for the mixing region [6]. Reduced pressures in the base also effect the boundary layer upstream of separation by imposing a favorable pressure gradient along the wall-bounded region [1, 3-4]. Unlike a smooth, continuous aftbody geometry for which flow separation is a result of an adverse pressure gradient, flow separation for a bluff body occurs in a region of a favorable pressure gradient [1].

Further downstream of separation, the reduced pressure in the base region draws the separated streams together until they converge in a region characterized by a high adverse pressure gradient. The location of convergence is called the wake stagnation point. The lower velocity fluid in the shear layer is unable to overcome the sharp rise in pressure and is returned to the base region, while the higher velocity fluid continues downstream into the far-wake region. Under steady flow conditions, a balance must exist between the fluid returned to the base region at the wake stagnation point, and the fluid entrained via the mixing process [4]. This results in a region of steady recirculating flow in the near-wake.

If a laminar boundary layer is present at separation, then at some location in the free shear layer, transition to turbulent flow occurs. The mixing process is enhanced the further the transition point is away from the wake stagnation point, therefore, more fluid is entrained from the base region. The resulting reduction in pressure within the separated region causes an increase in the curvature of the free shear layer [7]. The development of the free shear layer has its origins in the incoming boundary layer. Thus, any variation in the incoming boundary layer, such as a change in boundary layer state, influences the development of the free shear layer, and therefore, the development of the entire near-wake region.

1.3 *Dissertation Objective*

The objective of this dissertation is to detail the relationship between the incoming boundary layer and the fundamental properties of a bluff body near-wake. Efforts are directed towards steady near-wake properties, such as, the base pressure coefficient and the wake stagnation point location, as well as, unsteady large-scale near-wake structures. This dissertation is founded on wind tunnel experiments, however, an attempt at numerical verification is made. An objective is to seek a correlation between near-wake properties and properties of the incoming boundary layer.

The current research is a continuation of previous slanted-base bluff body research. Previous bluff body research, which is discussed in detail in Chapter 2, has identified the existence of a relationship between the incoming boundary layer and near-wake parameters. The current research, examines this relationship in detail. As discussed previously, the near-wake region can constitute a majority of the vehicle drag, therefore, practical applications of this research are found in aircraft fuselage, road-vehicle, and projectile near-wake aerodynamics.

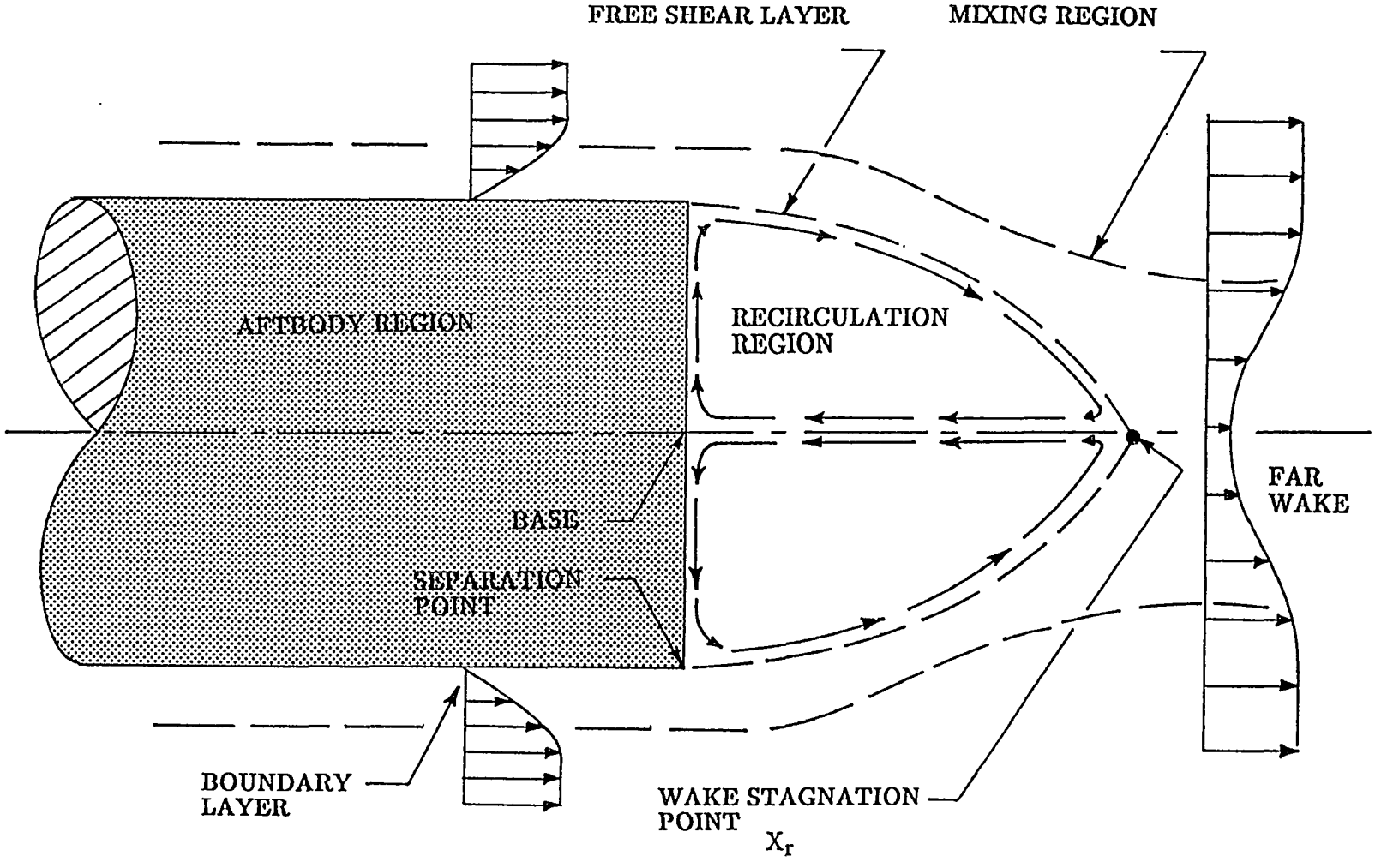

Fig. 1.1 Components of a Bluff Body Near-Wake.

Chapter 2 STEADY NEAR-WAKE STRUCTURE

This Chapter is intended to report on previous findings that detail the relationship between the steady subsonic near-wake structure behind a bluff body and its boundary layer state.

2.1 *Boundary Layer Influences: Backward Facing Step*

The simplest bluff body near-wake, which still contains the essential features of a bluff body flow, is the flow over a backward facing step. The streamlines at separation are nearly parallel to the wall at the step, and only one free shear layer exists. The primary components of a backward facing step flow are shown in Fig. 2.1. The most important dependent parameter that characterizes the near-wake flowfield of a backward facing step is the reattachment length [8].

The state of the boundary layer at separation on a two-dimensional backward facing step was studied by Eaton and Johnston [8], and was shown to have a pronounced effect on the reattachment length. This is shown in Fig. 2.2 where the reattachment length for a laminar boundary layer at separation is considerably less than that for a turbulent boundary layer. This was attributed to a more rapidly growing free shear layer originating from an initially laminar boundary layer than that originating from a turbulent boundary layer [9]. It is also shown in Fig. 2.2 that the reattachment length is strongly dependent on the Reynolds number, based on the momentum thickness throughout the

laminar/transitional regime. The reattachment point is shown to be only weakly dependent on the Reynolds number when the boundary layer at separation is fully turbulent.

The effect of the boundary layer thickness at separation was studied by Narayanan and Khadgi [10]. It was concluded in this study that the initial boundary layer thickness only has a weak effect on the reattachment location as shown in Fig. 2.3. This result was disputed by Eaton and Johnston [8] who compared data from ref. [10] to similar values from other authors under similar conditions. Their survey indicated a much stronger effect of the boundary layer thickness as shown in Fig. 2.3. Both studies show that the reattachment length decreases with increasing boundary layer thickness. Further studies are needed to resolve this issue.

2.2 *Boundary Layer Influences: Axisymmetric Bluff Bodies*

Previous analytical and experimental studies of axisymmetric bluff body flows have detailed the relationship between the steady near-wake structure and the incoming boundary layer state in both the subsonic and supersonic regimes.

Kurzweg [11] studied boundary layer effects on the base flow of projectiles in the supersonic regime. It was determined that a distinct difference existed in base pressure data, depending on the boundary layer state at separation. This is shown in Fig. 2.4. Base pressures with a laminar boundary layer at separation show a much greater variation with Reynolds number. The base pressure ratio appears to approach a constant value at the higher Reynolds numbers ($Re_D > 3.5 \times 10^6$) suggesting that natural transition has occurred on the body.

A detailed study of subsonic axisymmetric bluff body flows was carried out by Porteiro, Przirembel, and Page [12]. Measurements were made behind a long

cylindrical body that extended upstream through the wind tunnel contraction. This arrangement eliminated the need for a support strut. The boundary layer thickness at separation was controlled by applying suction through a porous section of the body upstream of the base, however, the boundary layer at separation was always turbulent. The intent of this study was to measure and relate the incoming boundary layer momentum thickness, θ to near-wake parameters, such as base pressure and the wake stagnation point location.

The wake stagnation point locations, shown in Fig. 2.5, are found to be weakly dependent on the boundary layer momentum thickness. Thicker boundary layers were found to move the stagnation point closer to the base. Porteiro, Przirembel, and Page [12] also related the base pressure to the incoming momentum thickness. It was determined that an increase in the base pressure coefficient occurred with increasing boundary layer momentum thickness as shown in Fig. 2.6.

It appears that the wake stagnation point location and base pressure measurements of Porteiro, Przirembel and Page [12] are in disagreement. A decrease in the base pressure should increase the curvature of the free shear layer and move the wake stagnation point towards the base. Conflicting trends are shown to occur in Figs. 2.5-2.6. An explanation can be found in the near-wake pressure distribution along the wake centerline as shown in Fig. 2.7. A greater adverse pressure gradient is found for the lower base pressure. A greater adverse pressure gradient, represented in Fig. 2.8 as an expansion ratio, has been shown through data compiled by Eaton and Johnston [8] to lengthen the reattachment location, counteracting the effects of the reduced base pressure.

Page [13-14] developed a theoretical representation of compressible, subsonic axisymmetric base flows, including the influence of the boundary layer. It was determined that the base pressure is weakly dependent on the Mach

number; however, it was determined that the approaching boundary layer has a significant influence on the base pressure. Specifically, an increase in the base pressure is shown with an increase in the momentum thickness of the approaching boundary layer as shown in Fig. 2.6. This is in agreement with the base pressure study of Porteiro, Przirembel, and Page [12]. A highly non-linear relationship is also shown to exist between the base pressure coefficient and boundary layer momentum thickness in the region of the limiting base pressure ($\frac{2\theta}{D} \rightarrow 0$).

2.3 *Boundary Layer Influences: Slanted-Base Bluff Bodies*

Previous research with slanted-base bluff bodies were of particular interest to road vehicle near-wake flow-field studies. This is shown in Fig. 2.9, in which the primary rear-window designs are represented by simplified bluff body configurations. Such simplifications were necessary because accurate prediction methods for determining the near-wake flow-field characteristics of an actual road vehicle design were unreliable. Scaled road vehicle models for wind tunnel testing were expensive and time consuming to manufacture. Fortunately, some of the essential features of road vehicle aerodynamics were captured by modifying these simple bluff body configurations [15].

The "square-back" configuration of Fig. 2.9 is associated with the quasi-symmetric, closed near-wake structure described in Chapter 1. For the other configurations of Fig. 2.9 a completely different near-wake is present. Pairs of longitudinal vortices can form behind these configurations as shown in Fig. 2.10 [16]. In fact, it was determined by Janssen and Hucho [17-18] during the development of the Volkswagen Golf that two completely different near-wake flows occur depending on the rear window inclination angle. Results of their study are shown in Fig. 2.11. A significant increase in drag occurred as the rear window inclination angle was increased from the horizontal. A maximum drag

coefficient was reached around an angle of 30°. It was argued that drag increases were a result of the intense trailing vortices forming from the corners of the sloping rear window. These vortices induced very low pressures on the slanted surface of the vehicle. It was further determined that a bi-stable near-wake existed between $28° < \psi < 32°$, depending on small changes in the roof's rear edge curvature. Janssen and Hucho [17-18] observed that minimum drag occurred for a square-back rear window configuration.

Morel [19-20], Maull [21] and Xia and Bearman [22] studied the effects of the rear window on the near-wake by studying a greatly simplified configuration known as a slanted-base ogive cylinder. This configuration is shown in Fig. 2.12. (Notice that the orientation of the slant-angle has been changed.) It was determined in these studies that a large jump in the overall model drag coefficient occurred around a slant-angle of 45°. The drag jump was accompanied by a sudden change in the near-wake flow pattern. Specifically, a quasi-symmetric, turbulent closure pattern was present for lower angle slanted-bases, while a longitudinal vortex flow was present for the higher angle slanted-bases. The variation in drag with increasing slant-angle and the corresponding near-wake flow patterns are shown in Fig. 2.13.

Additional studies with slanted-base ogive cylinders were conducted by Britcher and Alcorn [23-24], Britcher and Kilgore [25], and Alcorn [26] in the NASA Langley Research Center 13-Inch Magnetic Suspension and Balance System (MSBS). Test results in this facility were free of all flow disturbances related to mechanical supports [27]. Studies revealed the presence of a Reynolds number effect. Specifically, the switch in the near-wake structure, with the accompanying drag jump, was found to occur on the 45° base model with increased Reynolds number ($Re_D \geq 60{,}000$). Hysteresis was present in these measurements as the vortical near-wake flow pattern remained fixed upon reducing the Reynolds

number below the critical value. Flow visualization using stress-sensitive liquid crystals confirmed this phenomena. Trends for the 45° base drag coefficient are shown in Fig. 2.14. The dependency of the near-wake structure on the Reynolds number suggests, in turn, a dependency on the centerbody boundary layer.

The effect of fixing boundary layer transition on the development of the near-wake was also studied in the LaRC 13-inch MSBS [24]. Of particular interest in this study was the effect of fixed-transition on the leading edge of the centerbody. Results for the lower angle slanted-bases ($\theta < 45°$) revealed a significant increase in the overall drag with fixed-transition as shown in Fig. 2.15. This was related to the increased skin friction associated with a turbulent boundary layer. Furthermore, it was demonstrated that higher angle slanted-bases ($\theta > 45°$) do not show an increase in the overall drag with fixed boundary layer transition. Base pressure studies on the higher angle slanted-bases using remote data telemetry [28] revealed significantly higher pressures (less negative) in the region of the vortices with fixed-transition. This counteracted the increase in skin friction along the centerbody. Figure. 2.16 shows results from this base pressure study. Results for the 45° base, shown in Fig. 2.17, indicate that fixing transition on the centerbody leading edge prevents the change in wake structure that occurred with free transition. Fixed-transition results in the 13-inch MSBS clearly indicated that the state of the boundary layer ahead of separation influenced the wake structure greatly [24].

2.4 *Objectives: Boundary Layer Influences*

The intent of the current research was to examine in detail the relationship between the approaching boundary layer and the near-wake structure of a bluff body. Specifically, base pressures and the location of the wake stagnation point have been studied in detail for axisymmetric and non-axisymmetric bluff bodies.

The particular model chosen for this study was a slanted-base cylindrical bluff body, due to its sensitivity to upstream boundary layer effects. Boundary layer thicknesses at separation were varied by varying the Reynolds number and by the use of boundary layer trips along the centerbody of the model. The measurements necessary to accomplish this task are as follows:

(1) Detailed base pressure measurements for various slanted-base configurations with varying Reynolds number and boundary layer trip locations.

(2) Wake stagnation point location measurements for various slanted-base configurations with varying Reynolds number and boundary layer trip locations.

(3) Boundary layer velocity profile measurements ahead of separation for various slanted-base configurations with varying Reynolds number and boundary layer trip locations.

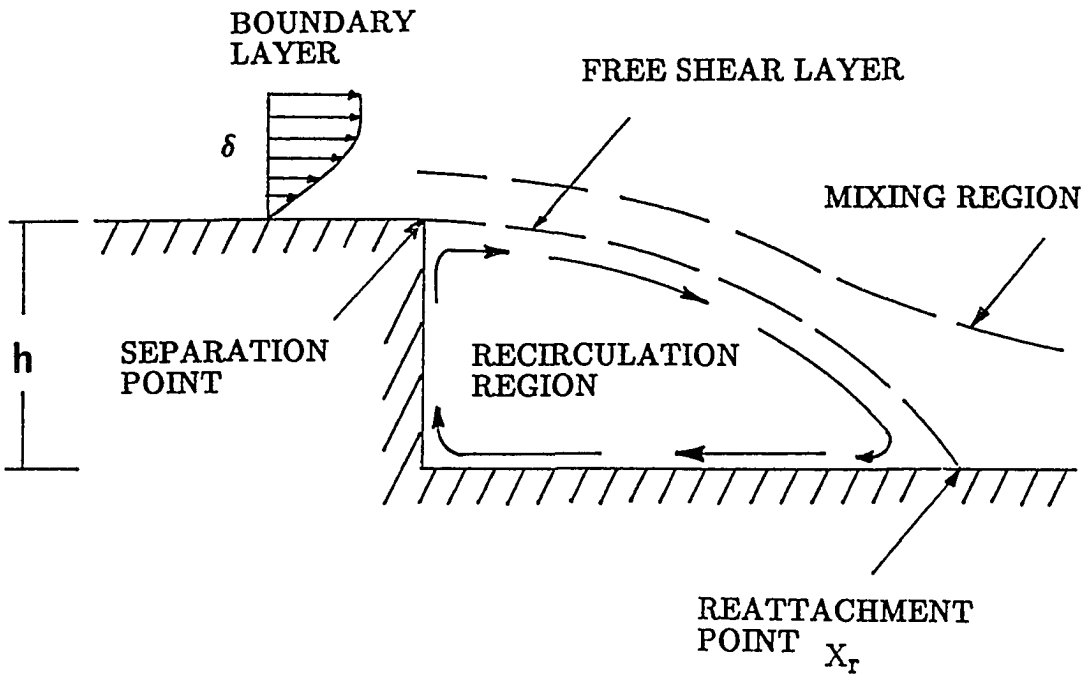

Fig. 2.1 Designation of Flow Zones for a Backward Facing Step Flow

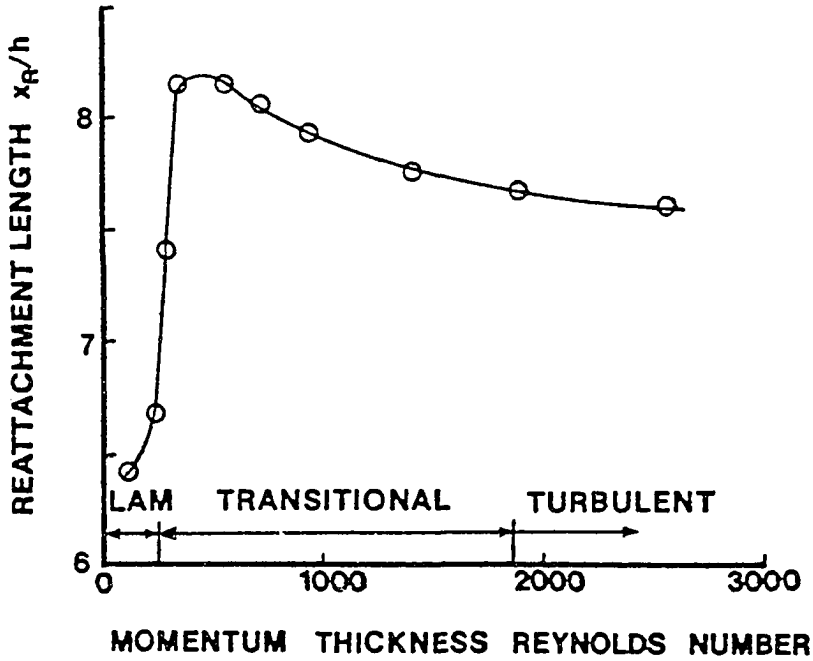

Fig. 2.2 Effect of Boundary Layer State on Flow Reattachment: Backward Facing Step

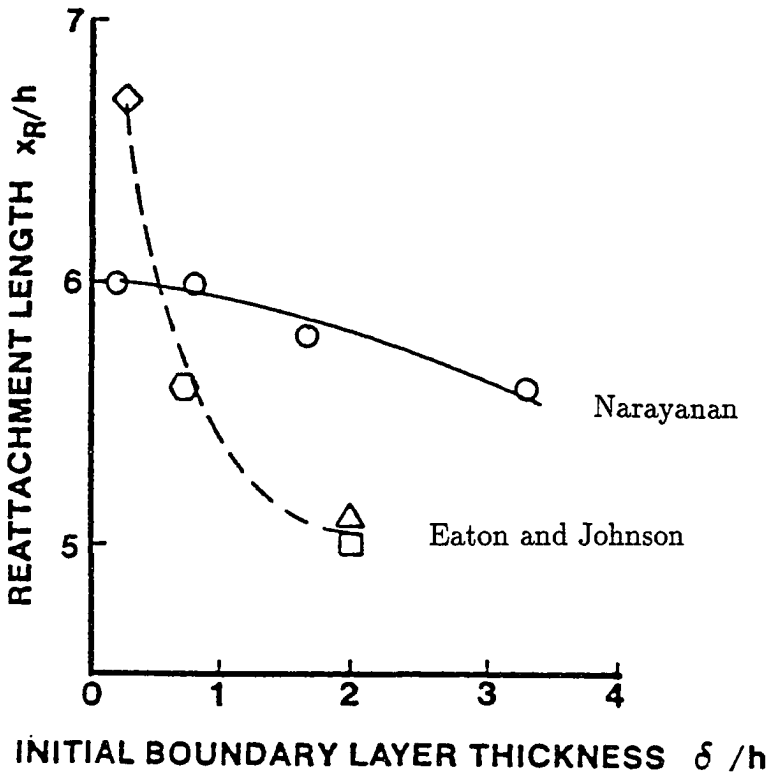

Fig. 2.3 Comparison of Flow Reattachment Locations: Backward Facing Step

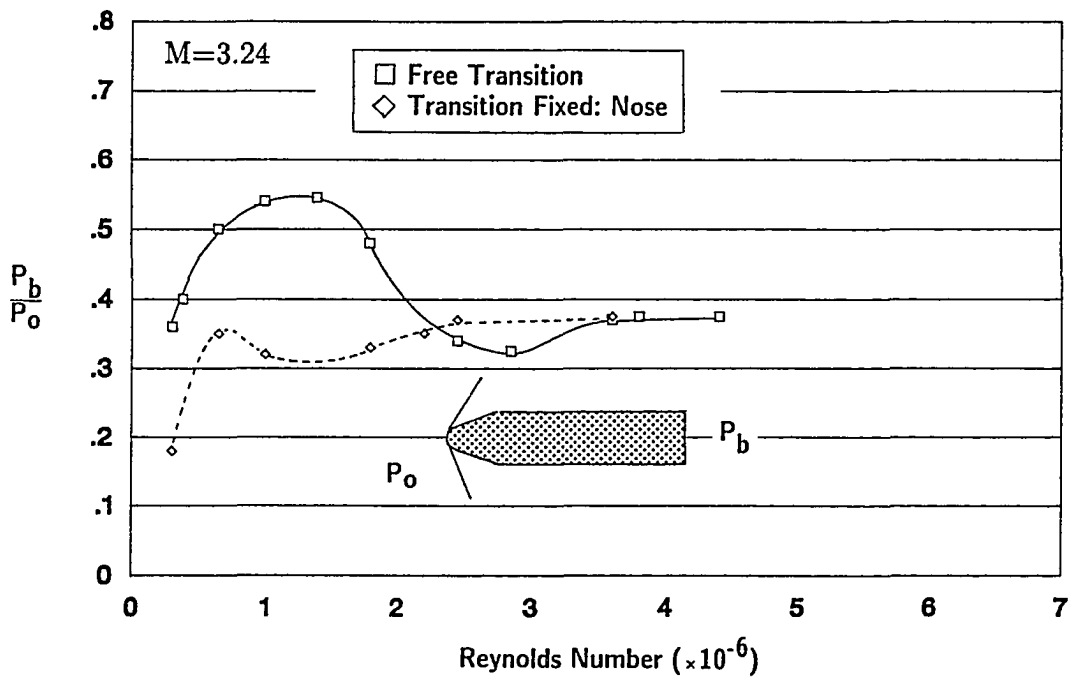

Fig. 2.4 Effect of Boundary Layer State on Base Pressure (Supersonic)

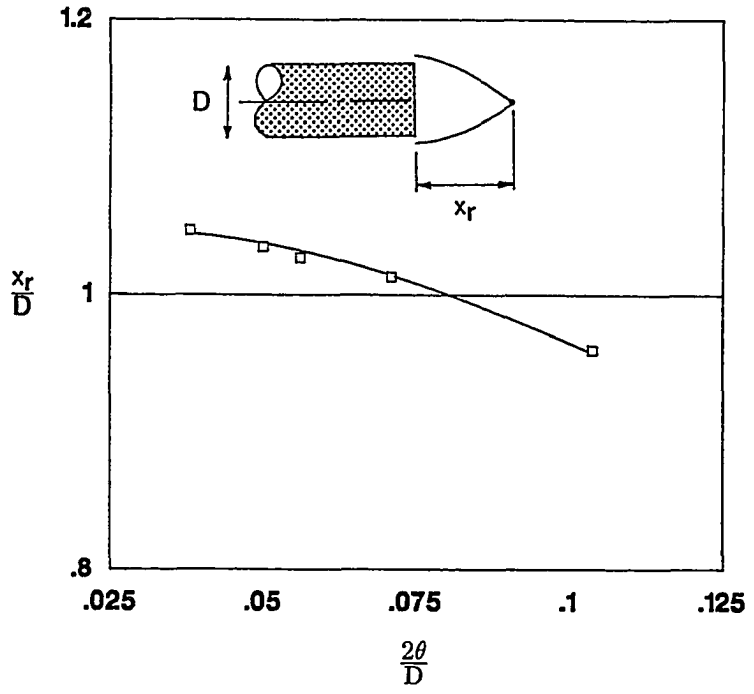

Fig. 2.5 Effect of Momentum Thickness on Wake Stagnation Point Location (Porteiro)

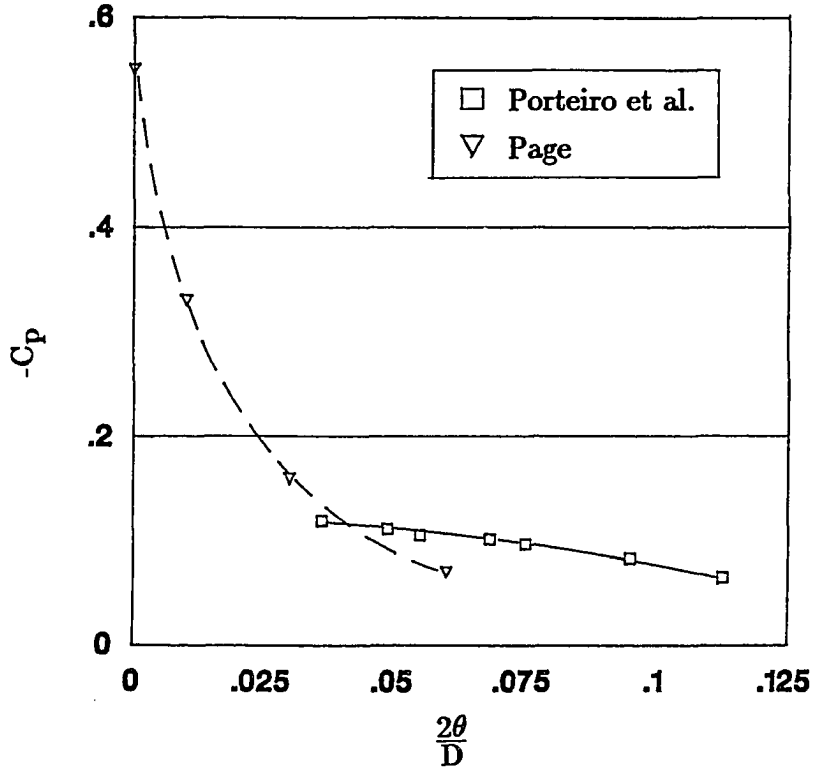

Fig. 2.6 Effect of Momentum Thickness on Base Pressure

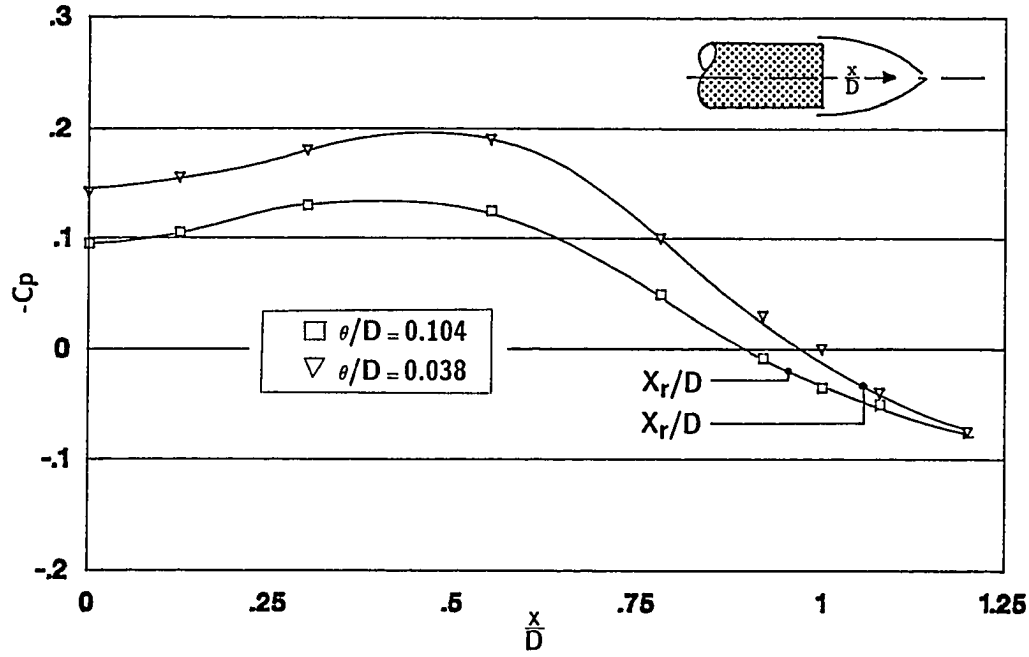

Fig. 2.7 Static Pressure Distribution through the Near-Wake

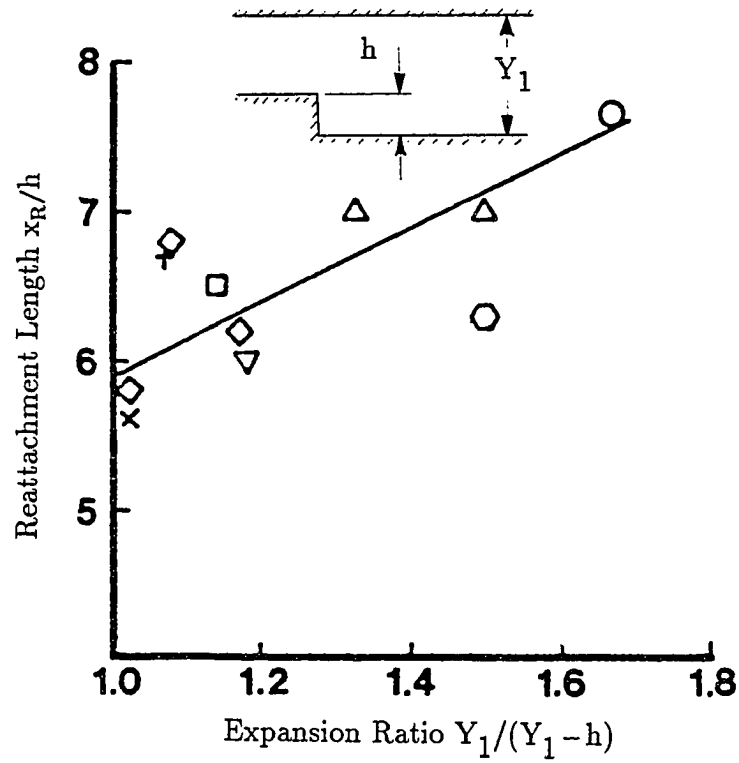

Fig. 2.8 Effect of Pressure Gradient on Reattachment Point Location

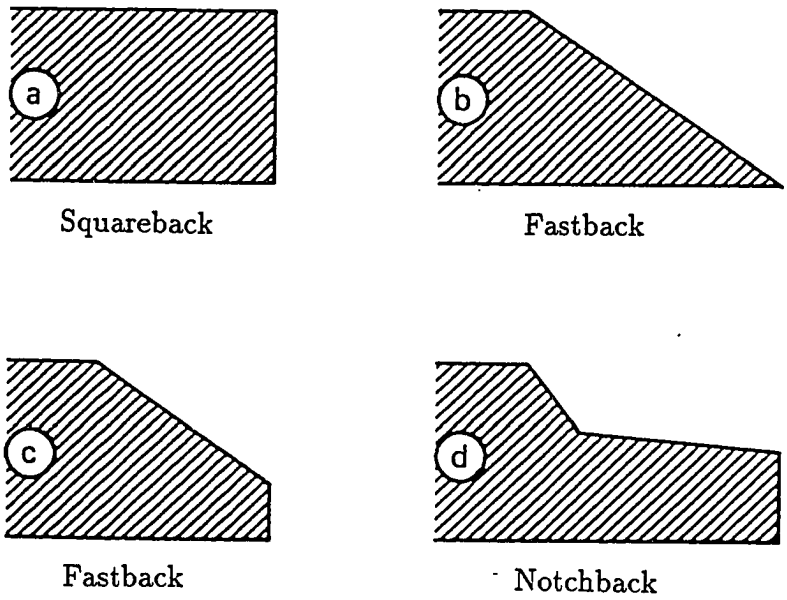

Fig. 2.9 Road Vehicle Slanted Base Configurations

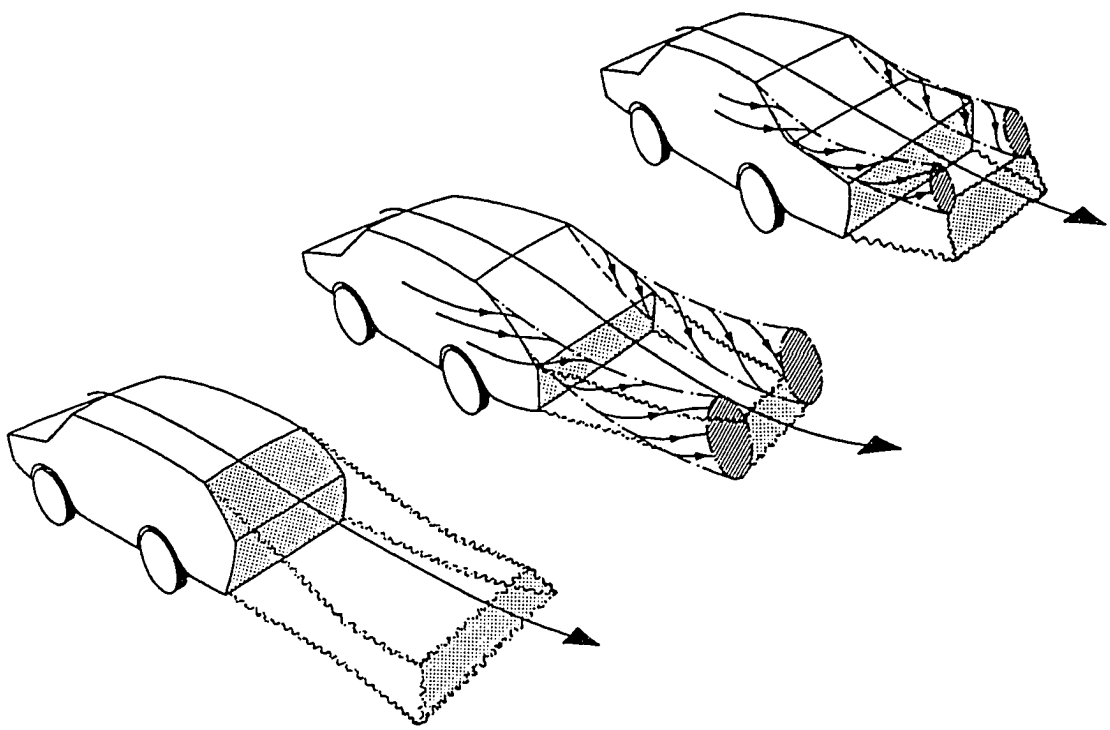

Fig. 2.10 Wake Flow Pattern for Various Road Vehicle Configurations

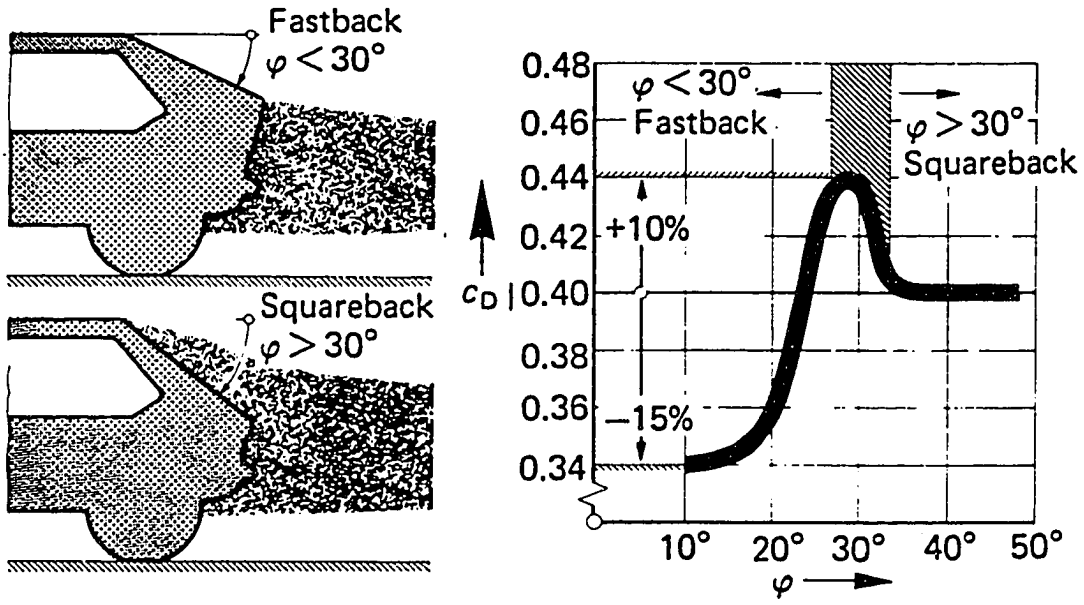

Fig. 2.11 Influence of Rear-Window Angle on Vehicle Drag: VW Golf

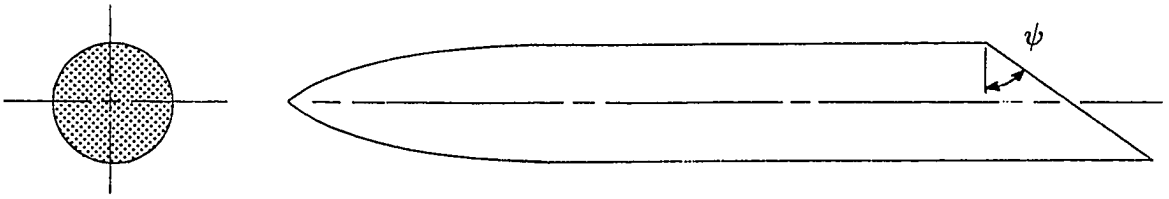

Fig. 2.12 Slanted-Base Ogive Cylinder Configuration

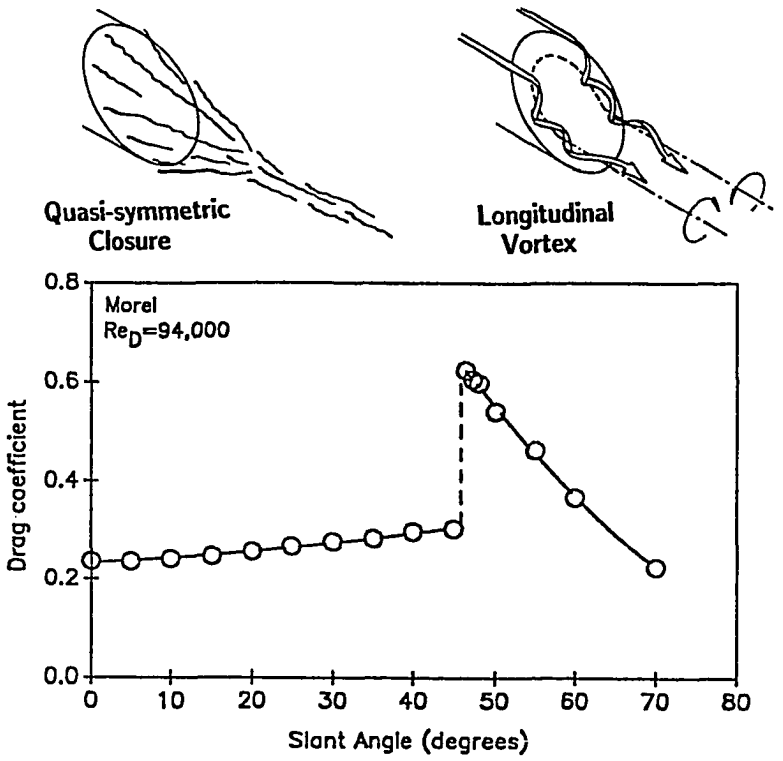

Fig. 2.13 Influence of Slant-Angle on Drag Coefficient: Slanted-Base Ogive Cylinder

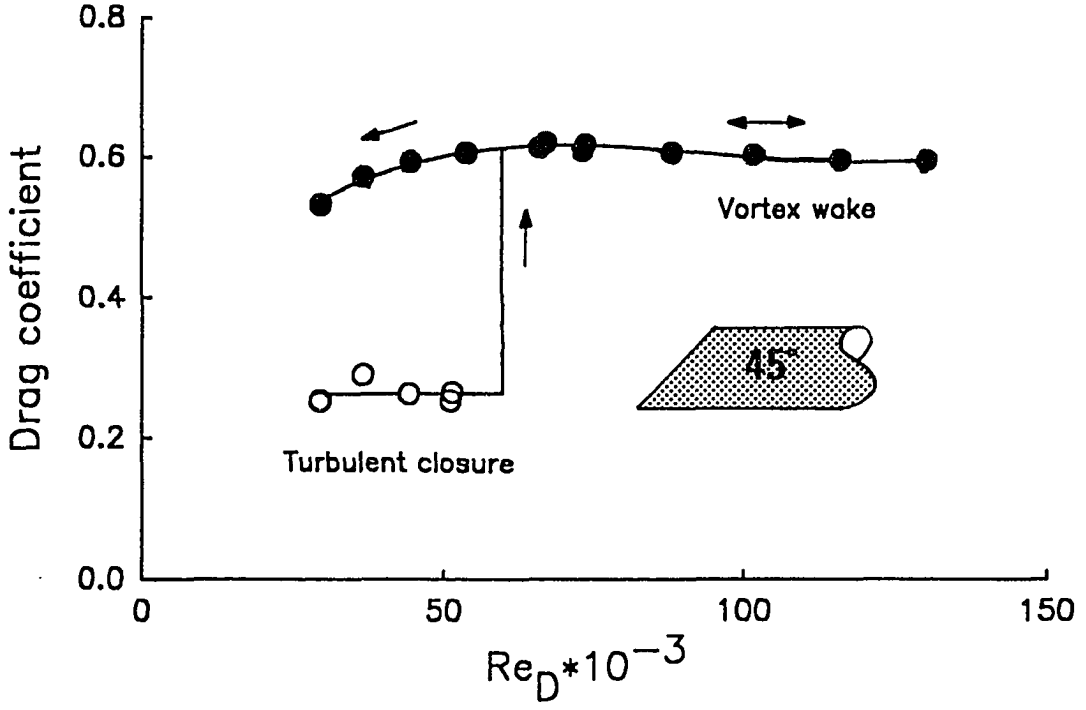

Fig. 2.14 Free-Transition Drag Results: 45° Base

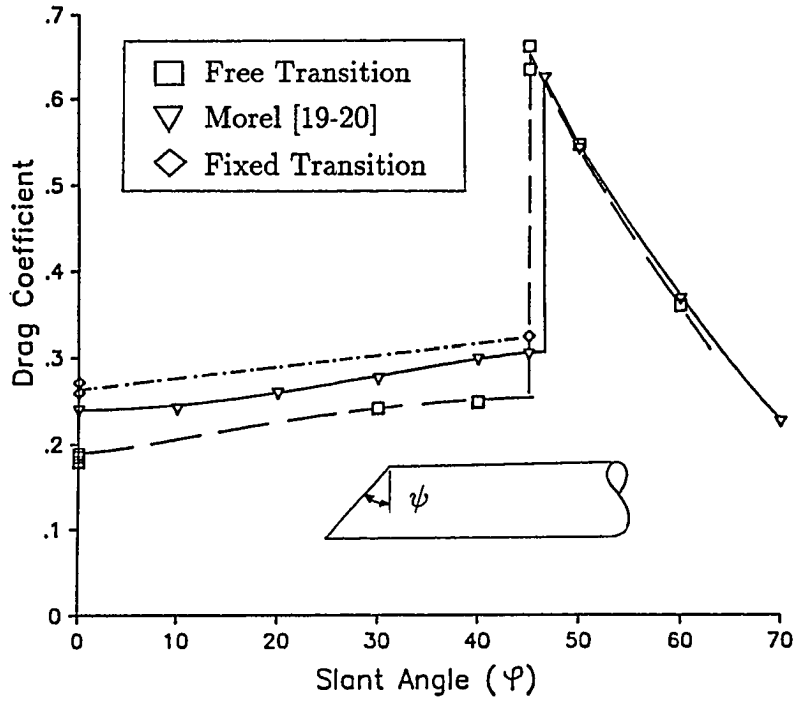

Fig. 2.15 Comparison of Free- and Fixed-Transition Drag Results: Slanted-Base Ogive Cylinder

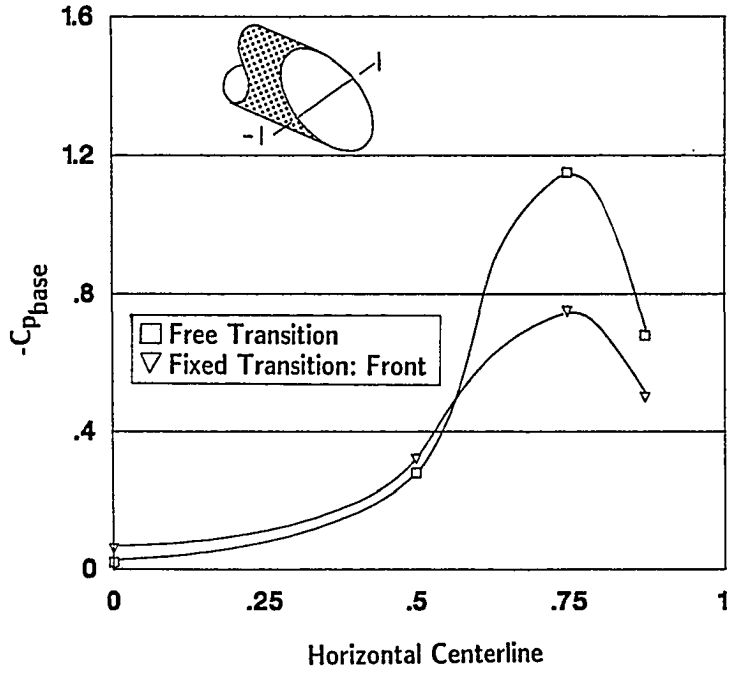

Fig. 2.16 Base Pressure Measurements: 50° Base

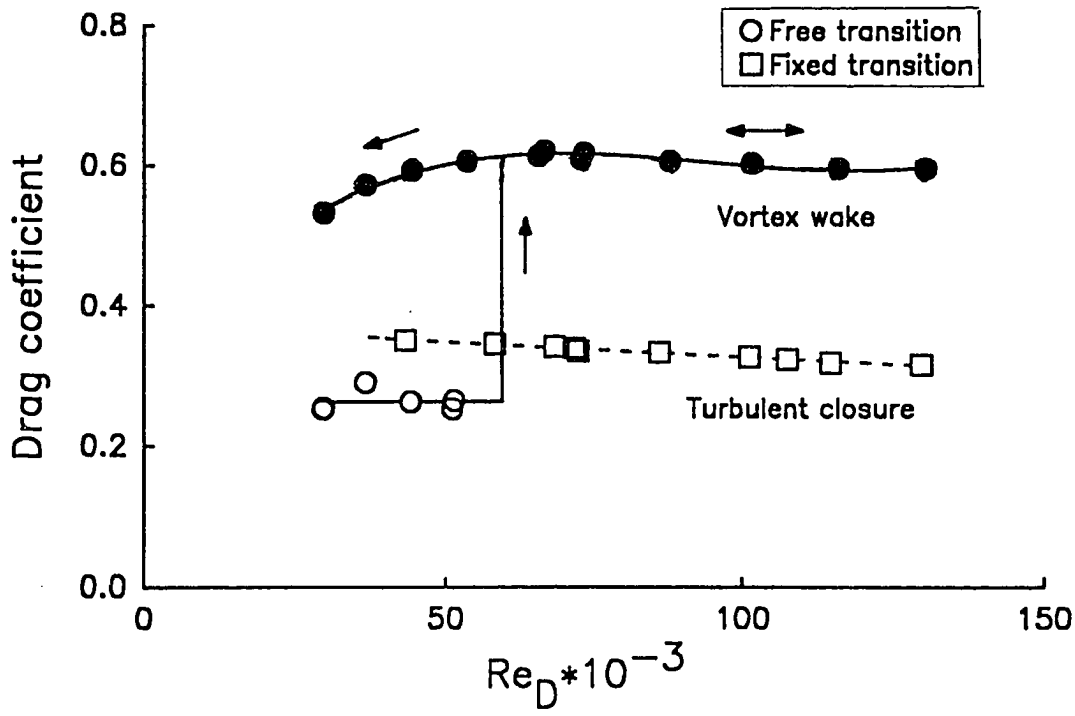

Fig. 2.17 Free- and Fixed-Transition Drag Results: 45° Base

Chapter 3 LARGE-SCALE WAKE STRUCTURES

Dominant features of the unsteady structure of the wake behind two-dimensional bluff bodies have been known and characterized for many years. A classical example is a circular cylinder placed normal to the flow, which was studied in detail by von Kármán [29], and is also discussed by Schlichting [30]. It was determined that radical differences in the flow-field existed between the potential flow solution and that observed experimentally. The cause for such changes are due to boundary layer separation resulting from adverse pressure gradients along the aft portion of the cylinder. Boundary layer separation gives rise to flow reversal and the formation of a vortex as shown in Fig. 3.1. The vortex is shed from the body and moves downstream through the wake, completely changing the flow-field characteristics. Away from the body, a regular pattern of vortices is present, which move alternatively clockwise and counterclockwise as shown in Fig. 3.2. This particular class of vortex shedding is known as a von Kármán vortex sheet [29-30].

3.1 *Bluff Body Flows*

In axisymmetric bluff body flow, large-scale structures, such as periodic vortex shedding, are not as pronounced as those existing in two-dimensional flows [31]; however, large-scale structures in axisymmetric and three-dimensional flows do play an important roll in practical aerodynamic problems. If such structures are repetitive in nature, with significant life cycles, then they can contribute significantly to important practical flow problems, such as aerodynamic noise

[32-34]. Intense vibrations resulting from the extension of dive brakes and other high drag devices is believe to be associated with large-scale fluctuations in the wakes of these devices [35]. In recent years, great emphasis has been placed on understanding these large-scale structures or "coherent structures" in free shear layers.

Coherent structures are of interest in four main classifications of free shear flows as shown in Fig. 3.3 [36-37]. These illustrations are greatly simplified, and in real flows, coherent structures may be more complicated than Fig. 3.3 suggests. For example, coherent structures in a three-dimensional jet are more complicated than the ring vortices shown. This pattern is present in a laminar shear layer shed from a three-dimensional jet as shown in Fig. 3.4, and is a result of inviscid instability and roll-up of the free shear layer. It has been demonstrated by Wille [38] that tripping the boundary layer destroys much of the order associated with a laminar shear layer as shown in Fig. 3.5, however, this does not mean that a turbulent shear layer is devoid of organized large-scale structures. Further downstream, a new set of highly organized coherent structures are present due to another instability mechanism associated with the growing turbulent shear layer [36].

This discussion is not limited to jet flows. Perry and Lim [39] demonstrated through smoke flow visualization studies that the wake of an axisymmetric bluff body can be represented as a modified vortex tube, as shown in Fig. 3.6. A secondary flow causes the vorticity vector in a neutrally buoyant wake to be slanted and it bears a resemblance to a Kármán vortex street. It is suggested that a laterally stretched wake structure, as would occur for a high aspect ratio rectangular tube, would further resemble the classic two-dimensional Kármán vortex street. It was further demonstrated that the essential features of the wake were not altered by variations in the length of the tube. Further

examples of coherent structures are shown in Figs. 3.7-3.8. Figure 3.7 shows the roll-up of the initial shear layer in the wake of a sphere [36, 40-41]. Figure 3.8 shows similar organized structures in a plane mixing layer at three chord Reynolds numbers [36, 42-44].

It is noticed in Fig. 3.8 that considerable variations occur in the small-scale structures with increasing Reynolds number, however, no significant variations are shown in the large-scale structures. It has been demonstrated for a turbulent high Reynolds number flow that the spreading rate of a mixing layer, which Roshko related to the engulfing action of large coherent eddies, is dependent on the presence (or absence) of a boundary layer trip [42, 45]. This suggests that a dependence of the mean flow or large-scale structures on the Reynolds number appears indirectly through the initial free shear layer conditions, such as the boundary layer momentum thickness, and not as a result of viscosity [42]. In fact, it has been shown that similarity in the mixing region is not present, even at distances beyond 1000 initial momentum thicknesses downstream of separation [46].

3.2 *Spectral Analysis*

Advancements in hot-wire instrumentation in the 1970's permitted detailed studies of the periodic nature of free shear layer flows. Techniques, such as spectral analysis of individual hot-wire signals allow for the resolution of frequencies associated with large-scale structures. Cross-spectral analysis of a pair of hot-wire signals allows for a degree of statistical correlation between two spatially different points in the flow.

3.2.1 *Spectral Analysis: Predominant Frequency*

The periodic phenomena in the subsonic wake of a 60° cone was studied by Calvert [47]. Resolution of the frequencies was determined by feeding the hot-wire output signal through a frequency analyzer. A slow traverse across the frequency spectrum was made to avoid erratic and unrepeatable results. Though crude by today's standards, the frequency spectrum of velocity fluctuations revealed a strong peak or predominant frequency which was not detectable by inspection of an oscilloscope trace. The predominant frequency, shown in Fig. 3.9, did not vary from location to location in the wake; however, the peak was not resolvable just past the separation point, i.e., upstream of the static pressure minimum.

The advances in hot-wire technology in the early 1970's allowed for spectral and cross-spectral analysis of hot-wire signals. Roberts [48], studying the wake structure of a disk placed normal to the freestream, performed spectral measurements using a single hot-wire. Due to the uncertainty of hot-wire measurements in highly turbulent flows (turbulence intensities $> 10\%$), measurements were restricted to the far-wake, at least 9 diameters downstream of the disk ($\frac{x}{D} > 9$). Spectral analysis revealed a definite peak at all locations in the wake, except directly on the axis of symmetry. A typical power spectra is given in Fig. 3.10. The peak occurred at a Strouhal number $\left(\frac{fD}{U_\infty}\right)$ of $St_D = 0.135$. The frequency of the peak was independent of probe position which is in agreement with the earlier measurements of Calvert [47]. The magnitude of the peak was, however, determined to be a function of probe position. A maximum spectral peak was reached at a radial distance of 0.83 disk diameters ($\frac{r}{D} = 0.83$) and the minimum axial location of $\frac{x}{D} = 9$. The spectral peak decreased with increasing distance from the disk.

The predominant frequency in the wake of slanted-base bluff bodies was studied by Xia and Bearman [22] with a single hot-wire. Measurements were restricted to the free shear layer in a plane, one diameter from the model base. Spectral analysis of the fluctuating streamwise velocity component revealed definite peaks for the lower angle slant-bases, i.e., when the closed near-wake structure was present. The predominant frequency of an axisymmetric bluff body, $St_{D_{PRED}} = 0.25$, was determined to be almost twice that determined for an axisymmetric wake of a disk placed normal to the freestream. The strongest peak in the measurements of Xia and Bearman [22] occurred for a slant-angle of 30°; however, a predominant frequency became increasingly difficult to measure as the critical slant-angle was approached. The predominant frequency was shown to increase with increasing base slant-angle. The relationship between the base slant-angle and the predominant frequency is shown in Fig. 3.11. When the longitudinal vortex near-wake was present, no predominant frequencies were resolved. Furthermore, a systematic variation in the predominant frequency with variations in the Reynolds number could not be resolved.

3.2.2 *Cross-Spectral Analysis: Coherence*

Roberts [48] demonstrated how cross-spectral measurements could be performed by the analysis of two concurrent hot-wire signals in an axisymmetric wake of a disk. The cross-spectra, unlike the power spectra, is a complex function defined as:

$$P(\xi, \omega) = C_\omega + iQ_\omega \qquad (3.1)$$

Cross-spectra measurements were taken around a prescribed circle at various angular separations between the probes as shown in Fig. 3.12. The imaginary cross-spectrum component, Q_ω, was determined to be insignificant over the whole

frequency range tested, showing that signals were either in phase or 180° out of phase.

Roberts [48] then determined the coherence of the hot-wire signals, which is defined as:

$$\Gamma = \frac{\sqrt{C_\omega{}^2 + Q_\omega{}^2}}{P_1(\omega)\ P_2(\omega)} \tag{3.2}$$

where $P_1(\omega)$ and $P_2(\omega)$ are the power spectra of the two hot-wire signals. Variations of coherence with frequency, for various angular separations are shown in Fig. 3.13. Peaks in the coherence appear at the same frequency as the power spectra ($St_{D_{PRED}} = 0.135$). Variations in coherence at constant frequency are shown in Fig. 3.14. At small angular separations, the coherence at the predominant frequency is highly positive, but decreases with increasing $\Delta\beta$. For $\Delta\beta > 90°$, the coherence continues to drop, reaching a value of -0.8 at $\Delta\beta = 180°$. Roberts reasoned that the highly negative coherence found at the predominant frequency for an angular separation of 180° was consistent with a flapping motion of the near-wake. Therefore, the coherent structures tended to be out of phase, engulfing the hot-wire probes alternately.

Xia and Bearman [22] performed cross-spectral measurements in the wake of an axisymmetric bluff body. Measurements were restricted to the free shear layer in a plane located one diameter from the model base. Variations in coherence at constant frequency are shown in Fig. 3.15. At the predominant frequency, the coherence is highly positive for small angular separations, $\Delta\beta$, but decreases rapidly with increasing $\Delta\beta$. A minimum value of -0.8 is reached at $\Delta\beta = 180°$, similar to the measurements for a disk normal to the freestream. At low frequencies, C_ω remains highly positive for $0° < \Delta\beta < 180°$, reaching a minimum value of $C_\omega \simeq 0.7$ for $\Delta\beta = 180°$. This is a significant departure from the

low frequency measurements in the wake of a disk. This may be attributed to variations in the low frequency wake characteristics as the wake structures are convected downstream. It is recalled that the measurement location of Roberts was further downstream ($\frac{x}{D} = 9$) than that of Xia and Bearman ($\frac{x}{D} = 1$).

Fuchs, Mercker, and Michel [36-37] also performed cross-spectral measurements in the axisymmetric wake of a disk. The hot-wires were restricted to the far-wake of the disk ($\frac{x}{D} = 9$). Variations in coherence at constant frequency, shown in Fig. 3.16, are in agreement with previous disk wake measurements.

The symmetry imposed by the disk allowed for an illustrative description of the large-scale wake structures by examining elementary modes of instability or azimuthal constituents. The percentage of fluctuating energy contained in individual modes was determined through a procedure discussed in detail in Chapter 5. It was determined that only a small number of modes were necessary to describe the unsteady behavior of an axisymmetric bluff body wake or jet. Results of this study for an axisymmetric wake are presented in Fig. 3.17. The $m = 1$ mode is dominant at the predominant frequency, suggesting that a well ordered turbulent structure, similar to a Kármán vortex sheet was present. (This is also evident by the highly negative coherence at the predominant frequency for $\Delta\beta = 180^\circ$ in Fig. 3.13.) At lower frequencies, the $m = 2$ mode dominates. Of particular interest is the dominance of the m=1 and m=2 modes for wake flows, while m=0 and m=1 is shown to dominate jet flows [36-37]. A further discussion of the interpretation of modes is given in Chapter 5.

Large-scale structures are particularly relevant when considering oscillating forces. The domination of the $m = 1$ mode in an axisymmetric wake can be associated with oscillating lift forces and moments on the body. The direction of the oscillatory lift and moment would vary randomly in a plane normal to the freestream. Oscillating drag forces on the body could be present if a dominant

$m = 0$ mode was represented, however, this was shown not to be the case for an axisymmetric wake. Fuchs, Mercker, and Michel [36-37] contend that higher order modes ($m > 1$) cannot produce net forces on the body.

A more recent use of the modal expansion technique was made by Kiya, et al. [49] studying axisymmetric separating and reattaching flows on blunt circular cylinders. Azimuthal constituents were determined from pressure fluctuations measured on the reattachment line using a semiconductor strain gage pressure transducer. The m=1 mode showed a maximum, however, a maximum was also shown for m=9. The $m = 9$ mode is attributed to a 9-cell structure along the reattachment line.

3.3 *Objectives: Large-Scale Structures*

Upon completion of the objectives discussed in the previous chapter, it was intended to study the development of large-scale structures in the wake of axisymmetric and slanted-base bluff bodies. Previous research by Roberts [48] and Fuchs, Mercker, and Michel [36-37] provided the ground work for such a study. Of particular interest is the influence of the developing boundary layer ahead of separation on large-scale structures in the wake. This study is in the spirit of Wille's early work with three-dimensional jet flows [38].

It is also intended to expand on the work of Xia and Bearman [22] by examining Reynolds number effects on large-scale structures behind slanted-base bluff bodies. The effects of tripping the boundary layer upstream of separation shall be examined. The measurements necessary to accomplish these task are as follows:

(1) Wake periodicity measurements using a single hot-wire at different locations in the wakes of slanted-base bluff body models versus Reynolds number.

(2) Wake periodicity measurements in the wakes of slanted-base bluff body models with boundary layer trips ahead of separation.

(3) Coherence measurements using two hot-wires positioned along a plane in the wake of an axisymmetric bluff body. The intent of these measurements is to examine the effects of boundary layer transition ahead of separation, and to compare these results with an initially laminar free shear layer.

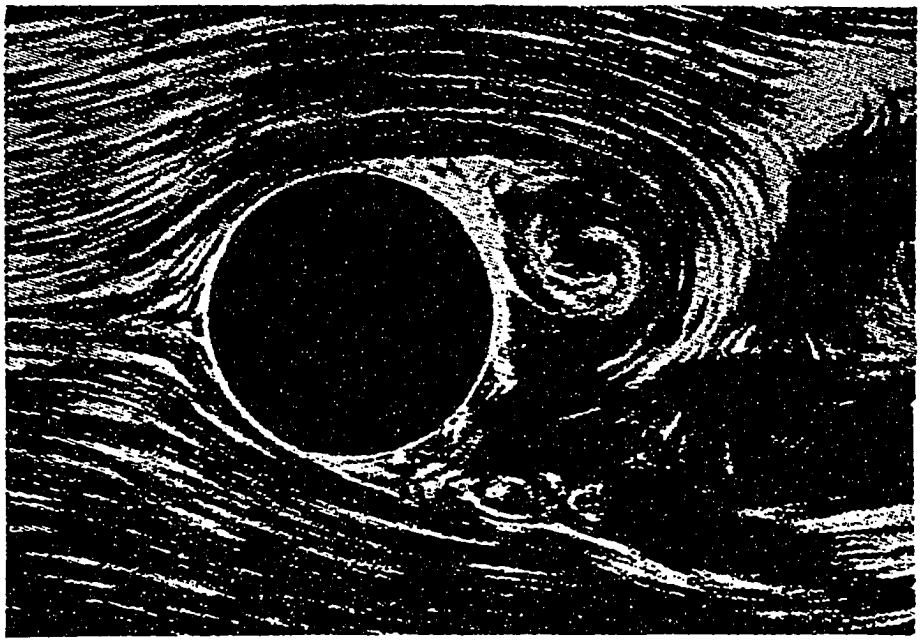

Fig. 3.1 Boundary Layer Separation in the Wake of a Circular Cylinder

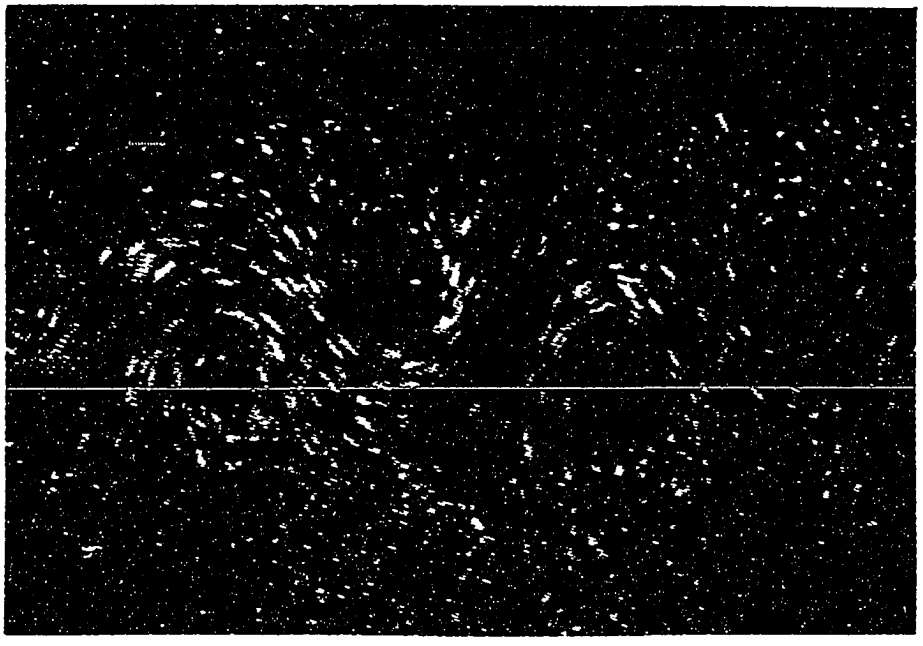

Fig. 3.2 Kármán Vortex Street in the Wake of a Circular Cylinder

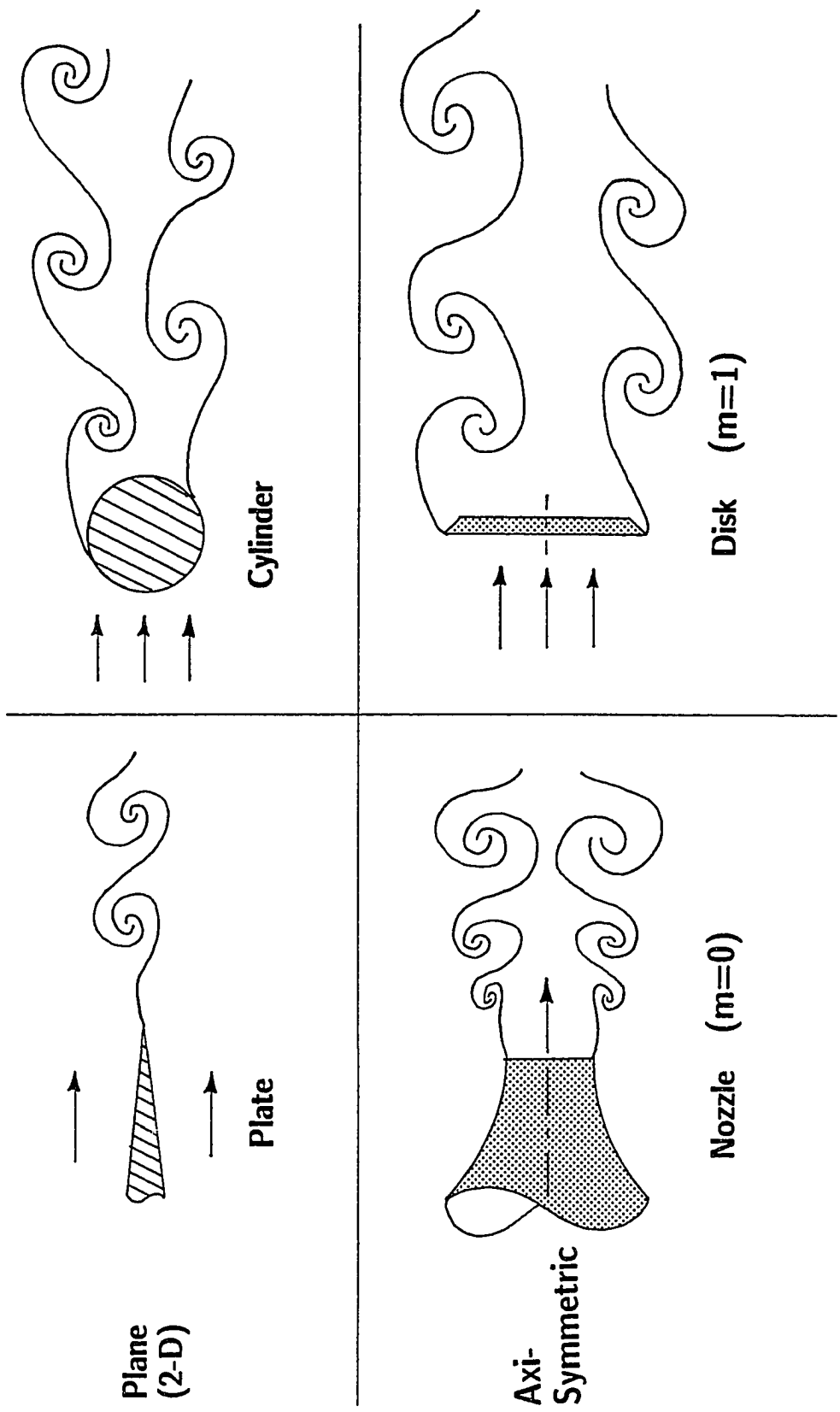

Fig. 3.3 Coherent Structures in Free Turbulent Shear Flows

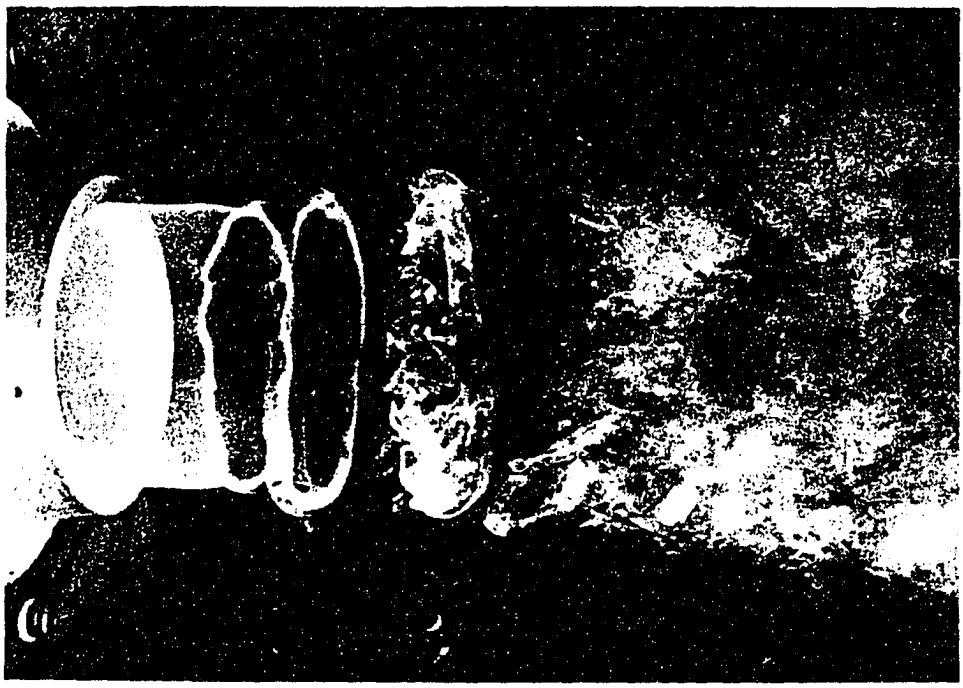

Fig. 3.4 Ring Vortices in the Wake of a Circular Jet

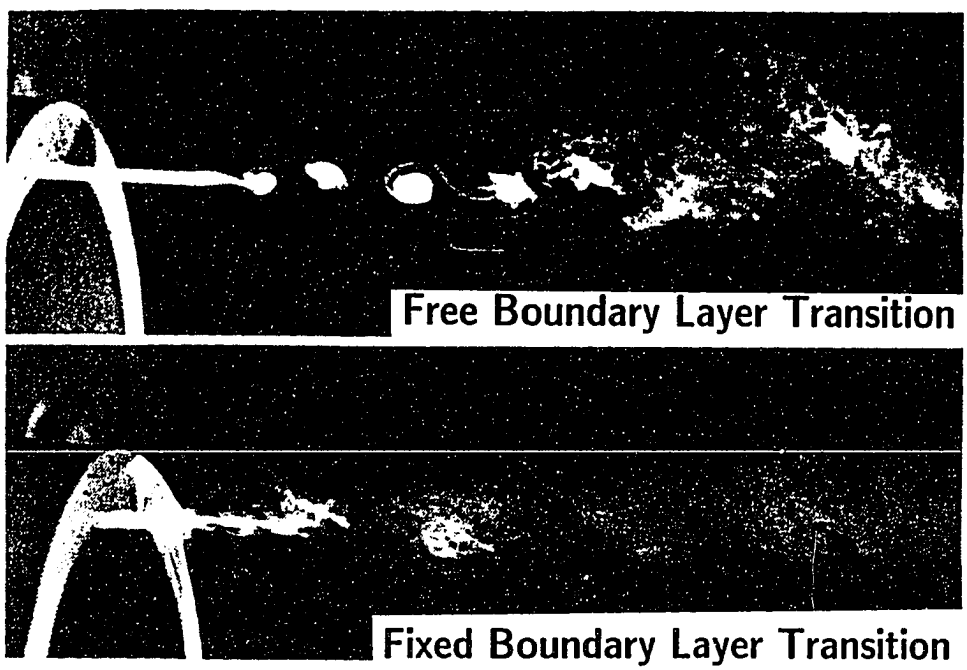

Fig. 3.5 Effect of Boundary Layer State on Ring Vortex Development

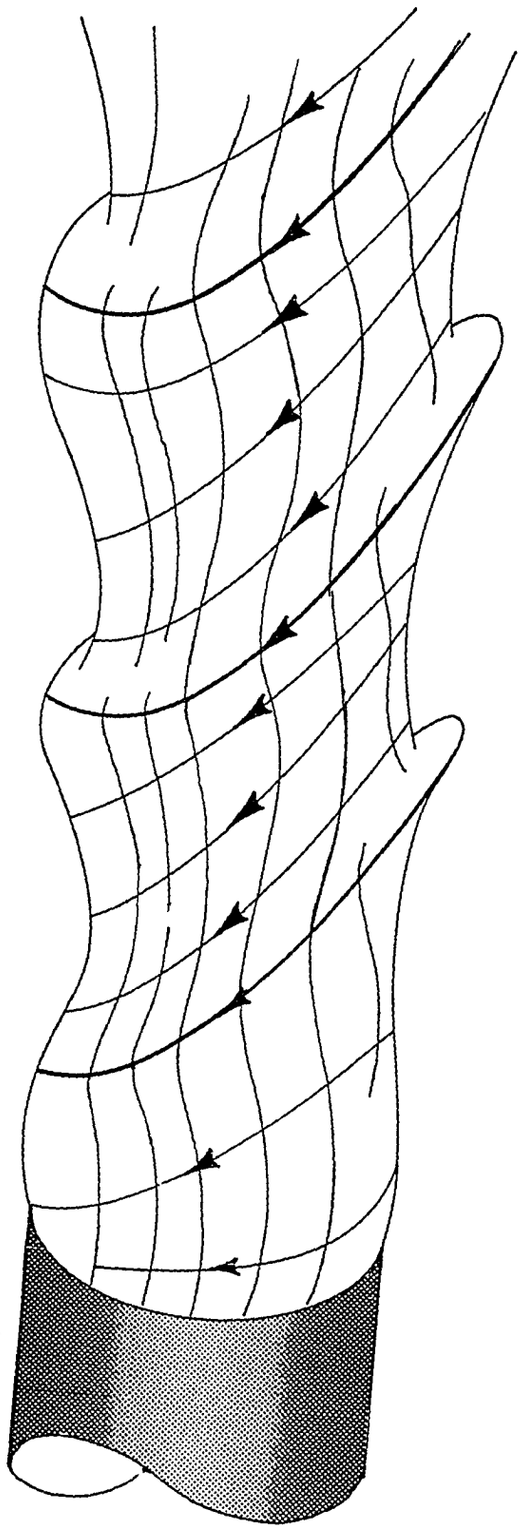

Fig. 3.6 *Organized Structures in the Wake of a Cylinder Aligned with the Flow*

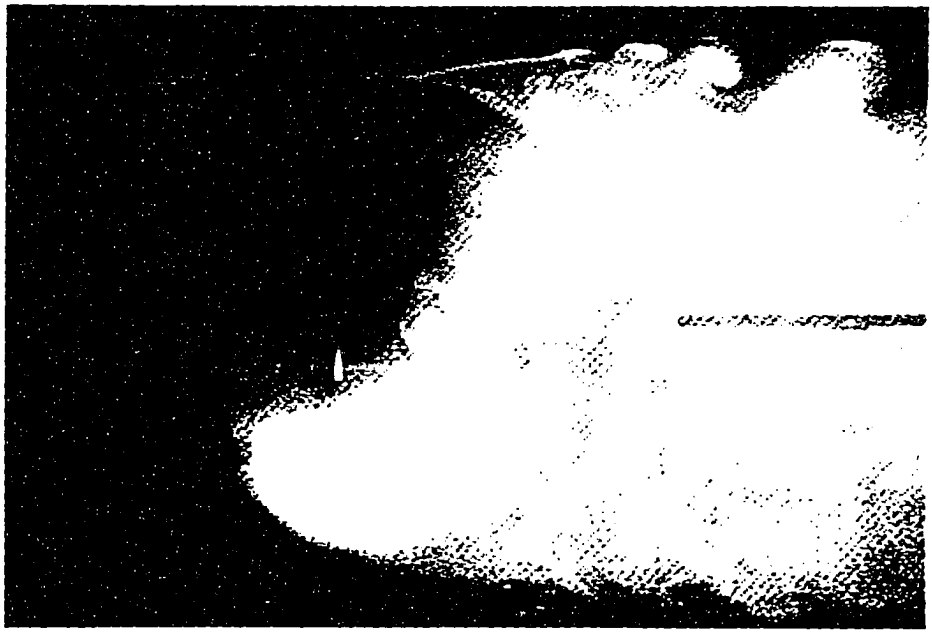

Fig. 3.7 Organized Structures in the Wake of a Sphere

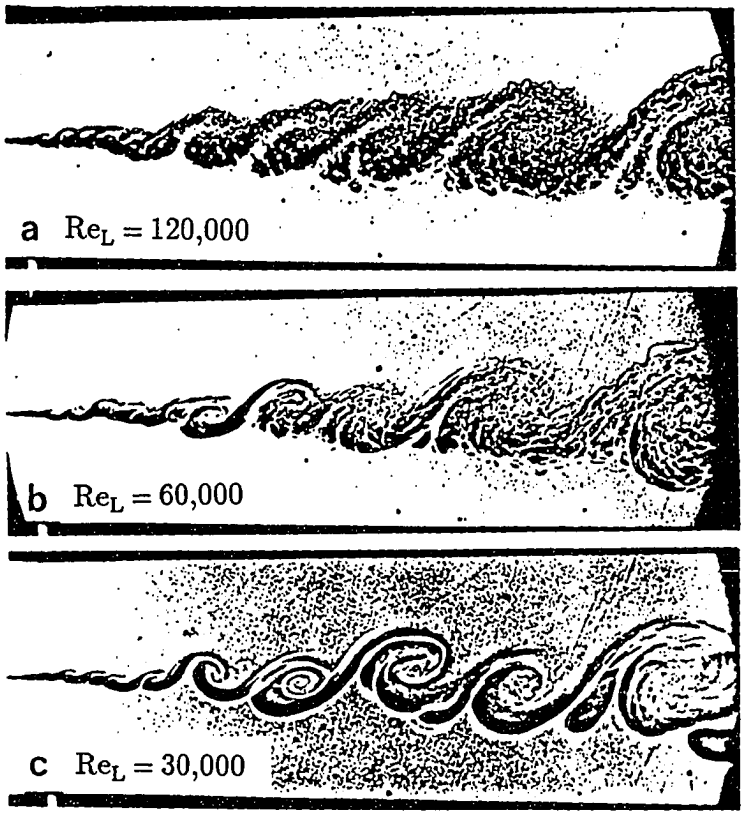

Fig. 3.8 Organized Structures in a Plane Mixing Layer

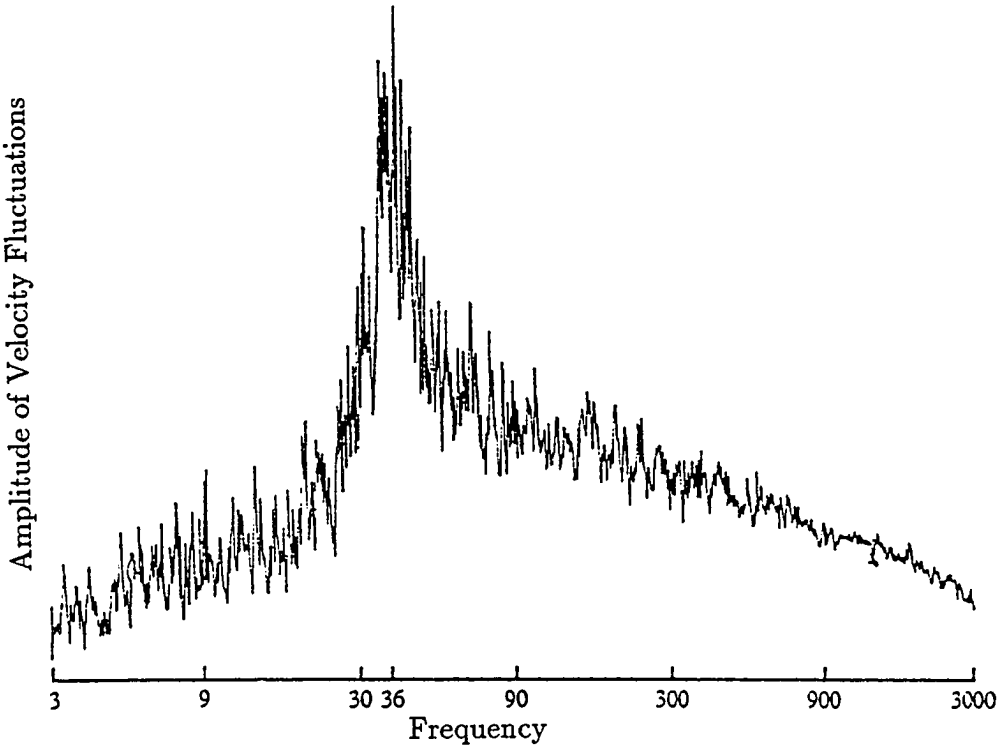

Fig. 3.9 Spectrum in the Wake of a 60° Cone

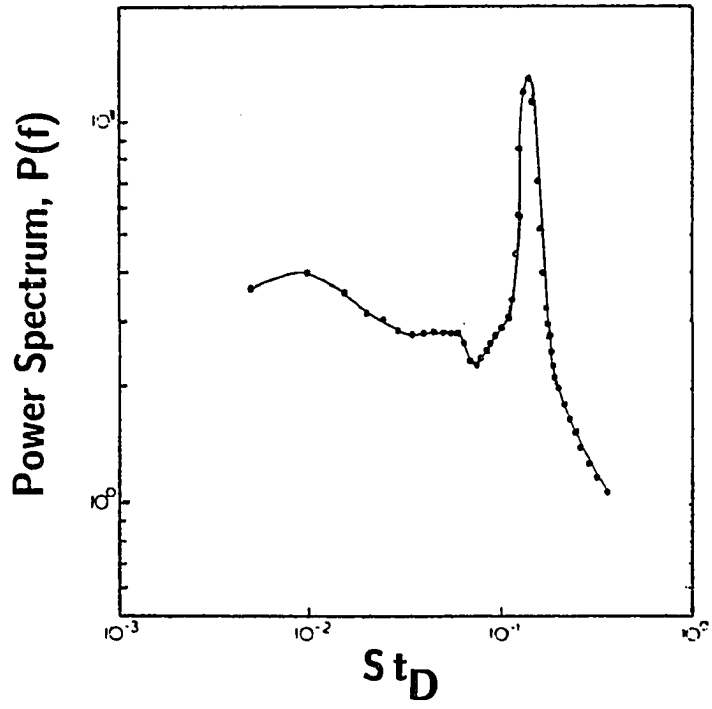

Fig. 3.10 Power Spectrum in the Wake of a Circular Disk

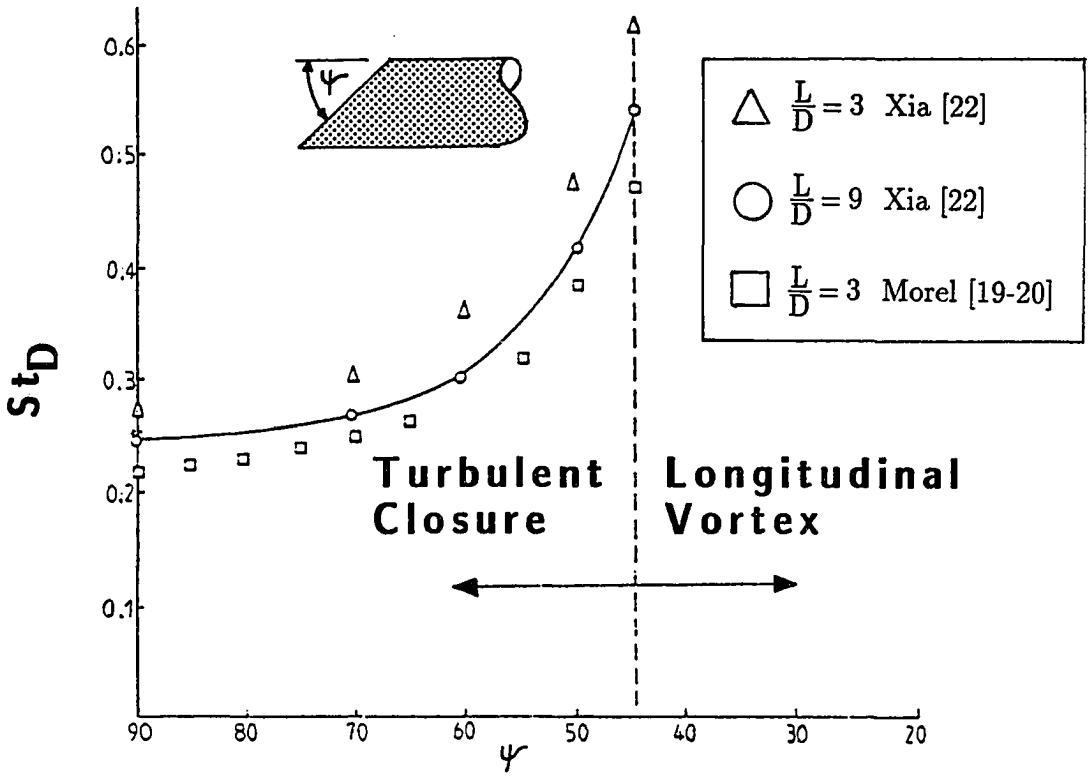

Fig. 3.11 Predominant Frequencies in the Wake of Slanted-Base Ogive Cylinders

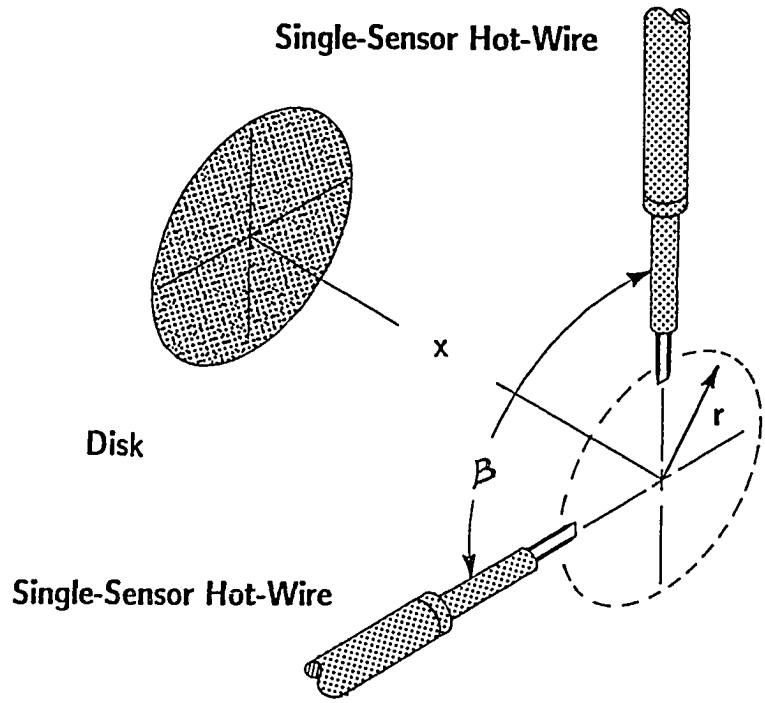

Fig. 3.12 Coordinate System for Cross-Spectra Measurements

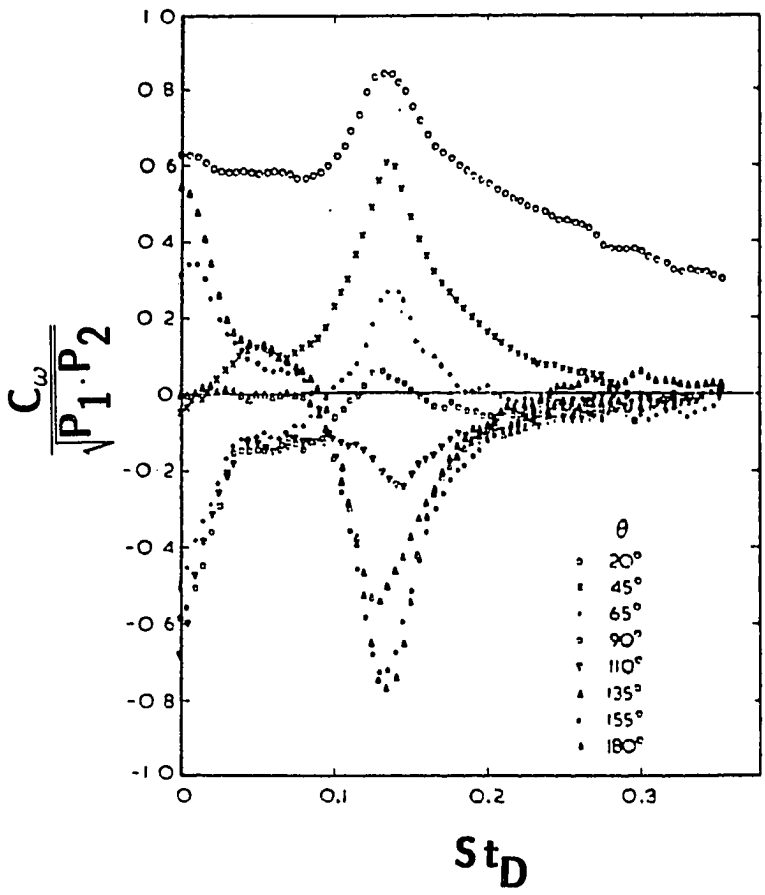

Fig. 3.13 Coherence Measurements in the Wake of a Circular Disk (Roberts)

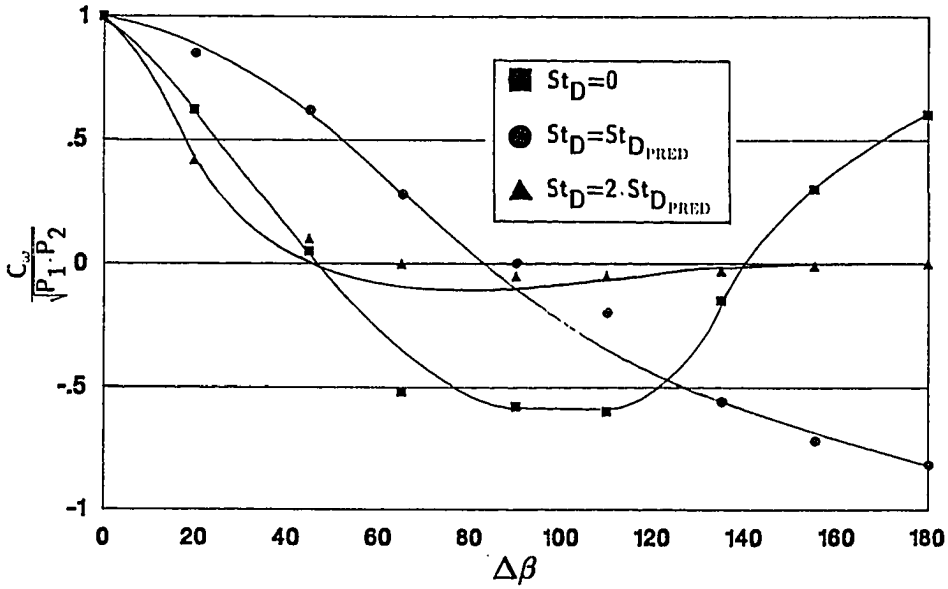

Fig. 3.14 Coherence Measurements at Constant Frequency (Roberts)

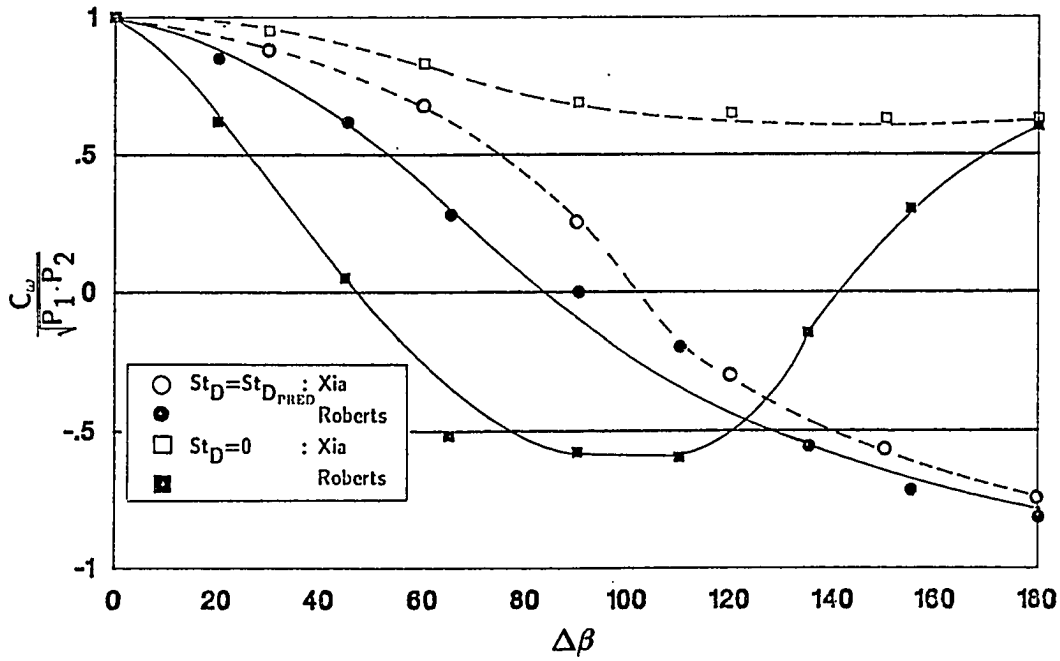

Fig. 3.15 Coherence Measurements at Constant Frequency (Xia)

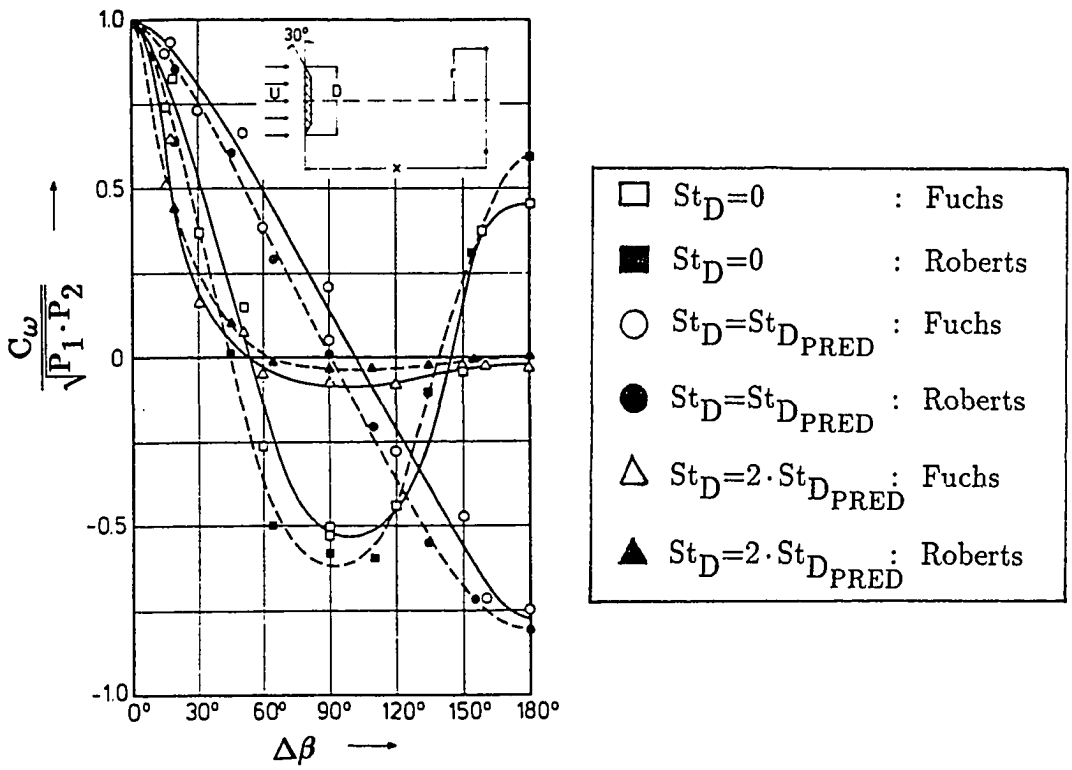

Fig. 3.16 Coherence Measurements at Constant Frequency (Fuchs)

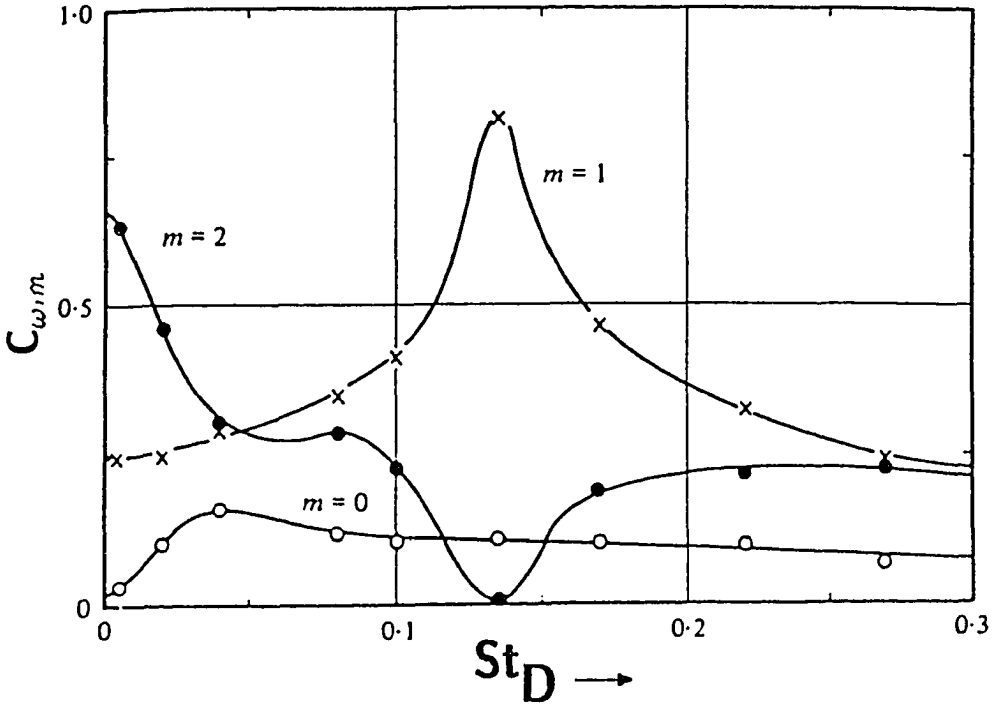

Fig. 3.17 Summary of Azimuthal Constituents in the Wake of a Circular Disk

Chapter 4 STEADY NEAR-WAKE ANALYSIS

The material in this chapter is intended for conceptual understanding of the steady development of slanted-base bluff body near-wake flows and is not intended to be an exhaustive study of the near-wake flow field. A full three-dimensional Navier-Stokes solution with an appropriate turbulence model would be necessary to fully describe the complex near-wake formations behind bluff bodies. Instead, classical theories with appropriate simplifications are used to provide a physical understanding of base flow phenomena.

4.1 *Vortex Formation*

Flow visualization results from previous studies indicate that the formation of the vortical near-wake behind a slanted-base bluff body is accompanied by reattachment of the free shear layer on the base [16-26]. This is represented in Fig. 4.1. If flow reattachment can be related to the occurrence of these vortices through suitable arguments, then the formation of the vortical near-wake can be predicted in terms of the parameters influencing flow reattachment.

An idealized base flow model for a slanted-base bluff body was developed by Sedney [50] to study the vortical near-wake formation. A vehicle-like configuration was chosen for this study as shown in Fig. 4.2 due to its straight side edges. In order to form a simple solution to the base flow problem, it was assumed that the slanted-base was infinitely long so that no upstream or downstream base corner existed. Therefore, a solution could be developed

independent of variations along the base. This assumption is common in the study of infinite swept wings [50-51]. Further simplifications made in this study were to neglect the upstream influences on the resulting base flow, such as the boundary layer, streamline curvature, and the pressure gradients along the centerbody. This allowed the external flow upstream of the base to be considered equivalent to the freestream velocity, U_∞, moving parallel to the top and side surfaces as shown in Fig. 4.3.

Under these assumptions, the side-flow component normal to the separation line, U_n, is represented as

$$U_n = U_\infty \cdot \cos\psi \tag{4.1}$$

An estimate of the side-flow component parallel to the edge, U_t, is represented as

$$U_t = U_\infty \cdot \sin\psi \tag{4.2}$$

An important parameter that can be estimated from this simplified base flow model is the swirl angle of the near-wake vortex, defined as

$$\phi = \tan^{-1}\left(\frac{U_s}{U_\beta}\right) \tag{4.3}$$

where U_β and U_s are respectively the angular and streamwise vortex velocity components. Sedney estimated the vortex velocity components as

$$U_\beta = \mathcal{O}(U_n) = \mathcal{O}(U_\infty \cdot \cos\psi) \tag{4.4}$$

$$U_s = \mathcal{O}(U_t) = \mathcal{O}(U_\infty \cdot \sin\psi) \tag{4.5}$$

Therefore, the vortex swirl angle, in the presence of flow reattachment, is estimated as

$$\phi \simeq \psi \tag{4.6}$$

4.2 *Parameters Influencing Reattachment*

A literature survey on the requirements for a completely laminar free shear layer behind a bluff body was conducted by Roshko and Lau [52]. The results of their survey are shown in Fig. 4.4. It is shown that the criterion for a completely laminar free shear layer is

$$Re_D \leq 100 \cdot \frac{L}{D} \tag{4.7}$$

or

$$Re_L \leq 100 \cdot \left(\frac{L}{D}\right)^2 \tag{4.8}$$

This criterion depends on the Reynolds number and the fineness ratio, $\frac{L}{D}$, of the bluff body. Equation (4.8) can be modified by assuming that a Blausius boundary layer velocity profile is present at separation. The boundary layer thickness at separation, δ_S, can therefore be approximated as

$$\frac{\delta_S}{L} = \frac{5}{\sqrt{Re_L}} \tag{4.9}$$

Substituting Eqn. (4.9) into Eqn. (4.8) allows the laminar reattachment criterion to be express in terms of the boundary layer thickness at separation.

$$\frac{\delta_S}{R} \sim 1 \tag{4.10}$$

where R is the radius of a bluff body, or the step height of a backward facing step. Equation (4.10) shows that laminar reattachment of a free shear layer is not possible if the shear layer thickness is small compared to R. This suggests that increasing the Reynolds number results in transition in the free shear layer upstream of the wake stagnation point. This behavior is shown in the smoke visualization pictures in the free shear layer of a backward facing step shown in

Fig. 4.5. Transition in the free shear layer before reattachment results in increased mixing and therefore, a further reduction in base pressure compared to the case of no transition in the free shear layer. (Transition in the free shear layer is indicated by a dispersion of smoke due to turbulent mixing.) An increased curvature of the free shear layer towards the base axis also results, which may allow for reattachment to occur sooner.

For the case of a slanted-base bluff body, transition in the free shear layer may cause reattachment on the slanted-base, which would not occur for a laminar free shear layer. If the shear layer is turbulent from the onset of separation, as occurs for fixed boundary layer transition, then base flow reattachment is further enhanced. It has been demonstrated in previous studies that a turbulent centerbody boundary layer actually prevents the formation of the vortical wake resulting from base flow reattachment [24]. This was clearly shown in Fig. 2.17. Therefore, it is not possible to fully explain reattachment in terms of increased turbulence in the free shear layer.

To fully understand the occurrence and development of near-wake flow patterns behind slanted-base bluff bodies, it appears that one must also analyze the boundary layer state ahead of separation. The boundary layer displacement thickness, δ^*, indicates the distance external streamlines are shifted away from the wall due to viscous effects as illustrated in Fig. 4.6. Therefore, thicker boundary layers at separation result in the external streamlines being released further from the body, reducing the possibility of flow reattachment on downstream surfaces. The displacement thickness decreases with increasing Reynolds number until transition moves upstream from the free shear layer to the boundary layer ahead of separation. The possibility of flow reattachment on downstream surfaces is greatest when the displacement thickness is a minimum, i.e., the point where transition just occurs at separation. Therefore, a minimum

displacement thickness occurs simultaneously with increased mixing within the separated region. These two effects, occurring simultaneously, may be responsible for the change in flow structure in the near-wake. This is illustrated in Fig. 4.7. Nash [4] has concluded that transition occurring just ahead of separation on bluff bodies results in a minimum base pressure. Other authors simply speculated that this is attributed to some phenomena of turbulent flow occurring close to transition [53-54].

4.3 *Prediction of Reattachment: Theory of Nash*

A two-dimensional study relating the parameters that influence flow reattachment on slant-based bluff bodies is now considered. In this study, the theory of Nash [4] is employed. Earlier two-dimensional base flow theories were either unable to account for the boundary layer thickness at separation, or were unable to account for the static pressure rise at reattachment [55-57]. The theory of Nash accounts for such influences. This theory is developed in terms of the stream function, Ψ, where

$$\frac{\partial \Psi}{\partial x} \equiv -\rho v, \qquad v^* \equiv \frac{v}{U_e} \tag{4.11a}$$

$$\frac{\partial \Psi}{\partial y} \equiv \rho u \qquad u^* \equiv \frac{u}{U_e} \tag{4.11b}$$

Nash accounts for the boundary layer thickness at separation by replacing the real shear layer at separation by an equivalent shear layer growing from zero thickness as shown in Fig. 4.8. Nash contends that the total momentum within the free shear layer is conserved, i.e., the momentum of the equivalent free shear layer is equal to that of the real separating boundary layer. This is represented in the following integral relation:

$$\left\{\int_{\Psi_{DA}}^{\Psi_O} u^* \cdot d\psi\right\}_{\text{EQUIV SHEAR LAYER}} = \left\{\int_{\Psi_S}^{\Psi_O} u^* \cdot d\psi\right\}_{\text{BOUNDARY LAYER}} \equiv \bar{\Psi} \quad (4.12)$$

where Ψ_O represents an external streamline, Ψ_{DA} represents the lower boundary of the equivalent free shear layer, and Ψ_S is the separating streamline. The momentum thickness of the equivalent shear layer is

$$\rho_e U_e \theta_{SL} = \int_{\Psi_S}^{\Psi_O} (1 - u^*) \cdot d\Psi = \Psi_O - \Psi_S - \bar{\Psi} \equiv \Psi_M - \Psi_S \quad (4.13a)$$

The momentum thickness of the boundary layer at separation is

$$\rho_e U_e \theta_{BL} = \int_{\Psi_{DA}}^{\Psi_O} (1 - u^*) \cdot d\Psi = \Psi_O - \Psi_{DA} - \bar{\Psi} \equiv \Psi_M - \Psi_{DA} \quad (4.13b)$$

where ψ_M is defined as a "median streamline" such that

$$\Psi_M \equiv \Psi_O - \bar{\Psi} \quad (4.14)$$

Notice that $\Psi_S = \Psi_{DA}$ if the momentum thickness of the boundary layer, θ_{BL} is equal to the momentum thickness of the shear layer, θ_{SL} just after separation.

The equivalent free shear layer is assumed to grow linearly from its origin at a distance x' upstream of separation, such that the local velocity, u^*, can be expressed as follows:

$$\Psi_M - \Psi = \rho_e U_e (x + x') \cdot f(u^*) \quad (4.15)$$

such that, $$\Psi_M - \Psi_{DA}(x) = \rho_e U_e (x + x') \cdot f(0) \quad (4.16)$$

and at the separation point,

$$\Psi_M - \Psi_{DA}(0) = \rho_e U_e \, x' \cdot f(0) \quad (4.17)$$

The distance to the origin of the equivalent shear layer can be eliminated from Eqn. (4.15) by substitution of Eqns. (4.13)-(4.14) and (4.16)-(4.17).

$$\frac{\Psi_S - \Psi}{\rho_e U_e} = x \cdot f(u^*) - \theta\left\{1 - \frac{f(u^*)}{f(0)}\right\} \tag{4.18}$$

The velocity profile within the equivalent free shear layer is given by

$$u^* = \frac{1}{2}\cdot\left(1 + \mathrm{erf}\xi\right) \qquad \text{where, } \xi \equiv \frac{\sigma y}{\bar{x}} \text{ and } \sigma = 12 \tag{4.19}$$

$$\text{By definition, } \Psi \equiv \int^{y} \rho u \cdot dy \equiv \frac{\bar{x}}{\sigma}\int^{\xi} \rho u \cdot d\xi \tag{4.20}$$

Substitution of Eqn. (4.20) into Eqn. (4.15) allows $f(u^*)$ to be rewritten as follows:

$$f(u^*) = \frac{1}{\sigma}\int_{\xi}^{\xi_M} \rho^* u^* \cdot d\xi \qquad \text{where, } \rho^* \equiv \frac{\rho}{\rho_e} \tag{4.21}$$

$$\text{or,} \qquad f(u^*) = \frac{\sqrt{\pi}}{\sigma}\int_{u^*}^{u_M^*} \rho^* u^* e^{\xi^2} \cdot du^* = \frac{\sqrt{\pi}}{\sigma}\int_{u^*}^{u_M^*} \rho^* u^* \cdot du^*, \quad \xi \rightarrow \text{small} \tag{4.22}$$

The velocity, u^*, can be related to the density, ρ^*, through the following isentropic relation:

$$u^* du^* = \frac{d\rho^*/\rho^{*2}}{(\gamma - 1)M_e^2} \tag{4.23}$$

$$\text{such that,} \quad f(u^*) = \frac{\sqrt{\pi}}{\sigma(\gamma - 1)M_e^2}\int_{\rho^*}^{\rho_M^*} \frac{d\rho^*}{\rho^*} = \frac{\sqrt{\pi}}{\sigma(\gamma - 1)M_e^2}\cdot \ln(\lambda) \tag{4.24}$$

where,
$$\lambda = \frac{\rho_M^*}{\rho^*} = \frac{1 + \frac{\gamma-1}{2} \cdot M_e^2 \left(1 - u^{*2}\right)}{1 + \frac{\gamma-1}{2} \cdot M_e^2 \left(1 - u_M{}^{*2}\right)} \tag{4.25}$$

An advantage of using the median streamline as a reference in Eqn. (4.25) is that the velocity component, $u_M{}^*$, is constant at low speeds. Its value is determined to be, $u_M{}^* = 0.578$, by substitution of Eqns. (4.19), (4.23), and (4.21) into Eqn. (4.14).

To complete the base flow problem, Nash considers the pressure rise in the reattachment region [57-59]. The pressure rise along the reattachment streamline, Ψ_R, from a value of p_B to a value of p_r at reattachment is related to the density rise along the reattachment streamline by the following relation, assuming a polytropic compression:

$$\frac{\rho_r{}^*}{\rho_R{}^*} = \left(\frac{p_r{}^*}{p_B{}^*}\right)^{1/\gamma} \tag{4.26}$$

It is further assumed that the recovery temperature along the wall upstream of separation is equivalent to the recovery temperature in the base region, and that the Prandtl number, Pr→1. The following relation can now be included in the analysis:

$$\frac{\rho_B{}^*}{\rho_r{}^*} = \frac{p_B{}^*}{p_r{}^*} \tag{4.27}$$

such that,
$$\frac{\rho_B{}^*}{\rho_R{}^*} = \left(\frac{p_B{}^*}{p_r{}^*}\right)^{\frac{\gamma-1}{\gamma}} = \frac{\lambda_R}{\lambda_B} \tag{4.28}$$

Since the cavity fluid velocity, $u_B{}^*$, is considered negligible, λ_B can be expressed as follows:

$$\lambda_B \equiv \frac{1+\frac{\gamma-1}{2}\cdot M_e{}^2}{1+\frac{\gamma-1}{2}\cdot M_e{}^2\left(1-u_M{}^{*2}\right)} \tag{4.29}$$

Substitution of Eqn. (4.27) into Eqn. (4.24) gives the following relation:

$$f(u_R{}^*) = \frac{\sqrt{\pi}}{\sigma(\gamma-1)M_e{}^2}\cdot \ln\left\{\lambda_B\left(\frac{p_B{}^*}{p_r{}^*}\right)^{\frac{\gamma-1}{\gamma}}\right\} \tag{4.30}$$

such that,
$$\frac{f(u_R{}^*)}{f(0)} = 1-\frac{\ln\lambda_B\left(\frac{p_B{}^*}{p_r{}^*}\right)^{\gamma-1/\gamma}}{\ln\lambda_b} \tag{4.31}$$

It is now assumed that no base bleed is present such that,

$$\Psi_S - \Psi_R = 0 \tag{4.32}$$

Substitution of Eqns. (4.30)-(4.32) into (4.18), recalling that $x = L_r$ at reattachment, a relationship between the boundary layer momentum thickness, θ, and the reattachment length, L_r, is determined.

$$\frac{L_r}{\theta} = \frac{B}{CA(A-B)} \tag{4.33}$$

where,
$$A = \ln\left\{\frac{1+\frac{\gamma-1}{2}M_e{}^2}{1+\frac{\gamma-1}{2}\left(1-\phi_M{}^{*2}\right)M_e{}^2}\right\} \tag{4.34}$$

$$B = \ln\left\{\left(\frac{p_r}{p_B}\right)^{\frac{\gamma-1}{\gamma}}\right\} \tag{4.35}$$

$$C = \frac{\sqrt{\pi}}{(\gamma - 1)\sigma\epsilon} \tag{4.36}$$

For low subsonic Mach numbers, $\frac{L_r}{\theta}$ is shown in Fig. 4.9 to be very sensitive to the pressure ratio, $\frac{p_r}{p_B}$. Specifically L_r and θ are of the same magnitude as $\frac{p_r}{p_B} \to 1$. If the boundary layer momentum thickness at separation does not change appreciably with the slant-angle, then a result of $\frac{\theta}{L_r}$ increasing is that L_r decreases. Therefore, a decrease in the pressure ratio, $\frac{p_r}{p_B}$ may result in reattachment of the shear layer on the base.

For increasing base slant-angles, the reduced pressure in the base region, p_B, draws the upper separated stream, S_U, towards the lower separated stream, S_L, as illustrated in Fig. 4.10. For a sufficiently large base slant-angle, there is minimal curvature of the lower stream towards the base axis, as shall be shown in Chapter 7. The pressure in the lower stream may therefore be represented by a constant pressure mixing region [13]. Previous research into axisymmetric near-wakes by Merz, Page, and Przirembel [3] have shown that a 3.5% increase in the local Mach number ($M_\infty = 0.11$) occurs 0.17 base diameters upstream of separation. This is a result of the elliptic nature of subsonic flow, i.e., flow discontinuities are not present as in locally supersonic flow. It follows that the static pressure of the lower stream at separation is equivalent to the base pressure, i.e., $p_{S_L} \sim p_B$. Furthermore, considering a constant pressure mixing region, the pressure, p_{S_L} is equivalent to the recovery pressure, p_r. Under such conditions, the numerator of Eqn. 4.34 becomes small, suggesting that L_r is small. It follows that base flow reattachment may occur under these circumstances.

4.4 *Prediction of Reattachment: Theory of Stratford*

Stratford's zero skin friction limiting pressure distribution [60] for turbulent, incompressible flow is used to predict the conditions for reattachment

of the separated shear layer on slanted-base bluff bodies. The advantage of Stratford's method over other prediction methods is that detailed boundary layer calculations are not necessary, as is the case for differential or integral methods [61-62]. This method has predicted separation on a variety of two-dimensional configurations successfully with examples given in Refs. [61, 63-65]. Although Stratford's method is based on incompressible flow assumptions, it has been shown to accurately predict separation in compressible-subsonic and transonic flow regimes [64-65].

Research on cylindrical bodies in axial flow have shown that the developing boundary layer is substantially different than that occurring in planar two-dimensional flow as δ/R becomes large [66]. It is assumed that the boundary layer thickness, δ is small compared to the bluff body radius, R so that a two-dimensional analysis similar to Page [13] can be continued.

Stratford's method is based on the concept of a limiting pressure distribution, which is defined as the adverse pressure distribution for which zero skin friction exists, but separation is just avoided. This method is derived for fully turbulent flows on a flat plate with an adverse pressure gradient originating from the leading edge, and is based on sub-dividing the boundary layer into inner and outer regions. In the outer portion, the shear forces are small compared to either the inertial forces or the adverse pressure gradient. The following relations are applicable in the outer region:

$$\frac{U}{U_e} = \left(\frac{y}{\delta}\right)^{\frac{1}{n}} \tag{4.37}$$

$$\delta = \frac{(n+1)(n+2)}{n} \cdot \theta \quad 6 < n < 8 \tag{4.38}$$

$$\theta = 0.036x \cdot (Re_x)^{-\frac{1}{5}} \tag{4.39}$$

In the inner portion, the fluid inertia is small, therefore the pressure forces are balanced entirely by the shear forces. For zero shear stress, the dynamic pressure in the inner layer is expressed as:

$$\frac{1}{2}\rho U^2 = \frac{2}{(0.41\lambda)^2}\cdot\frac{\partial p}{\partial x}\cdot y \quad (\tau = 0) \tag{4.40}$$

where λ is an empirical constant used to represent any effects the adverse pressure gradient may have on the mixing length. The term λ is determined experimentally by maintaining a flow just at the separation condition. Stratford suggests that $\lambda = 0.66$ [67]. Stratford's limiting pressure distribution is derived via the following two conditions required to join the inner and outer regions:

$$\left(\frac{\partial U}{\partial y}\right)_{inner} = \left(\frac{\partial U}{\partial y}\right)_{outer} \tag{4.41}$$

$$\int_0^y \left(U\cdot dy\right)_{inner} = \int_0^y \left(U\cdot dy\right)_{outer} \tag{4.42}$$

The following equation for the limiting pressure distribution results:

$$C_p = 0.645\cdot\left\{0.435\cdot R_o^{\frac{1}{5}}\cdot\left(\chi^{-\frac{1}{5}}-1\right)\right\}^{\frac{2}{n}} \quad 6 < n < 8 \tag{4.43}$$

where, $$R_o = \frac{U_o\, x_o}{\nu}\ ,\ \chi = \frac{x}{x_{T_{EQ}}} \tag{4.44}$$

Modifications to Stratford's method account for regions of laminar flow and favorable pressure gradient, by replacing these regions with an equivalent constant pressure turbulent region growing over a distance, $x_{T_{EQ}}$. The equivalence criterion is the momentum thickness at the point of peak velocity [60]. For an

initially laminar boundary layer in the presence of a pressure gradient, the momentum thickness, θ_{L_1} at the transition point, X_{TR}, measured from the leading edge is

$$\theta_{L_1} = 0.664 \cdot \frac{\nu}{U_{TR}} \cdot \int_0^{X_{TR}} \left(\frac{U_e}{U_{TR}} \right)^5 dX \tag{4.45}$$

For a flat plate in the absence of pressure gradients, the momentum thickness is determined from classical laminar boundary layer theory to be:

$$\theta_{L_{EQ}} = 0.036 \cdot \left(\frac{\nu}{U \, x_{L_{EQ}}} \right)^{\frac{1}{5}} \tag{4.46}$$

Equations (4.45) and (4.46) allow for the solution of the equivalent flat plate length, $x_{L_{EQ}}$, of a laminar boundary in the presence of a pressure gradient. After some manipulation, $x_{L_{EQ}}$ is determined to be

$$x_{L_{EQ}} = 38.2 \cdot \left(\frac{\nu}{U_{TR}} \right)^{\frac{3}{8}} \cdot \left\{ \int_0^{X_{TR}} \left(\frac{U_e}{U_{TR}} \right)^5 dX \right\}^{\frac{5}{8}} \tag{4.47}$$

where X and x are distances from the actual and equivalent leading edges, respectively.

A similar manipulation occurs for a turbulent boundary layer in the presence of a pressure gradient. The required flat plate length, $x_{T_{EQ}}$, that yields equivalent turbulent boundary layer growth, in the presence of a pressure gradient, is determined to be

$$x_{T_{EQ}} = \int_0^{X_o} \left(\frac{U_e}{U_o} \right)^3 dX \tag{4.48}$$

where X and x are distances from the actual and equivalent leading edges respectively. Equation (4.48) can be rewritten in a more convenient form as follows:

$$x_{T_{EQ}} = \left(\frac{U_{TR}}{U_0}\right)^3 \cdot \int_0^{X_{TR}} \left(\frac{U_e}{U_{TR}}\right)^3 dX + \int_{X_{TR}}^{X_o} \left(\frac{U_e}{U_o}\right)^3 dX \qquad (4.49)$$

where X_{TR} is the actual location of the transition point. The first integral in Eqn. (4.49) accounts for the development of the laminar boundary layer, and is simply the equivalent length, $x_{L_{EQ}}$, developed previously. Therefore, the equivalent length, $x_{T_{EQ}}$, necessary in the development of Stratford's method can be written in its final form as:

$$x_{T_{EQ}} = 38.2 \cdot \left(\frac{\nu}{X \cdot U}\right)_{TR}^{\frac{3}{8}} \cdot \left(\frac{U_0}{U_{TR}}\right)^{\frac{1}{8}} \cdot \left\{ \int_0^{X_{TR}} \left(\frac{U_e}{U_0}\right)^5 d\left(\frac{X}{X_{TR}}\right) \right\} + \int_{X_{TR}}^{X_o} \left(\frac{U_e}{U_o}\right)^3 dX \qquad (4.50)$$

Equations (4.43), (4.44), and (4.50) are used in the following sections to predict reattachment on the 45° slanted-base for various free-stream and boundary layer conditions.

4.4.1 *Previous Reattachment Predictions (Airfoils)*

Stratford's method has been used successfully in predicting both separation and reattachment locations on two-dimensional surfaces [61, 63-65]. Reattachment is predicted by comparing the limiting pressure distribution defined in Eqns. (4.43), (4.44) and (4.50), to the pressure distribution required for attached flow. Van Ingen [68] applied this method to two-dimensional laminar separation bubbles on Wortmann airfoils [69] as shown in Fig. 4.11, starting the calculations from the measured transition point. It was demonstrated that at low Reynolds numbers,

($Re_C = 0.118x10^6$), the limiting pressure distribution curve failed to intersect the pressure distribution required for attached flow. Therefore, Stratford's method was unable to provide the required pressure rise for reattachment, and bursting occurred.

4.4.2 *Reattachment Predictions (Slanted-Base Bluff Bodies)*

Stratford's method is used to predict the effects of the Reynolds number, Re_D, and trip location, x_{TR}, on slant-based bluff body flow reattachment. The availability of surface pressure data over the length of a similar model used in a previous study [24, 70] provide the necessary inputs for Stratford's limiting pressure method [60, 67]. Figure 4.12 shows the configuration with accompanying surface pressure. In order to continue with this analysis, the location of the transition point within the separation region must be determined from experimental results. This requires high resolution of base pressures within the separated region. Base pressures were not resolved in great detail in this study, therefore, the transition location could not be determined by inspection of the pressure distribution. However, it is known that the switch in base flow patterns occurs at $Re_D \simeq 60{,}000$, signaling flow reattachment on the base. Furthermore, flow visualization with liquid crystals suggests that transition occurs at the base, $\frac{x_{TR}}{x_L} = 1$, for $Re_D \simeq 60{,}000$ and moves upstream with increasing Reynolds number [24].

Figure 4.13 shows limiting pressure distributions along the 45° slanted-base model for various boundary layer trip locations on the model. The minimum allowable pressure distribution necessary for reattachment in Fig. 4.13 is represented by a boundary layer trip location at separation, $\frac{x}{L} = 1$. It is shown that limiting pressure distributions associated with boundary layer trip locations ahead of separation are insufficient to provide for flow reattachment. This is in

agreement with previous measurements for the 45° base model which revealed that boundary layer trips ahead of separation prevented the formation of the vortical near-wake associated with base flow reattachment [24]. This was shown in Fig. 2.17.

Reattachment predictions for a fixed boundary layer trip location at separation are shown in Fig. 4.14. The minimum allowable pressure distribution necessary for reattachment is represented by Reynolds numbers above 60,000. It is shown that limiting pressure distributions associated with Reynolds numbers below 60,000 are insufficient to provide an adequate pressure distribution for reattachment. This is in agreement with previous free-transition results for the 45° base model, as shown in Fig. 2.14.

The trends that are presented in Figs. 4.13 and 4.14 are in agreement with trends of the previous research, therefore, an attempt was made to predict whether base flow reattachment could occur on the 45° base for a given Reynolds number and boundary layer trip location. This was accomplished by examining the corresponding limiting pressure distribution. If the limiting pressure distribution did not intersect the minimum pressure distribution necessary for reattachment, then reattachment was not present.

Figure 4.15 shows the envelope of boundary layer trip locations and Reynolds numbers necessary for flow reattachment. It is shown that the boundary layer trip location may move upstream with increasing Reynolds number and still provide an adequate pressure distribution for reattachment. For a Reynolds number of 300,000--the upper bounds of the 13-inch MSBS facility--base flow reattachment is predicted to occur for boundary layer trip locations, $\frac{x}{L}$, greater than 82%. The edge of the envelope is shown to decay with increasing Reynolds number, therefore, base flow reattachment cannot occur at a moderate Reynolds number for a boundary layer trip location at the centerbody leading edge of the 45° base model.

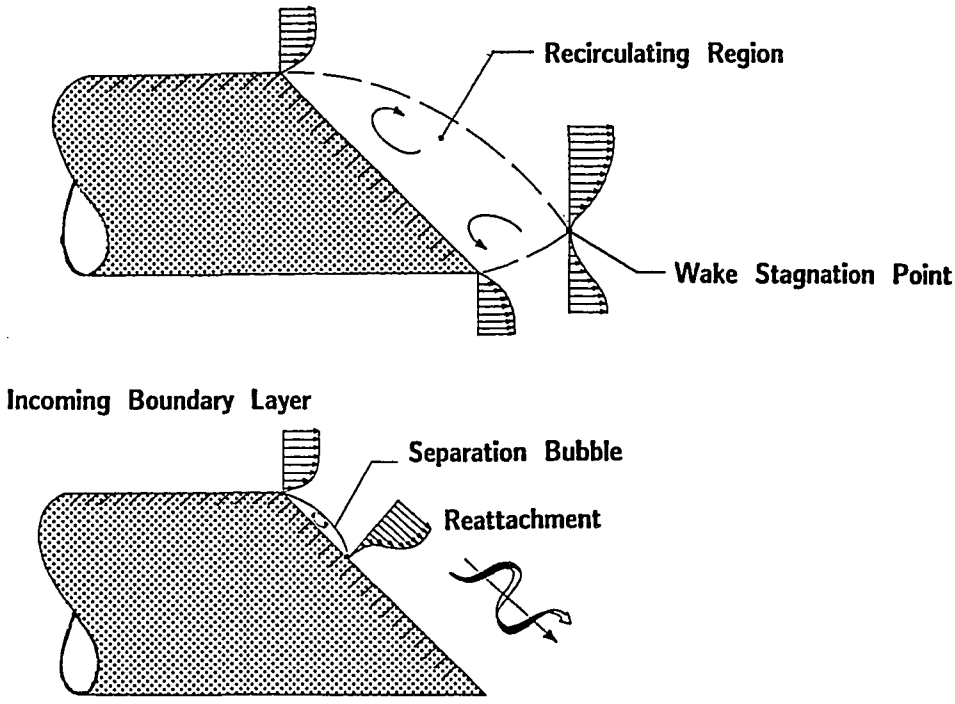

Fig. 4.1 Flow Reattachment on Slanted-Base

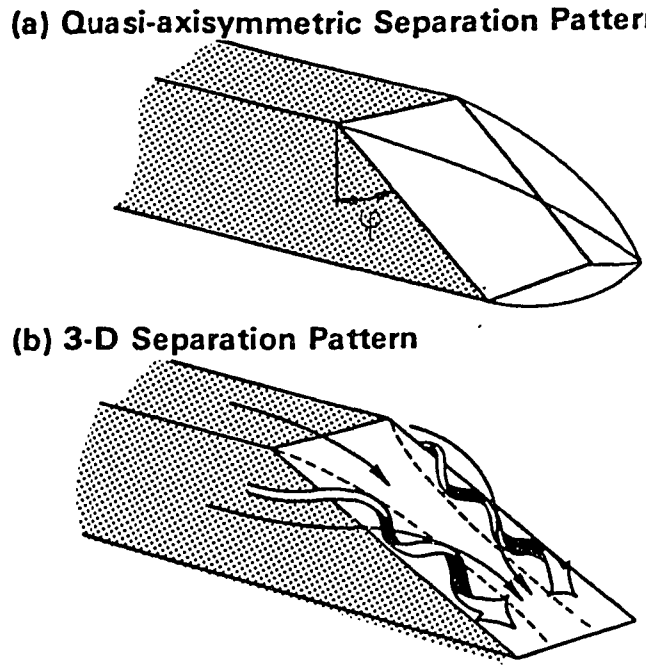

Fig. 4.2 3-D Slanted-Base Bluff Body

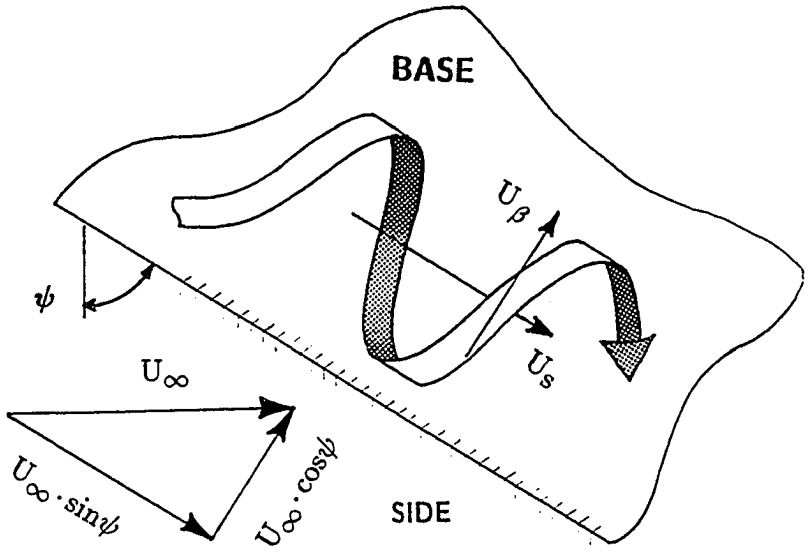

Fig. 4.3 Flow Model for Vortex Formation

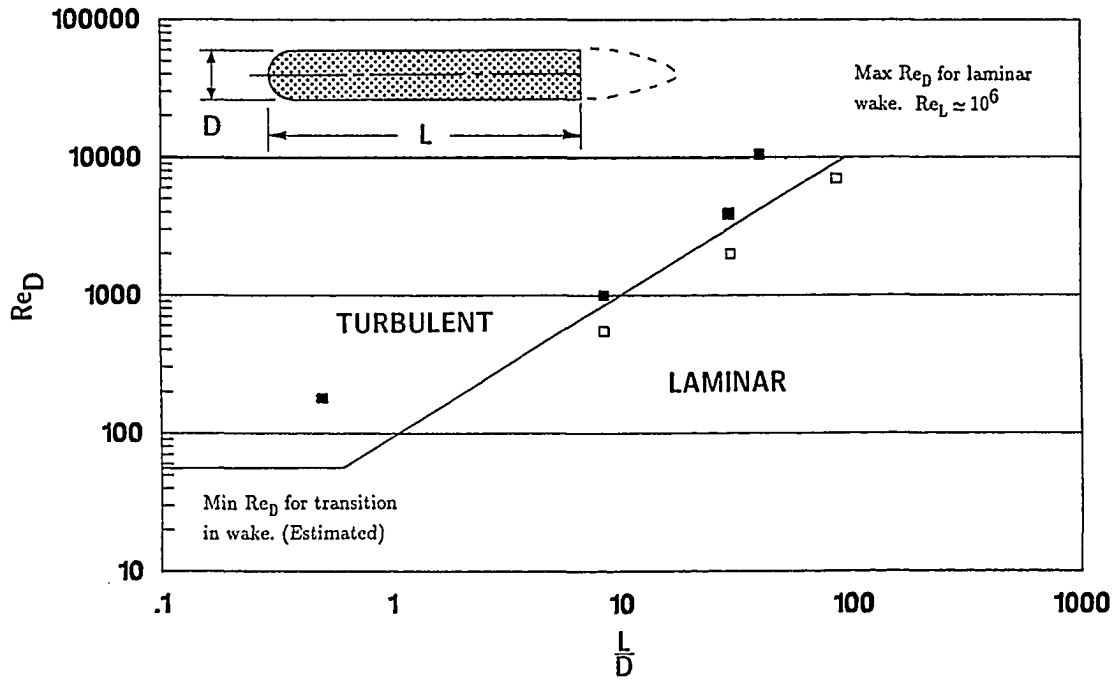

Fig. 4.4 Criterion for a Turbulent or Laminar Free Shear Layer

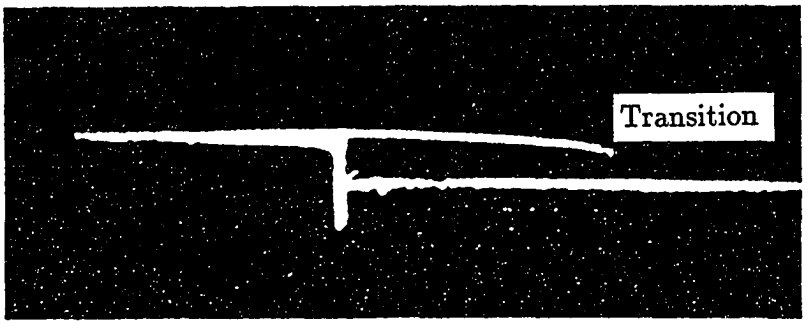

U_∞= 16.2 ft/sec

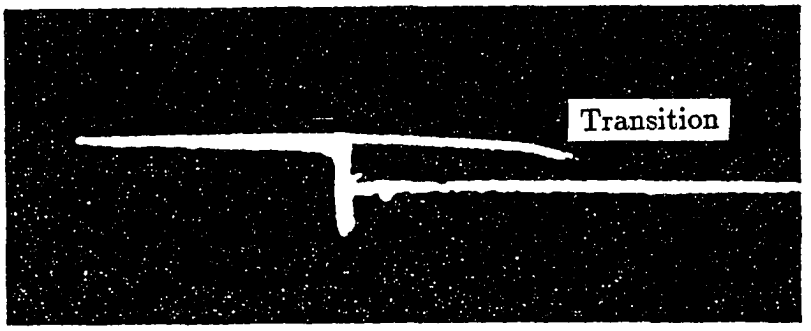

U_∞= 22.8 ft/sec

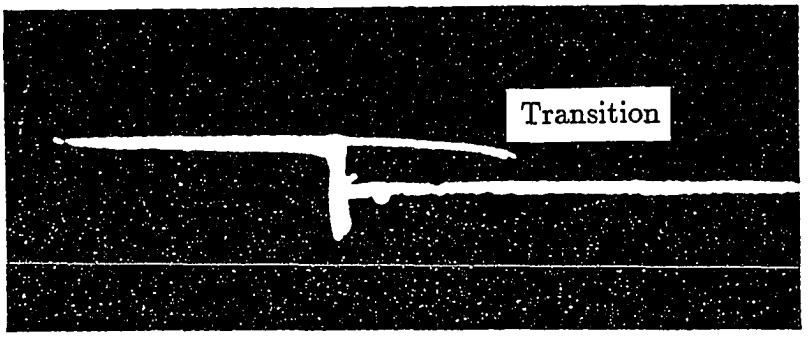

U_∞= 29.5 ft/sec

Fig. 4.5 Transition in a Free Shear Layer

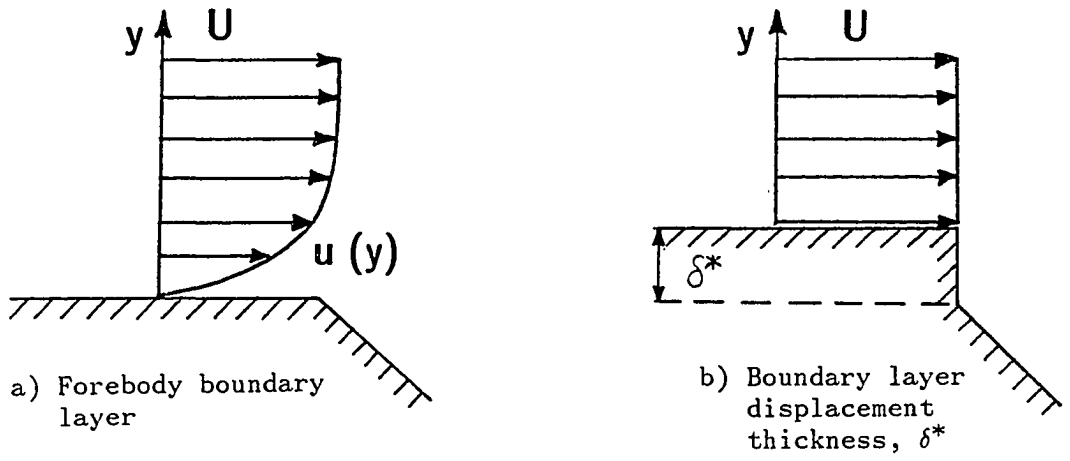

Fig. 4.6 Boundary Layer Displacement Thickness, δ^*

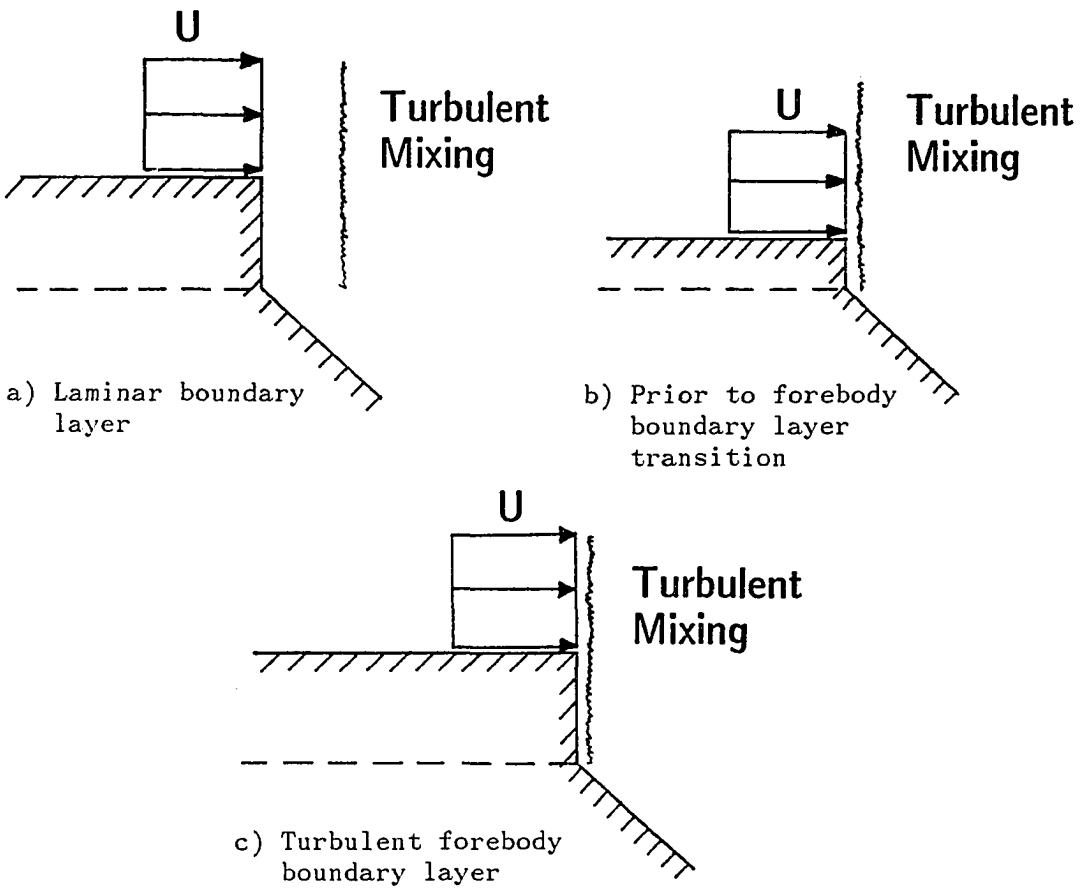

Fig. 4.7 Reynolds Number Influence on Displacement Thickness

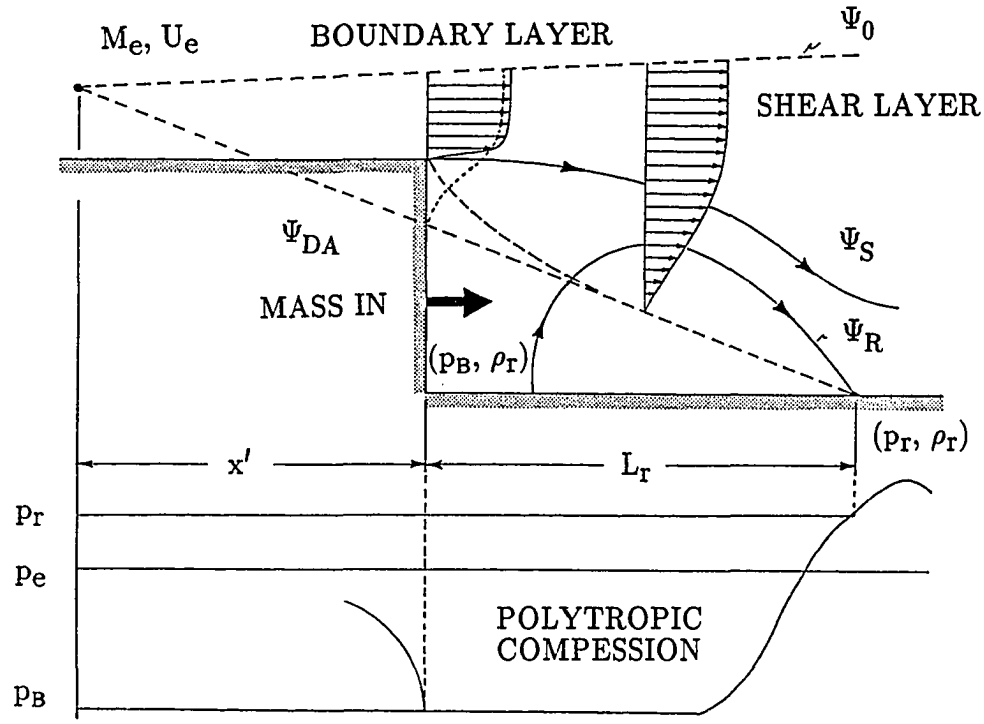

Fig. 4.8 Flow Model for Flow Reattachment: Theory of Nash

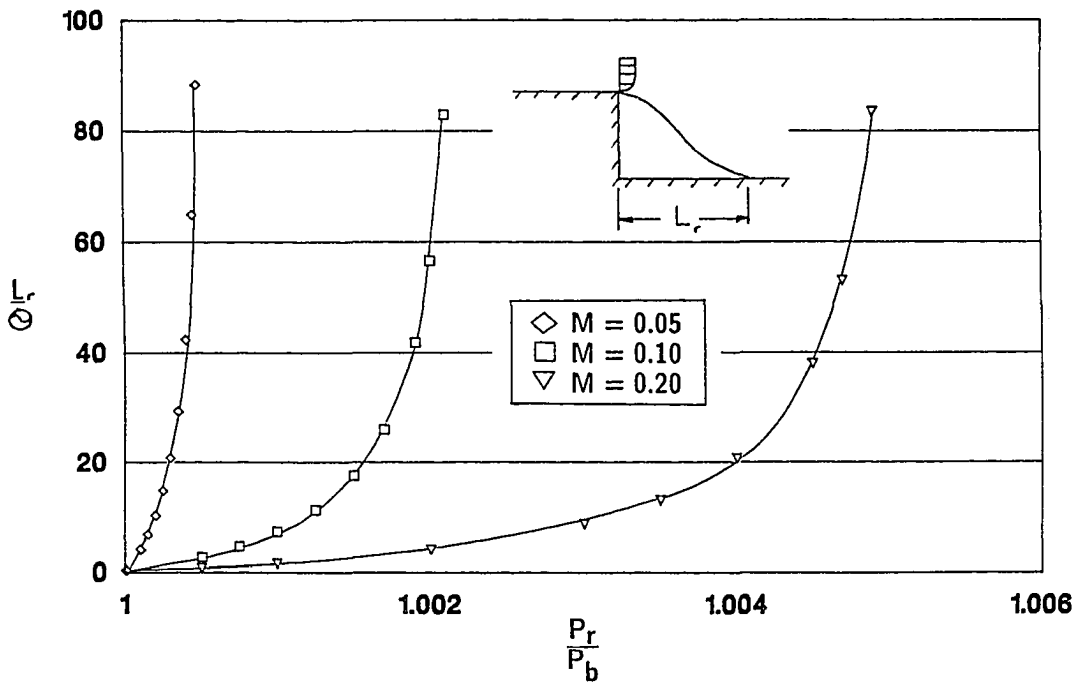

Fig. 4.9 Effect of Recovery Pressure, P_r, on Wake Stagnation Point

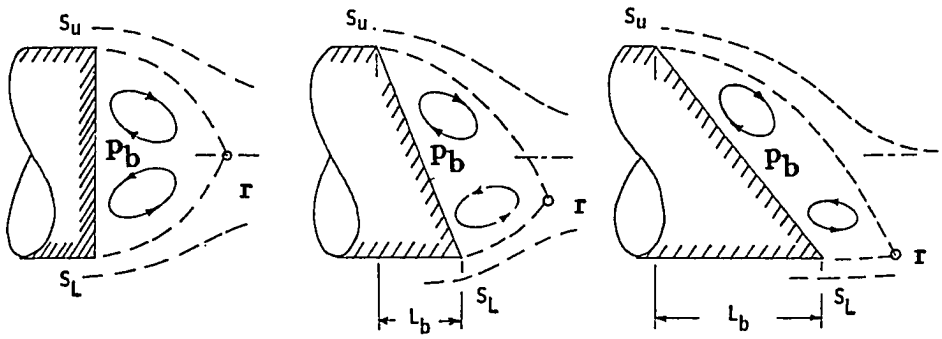

Fig. 4.10 Effect of Base Slant Angle on Wake Stagnation Point

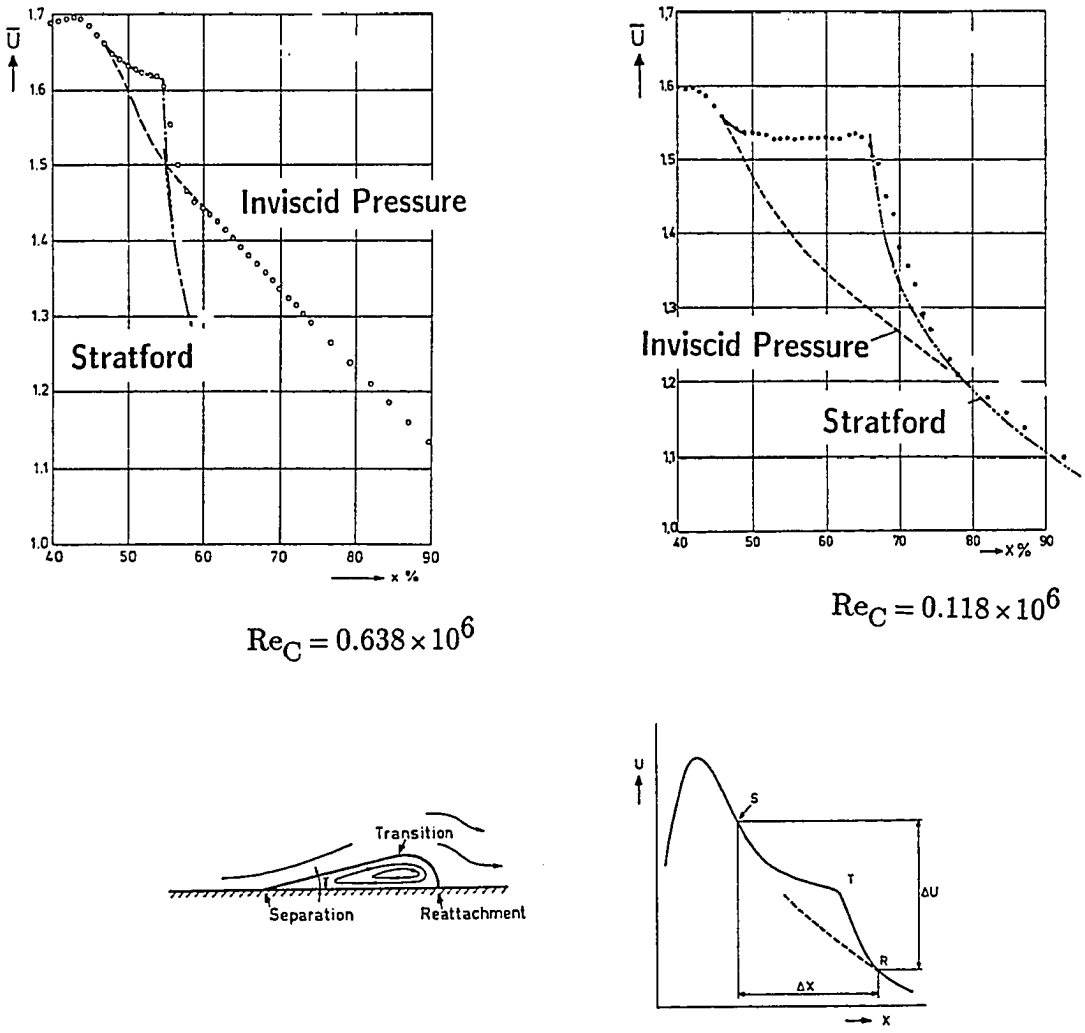

Fig. 4.11 Reattachment Predictions for a Wortmann Airfoil: Theory of Stratford

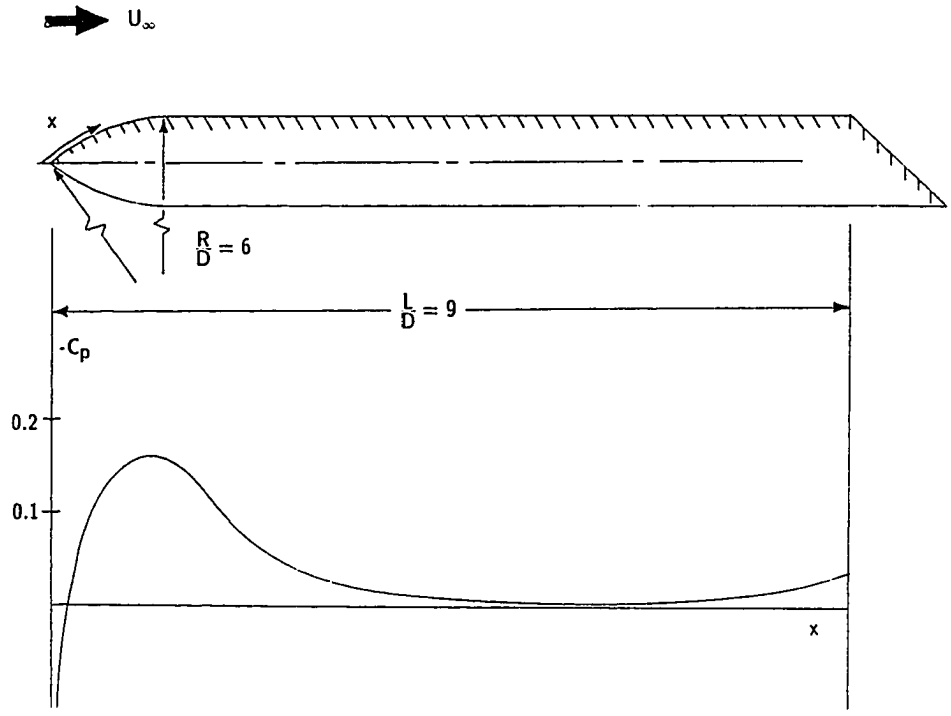

Fig. 4.12 Surface Pressure Distribution for an Ogive Cylinder Model

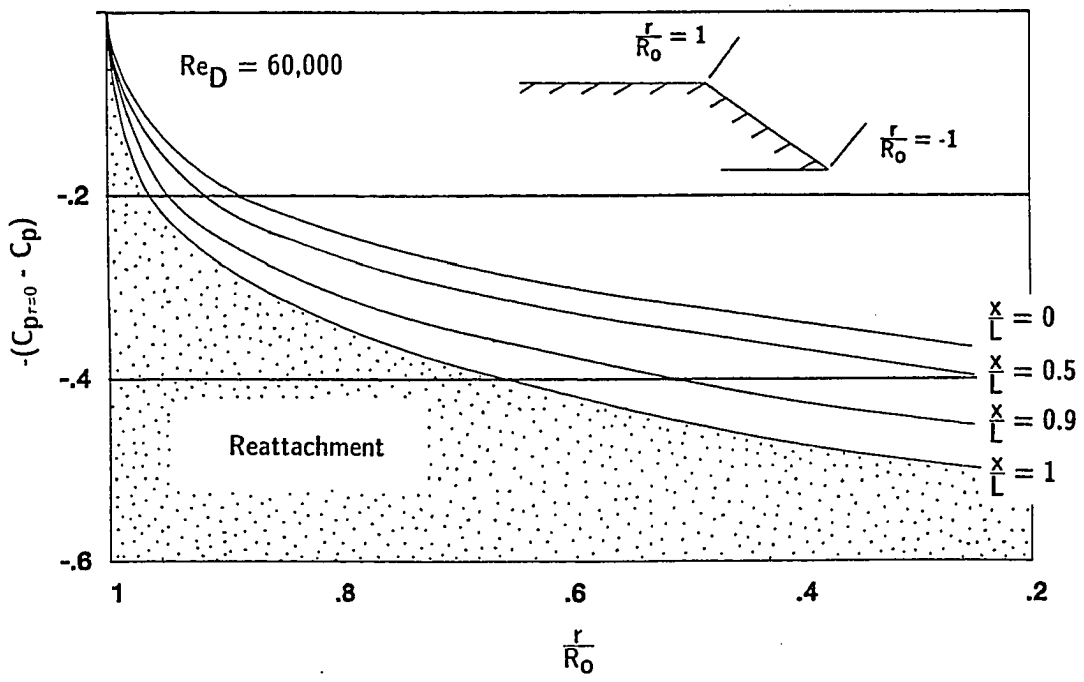

Fig. 4.13 Limiting Pressure Distribution for Various Centerbody Trip Locations

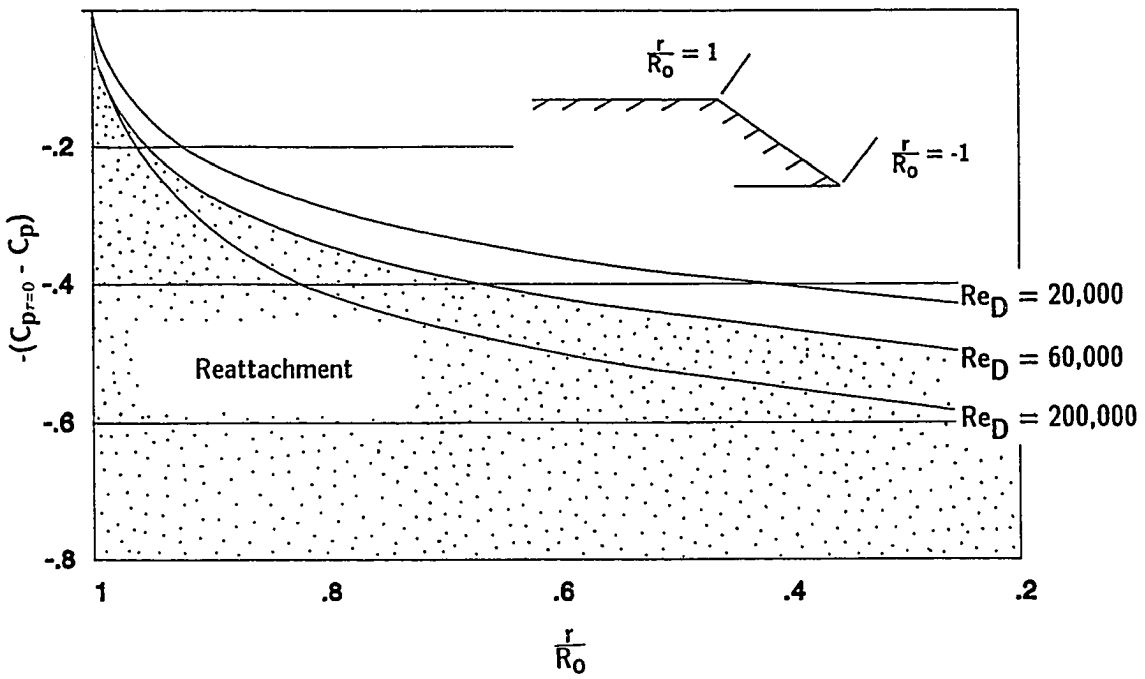

Fig. 4.14 Limiting Pressure Distribution as a Function of Re_D $\left(\frac{x}{L} = 1\right)$

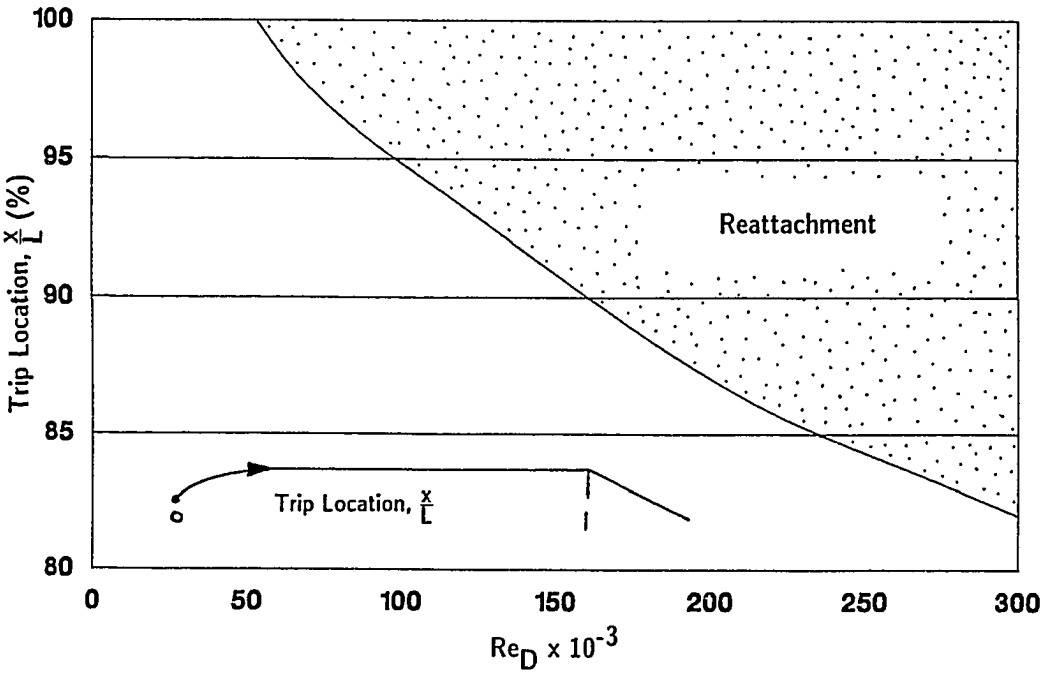

Fig. 4.15 Summary of Limiting Pressure Distribution

Chapter 5 TURBULENCE ANALYSIS

The nature of turbulence and the mechanisms that govern its development are poorly understood, therefore, continuing experimental and theoretical studies of this complex phenomenon are necessary. It is supposed that the necessary information about a turbulent flow is contained in the Navier-Stokes equations, and that turbulent motion can be predicted through direct numerical simulation using these equations. Unfortunately, this procedure is difficult to implement on turbulent flows of practical interest due to uncontrollable variations in the governing boundary and initial conditions which are not completely understood [71-72]. Thus, direct numerical simulation is not a feasible analytic tool at this time. However, statistical methods, such as spectral analysis, continue to be a useful approach to quantify turbulence.

It has been shown through spectral analysis that certain classes of turbulent flows are not completely random. For example, a bluff body wake may contain turbulent fluctuations whose power is associated with certain predominant frequencies [36-44, 47-49]. This suggests that characteristic structures are present in what has been generally perceived as a completely random process [73]. A technique for the measurement of predominant frequencies is discussed in Section 5.1. Section 5.2 discusses the cross-spectrum of two hot-wire signals.

A derivation of azimuthal constituents for an axisymmetric wake is also given in Section 5.2. It has been shown that large-scale structures in axisymmetric wakes (and jets) can be described in terms of several azimuthal

constituents [36-37]. An extension of this procedure to examine coherent structures behind slanted-base bluff bodies has not been attempted due to added complexities associated with a non-axisymmetric wake. Proper cross-spectral measurements in a non-axisymmetric wake would require detailed knowledge of the wake deflection to allow for correct positioning of the hot-wire probes in a plane normal to the wake. Furthermore, the presence of mean swirl, or helicity in those flows prevents the analysis of azimuthal constituents as described in Section 5.2.

5.1 *Spectral Analysis: Power Spectrum*

The power spectrum, $P(\omega)$, indicates the power associated with turbulent fluctuations. The power spectrum of some stationary turbulent fluctuation, $u'(t)$, is defined by taking the Fourier transform of the time correlation as shown in the following equation:

$$R(\tau) = < u'(t)\, u'(t + \tau) > \tag{5.1}$$

The power spectrum may be written as:

$$P(f) = \frac{1}{2\pi}\int_{-\infty}^{\infty} R(\tau)\, e^{-if\tau}\, d\tau \tag{5.2}$$

$R(\tau)$ is symmetric in time, therefore, the power spectrum is a real function of the frequency, f.

$$P(f) = \frac{1}{\pi}\int_{0}^{\infty} R(\tau)\cos(f\tau)\, d\tau \tag{5.3}$$

The inverse may be written as:

$$R(\tau) = \int_{-\infty}^{\infty} P(f)\, e^{if\tau}\, df \;=\; 2\int_{0}^{\infty} P(f)\cos(f\tau)\, df \tag{5.4}$$

For $\tau = 0$, one may write:

$$R(0) = < u'^2(t) > = 2\int_{0}^{\infty} P(f)\, df \tag{5.5}$$

Note that $< u'^2(t) >$ is the variance, i.e., a measure of the intensity of the turbulent fluctuations. Therefore, Eqn. (5.5) shows the power of the turbulent fluctuations is simply the sum of powers of individual harmonic components of these fluctuations [72].

5.2 *Cross-Spectral Analysis: Coherence*

Similar to the development of the power spectrum, P(f), one can define the wavenumber frequency spectrum by taking the Fourier transform of a space-time correlation function,

$$E(k_1,k_2,k_3, f) = \frac{1}{(2\pi)^4}\int_{-\infty}^{\infty}\int_{-\infty}^{\infty}\int_{-\infty}^{\infty}\int_{-\infty}^{\infty} R(\vec{\xi}, \tau)\, e^{-i(\vec{k}\cdot\vec{\xi}+f\tau)} d\xi_1 d\xi_2 d\xi_3 d\tau \tag{5.6}$$

where $\vec{\xi}$ is the vector separating two points in space with vector components ξ_1, ξ_2, ξ_3, $\vec{k}$ is the wavenumber vector with components, k_1, k_2, k_3, and $R(\vec{\xi}, \tau)$ is the space-time correlation function defined as [72]

$$R(\vec{\xi}, \tau) = < u'(\vec{x}, t)\, u'(\vec{x} + \vec{\xi}, t + \tau) > \tag{5.7}$$

A cross-spectrum, in terms of the space-time correlation, is similar to the development of the power spectrum in Eqn. (5.2), and is defined as follows:

$$P(\vec{\xi}, f) = \frac{1}{2\pi} \int_{-\infty}^{\infty} R(\vec{\xi}, \tau)\, e^{-i f \tau}\, d\tau \tag{5.8}$$

Expressing Eqn. (5.8) in terms of the wavenumber frequency spectrum:

$$P(\vec{\xi}, f) = \int_{-\infty}^{\infty} \int_{-\infty}^{\infty} \int_{-\infty}^{\infty} E(\vec{k}, \tau)\, e^{-i\, \vec{k} \cdot \vec{\xi}}\, dk_1 dk_2 dk_3 \tag{5.9}$$

The inverses of Eqns. (5.8)-(5.9) are as follows:

$$R(\vec{\xi}, \tau) = \int_{-\infty}^{\infty} P(\vec{\xi}, f)\, e^{i f \tau}\, df \tag{5.10}$$

$$E(\vec{k}, f) = \frac{1}{(2\pi)^3} \int_{-\infty}^{\infty} \int_{-\infty}^{\infty} \int_{-\infty}^{\infty} P(\vec{\xi}, f)\, e^{-i\, \vec{k} \cdot \vec{\xi}}\, d\xi_1 d\xi_2 d\xi_3 \tag{5.11}$$

The functions $R(\vec{\xi}, \tau)$ and $E(\vec{k}, f)$ are not symmetric in terms of τ and $\vec{k}$, when $\vec{\xi}$ and, f, are non-zero, therefore, unlike the power spectrum, the cross-spectrum is complex.

$$P(\vec{\xi}, f) = C_\omega(\vec{\xi}, f) + i \cdot Q_\omega(\vec{\xi}, f) \tag{5.12}$$

The degree of correlation or <u>coherence</u> between two spatially separated points can now be defined as:

$$\Gamma = \frac{\sqrt{C_\omega{}^2 + Q_\omega{}^2}}{P_1(f)\ P_2(f)} \tag{5.13}$$

where $P_1(f)$ and $P_2(f)$ represent the respective power spectra of two spatially separated points. A swirl angle can be defined as

$$\phi = \tan^{-1}\left(\frac{Q_\omega}{C_\omega}\right) \tag{5.14}$$

The above equations can be greatly simplified if no mean swirl is present in the flow, i.e., there must be no preferred orientation of helical disturbances in the wake, such that $Q_\omega \equiv 0$. Random variations in the orientation of helical disturbances are acceptable, provided that sufficiently long time-averaged cross-correlations are made. Coherence measurements in an axisymmetric bluff body wake by Roberts [48], Fuchs, Mercker, and Michel [36-37], and Xia and Bearman [22] have demonstrated that no preferred helical disturbances are present, provided that the bluff body model is properly aligned with the oncoming flow. In these studies, Q_ω was determined to be effectively zero over the whole frequency range; therefore, signals were either in phase or 180° out of phase [48].

The effect of the model support strut on spectral measurements in the wake must also be considered. It is believed that the strength of any vortices shed from the strut are negligible, compared to any existing large-scale structures in the bluff body wake, provided the strut is properly aligned with the flow. It is also believed that any large-scale unsteady motion due to the interface between the strut and the model will be damped-out in the boundary layer on the model. Spectral measurements in the wake of the strut shall be made in order to examine the magnitude and frequency of any spectral peaks.

Continuing with the analysis, cross-spectral measurements in an axisymmetric wake allow the vector, $\vec{\xi}$, to be written as $(\xi_1, \xi_2, \xi_3) \Rightarrow (r, \Delta\beta, x)$ as shown in Fig. 5.1. Furthermore, in an axisymmetric flow with P_1 and P_2 measured on a constant radius, r, in a plane normal to the axis of symmetry, x=constant, Eqn. (5.12) may be rewritten as follows:

$$P(\Delta\beta, f) = C_\omega(\Delta\beta, f) = C_\omega(-\Delta\beta, f) \tag{5.15}$$

Spatial periodicity also exists for axisymmetric flows, such that for any arbitrary radius

$$C_\omega(\Delta\beta + 2n\pi, f) = C_\omega(\Delta\beta, f) \qquad n=0, 1, 2, \ldots \qquad (5.16)$$

Under these special conditions, the wavenumber frequency spectrum of Eqn. (5-6) can be greatly simplified.

$$E(f) = \frac{1}{\pi}\int_0^\pi C_\omega(\Delta\beta, f)\cdot\cos(m\cdot\Delta\beta)\, d\beta = C_{\omega,m}(f) \quad m = 0, 1, 2, \ldots \qquad (5.17)$$

where, $$C_\omega(\Delta\beta, f) = \sum_0^\infty C_{\omega,m}(f)\cos(m\cdot\Delta\beta) \qquad m = 0, 1, 2, \ldots \qquad (5.18)$$

Of interest is C_ω for $\Delta\beta = 0$:

$$C_\omega(0, f) = \sum_0^\infty C_{\omega,m}(f) = P(0, f) \qquad (5.19)$$

Equation (5.19) is therefore identical to the power spectrum of Eqn. (5.2). This shows that the total fluctuating energy is equal to the sum of the energy contained in each azimuthal constituent of order m, $C_{\omega,m}$ [36-37, 72].

A physical description of the azimuthal constituents in a plane normal to the base axis is possible by expanding Eqn. (5.18):

$$C_\omega(\Delta\beta, f) = C_{\omega,0}(f) + C_{\omega,1}(f)\cdot\cos(\Delta\beta) + C_{\omega,2}(f)\cdot\cos(2\Delta\beta) + \ldots \qquad (5.20)$$

The $m = 0$ contribution may be called axisymmetric since its magnitude and phase are independent of $\Delta\beta$ [74-75]. This mode is characteristic of vortex rings as found in a laminar shear layer shed from a circular jet as shown in Fig. 3.4 [36-38]. The $m = 1$ contribution changes sign twice from $0^\circ < \Delta\beta < 360^\circ$. It may be positive on one half of the circle and negative on the other half as shown in Fig. 5.2 [75]. For this reason, the $m = 1$ term is a helical structure characteristic of vortex shedding as shown in Fig. 3.6. The $m = 2$ contribution changes sign four

times from $0^\circ < \Delta\beta < 360^\circ$ and is known as the quadrupole structure [74-75]. Obviously, very detailed structures develop for higher order azimuthal constituents [74-77].

5.3 *Two-Dimensional Analysis of Unsteady Wake Parameters*

It has been demonstrated in Chapters 2 and 3 that the slant angle and the state of the approaching boundary layer have a pronounced effect on the steady characteristics of the wake. An attempt is now undertaken to relate fluctuating near-wake properties to time-averaged near-wake parameters for slant-based bluff bodies.

The following analysis depends on several assumptions about the nature of the unsteady wake. Fuchs, Mercker, and Michel [36-37] contend through spectral and cross-spectral analysis, that the unsteady wake behind an axisymmetric body normal to the flow is of the same nature as a Kármán vortex sheet behind a circular cylinder. This is demonstrated by the dominance of the m=1 mode through modal analyses. Perry and Lim [39] demonstrated through smoke flow visualization studies that the wake of an axisymmetric bluff body can be represented as a modified vortex tube as was shown in Fig. 3.6. Furthermore, the dominance of the vortex shedding mode was verified via spectral analysis in the current research, and will be discussed in detail in Chapter 8. Therefore, a two-dimensional flow model representing a vortex street is used to represent a bluff body near-wake. The model chosen, due to its simplicity, was first theorized by von Kármán [29-30, 78] and relates vortex street parameters in a closed-form solution. The vortex street is represented by two staggered rows of point vortices. The relationship is as follows:

$$C_{D_S} = \frac{4}{\pi}\left(\frac{U_\infty}{U_S}\right)^2 \left\{ \coth^2\left(\frac{\pi b}{a}\right) + \left(\frac{U_\infty}{U_S} - 2\right)\frac{\pi b}{a}\coth\left(\frac{\pi b}{a}\right)\right\} \qquad (5.21a)$$

$$C_{D_S} = \frac{D_S}{\frac{1}{2}\rho a {U_\infty}^2} \qquad (5.21b)$$

where D_S is the vortex street drag per unit length, "a" is the longitudinal vortex spacing, b is the lateral vortex spacing, and U_S is the vortex velocity relative to the freestream. Von Kármán demonstrated that the vortex street behind a circular cylinder is, in general, unstable. Figure 5.3 shows the only arrangement that corresponds to neutral stability [29-30],

$$\frac{b}{a} = 0.281 \text{ (Neutrally stable)} \qquad (5.22)$$

Equation (5.21a) can be greatly simplified by substituting the stability criteria for vortex streets.

$$C_{D_S} = 1.583\left(\frac{U_S}{U_\infty}\right) - 0.63\left(\frac{U_S}{U_\infty}\right)^2 \qquad (5.23)$$

It appears advantageous to relate the vortex street drag, C_{D_S}, to a more familiar quantity, such as the base drag, C_{D_B}. This is accomplished by considering a simple model for the near-wake geometry of a bluff body configuration as shown in Fig. 5.4. This model requires knowledge of the wake stagnation point location in relation to the bluff body base. For an axisymmetric bluff body parallel to the flow, reattachment may be assumed to occur along the centerline. For a slanted-base configuration, the incoming flow tries to negotiate the upstream base corner, resulting in a downward deflection of the flow as previously discussed in Chapter 4. By referring to Fig. 5.4, the following relation for the vortex-street drag may be written.

$$C_{D_S} = \frac{\pi}{4}\left(\frac{b}{a}\right)\left(\frac{D}{b}\right)\frac{C_{D_B}}{\cos(\eta)} \qquad (5.24)$$

Furthermore,

$$b = D\frac{\cos(\psi+\eta)}{\cos(\psi)} \tag{5.25}$$

Therefore, the ratio of the base diameter to the lateral vortex spacing in Eqn. (5.24) can be replaced by Eqn. (5.25) as follows:

$$C_{D_S} = \frac{\pi}{4}\left(\frac{b}{a}\right)\frac{C_{D_B}}{\cos(\psi+\eta)} \tag{5.26}$$

The shedding frequency can be nondimensionalized as:

$$St_D = \frac{fD}{U_\infty} \tag{5.27}$$

where, St_D, is the Strouhal number. If U_N is defined as the vortex velocity relative to the model, then the shedding frequency, f, may be rewritten as:

$$f = \frac{U_M}{a} \tag{5.28}$$

A result of this model in Fig. 5.4 is that the lateral spacing between vortices, i.e., the wake width, decreases with increasing slant angle. In view of the vortex stability criterion of Eqn. (5.22), the longitudinal vortex spacing must decrease proportionally with the lateral spacing, resulting in an increased shedding frequency as shown through Eqn. (5.28). It has been observed previously that bluff bodies with narrower wakes are associated with increased shedding frequencies and higher base drags [79]. This is demonstrated in Chapter 3 by the differences in the predominant frequency between an axisymmetric bluff body and a disk placed normal to the flow. This has also been demonstrated for increasing base slant angle in the absence of base flow reattachment. Therefore, the above model for the near-wake geometry gives an indication as to why increased

shedding frequencies are associated with higher slant angles in this study. In continuing, the freestream velocity, U_∞, may be represented as:

$$U_\infty = U_M + (U_\infty - U_M) \tag{5.29}$$

The terms within the parenthesis simply represent the vortex street velocity relative to the freestream velocity, i.e.,

$$U_\infty = U_M + U_S \tag{5.30}$$

By substituting Eqns. (5.25), (5.27), and (5.28) into Eqn. (5.30), and after some manipulation, the following relationship can be developed:

$$\frac{U_S}{U_\infty} = 1 - \frac{a}{b} \cdot \frac{\cos(\psi + \eta)}{\cos(\psi)} \cdot St_D \tag{5.31}$$

By substituting Eqns. (5.26) and (5.31) into Eqn. (5.23), the following relation between the Strouhal number and time-averaged quantities may be written.

$$C_{D_B} = 4.32 \cdot \cos(\psi + \eta) - 5.21 \cdot \frac{\cos^2(\psi + \eta)}{\cos(\eta)} St_D - 36.15 \cdot \frac{\cos^3(\psi + \eta)}{\cos^2(\eta)} St_D{}^2 \tag{5.32}$$

Therefore, fluctuating near-wake properties can be related to time-averaged near-wake parameters for slanted-base bluff bodies. Knowledge of the base drag, C_{D_B}, allows for the calculation of the vortex shedding frequency, f, via a second order polynomial. Equation (5.32) can be greatly simplified by considering the 0° base, where ψ and η are identically 0, so that

$$C_{D_B} = 4.32 - 5.21\, St_D - 36.15\, St_D{}^2 \tag{5.33}$$

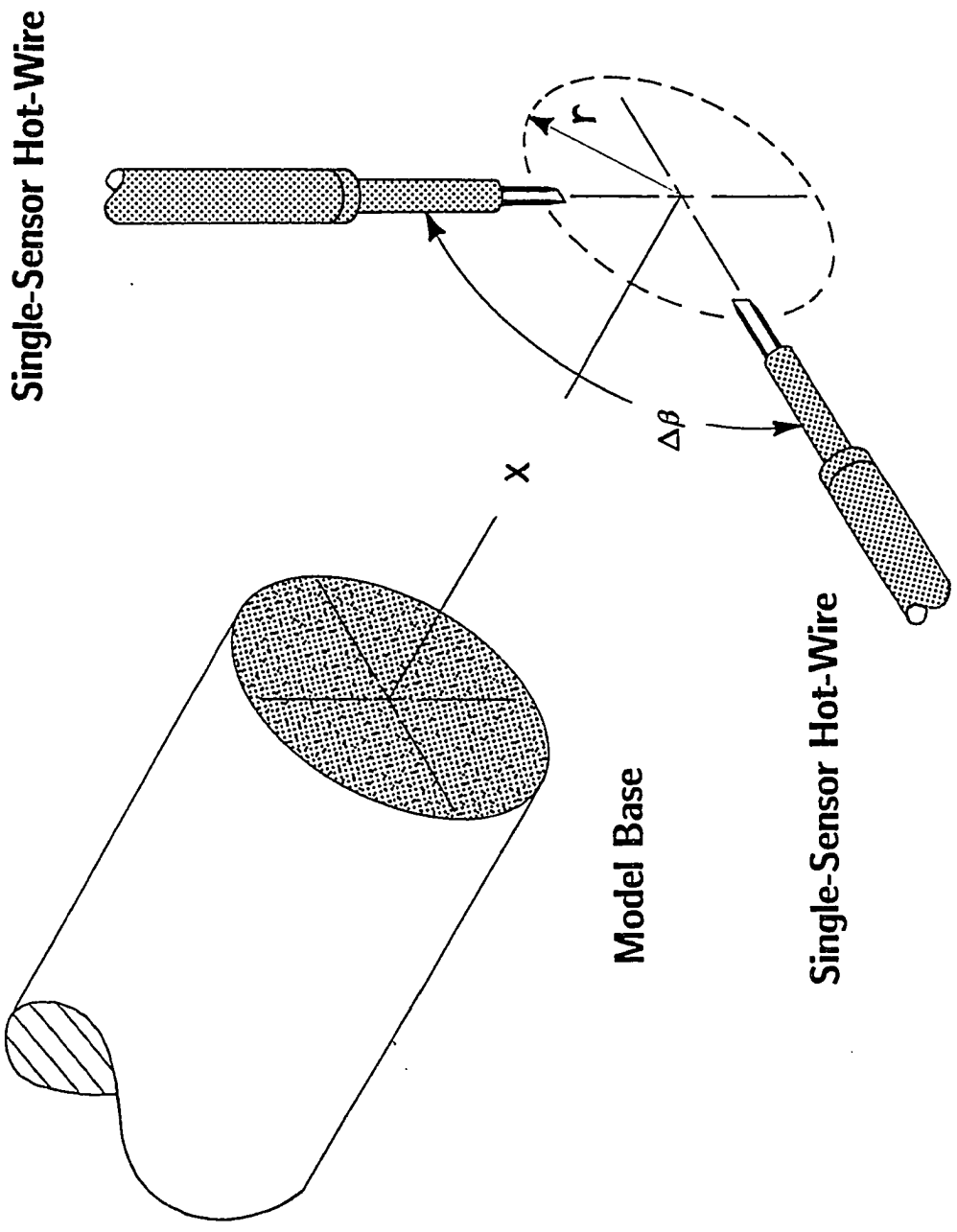

Fig. 5.1 Coordinate System for Coherence Measurements

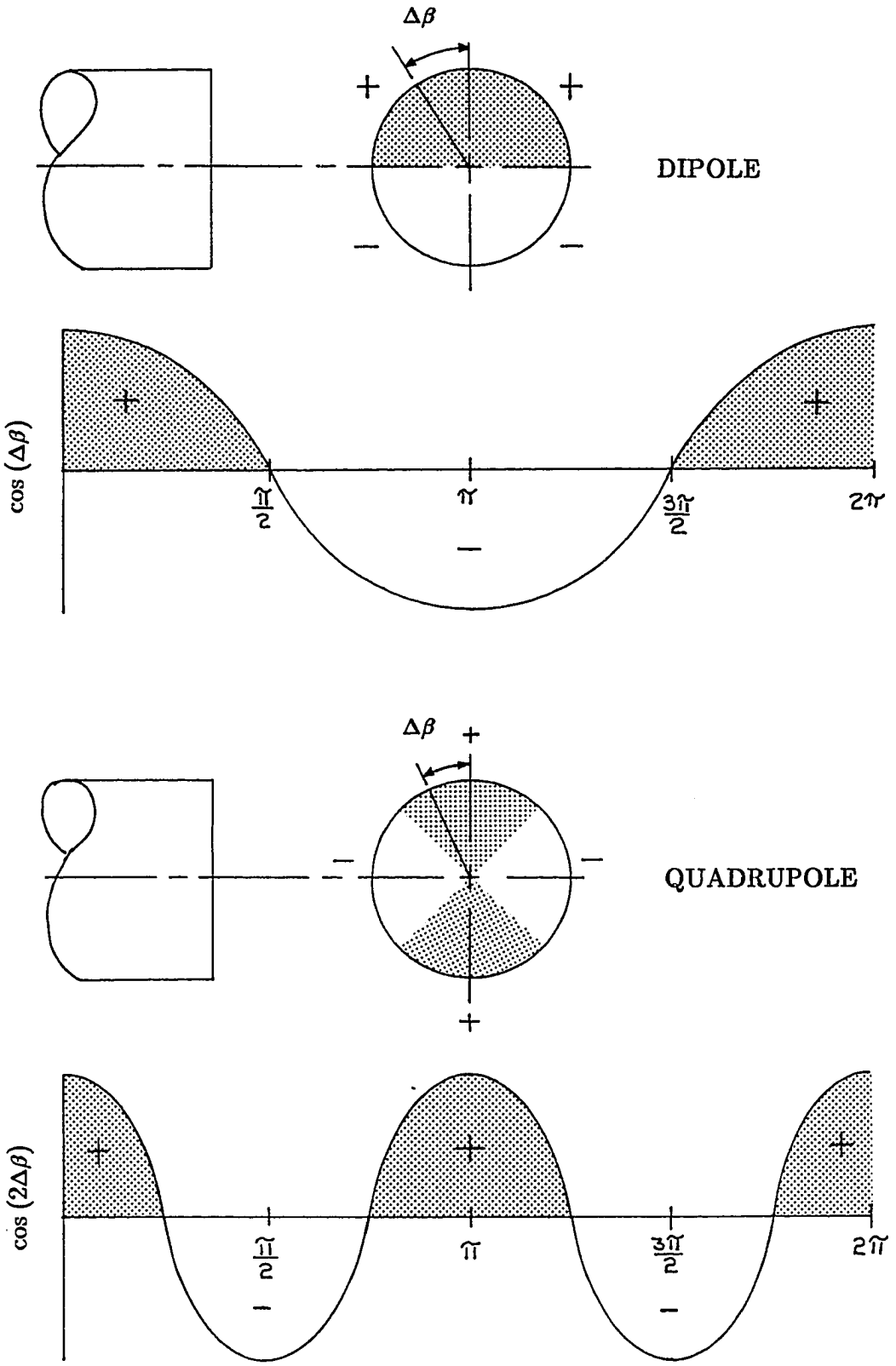

Fig. 5.2 Representation of m=1 and m=2 Azimuthal Constituents .

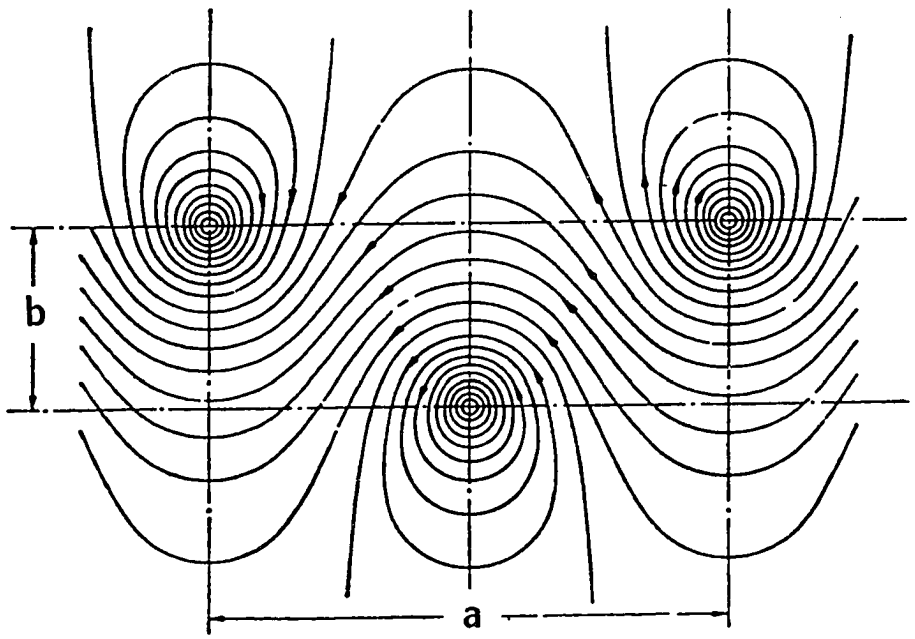

Fig. 5.3 Streamlines in a Stable Vortex Street

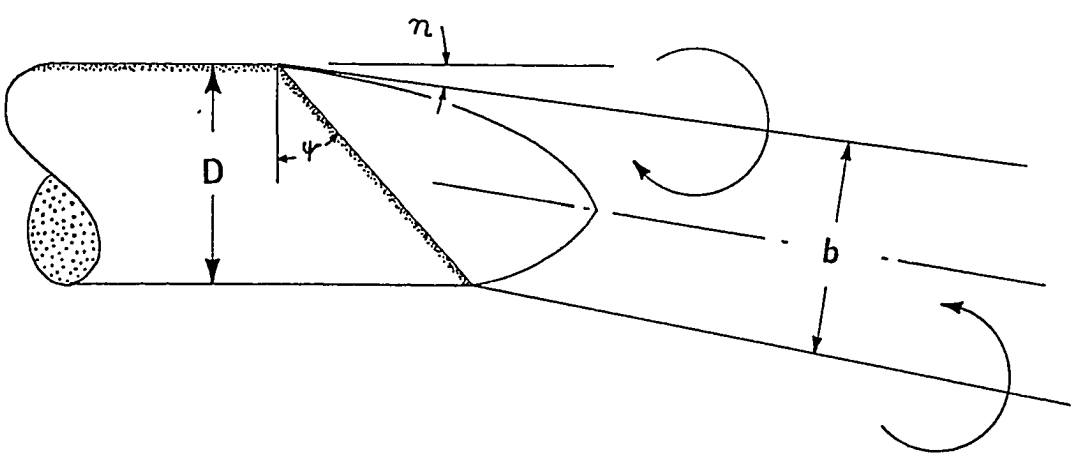

Fig. 5.4 Geometric Model for St_D Variations with Base Drag

Chapter 6 EXPERIMENTAL DETAILS

The current study has been conducted in two facilities, namely the NASA Langley Research Center 6-inch Magnetic Suspension and Balance System (MSBS), and the Old Dominion University (ODU) 4-foot x 3-foot low-speed wind tunnel. The model in the 6-inch facility is magnetically suspended inside the test section and is therefore free of any support interference. Measurements in the 6-inch MSBS facility were not meant to be an exhaustive survey of the wake structure behind slanted-base bluff bodies, but rather to account for how the boundary layer state affects the overall drag coefficient. This facility is described in Section 6.1 below.

The study conducted in the ODU facility was intended to be a comprehensive survey of near-wake parameters in relation to the upstream boundary layer thickness and boundary layer state. All base pressure, wake stagnation point, and boundary layer momentum thickness measurements, as well as near-wake spectral measurements have been made in this facility, which is described in Section 6.2.

6.1 *NASA Langley 6-inch MSBS*

The 6-inch Magnetic Suspension and Balance System is installed in a low-speed open-circuit wind tunnel, capable of Mach numbers exceeding 0.5. The facility is illustrated schematically in Fig. 6.1. The test section for this facility is octagonal with 6.25 inch spacings across the flats. A calibration of the test section

freestream velocity with the pressure drop across the contraction is given in Appendix A.1 for this facility.

The facility was constructed at the Massachusetts Institute of Technology (MIT) in the late 1960's [80-81]. It was relocated to NASA Langley Research Center in 1984 for use in MSBS research [82-83]. The models used in this facility, described in detail in the following section, were constructed entirely of solid, low-hysteresis iron and magnetized by a steady field applied along the test section axis. Forces and torques are generated by applied magnetic field gradients and transverse fields, respectively, according to the magnetic field relations

$$\vec{F} = \int_V (\vec{M} \cdot \nabla)\vec{B}\, dV \tag{6.1}$$

$$\vec{T} = \int_V (\vec{M} \times \vec{B})\, dV \tag{6.2}$$

The model position was monitored continuously, in five degrees-of-freedom, by an Electro-Magnetic Position Sensor (EPS) system. The electro-magnet power supplies are a combination of 3-phase thyratron supplies, field controlled motor generator sets, and D. C. motor-generators. Recent hardware improvements, such as completely rebuilt position sensing electronics, have greatly reduced signal noise and drift [82-83]. Signal coil outputs provide signals in five degrees-of-freedom. Roll information is available for non-axisymmetric models.

6.1.1 *Wind Tunnel Models*

Two bluff body models were used in this study-namely, a 0° base and a 45° slanted-base ogive cylinder as illustrated in Fig. 6.2. As mentioned previously, the models were fabricated from solid low hysteresis iron and were magnetized by

a steady field applied along the axis of the test section. Both models consisted of a 2.5-inch ogive radius forebody and 3.5-inch cylindrical centerbody. Model diameters are 1-inch with a length to diameter ratio of 5:1.

6.1.2 *Drag Calibration*

Due to the absence of struts and other mechanical support devices, drag measurements cannot be made using conventional methods. It is possible, however, to perform a calibration of model axial force to the axial electromagnet current in order to derive drag coefficients during testing. The calibration is performed with the model suspended at zero incidence and side-slip as illustrated in Fig. 6.3. Thread is carefully attached to the model base region and is routed over a pulley, outside the test section. Known weights are attached to the thread to provide axial loading. The calibration is also shown in Fig. 6.3. The calibration is very linear due to the design of the 6-inch MSBS [83].

6.1.3 *Flow Visualization*

Smoke flow visualization using vaporized propylene glycol was used to detail the near-wake of the 45° base model. Propylene glycol was vaporized and injected upstream of the honeycomb structure. A 5 mW laser, in conjunction with a cylindrical lens, was used to create a light sheet that illuminated the near-wake. The light sheet could be oriented to pass either parallel or perpendicular to the model axis. Flow visualization images were recorded on Super VHS tape using a small CCD camera. The model was painted flat black for these tests to help prevent wash-out of the images, if a portion of the laser sheet intersected the model. Appropriate images could be downloaded from tape to a computer for the purpose of digital enhancement [82].

6.2 *ODU 4-foot× 3-foot Low-Speed Facility*

Extensive bluff body wake and boundary layer measurements were carried out in the Old Dominion University (ODU) 4-foot × 3-foot Low-Speed Facility, illustrated schematically in Fig. 6.4. The wind tunnel is driven by a 125 horsepower motor and is capable of reaching speeds in excess of 130 mph [84]. The freestream turbulence intensity ($\sqrt{u'^2}/U_\infty$) in this facility did not exceed 0.2%, as shown in Appendix A.2. For the current study, the Reynolds numbers, based on the model base diameter (Re_D), ranged from 40,000 to 250,000.

Pressure differentials and test section temperatures in this facility were acquired by a Hewlett Packard 3497A Data Acquisition and Control Unit. The data acquisition software that drives the HP3497A was controlled with an IBM PC. A typical data acquisition software program is given in Appendix B. Pressure differentials were measured by 10-torr MKS^{TM}, Model 310 differential pressure transducers in conjunction with MKS^{TM}, Model 170 amplifiers. Test section temperatures were measured with Type-J thermocouples. A schematic of the experimental set-up is shown in Fig. 6.5. The pressure drop across the contraction was determined from the average of a 100 data samples, and is related to the test section velocity via an earlier calibration. Stagnation and static test section pressures were measured relative to the static pressure at the test section entrance, and are related to the static pressure at the longitudinal measuring station through another calibration. Wind tunnel calibrations for the ODU facility are given in Appendices A.3-A.4.

A three-axis traverse shown in Fig. 6.5, located on the test section upper wall, was installed for use in boundary layer measurements and wake surveys. The traverse position was adjusted via external controls and could be monitored to within 0.001 inches in the vertical direction and 0.01 inches in the longitudinal and lateral directions.

6.2.1 *Wind Tunnel Model*

The model used in this study is illustrated in Fig. 6.6. The model was supported by a swept, wing-like strut attached to the front of the aluminum forebody, in a favorable pressure gradient. This was thought to reduce the disturbance of the boundary layer, whereas attaching the strut to the centerbody was likely to cause boundary layer tripping, as indicated in an earlier study [24]. Interchangeable centerbody and base components, manufactured from 3.5-inch o.d. PVC tubing, cover a range of slant-angles (0°, 40°, 45°, and, 50°). The centerbody was manufactured with a slight taper in order to delay boundary layer transition to a higher Reynolds number. The taper angle was 0.3°, while the length-to-base diameter ratio for all models was 6:1, where the length of the model was measured from the forebody leading edge to the leading edge corner of the base. Blockage or other boundary corrections were considered to be unnecessary because the model cross-sectional area ratioed to the test section area is less than 1% [85-88]. Shop drawings of this model are given in Appendix C.

6.2.2 *Base Pressure Measurements*

Base pressures were measured through a number of pressure taps positioned on each base. A large number (44) of taps were densely packed on the 45° and 50° bases, where large pressure gradients were expected to exist due to the presence of longitudinal vortices. The spacing was determined from flow visualization results in an earlier slanted-base study [24]. A sparse pressure tap pattern was employed on the 0° and 40° bases because the near-wake was known to be a turbulent closure with weaker pressure gradients. Previous flow visualization results from an earlier slanted-base study also indicated that the base flow patterns were quite symmetric along the vertical centerline of the bases [24]. This allowed symmetry to be exploited in the placement of the pressure taps. Figure

6.7 illustrates the pressure tap pattern for several bases. To eliminate the necessity for routing a large number of pressure tubes out of the model, a 48-channel Scanivalve^{TM} was located inside the centerbody. The associated electrical wiring and a single pressure tube were fed through the forebody, down a groove in the strut and out of the test section to the channel switching electronics and pressure transducers.

6.2.3 *Wake Stagnation Point Measurements*

A specially manufactured pressure probe enabled the measurement of the wake stagnation point location behind the lower angle slanted-bases. The configuration is attributed to Gai and Patil [5] and is illustrated in Fig. 6.8. The probe was manufactured from two $\frac{1}{16}$ inch O.D. brass tubes that were epoxied together after their bonding surfaces were sufficiently flattened. The tips were ground and smoothed to a 30° angle, measured with respect to the probe stem.

This probe configuration could measure the velocity head directly, at any near-wake location behind an axisymmetric bluff body, with proper calibration. For the current research, the probe was used only to locate the region where no measurable velocity head was present. This location could correspond to two possible flow orientations – namely, the location of zero velocity (wake stagnation), or friction-free flow, parallel to the probe stem. With proper orientation of the probe, the latter could be excluded. The probe was mounted to the three-axis traverse, discussed previously. The pressure differential was measured by a similar arrangement to that used for base pressure measurements, described in the previous section.

6.2.4 *Boundary Layer Measurements*

Boundary layer velocity profiles were measured ahead of the leading edge corner of the base at a longitudinal location of $\frac{X_{BL}}{D} = -0.20$. A boundary layer stagnation probe was used for these measurements. The design is similar to an ordinary stagnation-type probe, however, the probe tip was flattened and its walls filed lightly to minimize its cross-sectional area. This results in an oval-shaped tip with a minimum outer diameter of 0.02 inches. The probe was traversed vertically through the boundary layer, with the vertical position determined to within 0.001 inches. The stagnation pressure was measured relative to the static pressure at the test section entrance, and is related to the static pressure at the longitudinal measuring station via the calibration discussed previously.

The vertical location of the wall (centerbody surface) was determined by inspection of the boundary layer stagnation pressure data. As the probe traversed downward through the boundary layer, the static pressure decreased until the wall was reached. If the probe was lowered further, the tip was designed to deflect upwards and into regions of higher stagnation pressure. This resulted in a minimum stagnation pressure as the probe's lower surface rested on the wall. By taking the sensing location to be the probe center, the wall location could be determined. This procedure is illustrated in Fig. 6.9.

6.2.5 *Predominant Frequency Measurements*

A TSI, IFA-100 constant-temperature, hot-wire anemometer, in conjunction with a TSI IFA-200 multi-channel digitizer and an 8086-based microcomputer were used for turbulence measurements. The TSI thermal anemometry software package controlled the probe calibration, data acquisition and the data analysis. The anemometer software and hardware allow for temperature compensation. The sensors used were commercial TSI-T1-5,

Tungsten wire sensors ($d = 5\mu m$, $l = 1.25$ mm), operated at an overheat of 1.8. A calibration program in the software package was used to generate a best fit 4th-order polynomial, relating the hot-wire probe voltage to velocity.

A single hot-wire was used to extract predominant flow frequencies. The hot-wire was supported on the three-axis traverse used for pressure measurements, and positioned along a vertical plane in the wake at the axial position, $\frac{X}{D} = 7$. The selected radial position for the probe corresponded to the location where the hot-wire signal was most periodic. A schematic of the set-up is shown in Fig. 6.10. Turbulence intensities at this location were below 10%, and therefore, were within a suitable calibration range for the hot-wire system. Power spectra were constructed from more than 51,200 streamwise velocity samples, taken at sampling rates between 500-1000 Hz.

6.2.6 *Coherence Measurements*

Coherence measurements in the wake of the 0° base model were obtained in terms of the cross-correlation of the streamwise fluctuating velocity component, u'. Two single hot-wire probes, positioned along a plane at an axial wake location of $\frac{X}{D} = 7$, were used to measure the coherence of the fluctuating velocity components, as shown in Fig. 6.11. Coherence measurements were made by fixing one sensor support to the traverse and then rotating the other via an extension arm bolted to the traverse. Alignment of the probes was accomplished by using an aluminum template, shaped in the geometry of the 0° base and containing scribed radial and angular coordinates. The template was placed perpendicular to the wake axis, clamped firmly onto a support stand, and positioned near the hot-wire probes. The proper vertical alignment of the template was possible with the help of a cathetometer located outside the test section. Lateral alignment was made by visual inspection of the model with relation to the template.

Correlations were obtained at angular separations of 20° from $\Delta\beta = 20°$ to 180°. Each correlation was obtained using 32,288 velocity samples per station at a sampling rate of 500 Hz.

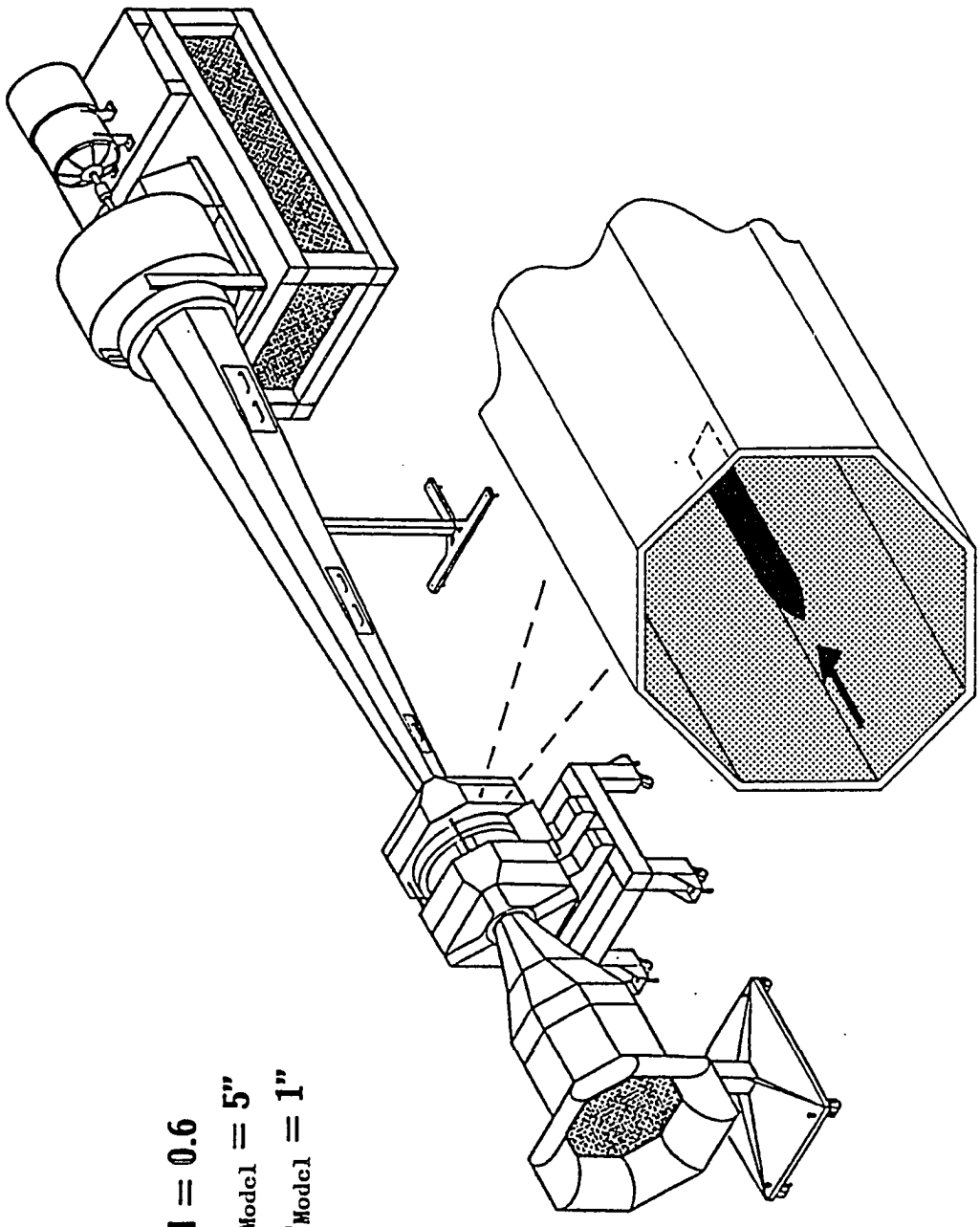

Fig. 6.1 NASA LaRC 6" Magnetic Suspension and Balance System

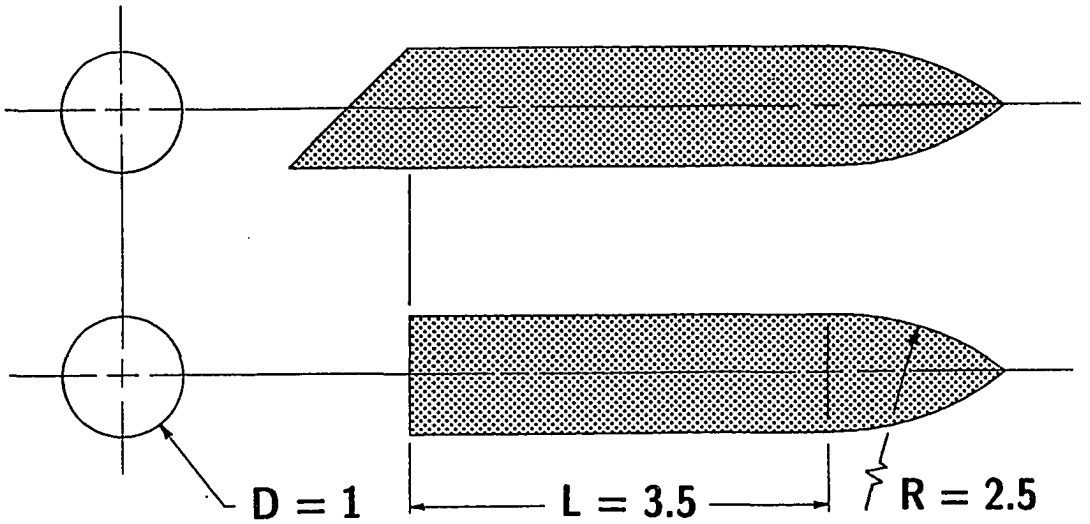

Fig. 6.2 Slanted-Base Wind Tunnel Models: 6" MSBS

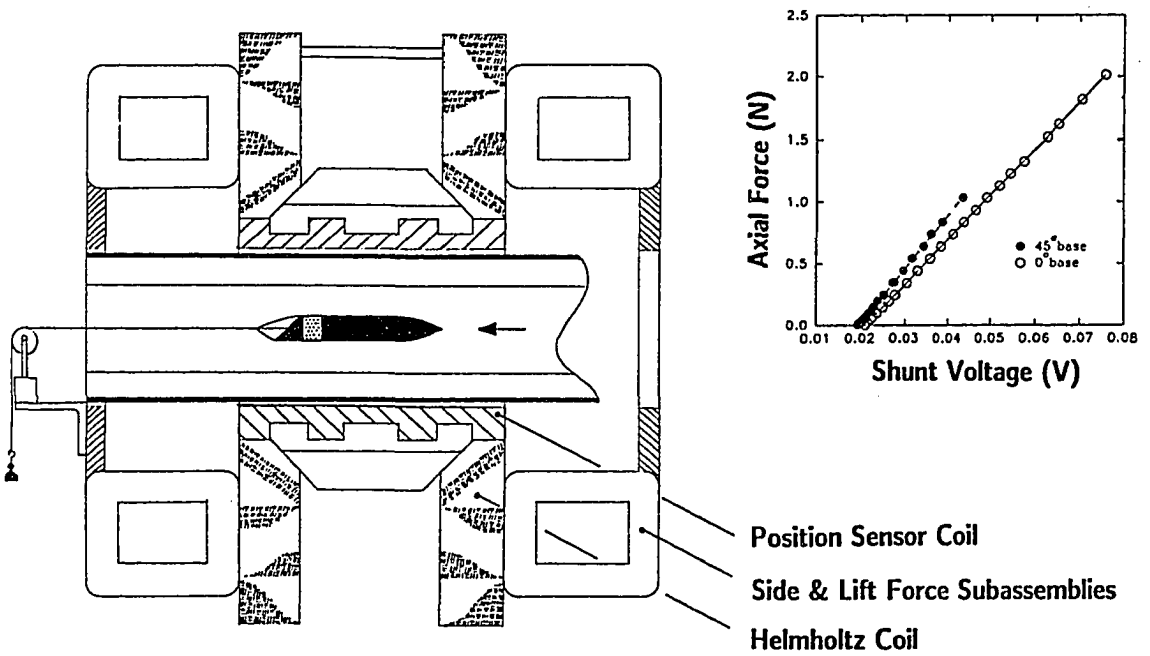

Fig. 6.3 6" MSBS Drag Calibration

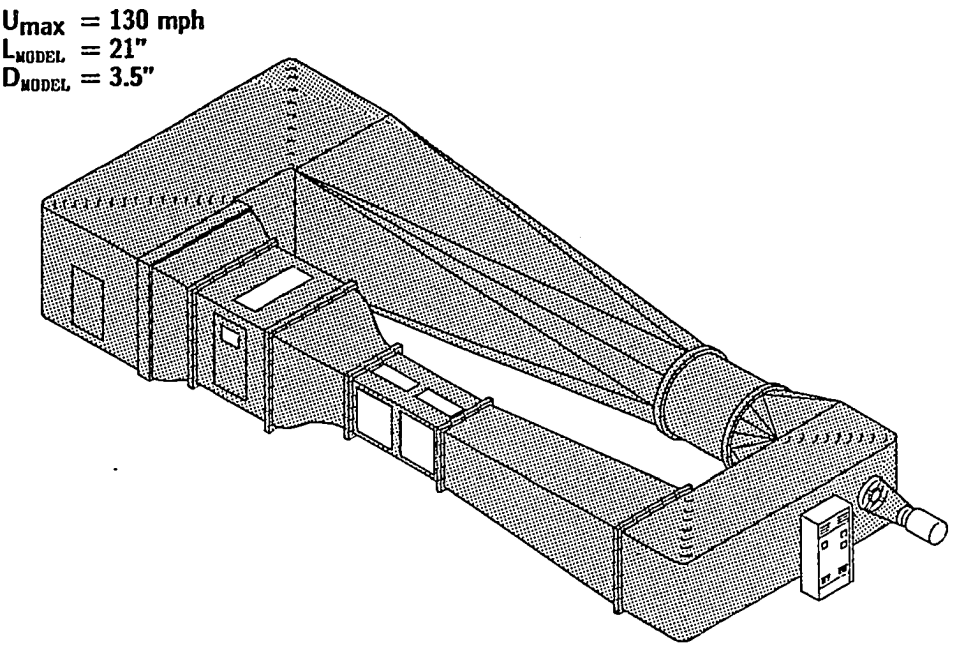

Fig. 6.4 ODU Low-Speed Wind Tunnel

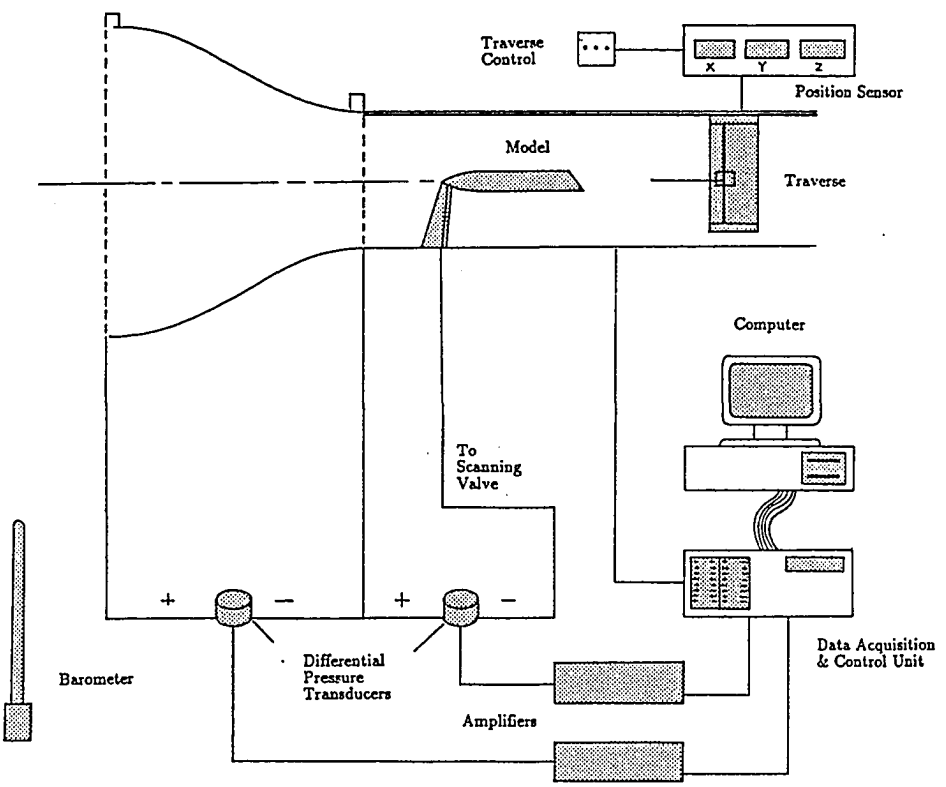

Fig. 6.5 Experimental Set-Up: Pressure Measurements

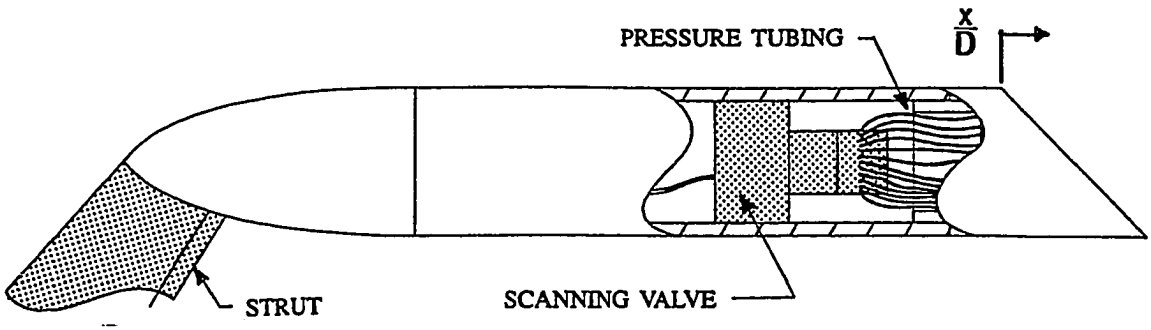

Fig. 6.6 ODU Wind Tunnel Model

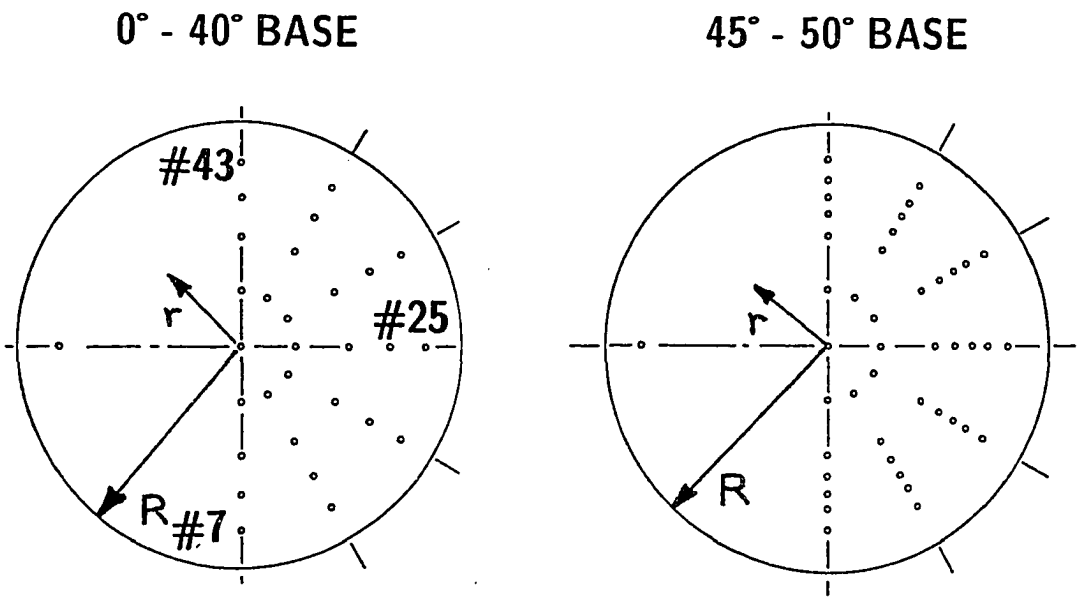

Port locations at $\frac{r}{R}$ = 0, 0.25, 0.50, 0.68 0.83. 30° spacing.

Port locations at $\frac{r}{R}$ = 0, 0.25, 0.50, 0.62, 0.68, 0.75, 0.83. 30° spacing.

Fig. 6.7 Location of Base Pressure Taps

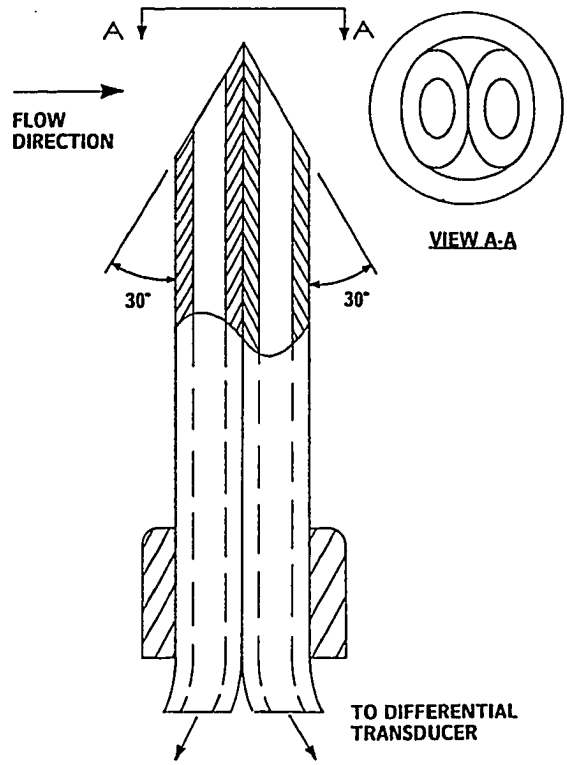

Fig. 6.8 Probe for Measuring Wake Stagnation Point Location

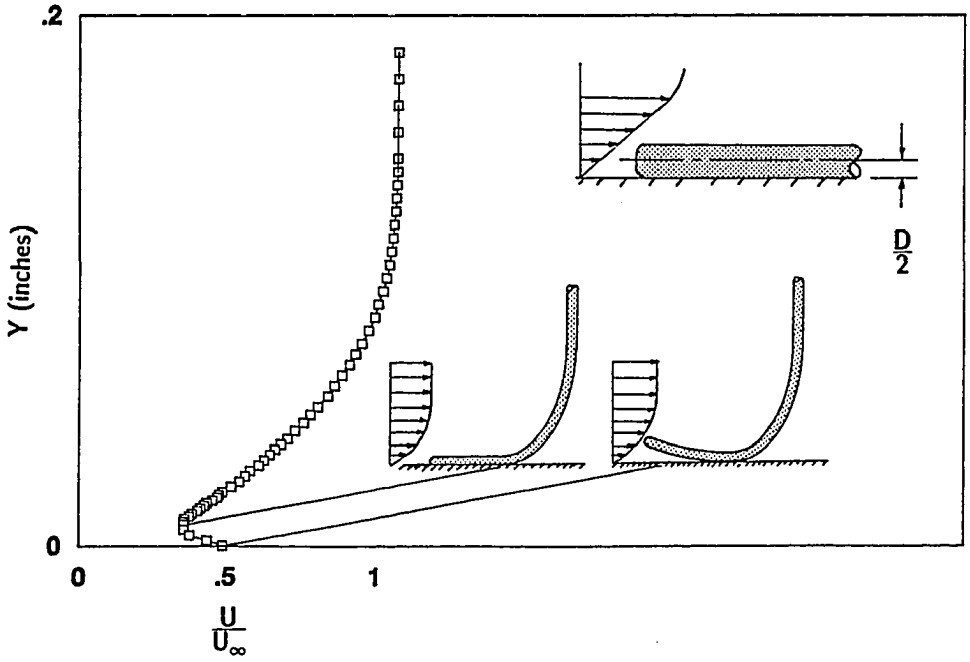

Fig. 6.9 Probe for Measuring Boundary Layer Velocity Profile

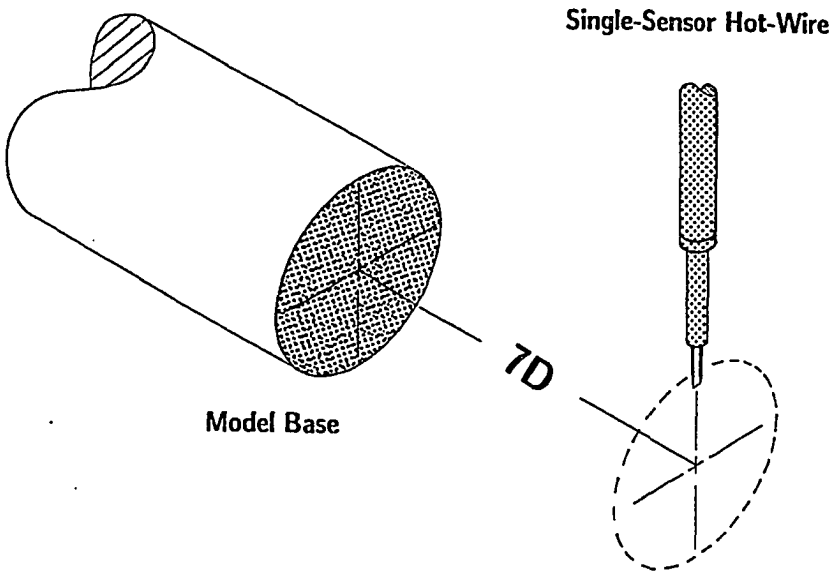

Fig. 6.10 Experimental Set-Up: Predominant Frequency Measurements

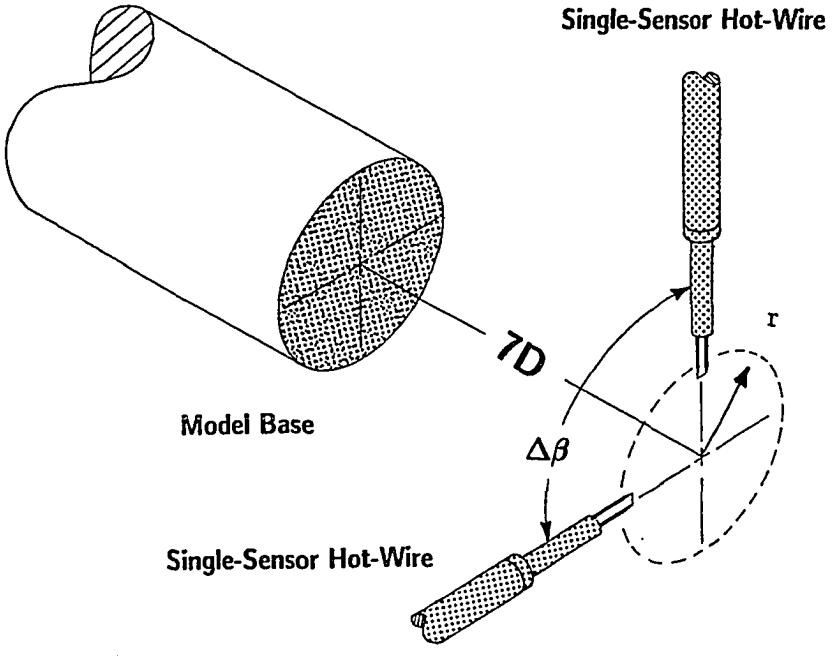

Fig. 6.11 Experimental Set-Up: Coherence Measurements

Chapter 7 STEADY FLOW RESULTS

Steady flow measurements were conducted in two facilities; namely the NASA Langley Research Center 6-inch Magnetic Suspension and Balance System (MSBS), and the ODU 4-foot by 3-foot low-speed wind tunnel. These facilities were described in detail in Chapter 6.

7.1 *Benchmark Tests: 6-Inch MSBS*

A series of tests were carried out at the 6-inch MSBS to examine the relationship between the near-wake behavior and the boundary layer state. Measurements were made with a clean model and with boundary layer trips at various locations along the model centerbody. Trip locations were located at the leading edge, center, and trailing edge of the model centerbody as illustrated in Fig. 7.1. The boundary layer was tripped using a $\frac{1}{8}$-inch wide ring of No. 60 grit around the circumference of the model. The grit particles were adhered to the model surface via a thin coat of lacquer.

7.1.1 *Drag Coefficients*

Fixed- and free-transition results for the 0° base model are presented in Fig. 7.2. Drag coefficients for a trip location on the centerbody leading edge are consistently higher than for the free-transition case. This difference is attributed to increased centerbody skin friction associated with a turbulent boundary layer, and to grit particle drag. It may also be argued that increased mixing associated

with a fully turbulent free shear layer (fixed boundary layer transition) may cause a noticeable increase in the overall model drag, compared to a partially laminar free shear layer.

Figure 7.3 compares free transition drag coefficients for the 0° and the 45° base models. The curve for the 45° base is similar to that determined in the 13-inch MSBS study described in Chapter 2 [24]. This degree of similarity is somewhat surprising considering that the length-to-diameter ratio for the model in the 13-inch study is much higher (12:1) than that for the current study (5:1). In the current study the large jump in drag, signaling a switch in the near-wake flow pattern, occurred at a Reynolds number Re_D of 55,000, compared to 60,000 for the 13-inch study. The magnitude of the jump was also similar, as was the presence of hysteresis with decreasing Reynolds numbers.

Figure 7.4 compares drag coefficients for the 45° base model with various boundary layer trip locations on the centerbody. It is shown that the change in the near-wake flow pattern did not occur for the forward and center trip locations. This is again consistent with 13-inch MSBS results with a boundary layer trip near the centerbody leading edge. Moving the trip location downstream, near the trailing edge of the centerbody gave a very different result. High drag coefficients, signaling the presence of a vortical near-wake, occurred over the entire Reynolds number range. This may have resulted from slight geometric modifications of the base due to the addition of the grit, or by the interaction between the local flow separations that are commonly expected to occur at the grit location, and the base flow [5].

7.1.2 *Flow Visualization*

Smoke flow visualization using vaporized propylene glycol was used to detail the near-wake of the 45° base model, as discussed in Chapter 6. A digitally

enhanced image of the near-wake is shown in Fig. 7.5 for a Reynolds number of 40,000. A closed near-wake is shown to be present with the laser light sheet passing parallel to the model axis. This image is devoid of any detail within the near-wake, however, a clear outline of the near-wake is shown due to smoke entrainment within the boundary layer. A deflection of the wake stagnation point away from the wake centerline and towards the base trailing edge is clearly seen. No curvature is evident in the free shear layer separating from the base trailing edge. These features are captured in the steady flow model shown in Fig. 4.10.

Figure 7.6 details the features of the longitudinal vortex wake for Reynolds numbers greater than 60,000. The free shear layer is shown to reattach on the base just downstream of the base leading edge, forming a separation bubble. This is consistent with the need for base flow reattachment in the presence of the longitudinal vortex wake.

7.2 *Detailed Near-Wake Measurements: ODU Facility*

The benchmark tests at the 6-inch MSBS showed the importance of the boundary layer on the near-wake flow pattern. In order to study this effect further, it was necessary to make localized measurements within the near-wake and within the boundary layer itself. A much larger model and facility were necessary to perform this study, therefore, the Old Dominion University 4-foot by 3-foot low-speed wind tunnel was used for the continuation of this research [89].

7.2.1 *Base Pressure Coefficients*

Base pressure distributions for the 45° and 50° bases, presented as contour plots in Fig. 7.7, reveal the characteristics of the two predominant near-wake flow patterns. The 45° base pressure contours show weak gradients along the lower quadrants indicating a pressure recovery as the flow attempts to reattach. The

50° base pressure contours reveal steep gradients along the upper quadrants, followed by a central region with little variation in pressure, consistent with flow reattachment. Flow visualization using stress-sensitive liquid crystals on the 50° base, shown in Fig. 7.8, reveal high stress regions which agree, as expected, with regions of large pressure gradients.

Figures 7.9 and 7.10 detail the base pressure distribution for the 45° and 50° bases along the vertical and horizontal centerline. Base pressures for the 45° base appear quite uniform along the horizontal centerline, however, non-uniformities exist along the vertical centerline associated with the turning of the external flow down the plane of the base. Base pressures along the 50° base show large pressure gradients near the base perimeter, characteristic of the attached horseshoe vortex.

The base drag, determined by integration of the base pressure, is presented in Fig. 7.11 for individual bases. Low base drag for the lower angle slanted-bases is a consequence of the closed near-wake pattern, however, more than a doubling in base drag results when the longitudinal vortex wake is present on the 50° base.

7.2.1.1 *Reynolds Number Effects: 0°, 40°, and 45° Bases*

Variations in the base pressure coefficients with Reynolds number for the lower angle slanted-bases at two locations along the symmetry plane are shown in Figs. 7.12-7.13. Base pressures near the perimeter of the base are shown to vary slightly at the lower Reynolds numbers; remaining fairly constant for $Re_D >$ 150,000. No significant deviations exist between fixed- and free-transition results. Centerline base pressures are also shown to vary slightly at the lower Reynolds numbers, however, more pronounced deviations exist between fixed- and free-transition results. These deviations exist up to the higher Reynolds numbers (>170,000). Base drag coefficients for the lower angle slanted-bases are presented

in Fig. 7.14. No measurable variation in base drag is shown with increasing Reynolds numbers.

7.2.1.2 *Reynolds Number Effect: 50° Base*

Variations in the base pressure coefficient for the 50° base at two locations along the symmetry plane are shown in Fig. 7.15. Unlike the lower angle slanted-bases, the 50° base pressures do show a significant dependence on the Reynolds number and the boundary layer trip location. It is shown in Fig. 7.15 that fixed- and free-transition results are identical for $Re_D < 80{,}000$, suggesting that boundary layer tripping has not occurred for these Reynolds numbers due to too small a grit size. Abrupt variations in base pressure coefficients occur as the Reynolds number is increased. Fixed-transition results deviate from free-transition at $Re_D \simeq 80{,}000$ for the forward trip location and for $Re_D \simeq 110{,}000$ for the center trip location. These deviations are shown to continue up to higher Reynolds numbers ($Re_D \simeq 170{,}000$) where fixed- and free-transition results again converge.

These variations are related to the combined effect of changes in vortex strength and location. Figs. 7.16-7.17 show the base pressure distribution on the vertical centerline for several Reynolds numbers and boundary layer trip locations. It is observed that the vortex strength increases and the vortices move toward the base perimeter with increasing Reynolds number. It is also shown that fixing boundary layer transition shifts the vortex towards the base perimeter. The results of Figs. 7.16-7.17 are further substantiated with liquid crystal flow visualization as shown in Fig. 7.18. The region of high stress along the vertical centerline, characterizing the horseshoe vortex, is observed to move towards the base perimeter with increasing Reynolds number. There appears to be a correlation between the position of the horseshoe vortex and the boundary layer

state ahead of separation. The boundary layer displacement thickness of Figs. 4.6 and 4.7 show the external streamlines shifting away from the model for fixed boundary layer transition, which corresponds to the shift in the horseshoe vortex position. More detailed pressure measurements are necessary to confirm a correlation.

The Reynolds number is shown in Fig. 7.19 to have an influence on the 50° base drag. Furthermore, it is shown in Fig. 7.20 that the base drag decreases by 10%-15% when transition is fixed at the leading edge of the centerbody. This is in agreement with previous research which showed that the overall drag for the 50° base model did not increase with fixed boundary layer transition on the centerbody. It was concluded that the increase in skin friction drag on the centerbody due to the turbulent boundary layer is counteracted by a decrease in base drag [24].

7.2.2 *Wake Stagnation Point*

Measured wake stagnation point locations in the ODU facility are made with the stagnation point pressure probe discussed in Chapter 6. A finite element method [90], described in Appendices D-E, is compared with results from this section to confirm observed trends.

7.2.2.1 *Base Slant-Angle Effect*

Experimental wake stagnation point locations, measured relative to both the leading and trailing edge of the base, are presented in Fig. 7.21. Wake stagnation point measurements relative to the base trailing edge are shown to decrease with increasing slant-angle; especially between the 40° and 45° slanted-bases. Measurements relative to the base leading edge are shown to increase with increasing slant-angle. Thus, it can be concluded that the distance the base

trailing edge extends into the wake is greater than the outward shift of the wake stagnation point.

7.2.2.2 *Reynolds Number Effects*

The effect of Reynolds number, Re_D, on the wake stagnation point location is presented in Fig. 7.22. Free-transition results for the 0° and 40° bases are similar; namely little change in the stagnation point at the lower Reynolds numbers. This is followed by a weak shift away from the base around $Re_D \simeq 160{,}000$. For the 45° base, a sudden and substantial shift in stagnation point location towards the base trailing edge is seen around $Re_D \simeq 160{,}000$. This is followed by another sudden and even larger shift in location away from the base. There was no evidence of hysteresis present in the wake stagnation point location for the 45° base model.

It is demonstrated for increasing Reynolds numbers ($Re_D > 160{,}000$) that the wake stagnation point shifts away from the base. This is believed to be related to the onset of natural transition as will be discussed in the following section. It is noted that current measurements are in agreement with available literature for flow reattachment behind a backward facing step as presented in Fig. 2.4 [8]. It is not, however, suitable to compare current measurements with previous bluff body wake stagnation point measurements [12]. In the previous axisymmetric bluff body study by Porteiro and Przirembel [12], the boundary layer was always turbulent at separation. Furthermore, the wake stagnation point in this study was located by extending a pitot-type probe from the base through the near-wake. This technique may have an adverse effect on the near-wake flow as suggested by Britcher [24].

The effect of the centerbody boundary layer state on the wake stagnation point location is also shown in Fig. 7.22. In all cases, the shift in the stagnation point away from the base begins at lower Reynolds numbers, with fixed-transition. It is now necessary to make a detailed boundary layer study on the centerbody near the base. From the analysis of Chapter 4, the boundary layer just upstream of the base leading edge appears crucial in determining the near-wake flow pattern. This is chosen as the location for the boundary layer survey.

7.2.3 *Boundary Layer Measurements*

Typical boundary layer profiles on the 50° base model, just upstream of the base leading edge, are shown in Fig. 7.23. The Reynolds number chosen for these measurements, $Re_D = 110{,}000$, corresponds to the value where large discrepancies existed between fixed- and free-transition base pressure measurements. The profiles of Fig. 7.23 obviously represent two distinct boundary layer states. For fixed boundary layer transition on the leading edge of the centerbody, the velocity profile has the characteristic full shape of a turbulent boundary layer, and is well represented by the $\frac{1}{7}$ Power Law. The free-transition profile is not nearly as robust and shows characteristics of a Blasius flat plate boundary layer profile.

The velocity profiles can now be integrated, assuming incompressible flow, to determine the boundary layer momentum thickness, θ. Results for the 50° base model are shown in Fig. 7.24. Free-transition results are shown to vary as $(Re_D)^{-1/2}$ for low to moderate Reynolds numbers in accordance with classical laminar boundary layer theory. Deviations from classical theory occur at $Re_D > 80{,}000$ for the forward trip location, at $Re_D > 110{,}000$ for the center trip location, and for $Re_D > 160{,}000$ for free-transition. Discrepancies are due to the onset of transition on the centerbody, i.e., the transition point moving from within the shear layer and onto the centerbody itself. The momentum thickness

increases beyond the critical Reynolds number as a result of the upstream movement of the transition point. Similar trends in momentum thickness also occur for the lower angle slanted-bases. From inspection of results discussed above, the onset of transition on the centerbody corresponds to deviations in base pressure for the 50° base, and the wake stagnation point location for the lower angle slanted-bases. It should be mentioned that the external flow velocity is approximately 8% higher than the freestream velocity at this measuring station due to reduced base pressures imposing a favorable pressure gradient along the centerbody [1, 3-4].

7.2.4 *Near-Wake Similarity*

It has been shown in Figs. 7.12, 7.15 and 7.22 that the Reynolds number based on the model diameter, Re_D, is not suitable to collapse near-wake data. The evidence presented above demonstrates the influence of the approaching boundary layer on near-wake parameters, therefore, a requirement for near-wake similarity is an independent variable based on an upstream boundary parameter. The obvious choice is the Reynolds number based on the incoming boundary layer momentum thickness:

$$Re_\theta = \frac{U_\infty \theta}{\nu}$$

7.2.4.1 *Base Pressure*

Base pressure results for the lower angle slanted-bases (0° and 45° bases) are replotted in Fig. 7.25 using Re_θ as the independent variable. Fixed- and free-transition results are now shown to collapse onto a single curve. A slight variation in base pressure exists for Reynolds numbers, $Re_\theta < 400$, however, the base pressure remains constant at the higher Reynolds numbers.

50° base pressure results from Fig. 7.15 using Re_θ as the independent variable are presented in Fig. 7.26. It is seen that fixed- and free-transition results, which showed large deviations with Re_D as the independent variable, now collapse. The exception is seen at the vertical centerline location, $\frac{r}{R} = 0.83$, which is attributed to model misalignment.

7.2.4.2 *Wake Stagnation Point*

Wake stagnation point location results from Fig. 7.22 are presented in Fig. 7.27 using Re_θ as the independent variable. Results for the 0° and 40° base are shown to collapse reasonably well. It is noticed that significant variations in the wake stagnation point location occur for $Re_\theta \leq 400$, which correspond to the measurements of Eaton and Johnston [8] for a backward facing step results shown in Fig. 2.2.

Results for the 45° base show some collapse, at the higher Reynolds numbers, however, in the vicinity of $Re_\theta \simeq 400$, where large shifts in the location of the wake stagnation point occur, the data do not "collapse" fully. The location of the wake stagnation point for the 45° base has been shown to be quite sensitive to small changes in the upstream boundary layer momentum thickness. This suggests that slight experimental differences between runs may influence boundary layer transition, therefore affecting the wake stagnation point location.

The Reynolds number based on the momentum thickness, Re_θ, is an appropriate choice to correlate near-wake parameters. This is shown for base pressures and wake stagnation point locations when the closed near-wake is present, and for base pressures when the vortical wake is present.

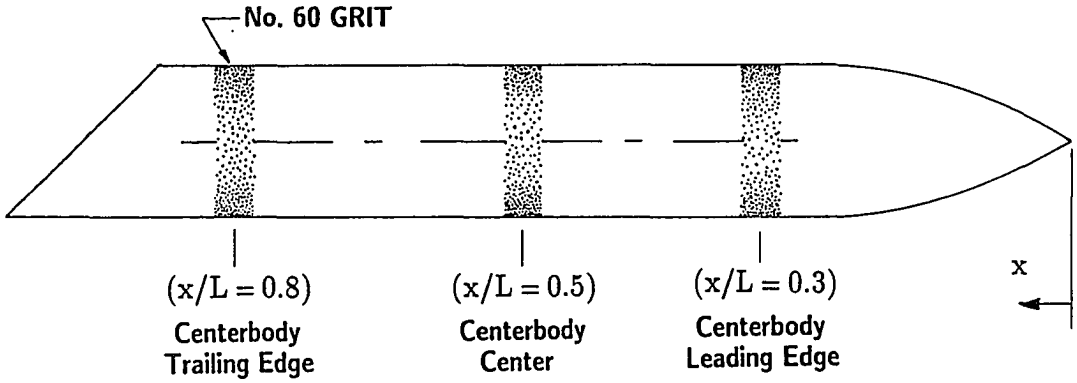

Fig. 7.1 Boundary Layer Trip Locations: 6-Inch MSBS Model

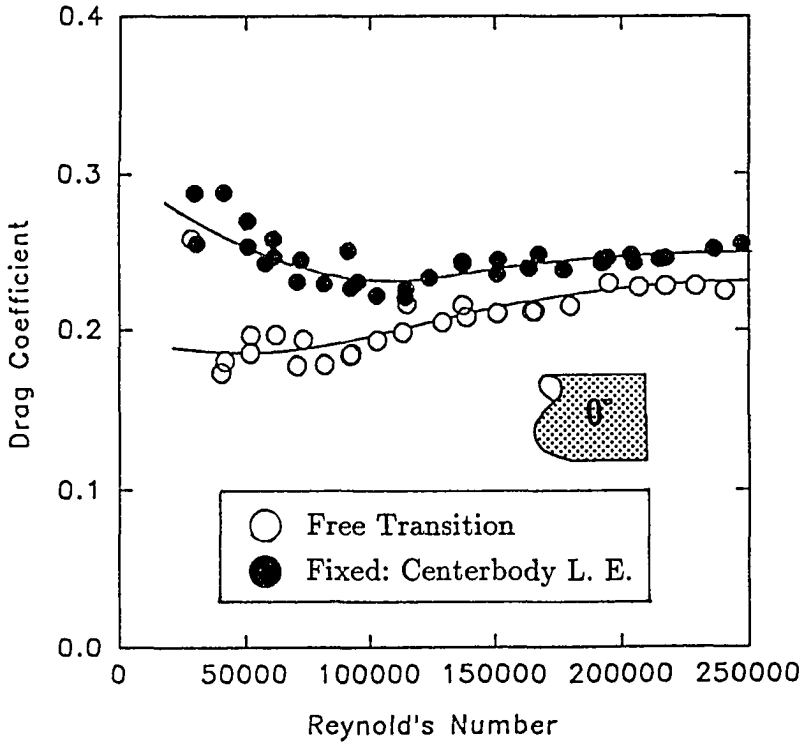

Fig. 7.2 Drag Coefficients for 0° Base Model

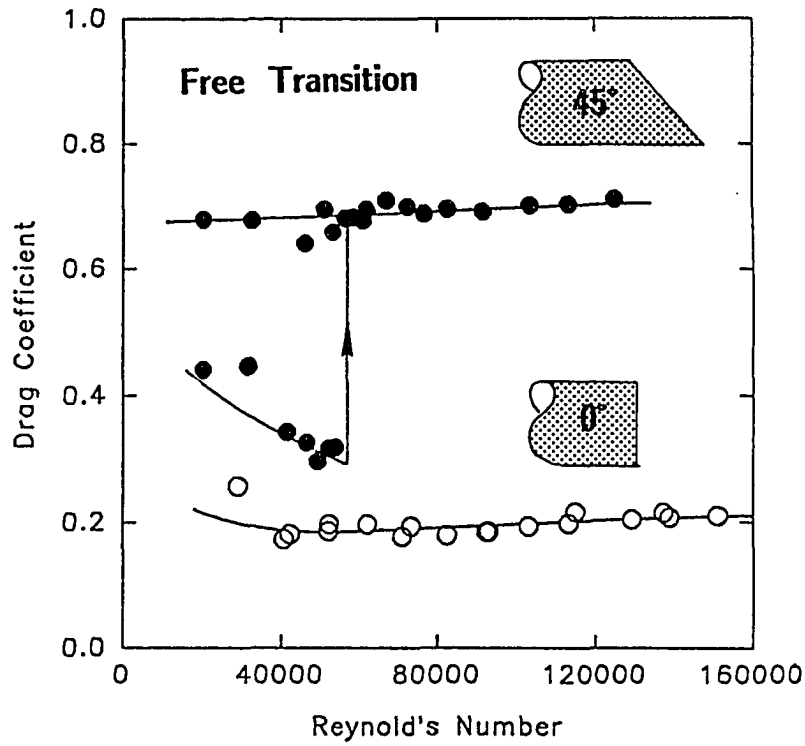

Fig. 7.3 Drag Coefficients for 0° and 45° Base Models: Free Transition

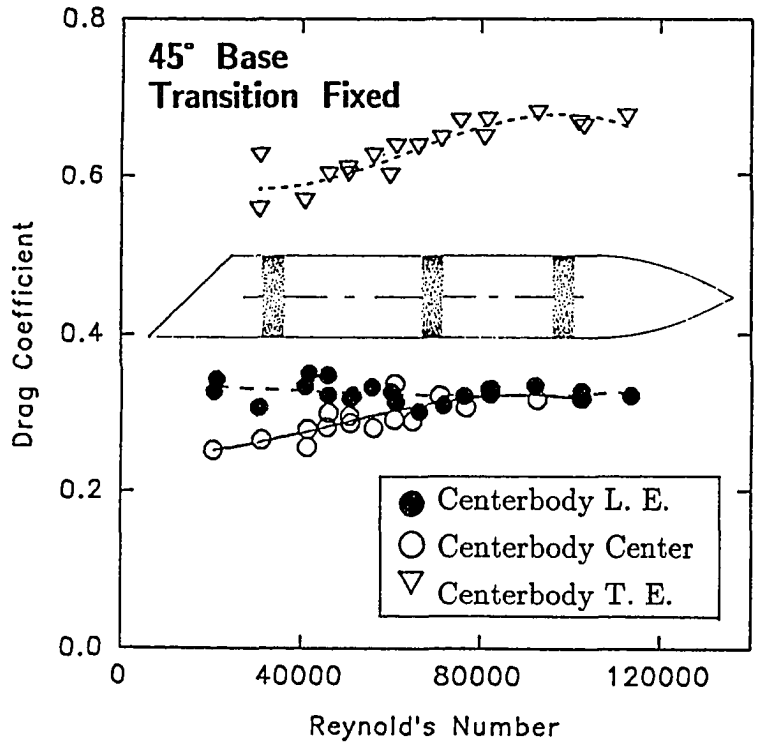

Fig. 7.4 Drag Coefficients for 45° Base Model: Fixed Transition

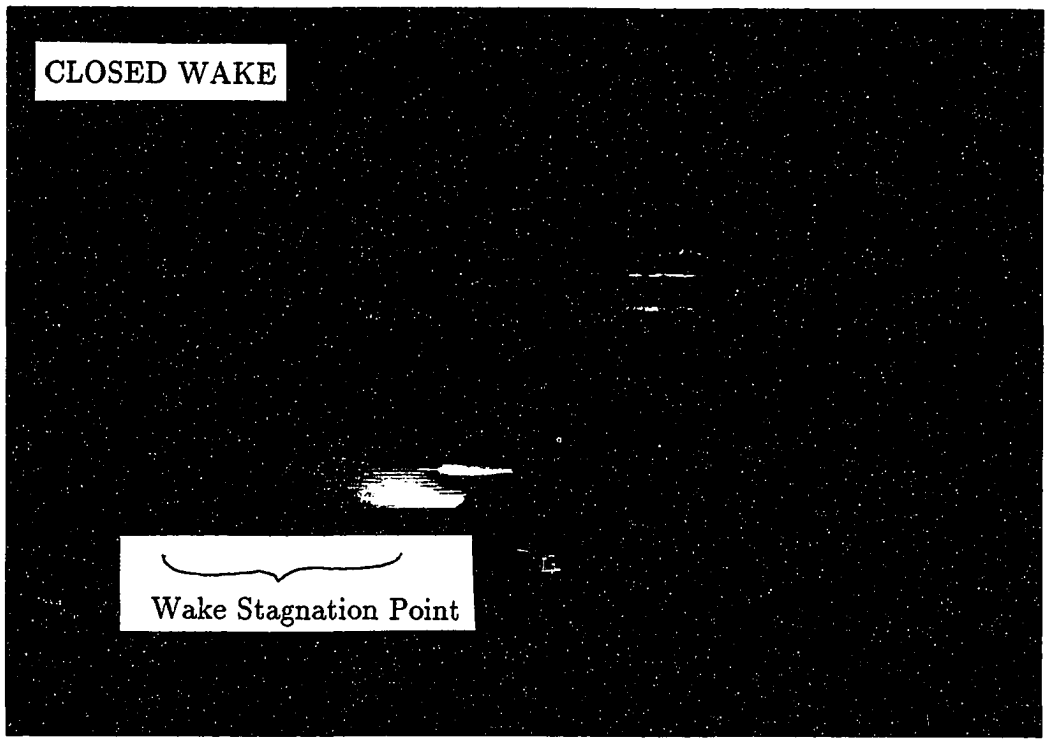

Fig. 7.5 Smoke Flow Visualization: $Re_D < 60{,}000$

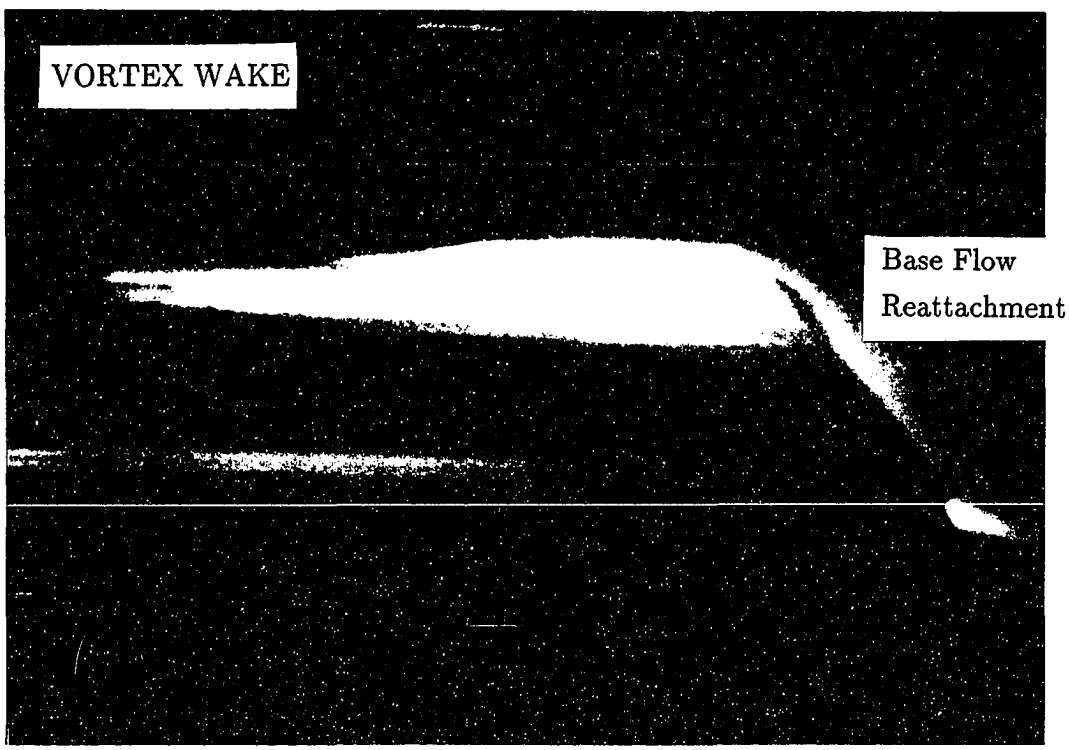

Fig. 7.6 Smoke Flow Visualization: $Re_D > 60{,}000$

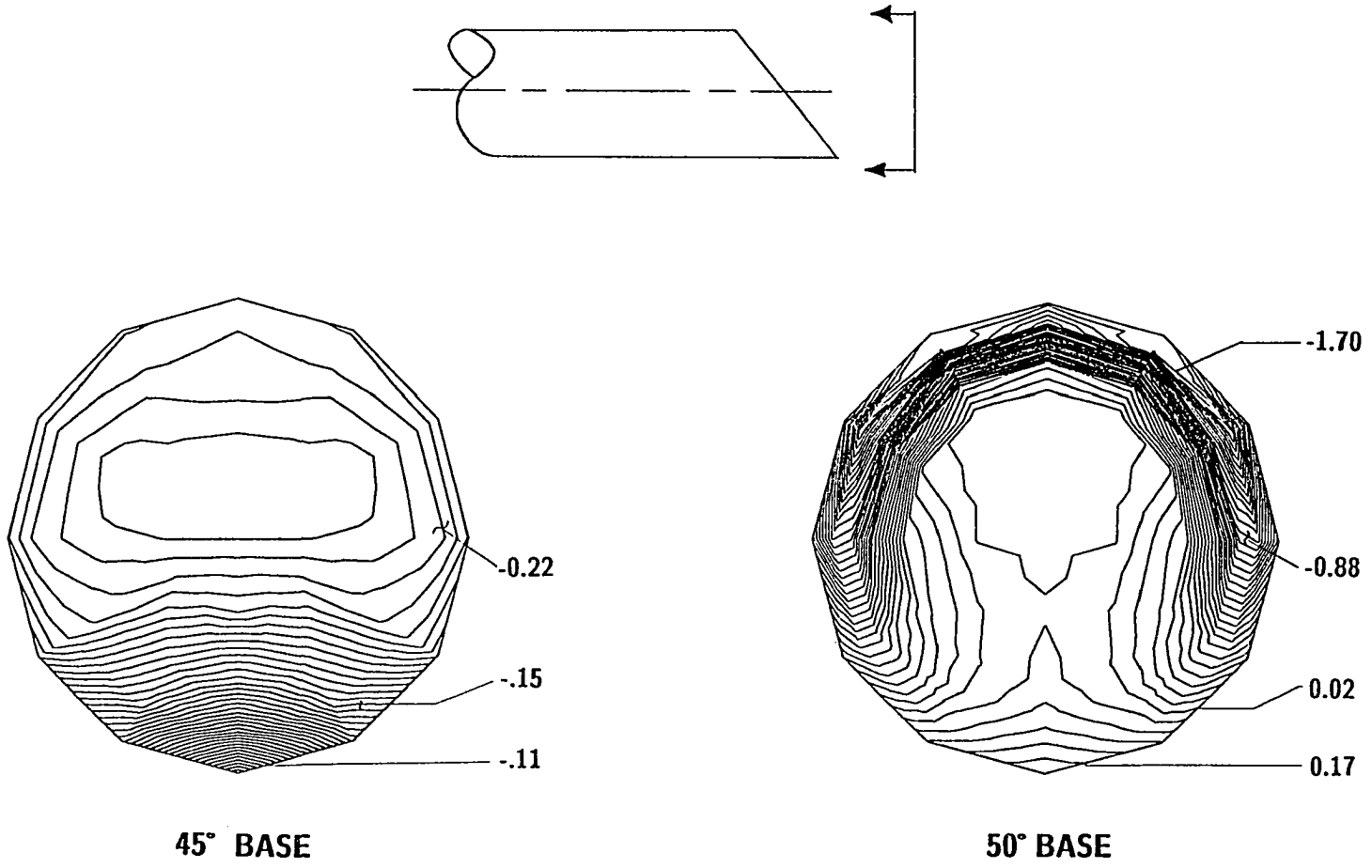

Fig. 7.7 Base Pressure Distributions: $Re_D = 165{,}000$

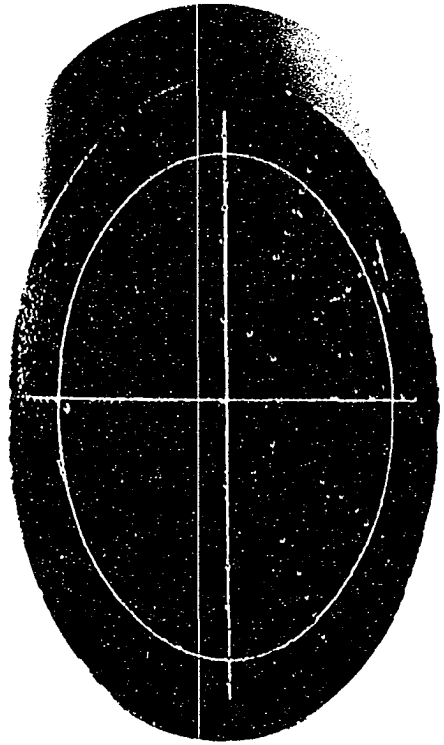

Flow-Visualization (Liquid Crystal)

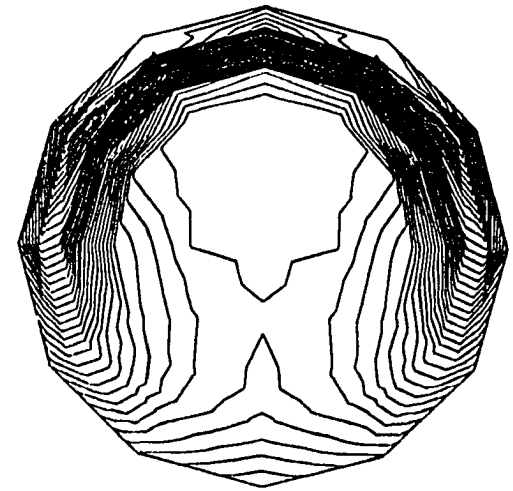

Contour Plot Base Pressure

Fig. 7.8 Liquid Crystal Flow Visualization: 50° Base

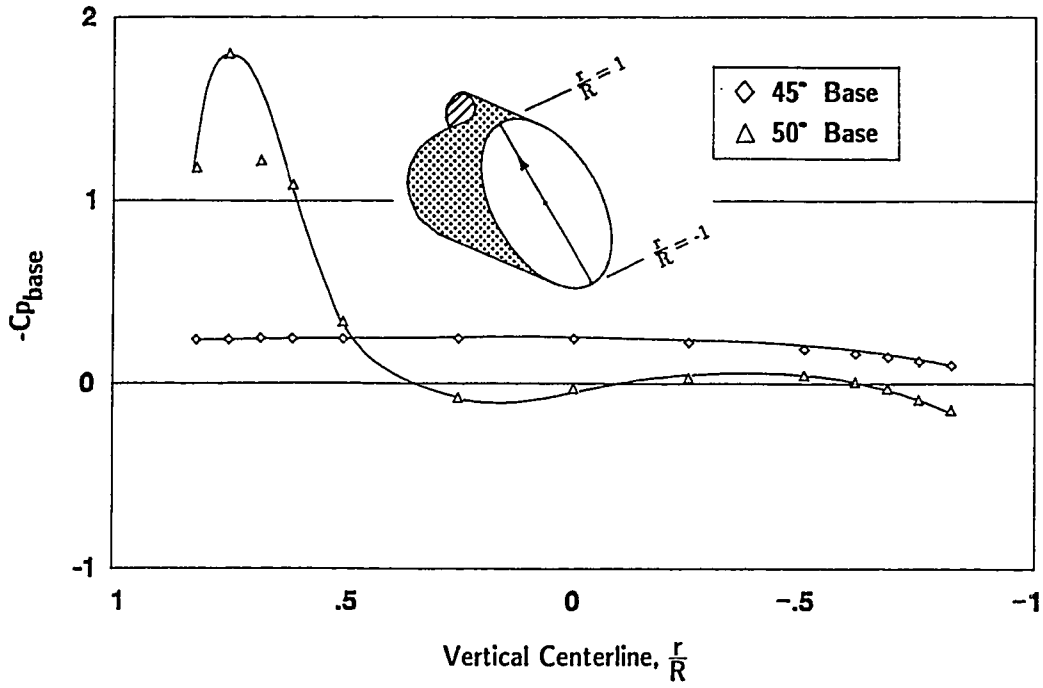

Fig. 7.9 Base Pressure Distribution along Vertical Centerline

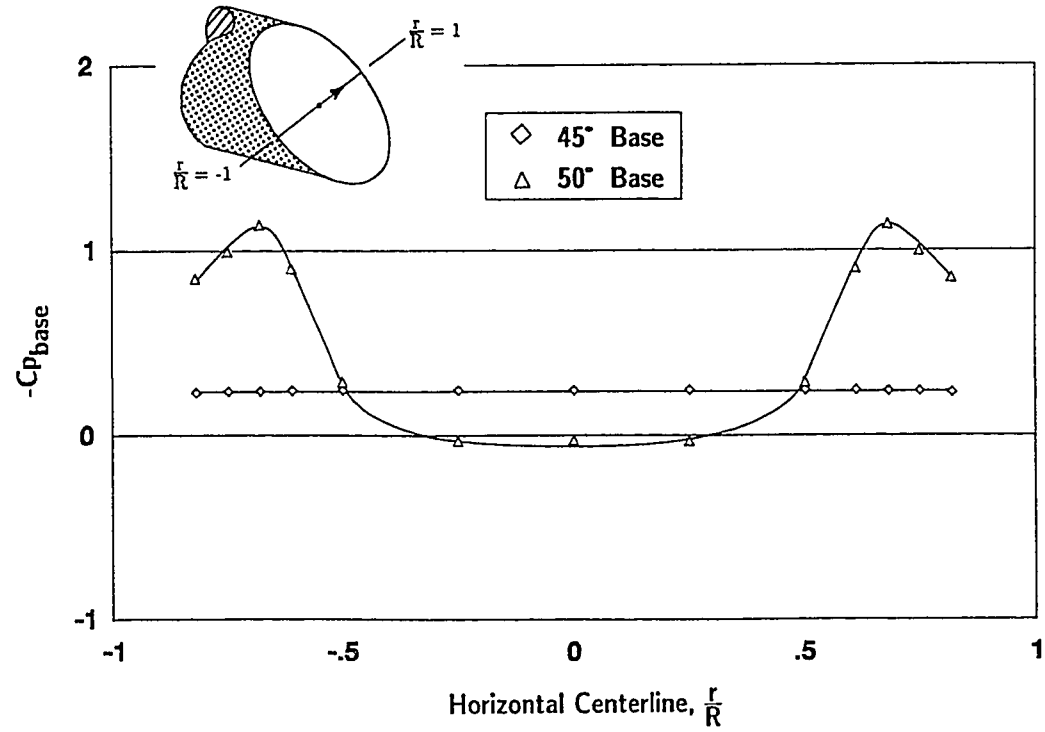

Fig. 7.10 Base Pressure Distribution along Horizontal Centerline

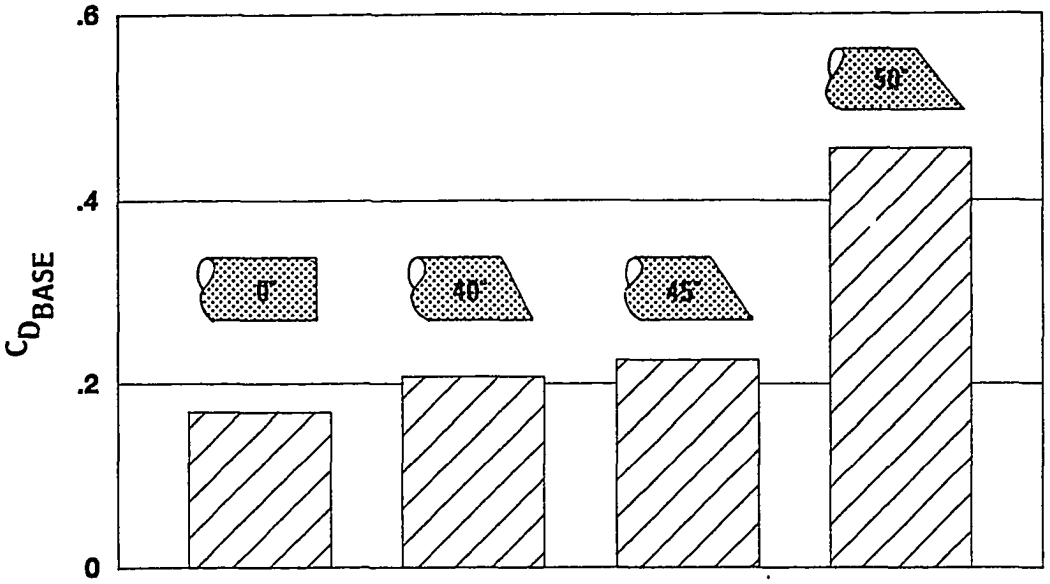

Fig. 7.11 Base Drag Coefficients: $Re_D = 60{,}000$

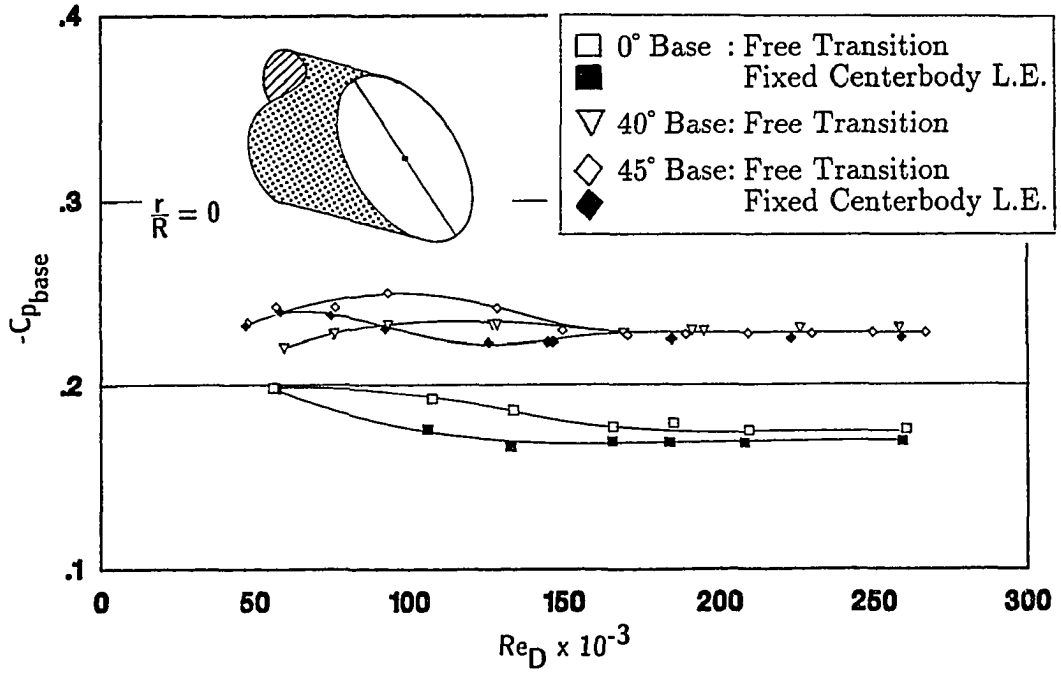

Fig. 7.12 Base Pressure Variations for Lower Slanted-Base Angles

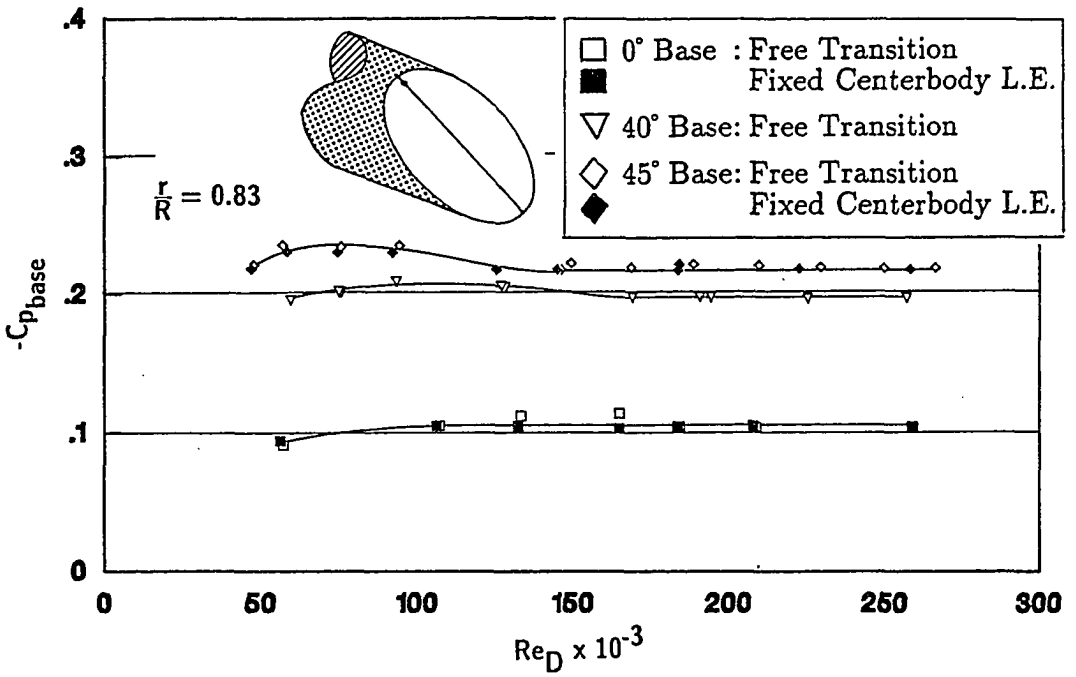

Fig. 7.13 Base Pressure Variations for Lower Slanted-Base Angles

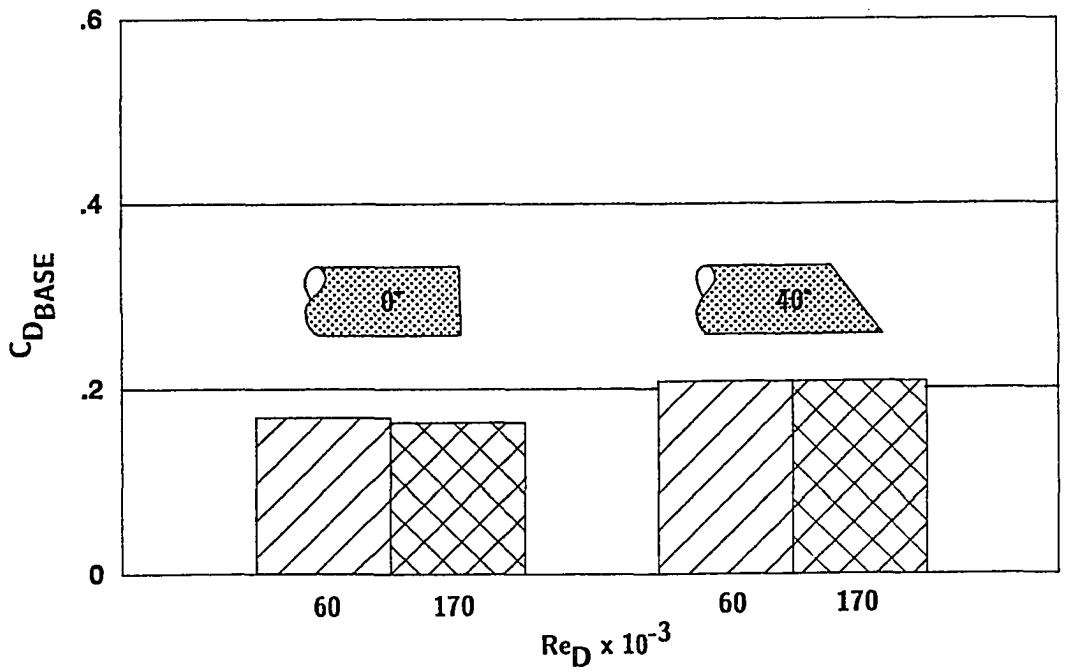

Fig. 7.14 Base Drag Variations for 0° and 40° Bases

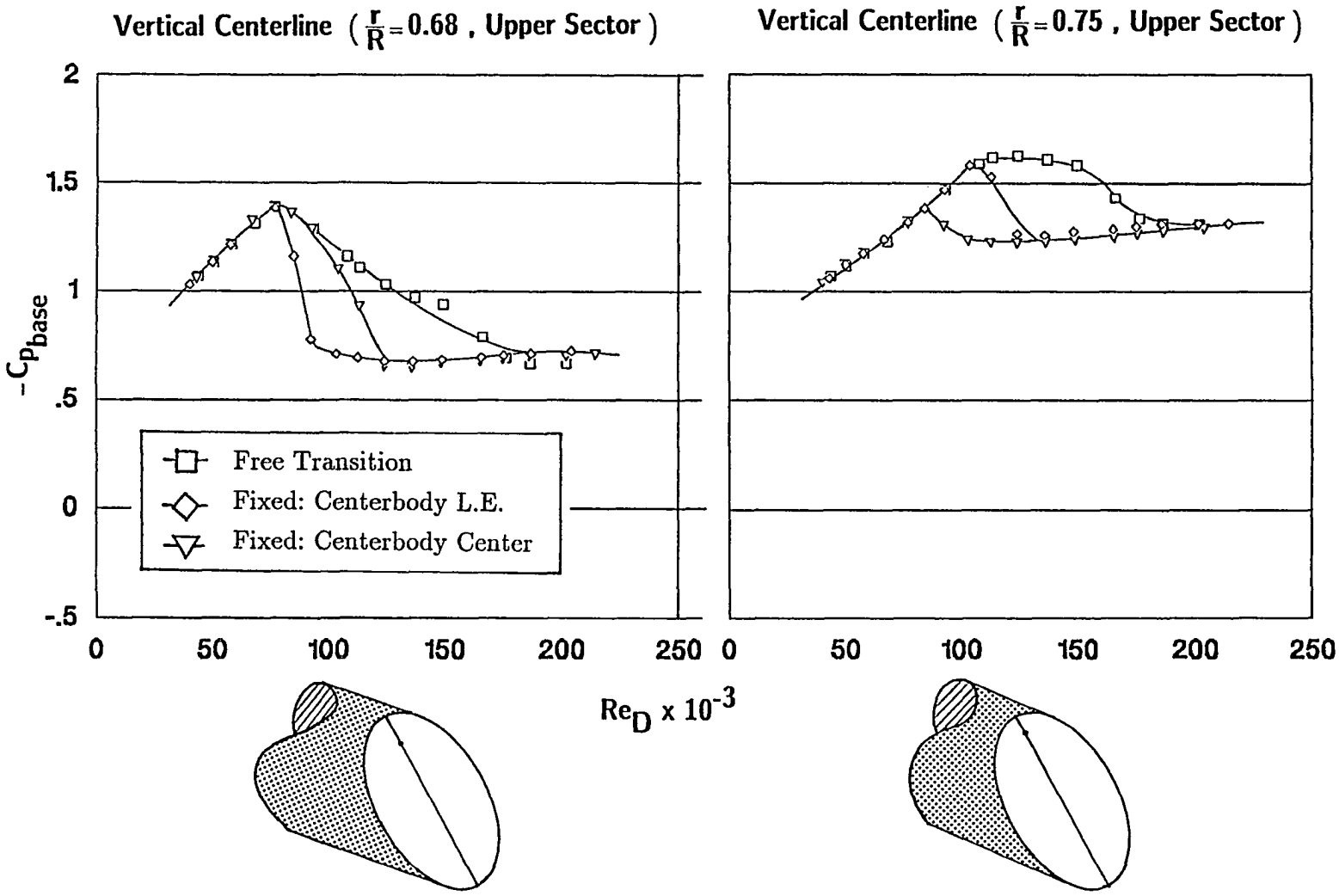

Fig. 7.15 Base Pressure Coefficients: 50° Base

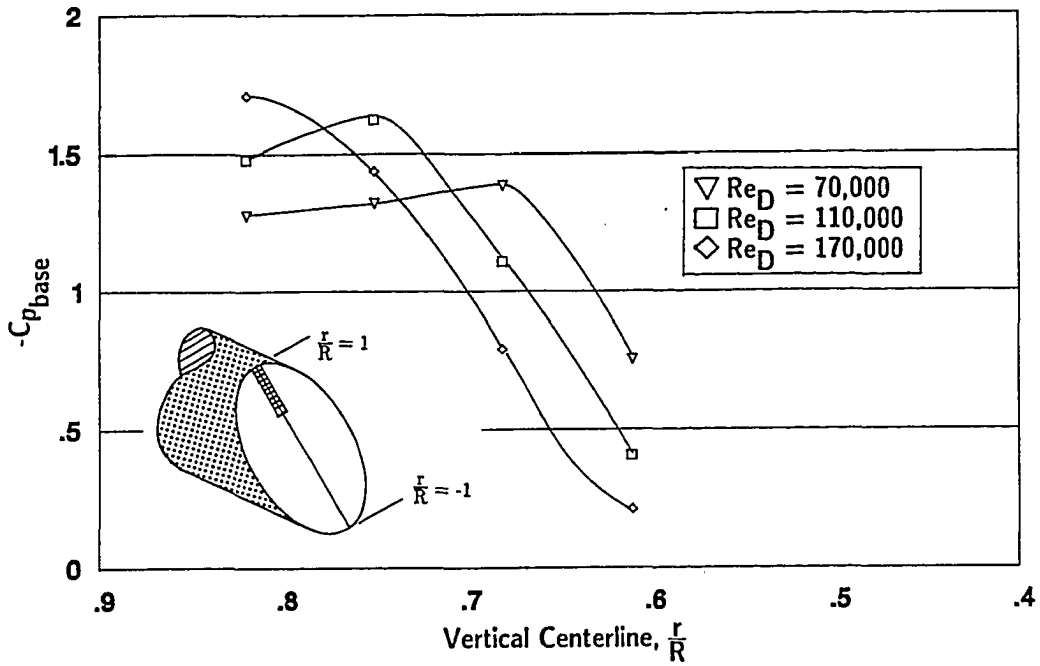

Fig. 7.16 Variations in Vortex Center with Reynolds Number

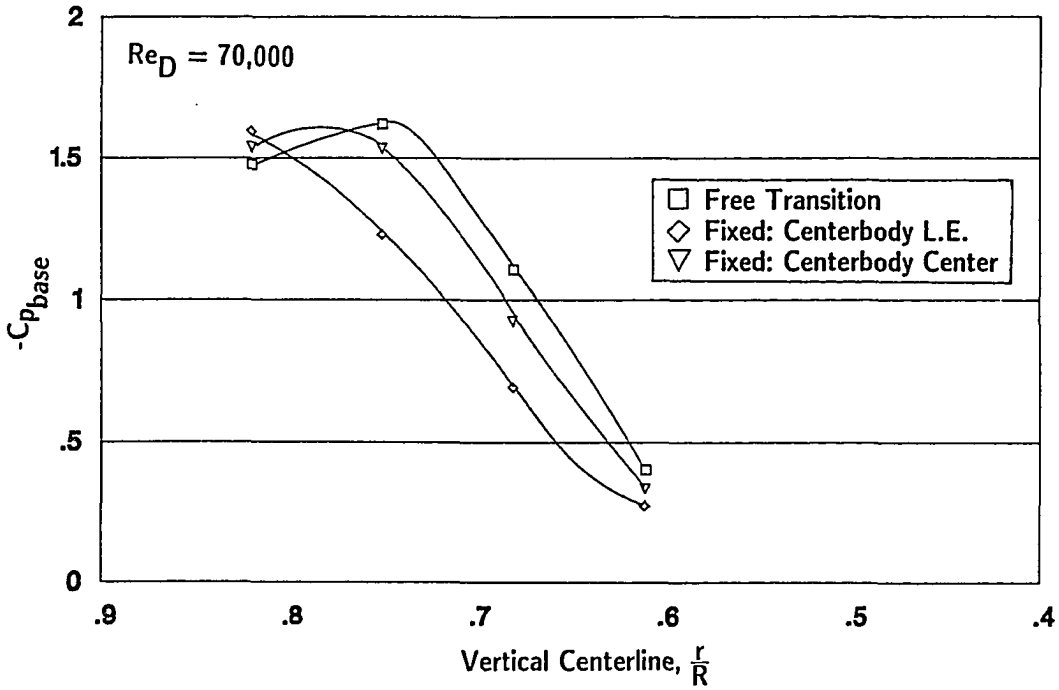

Fig. 7.17 Variations in Vortex Center for Fixed Transition

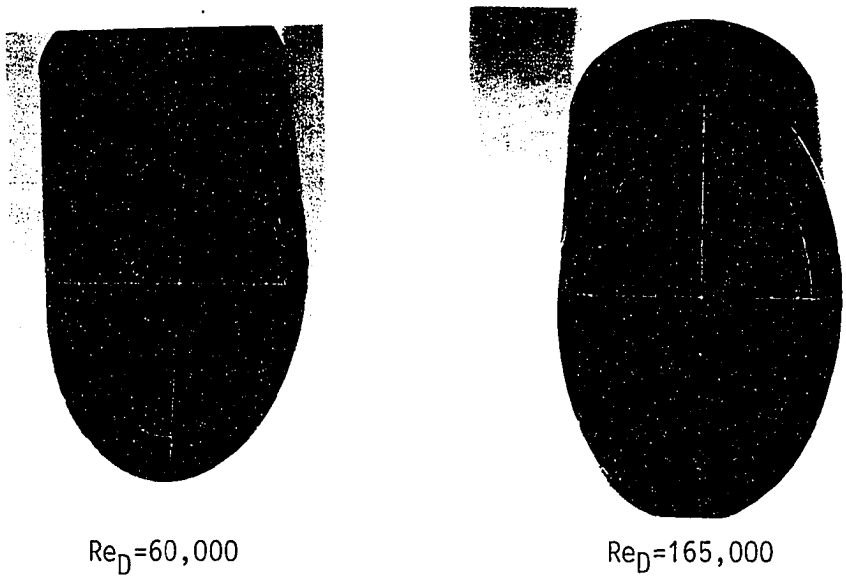

Fig. 7.18 Variations in Vortex Center for 50° Base: Liquid Crystals

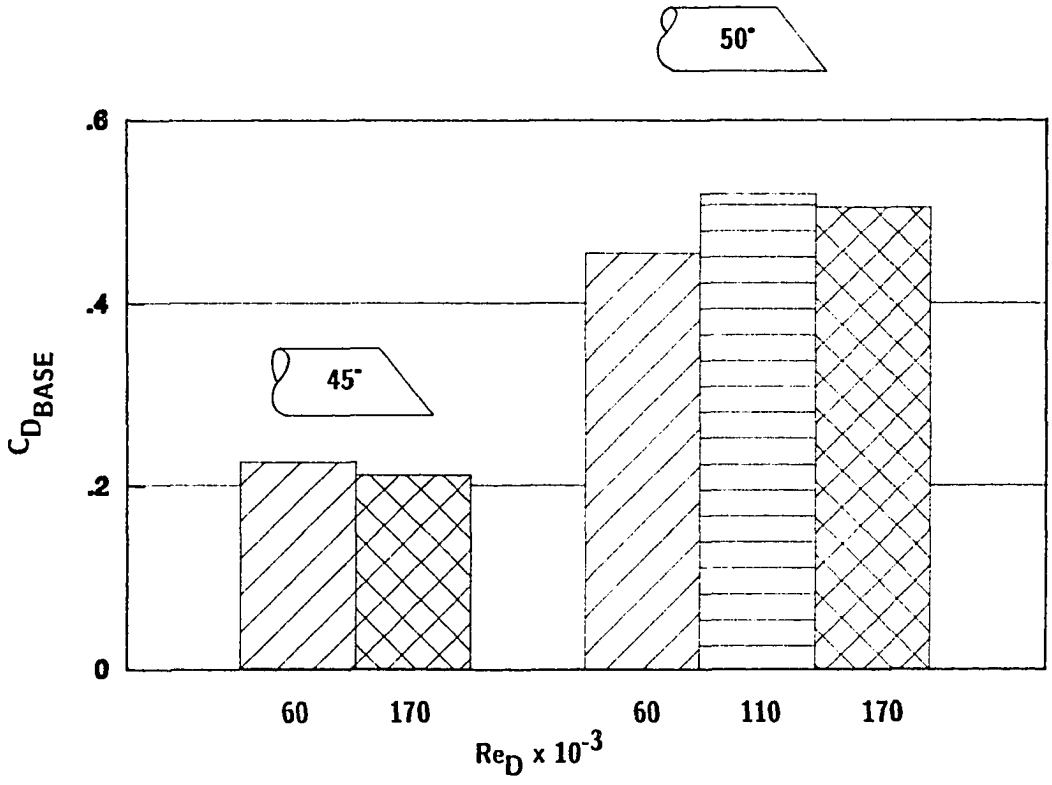

Fig. 7.19 Base Drag Variations for 45° and 50° Bases

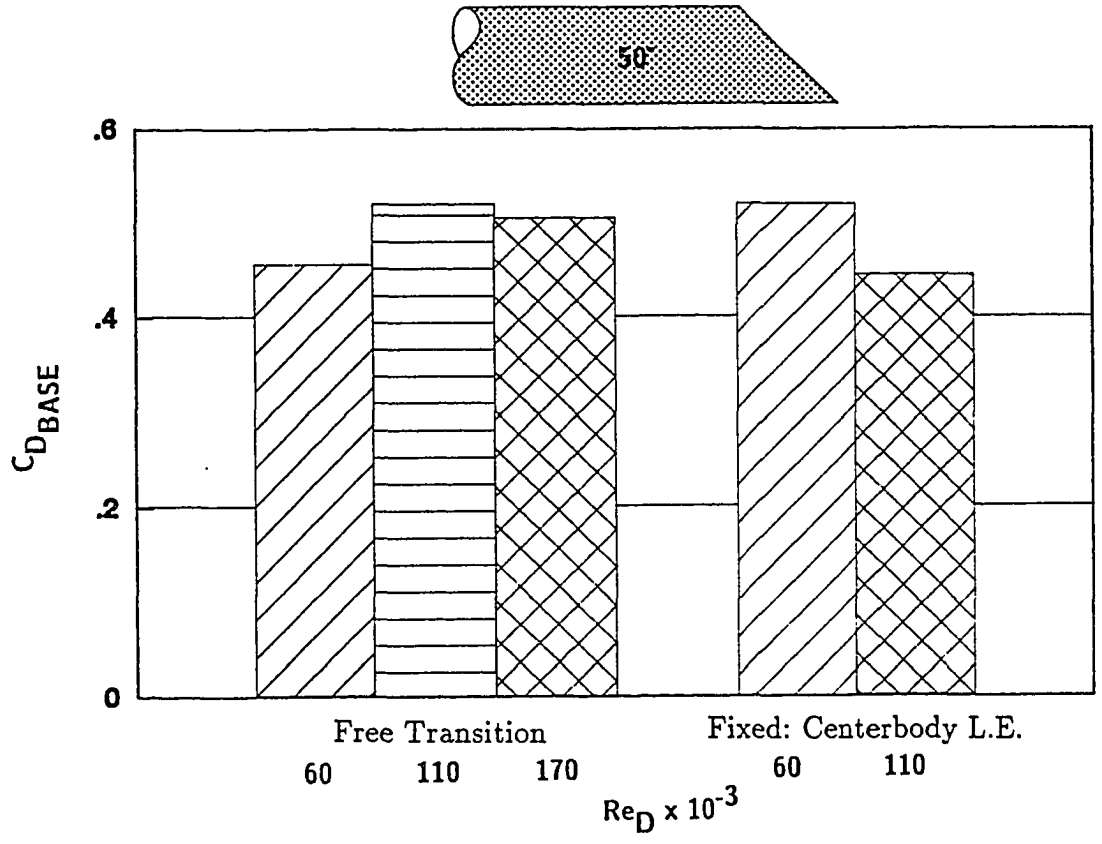

Fig. 7.20 Base Drag for 50° Base: Fixed and Free Transition

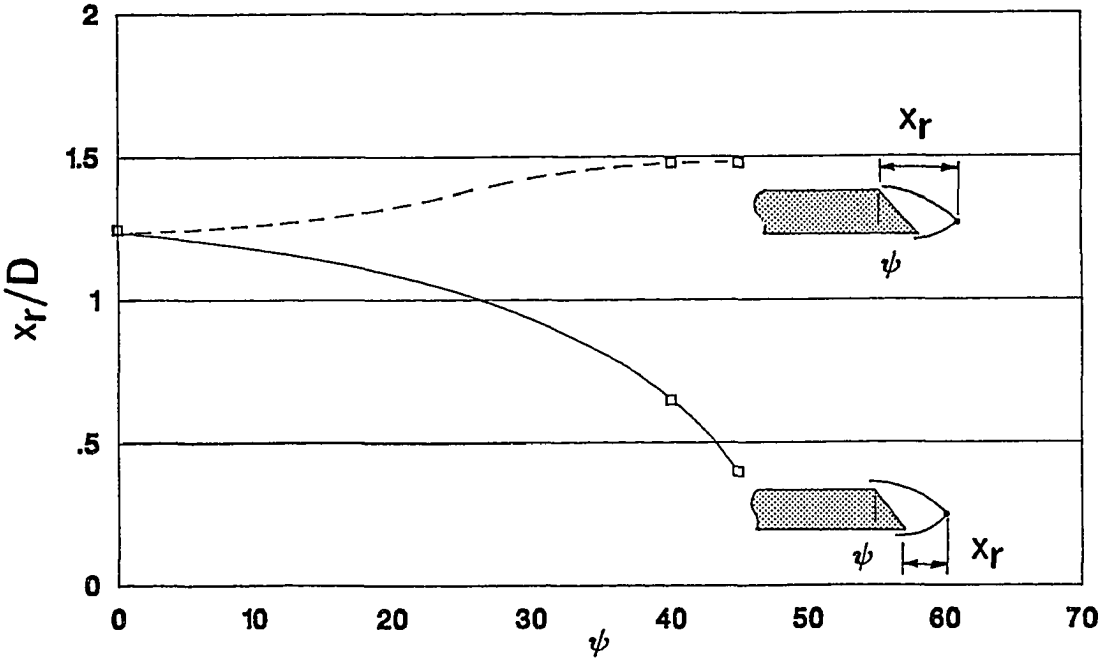

Fig. 7.21 Wake Stagnation Point Locations ($Re_D = 60{,}000$)

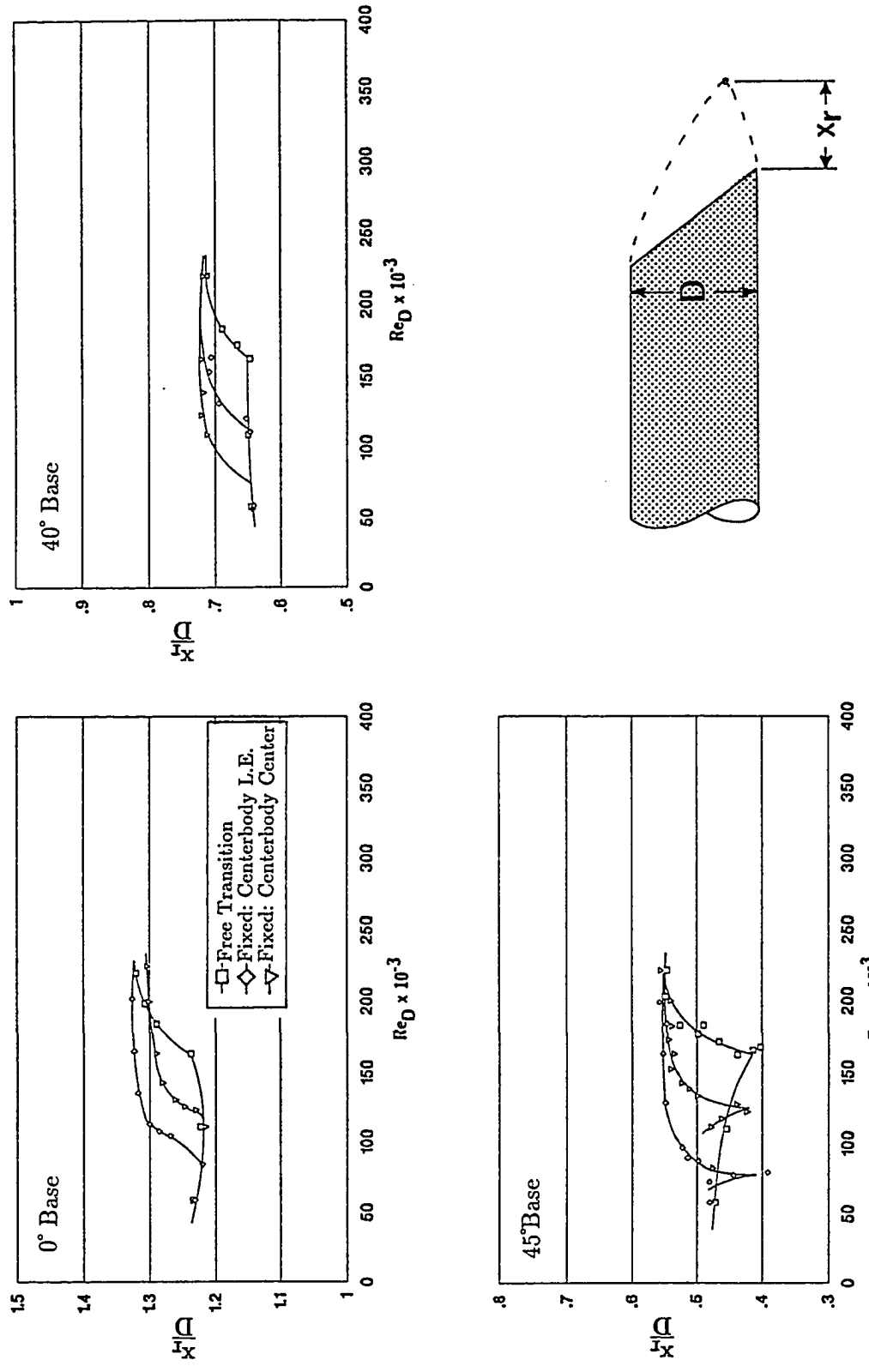

Fig. 7.22 Variation in Wake Stagnation Point Location with Re_D

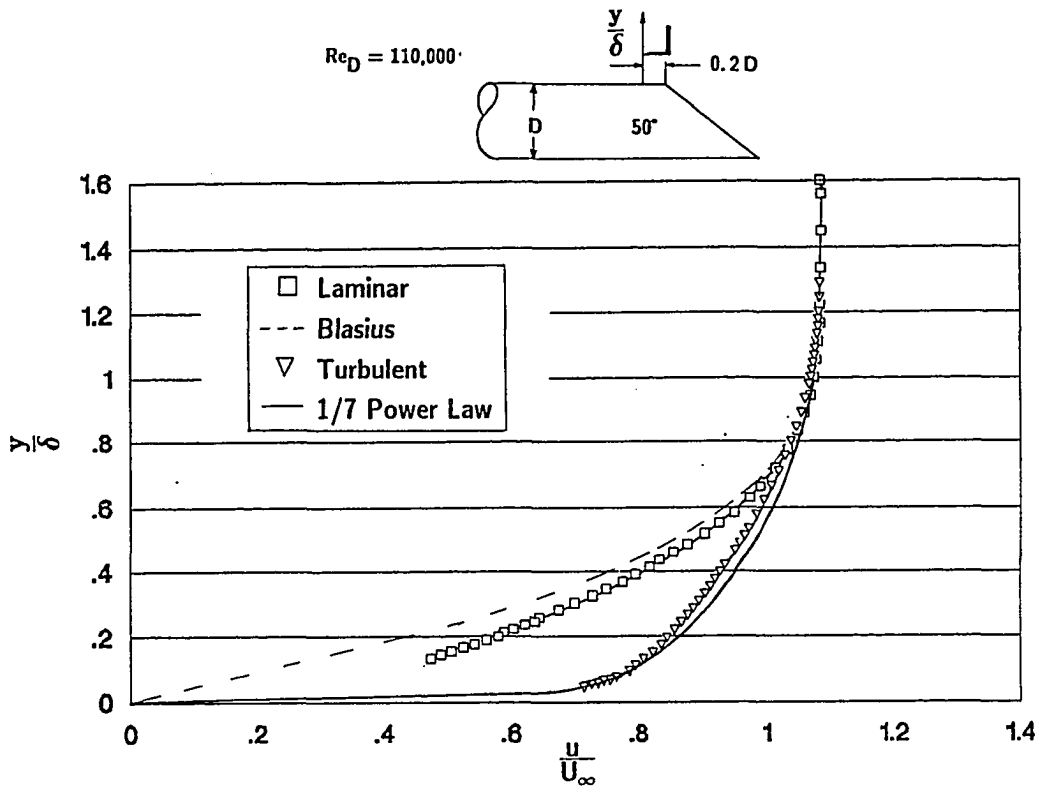

Fig. 7.23 Boundary Layer Velocity Profiles: $Re_D = 110{,}000$

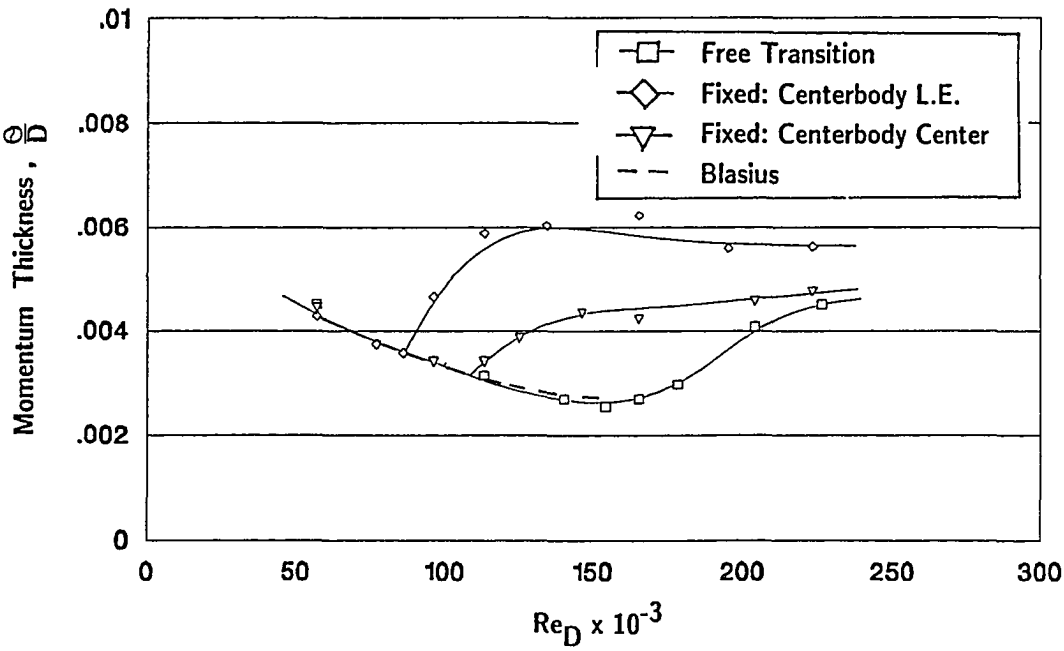

Fig. 7.24 Boundary Layer Momentum Thicknesses: Re_D=110,000

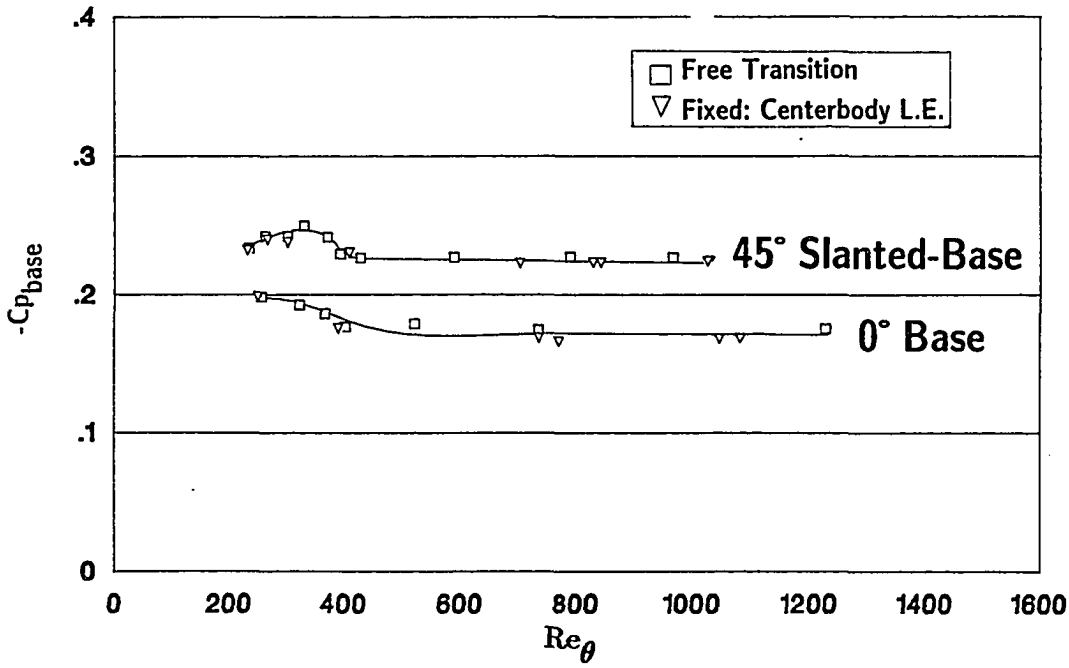

Fig. 7.25 Base Pressure Coefficients vs. Re_θ : 0° and 45° Bases

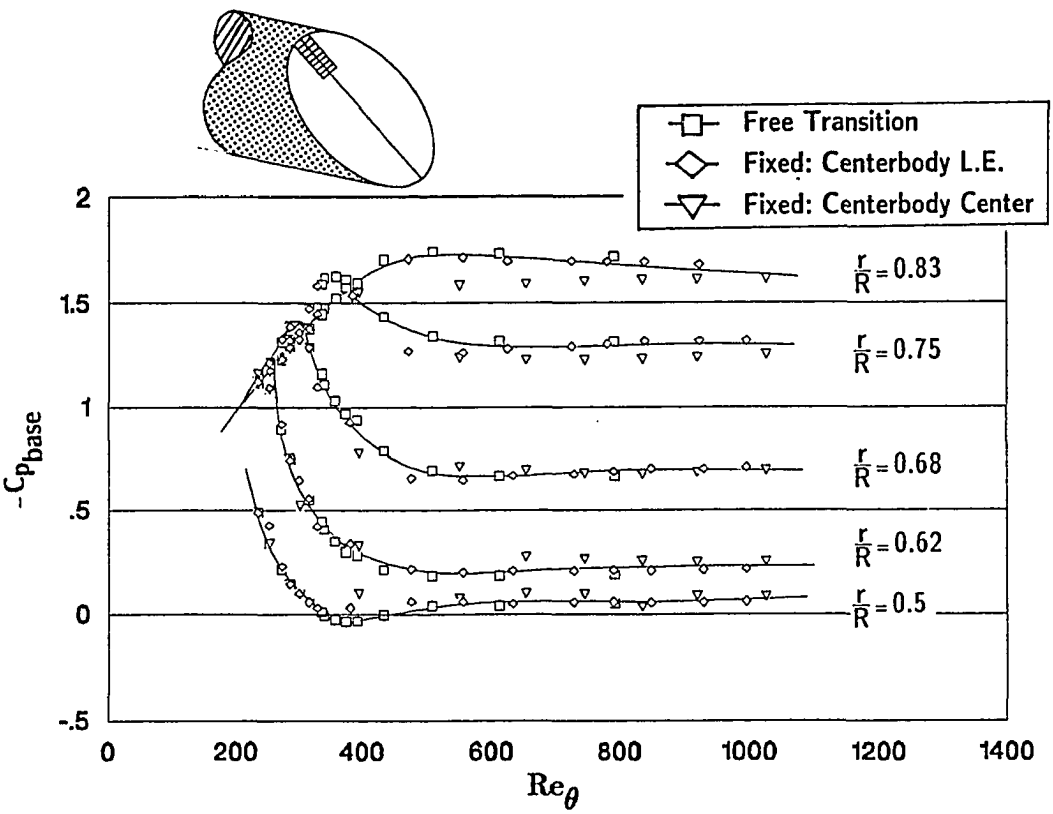

Fig. 7.26 Base Pressure Coefficients vs. Re_θ : 50° Base

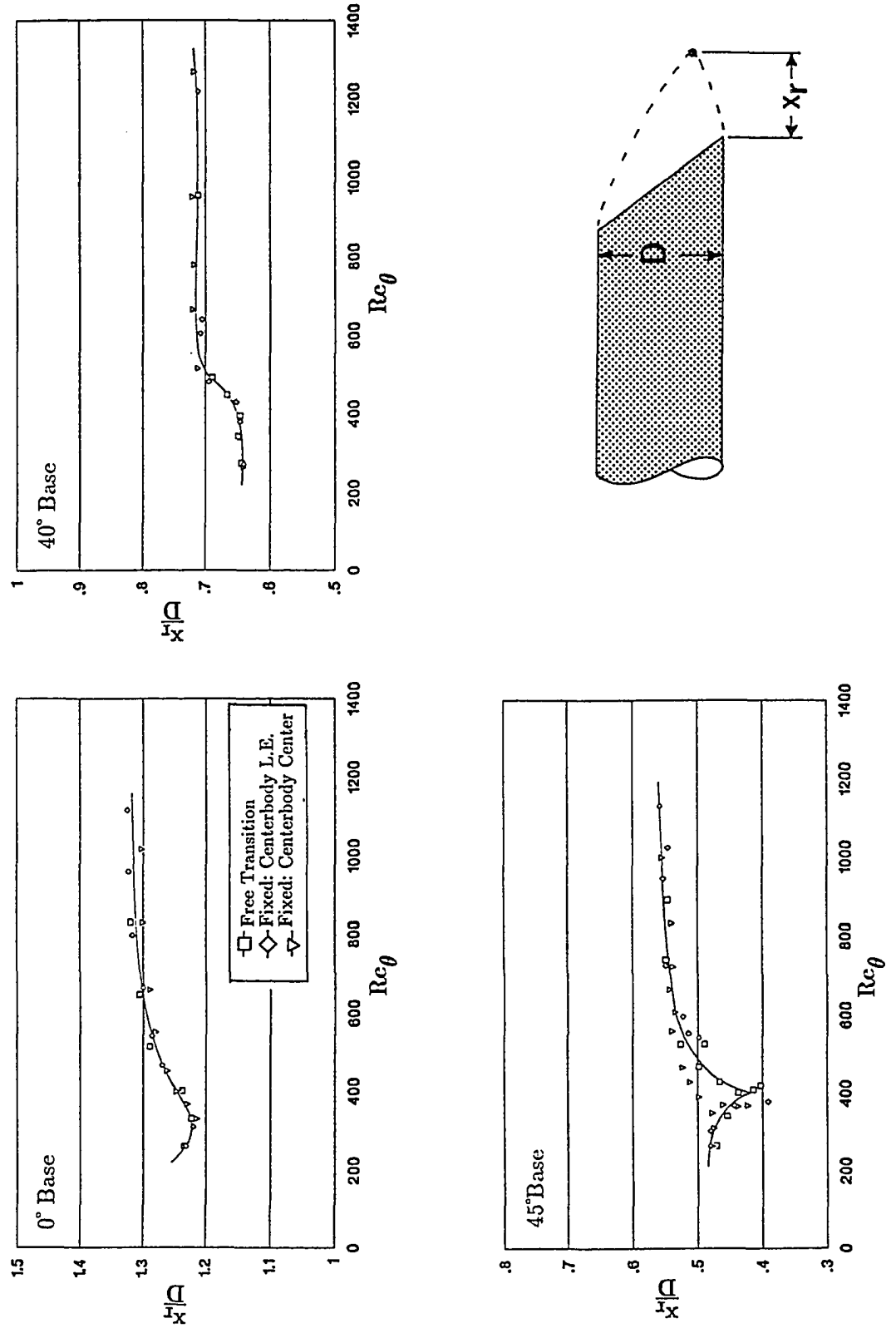

Fig. 7.27 Wake Stagnation Point Locations vs. Re_θ

Chapter 8 LARGE-SCALE STRUCTURES: RESULTS

Turbulence measurements in the wake of slanted-base bluff bodies were made in the ODU low-speed wind tunnel. Predominant frequency and coherence measurements are presented in the following paragraphs. These measurements lead to a better understanding of the unsteady wake structure, its variation with slant angle, and its dependency on the boundary layer state.

8.1 *Predominant Frequency Measurements*

A spectral analysis in the wake of slanted-base bluff bodies was performed to determine the occurrence of periodic phenomena using a single hot-wire sensor. The hot-wire sensor was positioned along a vertical plane in the wake at the axial position, $\frac{X}{D} = 7$. Crisp peaks in the power spectra, representing the predominant frequency, were present. Measurements were also made at a number of wake locations where the turbulence intensity was 10% or less. This generally corresponded to probe locations at least three diameters, (3D) downstream of the model base, and radial positions near the base perimeter. Measurements show that the predominant frequency was not a function of hot-wire probe position in the wake. Typical power spectra are shown in Fig. 8.1 with frequencies displayed as Strouhal numbers. A summary of results for the various slant angles is presented in Fig. 8.2. The predominant frequency, St_{PRED}, is shown to increase geometrically with increasing slant-angle. The theoretical results of the current study, also shown in Fig. 8.2, are discussed in Section 8.3.

It should be mentioned that spectral measurements in the wake of the support strut at an axial location of $\frac{X}{D} = 7$ showed no evidence of spectral peaks. Therefore, a degree of confidence exists that the strut wake is not interfering with spectral measurements in the wake of the bluff body. It should also be mentioned that it was considerably more difficult to extract predominant frequencies for bases above 40°, and that a predominant frequency for the 50° base could not be extracted from the samples taken. This result is also documented by Morel [19-20] and Xia and Bearman [22] and may be explained in terms of vortex shedding. Figure 5.3 shows the only neutrally stable vortex street pattern. For base slant angles greater than 0°, vortex shedding from the downstream base corner occurs further downstream than the vortex shedding from the upstream base corner. It was suggested by Xia and Bearman [22] that this may help to establish a stable vortex street orientation. Furthermore, beyond a certain slant-angle, a destabilizing effect may be present. This is consistent with the broad peak shown for the 45° base in Fig. 8.1 which may result from an unstable vortex street orientation.

Variations in the predominant frequency with Reynolds number are presented in Fig. 8.3. For the 0° base, St_{PRED} is relatively insensitive to Reynolds number for fixed and naturally occurring boundary layer transition. A similar trend is shown for the 40° base, however, St_{PRED} is shown to increase with slant-angle as shown in Fig. 8.1. The predominant frequency for naturally occurring transition on the 45° base is also shown to be relatively insensitive to Reynolds number; however, variations in St_{PRED} with Reynolds number are present for fixed boundary layer transition on the centerbody leading edge. This is attributed to difficulties in extracting predominant frequencies for this base, due to the broadness of its spectral peak.

8.2 *Coherence Measurements*

Coherence measurements in the wake of the 0° base bluff body were made in terms of the cross-correlation of the streamwise fluctuating velocity component, u'. The freestream Reynolds number, Re_D, chosen for coherence measurements was 110,000, which was the Reynolds number showing the greatest deviation in the incoming boundary layer momentum thickness between fixed-transition on the centerbody leading edge and free-transition results. In all cases, the imaginary part of the coherence, Q_ω, was insignificant compared to the real part, C_ω.

Variations in the real part of the coherence, C_ω, with frequency (presented as Strouhal numbers) are given in Fig. 8.4 for angular separations of 20° from $20° < \Delta\beta < 180°$. A significant amount of scatter exists in the data, however, definite trends are shown to exist. It is observed that trends in C_ω, presented here for a 0° base bluff body wake, are similar to trends documented by Roberts [48] and Fuchs, Mercker, and Michel [36-37] for a disk wake.

For $\Delta\beta = 20°$, the coherence is highly positive, reaching a weak maxima at $St_D = 0.25$, corresponding to the predominant frequency, and then begins a slow decay as the frequency is further increased. No significant variations in fixed- and free-transition measurements can be determined for $\Delta\beta = 20°$. For $\Delta\beta = 40°$, variations in fixed- and free-transition measurements are present, especially near the predominant frequency. Sharper peaks are shown for fixed-transition results. This trend continues to $\Delta\beta = 60°$ where larger peaks are present for fixed-transition. For $80° < \Delta\beta < 100°$, the coherence for all frequencies is very low. The existence of any peak is buried in noise. Distinct valleys in coherence are shown to be present at the predominant frequency for $\Delta\beta \geq 120°$, with variations in fixed- and free-transition measurements. The valleys for fixed-transition show more detail and have lower minimas than those associated with free-transition measurements.

These measurements suggest that the initial shear layer conditions influence the development of a bluff body wake in a similar manner as previously shown in Fig. 3.8 for a plane mixing layer. As previously discussed, Bradshaw [46] determined that a local similarity structure is found only for wake locations of $x/\theta > 1000$. For a Reynolds number, $Re_D = 110{,}000$, and an axial wake location of $x/D = 7$, the following conditions are noted:

Free-Transition		Fixed-Transition	
θ/D	x/θ	θ/D	x/θ
0.010	700	0.020	350

Table 8.1 Wake location with respect to momentum thickness, $Re_D = 110{,}000$.

It is shown that the wake location with respect to the momentum thickness just ahead of separation for both cases is well below the necessary similarity criterion set forth by Bradshaw [46]. Furthermore, the free-transition location is twice that determined for fixed-transition. In terms of the analysis discussed in Chapter 4, this difference would correspond to large shifts in the virtual origin.

8.2.1 *Coherence at Low Frequency*

Variations in wake coherence for the 0° base with angular separation are shown in Fig. 8.5 at a low frequency ($St_D = 0.04St_{D_{PRED}}$). Trends are similar to results of Fuchs, Mercker, and Michel [36-37] for a disk wake. For small angular separations, the coherence is highly positive, but falls slowly below zero with increasing angular separation. A more rapid decrease in coherence is associated with a disk wake. A minimum is reached between $100° \leq \Delta\beta \leq 120°$ before increasing and becoming positive. Differences in coherence are present for fixed and free boundary layer transition-appearing first at $\Delta\beta > 40°$, and remaining until

$\Delta\beta = 160°$. It is shown that the minima for fixed- and free-transition results occur at different angular separations. The minimum for free-transition is shown to occur at $\Delta\beta \simeq 100°$, while the minimum for fixed-transition is delayed until $\Delta\beta \simeq 120°$.

A modal analysis of the coherent structures was performed, as outlined in Chapter 5, to determine the percentage of fluctuating energy contained in individual azimuthal constituents. Figure 8.6 shows that at frequencies far below the predominant frequency, greater than 95% of the fluctuating energy is contained in the first three modes. The $m = 2$ component is most dominant, containing approximately 45% of the total turbulent energy. This mode is not as dominant as that for a disk wake, where it was determined that greater than 60% of the fluctuating energy was contained in that mode. Fixing boundary layer transition is shown to affect only the m=1 mode, with more energy associated with fixed-transition. The deficit of energy in this mode for free-transition is not shown to be compensated for by the $m = 0$ or $m = 2$ modes, and must clearly be compensated for in higher modes.

8.2.2 *Coherence at the Predominant Frequency*

Variations in coherence at the predominant frequency are presented in Fig. 8.7 for the 0° base, along with the results for a disk wake. As with results at low frequencies, coherence is highly positive for small angular separations, and decreases with increasing $\Delta\beta$. The decrease is shown to be more rapid than that for a disk wake. Unlike its low frequency counterpart, the coherence does not recover to positive values with increasing $\Delta\beta$, but continues its decline until $\Delta\beta = 180°$. Differences are also present for fixed- and free-transition results, appearing first for $\Delta\beta \simeq 40°$, and continuing up to $\Delta\beta = 180°$. The most

noticeable differences appear for $\Delta\beta > 100^{\circ}$ with fixed transition values more negative than their laminar counterparts.

Azimuthal constituents at the predominant frequency ($St_D = 0.25$) are presented in Fig. 8.8 with the results for a disk wake. The dominant nature of the $m = 1$ constituent is clearly shown for fixed- and free-transition boundary layer flows. This is an indication of strong vortex shedding similar to that occurring behind a disk [36-37, 48]. More than 80% of turbulent energy is contained in this mode for naturally occurring transition, and nearly 95% of turbulent energy is contained in this mode for fixed boundary layer transition. The energy deficit for free-transition flows in the $m = 1$ mode is compensated for in the $m = 0$ and $m = 2$ modes.

8.2.3 *Coherence at High Frequency*

Variations in wake coherence for the 0° base with angular separation are shown in Fig. 8.9 at a high frequency ($St_D = 2St_{D_{PRED}}$). Trends are again similar to the results of Fuchs, Mercker, and Michel [36-37] for a disk wake. For $\Delta\beta \simeq 20^{\circ}$, highly positive coherence is shown, but begins to drop rapidly with increasing azimuthal angles. A shallow negative lobe is seen in the data for $60^{\circ} > \Delta\beta > 120^{\circ}$ before leveling off to zero coherence at higher azimuthal angles.

Azimuthal constituents at $St_D = 2St_{D_{PRED}}$ are given in Fig. 8.10. The $m = 1$ constituent is shown to be not nearly as dominant as at the predominant frequency. It is noticed that less that 70% of the turbulent energy is contained in the first three modes, which shows an increased importance in the higher order modes at high frequency.

In summary, variations in the boundary layer state affect the distribution of turbulent energy, most notably for the $m = 1$ constituent at or below the

predominant frequency. At the predominant frequency, vortex shedding is stronger for fixed boundary layer transition, with a significantly larger portion of turbulent energy allocated to other modes for naturally occurring transition.

8.3 *Comparisons to Semi-Empirical Strouhal Numbers*

It has been demonstrated in the above sections that the predominant frequency for the 0° base is a result of vortex shedding, therefore, the basis for the analysis in Section 5.3 relating the Strouhal number, St_D, to the time-averaged base drag coefficient, C_{D_B}, is allowable.

$$C_{D_B} = 4.32 - 5.21\,St_D - 36.15\,St_D{}^2 \qquad (5.33)$$

The 0° base drag coefficient at $Re_D = 60{,}000$ was determined previously in Chapter 7 to be $C_{D_B} = 0.18$. Using Eqn. (5.33), this corresponds to a calculated Strouhal number of 0.28 which is in good agreement with the measured value of 0.25.

Due to the success of the above analysis for the 0° base, an extension to slanted-bases was now attempted. It is necessary to proceed with caution since the nature of the predominant frequency for slanted-bases is not fully understood. Specifically, the vortex shedding mode may not be as dominant as that existing for the 0° base. Furthermore, the basis for a modal analysis does not exist because the wake may no longer be considered axisymmetric. Proceeding with caution, the general relation between the Strouhal number and time-averaged quantities was:

$$C_{D_B} = 4.32 \cdot \cos(\psi+\eta) - 5.21 \cdot \frac{\cos^2(\psi+\eta)}{\cos(\eta)}\,St_D - 36.15 \cdot \frac{\cos^3(\psi+\eta)}{\cos^2(\eta)}\,St_D{}^2 \qquad (5.32)$$

The base angle, ψ, is known, and the base drag, C_{D_B}, has been determined in Chapter 7 by integration of the base pressures. An estimate of the wake deflection angle, η, was determined by location of the wake stagnation point in relation to the base center as shown in Fig. 5.4. A summary of results is presented in Table 8.2.

ψ	η	C_{D_B}	St_{EQN}	St_{MEAS}
0°	0°	0.19	0.28	0.25
40°	10.2°	0.20	0.43	0.39
45°	12.8°	0.22	0.51	0.52

Table 8.2. Parameters for St relation, $Re_D = 60{,}000$

It is shown that the semi-empirical relation and the measured results for all bases are in good comparison. The results given in Table 8.2 are also plotted in Fig. 8.2.

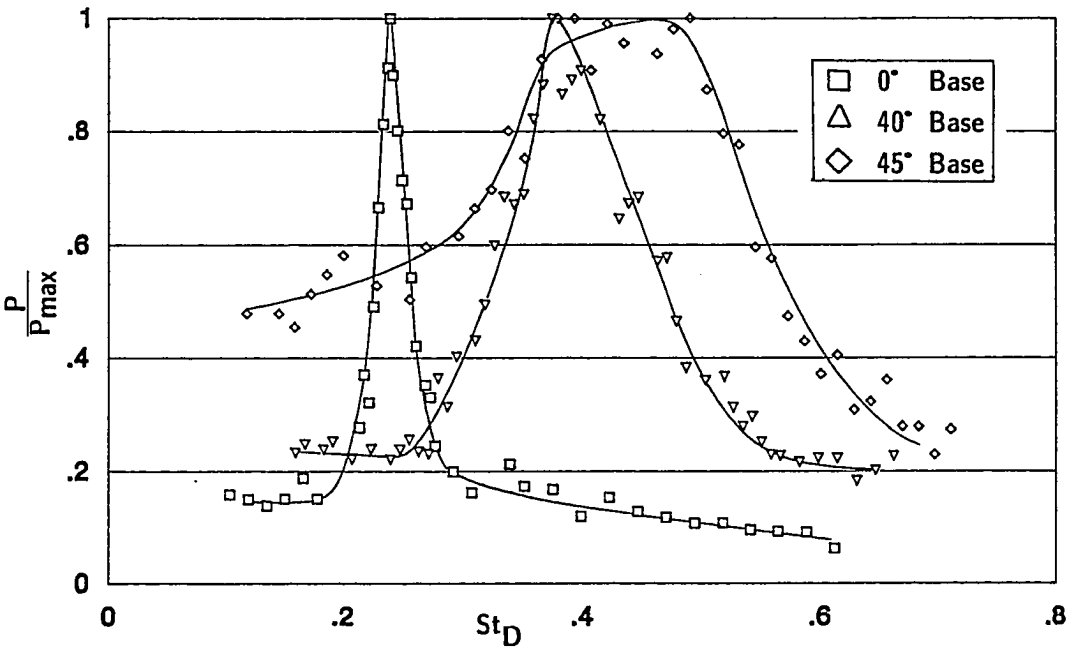

Fig. 8.1 Power Spectra: 0°, 40°, and 45° Bases
(Free Transition, $Re_D = 110{,}000$)

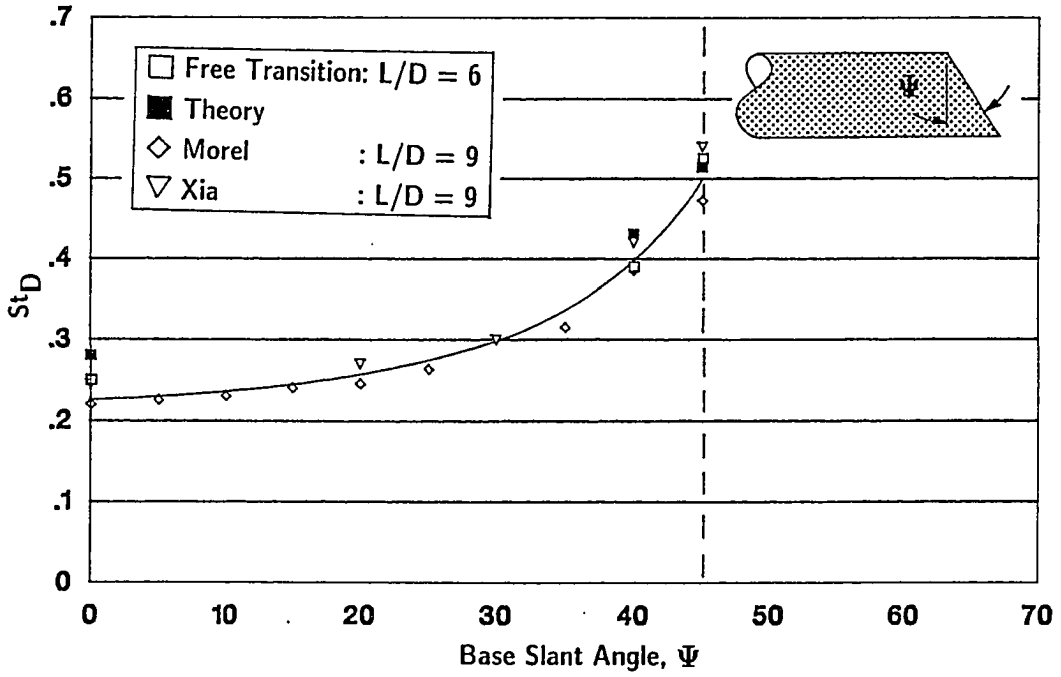

Fig. 8.2 Peak Frequency vs. Base Slant Angle

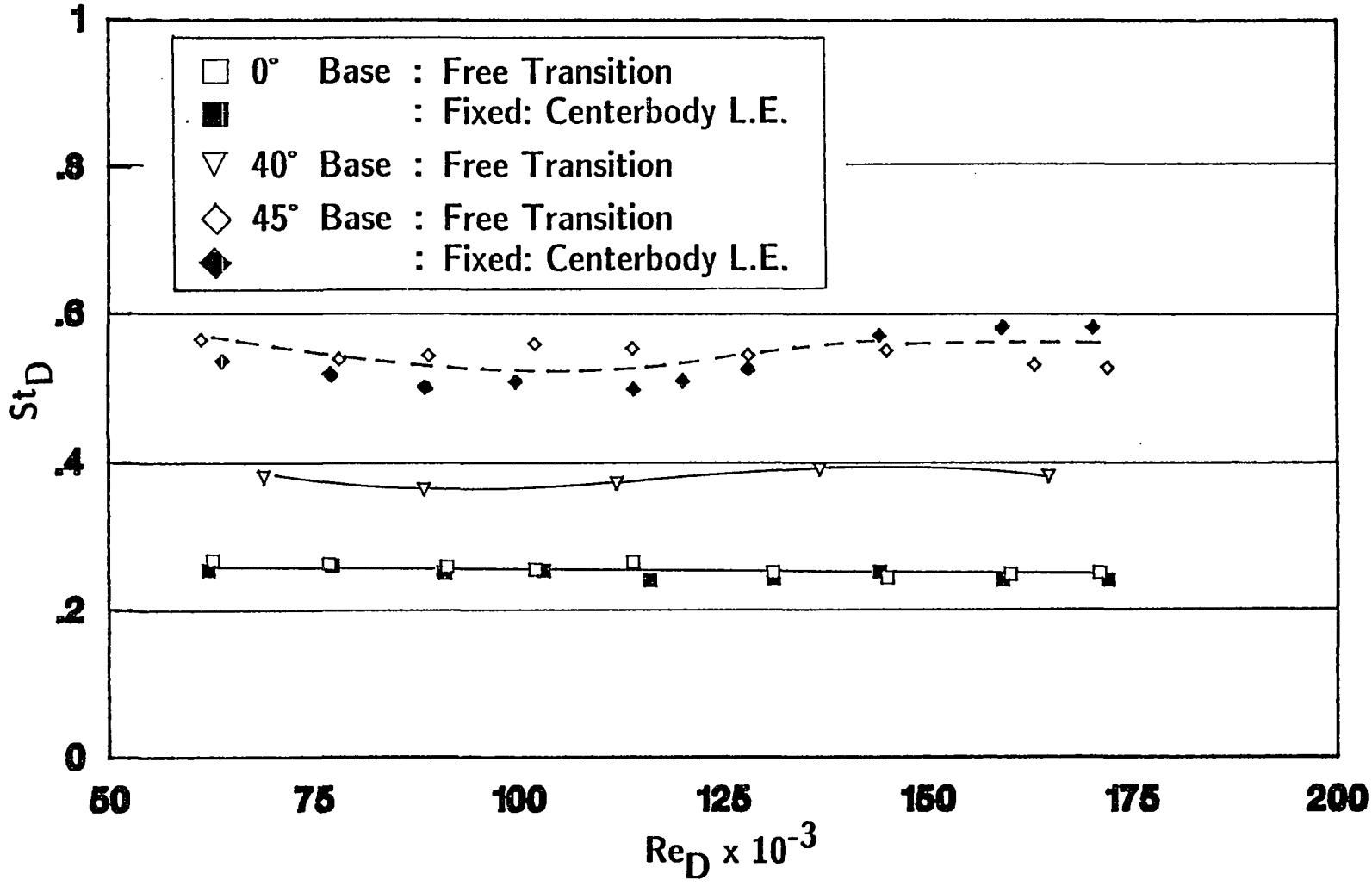

Fig. 8.3 Strouhal Number Variations with Reynolds Number

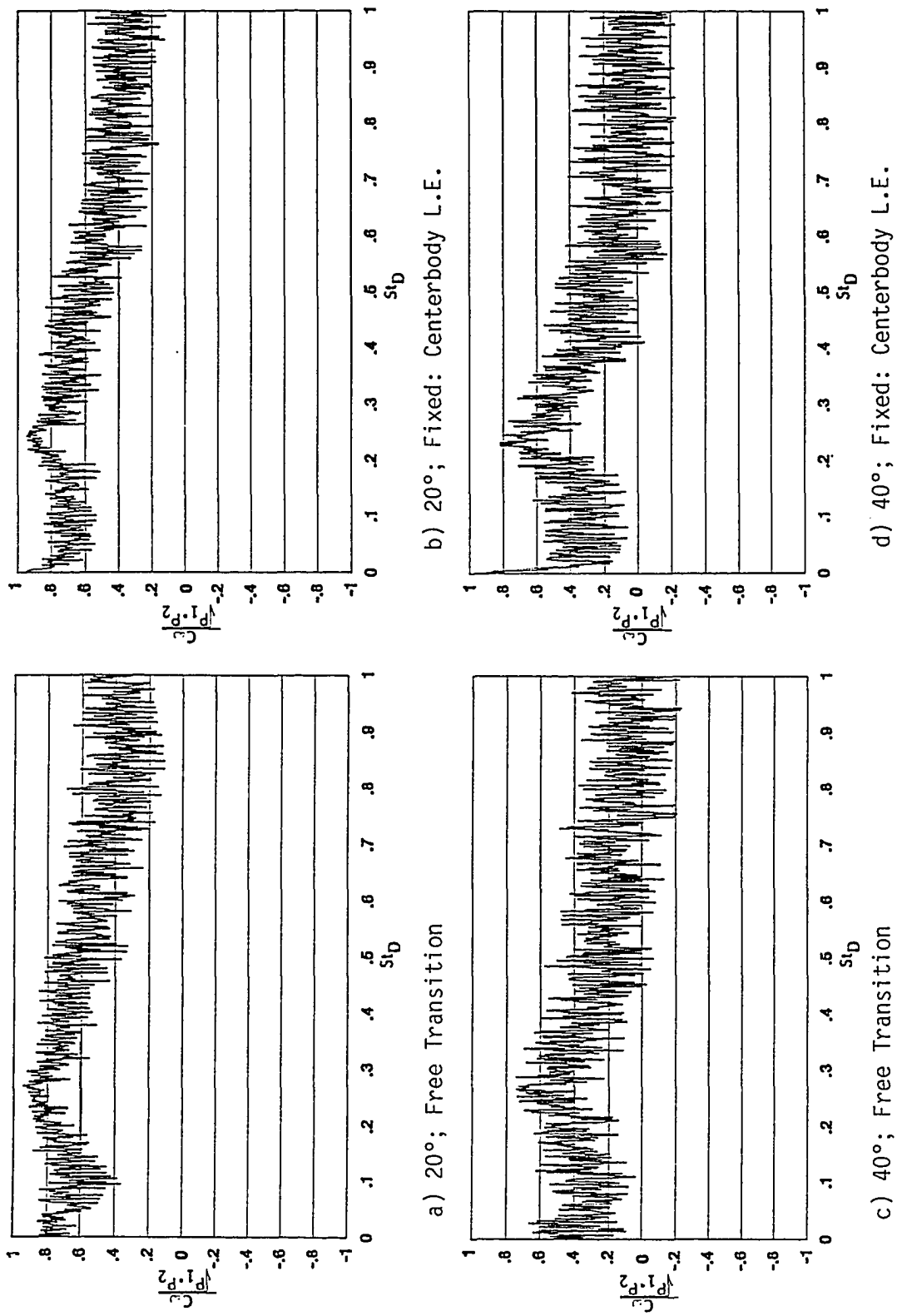

Fig. 8.4 Coherence Variations with Strouhal Number: 0° Base

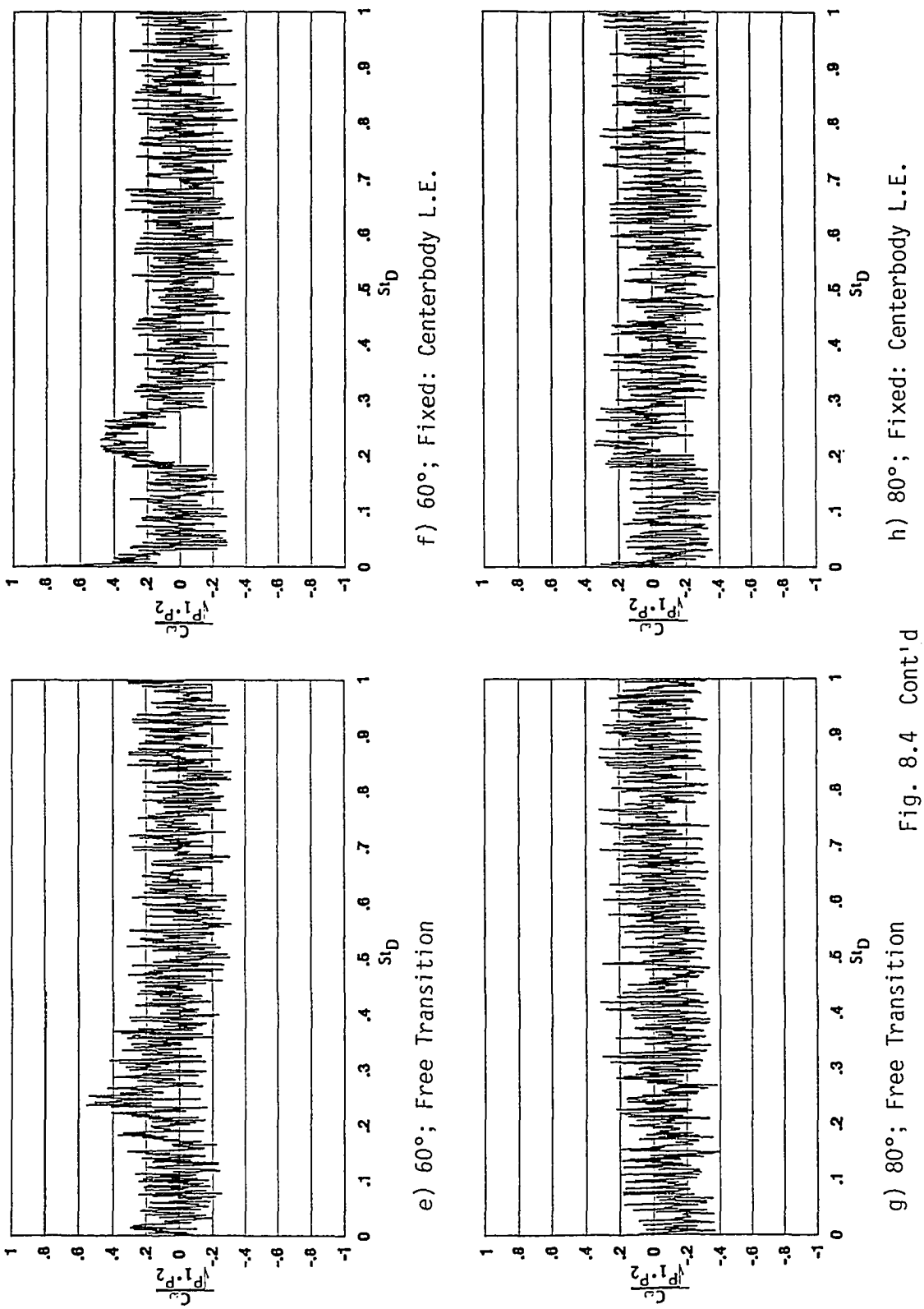

Fig. 8.4 Cont'd

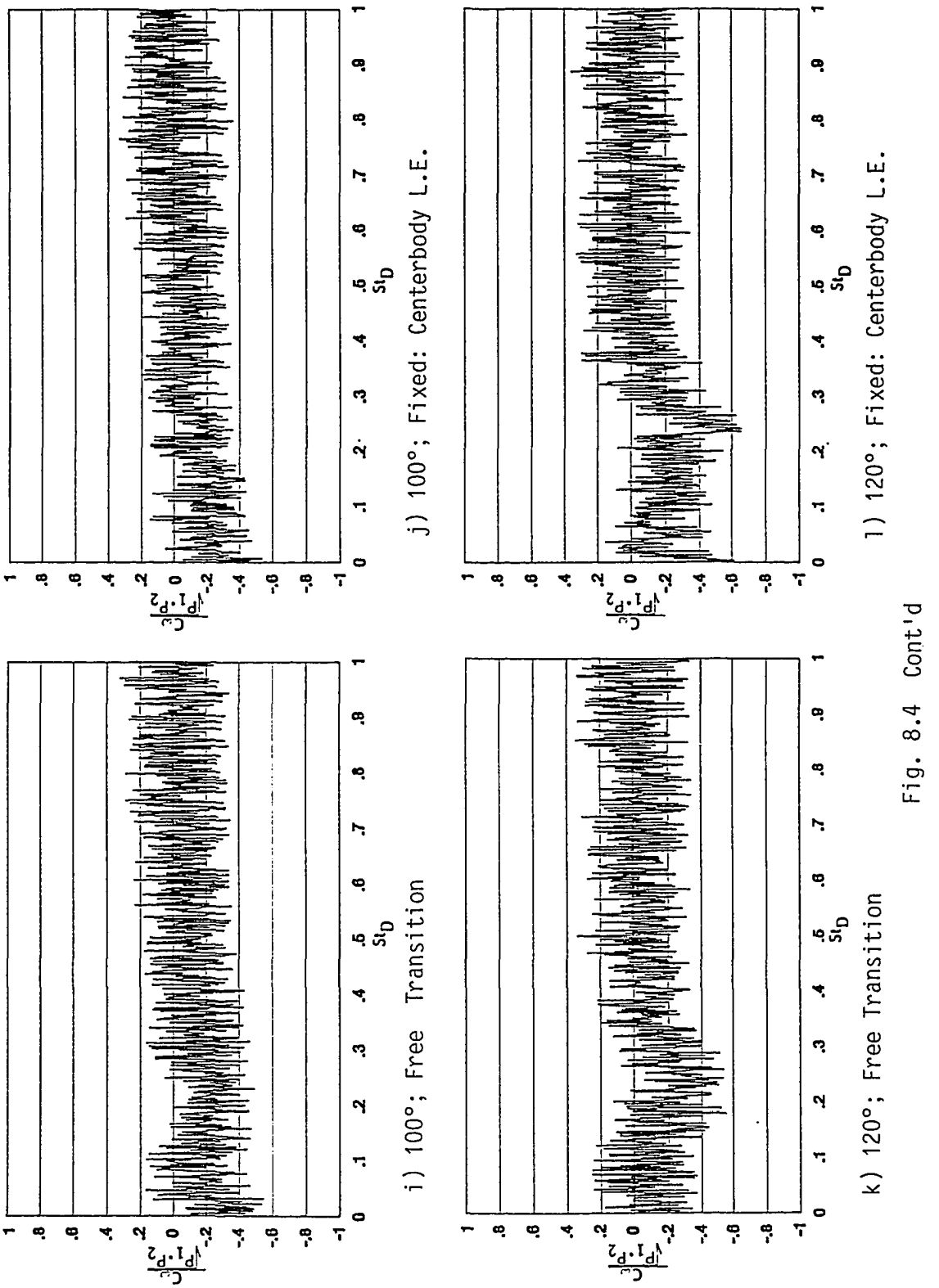

Fig. 8.4 Cont'd

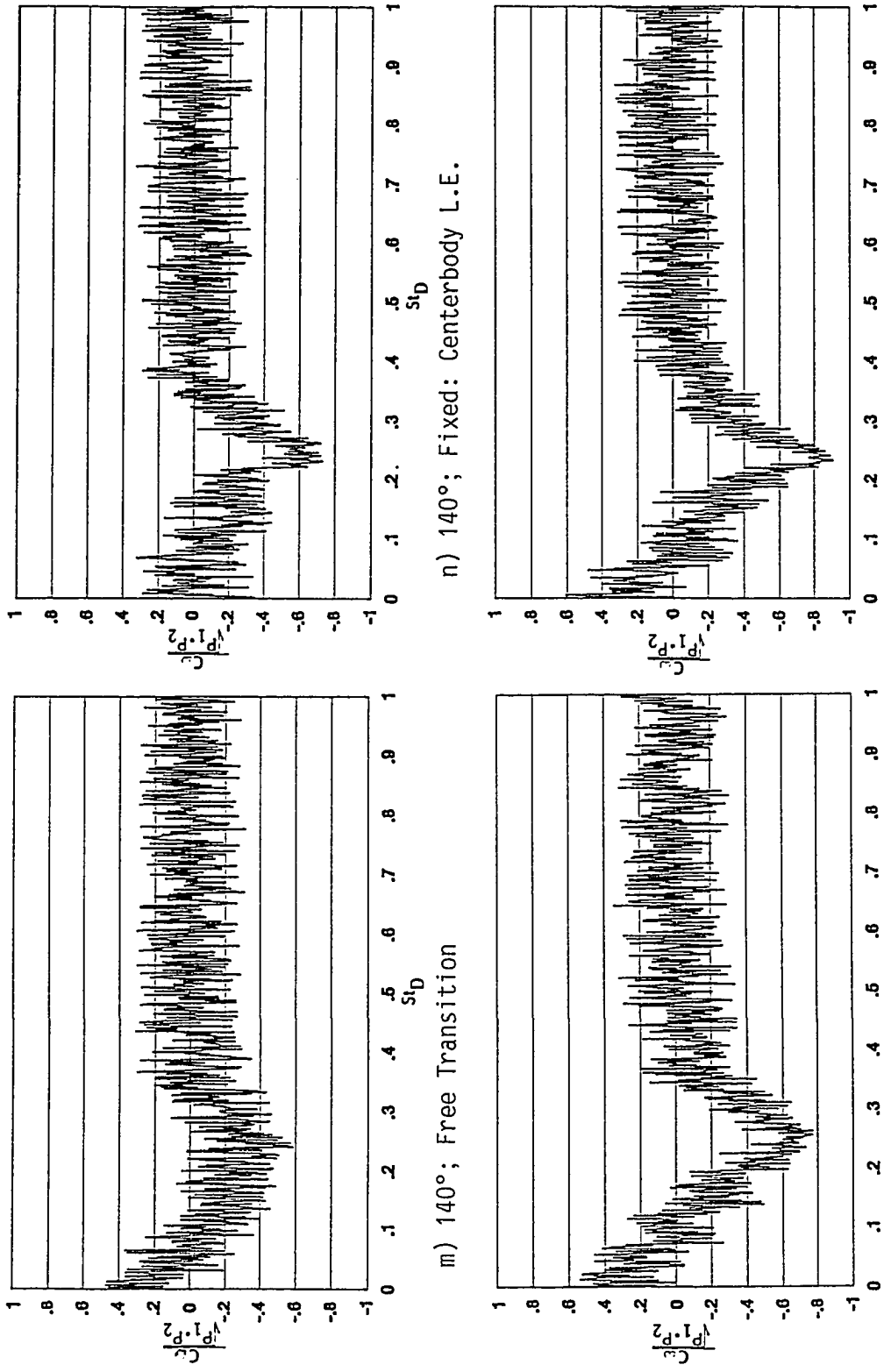

Fig. 8.4 Cont'd

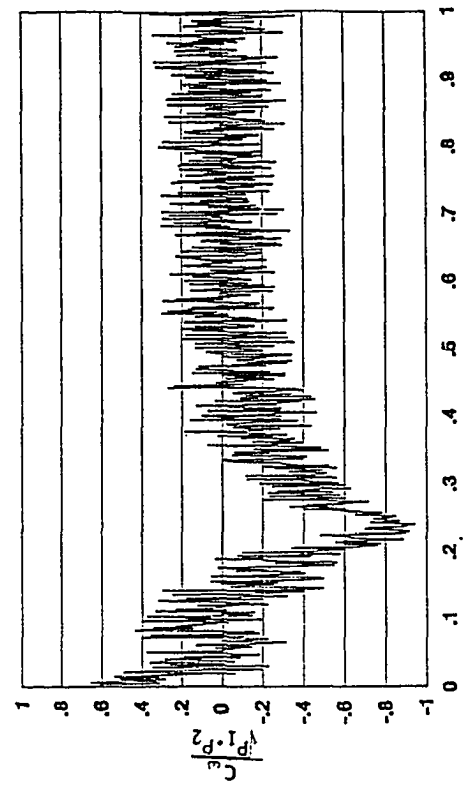

r) 180°; Fixed: Centerbody L.E.

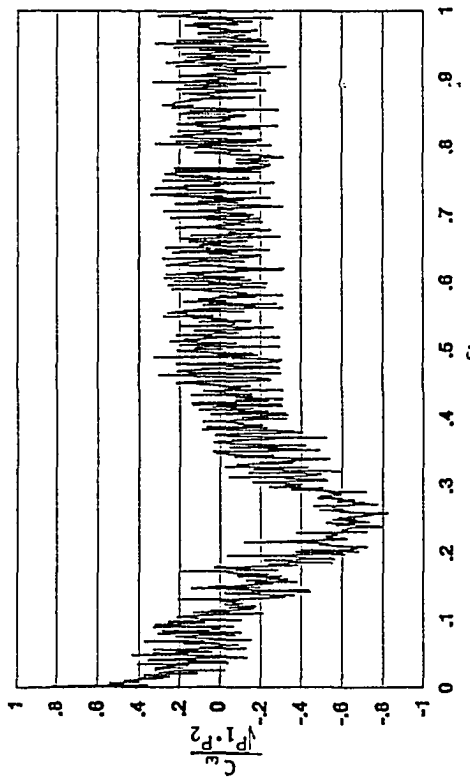

q) 180°; Free Transition

Fig. 8.4 Cont'd

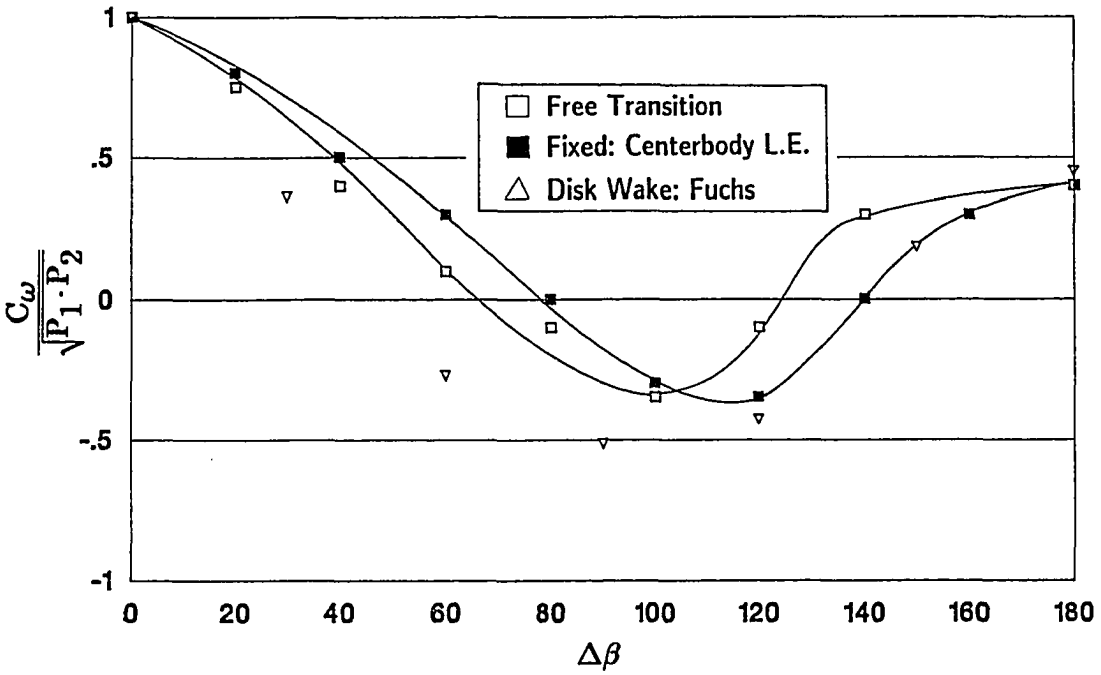

Fig. 8.5 Coherence Variations at $St_D = 0.04St_{D_{PRED}}$

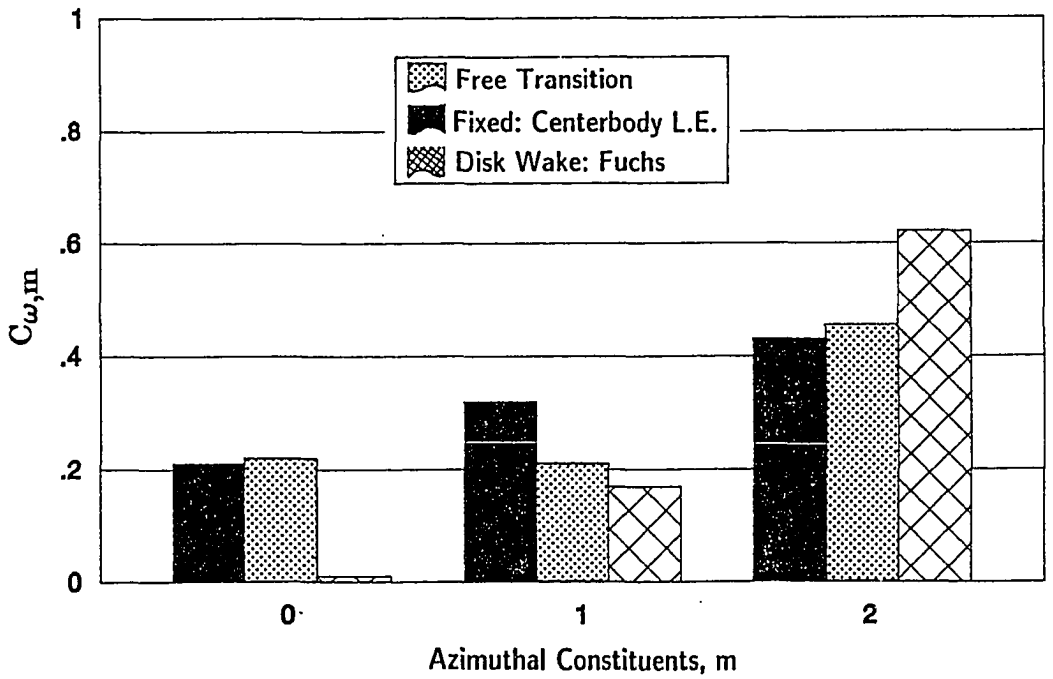

Fig. 8.6 Azimuthal Constituents at $St_D = 0.04St_{D_{PRED}}$

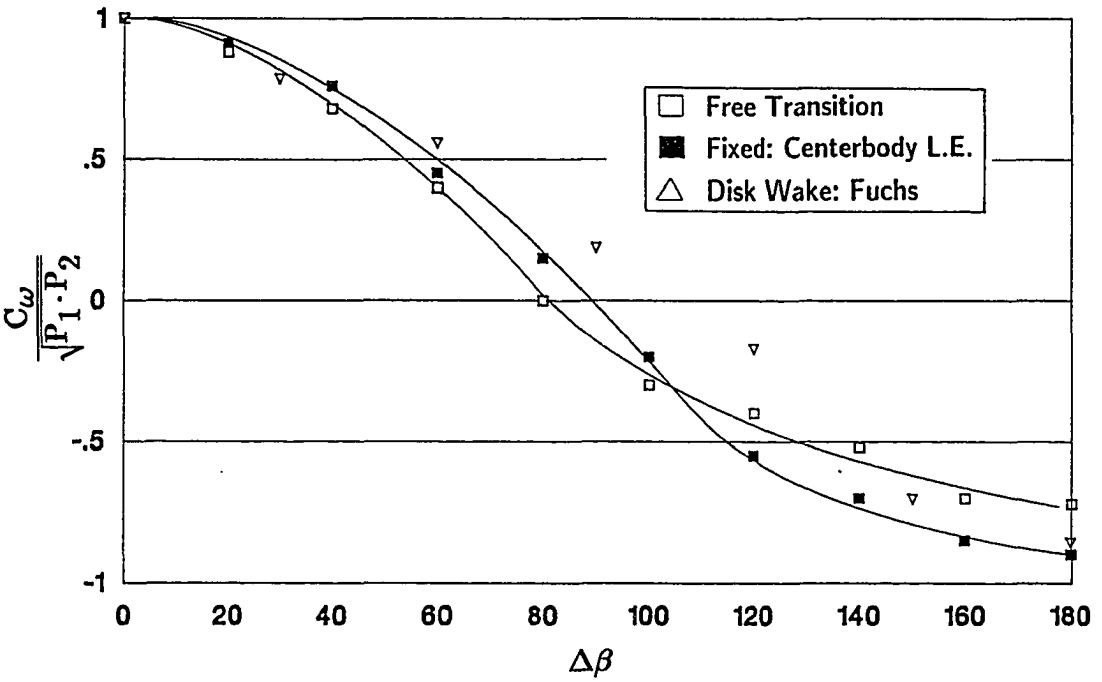

Fig. 8.7 Coherence Variations at the Predominant Frequency

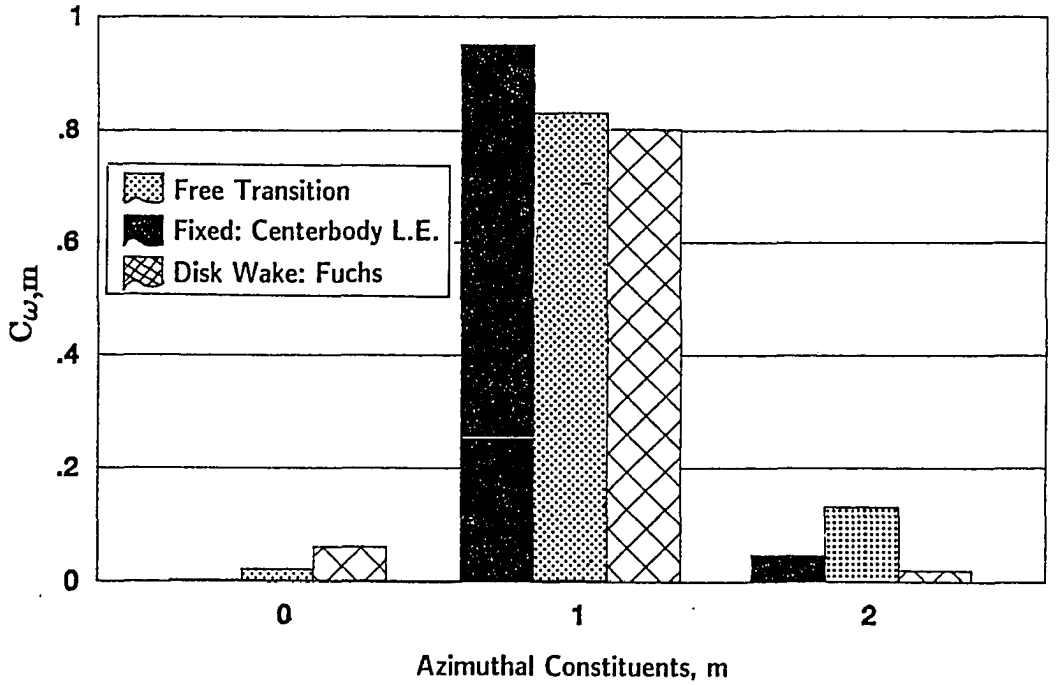

Fig. 8.8 Azimuthal Constituents at the Predominant Frequency

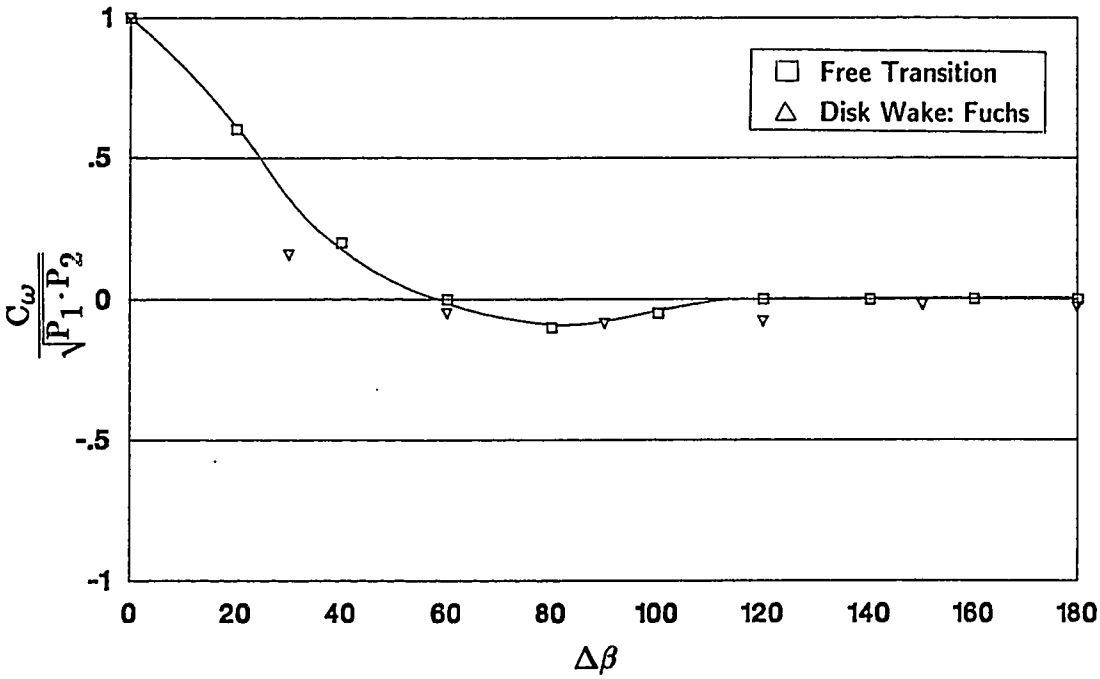

Fig. 8.9 Coherence Variations at $St_D = 2.0St_{D_{PRED}}$

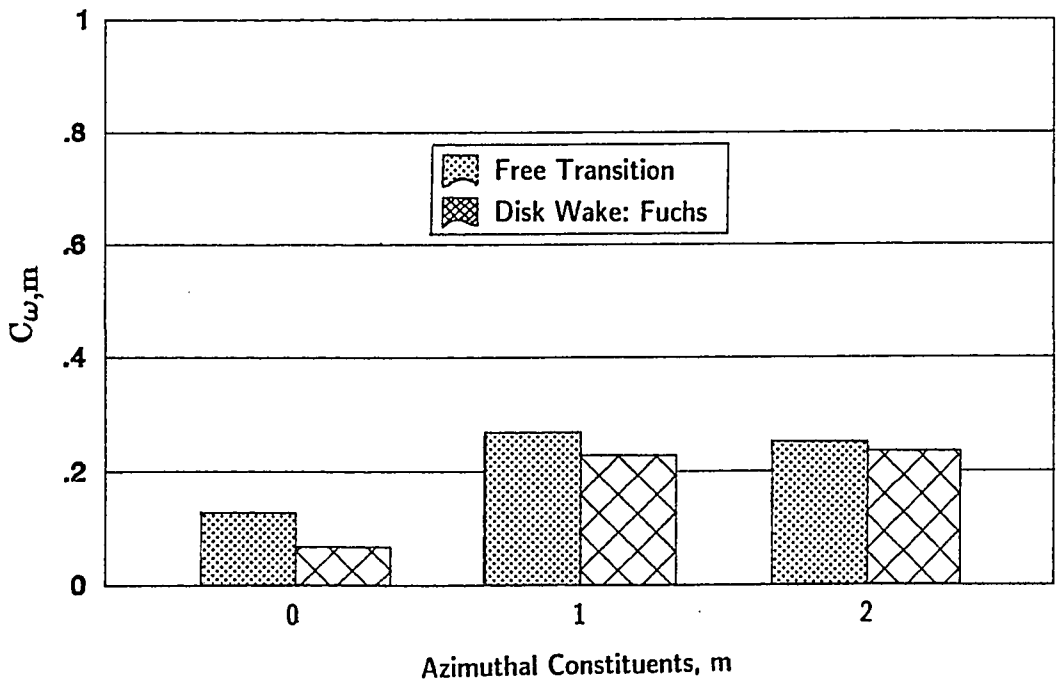

Fig. 8.10 Azimuthal Constituents at $St_D = 2.0St_{D_{PRED}}$

CONCLUSIONS

The subsonic wake of a family of slanted-base bluff bodies has been studied. Interference-free drag measurements confirmed earlier slanted-base studies, and demonstrated, by varying the centerbody boundary layer trip location, that the near-wake is influenced by the state of the boundary layer ahead of separation. Further testing detailed the steady structure of the near-wake, as well as the large-scale turbulent properties of the near-wake. The structure of the slanted-base bluff body near-wake was detailed through the following measurements:

- base pressure distributions
- wake stagnation point location
- boundary layer velocity profile
- predominant frequency
- coherence measurements

as well as through flow visualization using liquid crystals and smoke.

It was concluded that sudden changes in near-wake structure were related to flow reattachment onto the slanted-base. The free shear layer was shown to reattach on the base just downstream of the base leading edge, forming a separation bubble.

Noticeable variations in base pressure occurred with increasing Reynolds number, Re_D. The variations were more noticeable for the 50° base which is characterized by a longitudinal vortex wake. It was shown through base pressure measurements that fixing boundary layer transition on the model centerbody

resulted in deviations from free-transition measurements. These deviations occurred at $Re_D \simeq 80{,}000$ for the forward trip location, and for $Re_D \simeq 110{,}000$ for the center trip location, and continued to higher Reynolds numbers ($Re_D \simeq 170{,}000$) where free- and fixed-transition results again converged. Deviations in fixed- and free-transition base pressure measurements were also shown for the lower angle slanted-bases (characterized by a closed near-wake), however, deviations were not as large as those which occurred for the 50° base.

The wake stagnation point was shown to move away from the leading edge of the base with increasing base slant angle; especially between the 40° and 45° bases. This was confirmed through a simplified two-dimensional numerical analysis using a finite element computer code (FIDAP). The distance the base trailing edge extends into the wake with increasing base slant angle was greater than the outward shift of the wake stagnation point. The curvature of the free shear layer originating from the base trailing edge was shown, through smoke flow visualization and numerical analysis, to decrease with increasing base slant angle. This is in agreement with the analytical arguments presented in Chapter 4.

For the 45° base, experimental results showed that rapid variations in the wake stagnation point location occurred with Reynolds number. This could not be simulated in the numerical study for sharp-edged separation; however, noticeable variations in the wake geometry were shown with Reynolds number if the base leading edge was slightly rounded.

It was also demonstrated through wake stagnation point measurements that fixing boundary layer transition on the model centerbody resulted in differences from free-transition measurements for certain Reynolds numbers. These deviations occurred at $Re_D \simeq 80{,}000$ for the forward trip location, and for $Re_D \simeq 110{,}000$ for the center trip location, and continued to higher Reynolds numbers ($Re_D \simeq 170{,}000$) where free- and fixed-transition results again converged.

Fixing boundary layer transition on the model centerbody resulted in a movement of the wake stagnation point away from the base.

It was demonstrated in this research that similarity exists in base pressures and wake stagnation point locations with the appropriate choice of an independent variable. For fixed and free boundary layer transition, it was demonstrated that mean flow measurements collapse onto a single curve when the independent variable was the Reynolds number based on the incoming boundary layer momentum thickness, Re_θ. This is demonstrated most clearly for the 50° base, which is characterized by a strong dependence of base pressure on Reynolds number.

Spectral characterization of the wakes of the slanted-base models revealed predominant frequencies for the lower angle slanted-bases resulting from vortex shedding. Spectral peaks were not present for the longitudinal vortex wake. The vortex shedding frequency, presented as a Strouhal number was shown to increase with increasing base slant angle. Experimental measurements were in good agreement with the semi-empirical analysis presented in Chapter 5. No noticeable variations in the predominant frequency with Reynolds number could be seen for increasing slant-angle. Fixing boundary layer transition on the model centerbody resulted in only small variations in the predominant frequency for the 45° base model; however, these variations are attributed to difficulty in extracting a predominant frequencies from extremely broad spectral peaks.

A modal analysis for the 0° base model was performed for $Re_D = 110{,}000$ for fixed and free boundary layer transition. For frequencies at or below the predominant frequency, upwards of 99% of the fluctuating turbulent energy was contained in the first three modes. Trends are shown to be similar to those occurring in the wake of a disk placed normal to the oncoming flow. The dominance of the $m = 1$ constituent at the predominant frequency confirmed the

presence of strong vortex shedding. The importance of vortex shedding was shown to diminish slightly for free boundary layer transition. At low frequencies, no mode was clearly dominant, however, a majority of the fluctuating turbulent energy was contained in the $m = 2$ constituent. The only noticeable variation between fixed- and free- transition results is seen for the $m = 1$ mode, with lower energy content shown for free-transition. At high frequencies, less that 70% of the turbulent energy was contained in the first three modes. No mode was found to dominate at higher frequencies.

A detailed study has been conducted on the influence of the boundary layer on the development of a bluff body wake. While this research has answered many questions concerning the development of the near-wake, it has also revealed phenomena that need further study. For example, a strong dependency of the 45° base wake stagnation point on slight variations in the Reynolds number, Re_D was observed. This phenomenon warrents further study, both experimental and computational. The current research has shown computationally that the wake stagnation point location of higher angle slanted-bases is sensitive to Reynolds number variations, however, a three-dimensional study that includes the side flow may show a stronger influence.

This research has also demonstrated in an axisymmetric wake that the distribution of fluctuating energy contained in individual azimuthal constituents is affected by the state of the boundary layer. This study was carried out for a constant Reynolds number, $Re_D = 110{,}000$. Variations in large-scale axisymmetric wake structures with Reynolds number, such as that which occurs with the base pressure coefficients for $60{,}000 < Re_D < 110{,}000$, is a topic warranting further study. It is tempting to extend such a study to non-axisymmetric bases, however as discussed in Chapter 8, one must proceed with caution as the concept of azimuthal constituents is based on axisymmetry. The wake behind a slanted-base

is skewed, i.e., non-axisymmetric due to a deflection in the external flow as it tries to negotiate the leading edge base corner.

The current near-wake study was carried out without base bleed. It is suggested that future research consider boundary layer influences on steady and unsteady near-wake characteristics with mass addition. The steady analytical analysis in Chapter 4 can be modified to consider the effect of mass addition on the wake stagnation point.

BIBLIOGRAPHY

1. Berger, S. A.; Laminar Wakes, American Elsevier Publishing Company, Inc., New York, 1971.

2. Birkhoff, G., Zarantonello, E. H.; Jets, Wakes, and Cavities, Academic Press Inc., 1955.

3. Merz, R. A., Page, R. H., Przirembel, C. E. G.; "Subsonic Axisymmetric Near-Wake Studies," *AIAA Journal,* Vol. 16, July 1978, pp. 656-662.

4. Nash, J. F.; "An Analysis of Two-Dimensional Turbulent Base Flow, Including the Effect of the Approaching Boundary Layer", *ARC R&M 3344*, 1963.

5. Gai, S. L., Patil, S. R.; "Subsonic Axisymmetric Base Flow Experiments with Base Modifications," *AIAA Journal,* Vol. 17, Jan. 1980, pp. 42-46.

6. Tanner, M.; "Theoretical Prediction of Base Pressure for Steady Base Flow," *Progress in Aerospace Sciences,* Vol. 14, 1973, pp. 177-225.

7. Bearman, P. W.; "REVIEW-Bluff Body Flows Applicable to Vehicle Aerodynamics", *Journal of Fluids Engineering*, Vol. 102, Sept. 1980, pp. 265-274.

8. Eaton, J. K., and Johnston, J. P.; "A Review of Research on Subsonic Turbulent Flow Reattachment," AIAA Journal, Vol. 19, No. 9, Sept. 1981, pp. 1093-1100.

9. Bradshaw, P.; "The Effect of Initial Conditions on the Development of a Free Shear Layer", *Journal of Fluid Mechanics*, Vol. 26, Pt. 2, 1966, pp. 225-236.

10. Narayanan, M. A. B., Khadgi, Y. N., and Viswanath, P. R.; "Similarities in Pressure Distribution in Separated Flow behind Backward-Facing Steps," *Aeronautical Quarterly*, Vol. 25, Nov. 1974, pp. 305-312.

11. Kurzweg, H. H.; "Interrelationship Between Boundary Layer and Base Pressure," *Journal of the Aeronautical Sciences*, Vol. 18, Nov. 1951, pp. 743-748.

12. Porteiro, J. L. F., Przirembel, C. E. G., Page, R. H.; "Modification of Subonic Wakes Using Boundary Layer and Base Mass Transfer," *AIAA Journal*, Vol. 21, May 1983, pp. 665-670.

13. Page, R. H.; "Compressible, Subsonic, Axisymmetric Base Flows", *Symposium on Rocket/Plume Fluid Dynamic Interactions*, Huntsville Al, Apr. 1983.

14. Page, R. H., Ostowari, C.; "Turbulent Near-Wake of a Symmetrical Body", *AIAA Journal*, Vol. 26, No. 1, Jan. 1988, pp. 115-116.

15. Han, T., Hammond, D.C., and Sagi, C. J.; "Optimization of Bluff Body for Minimum Drag in Ground Proximity", *AIAA Journal*, Vol. 30, No. 4, April 1992, pp. 882-889.

16. Ahmed, S. R., W. Baumert; "The Structure of Wake Flow Behind Road Vehicles," Aerodynamics of Transportation, ASME-CSME Conference, Niagara Falls, June, 1979, pp.93-103.

17. Jansson, L. J. and Hucho, W. H.; "Aerodynamische Formoptimerung der Type VW-Golf und VW-Scirocco", *Kolloquium über Industrie-Aerodynamik*, Aachen, Part3, 1974, pp. 46-49.

18. Hucho, W. H.; Aerodynamics of Road Vehicles, Butterworths, 1987.

19. Morel, T.; "Effect of Base Slant on the Flow Patterns and Drag of Three-Dimensional Bodies with Blunt Ends," *Symposium on Aerodynamic Drag Mechanisms of Bluff Bodies and Road Vehicles*, Sept, 1976, Plenum, New York, 1978.

20. Morel, T.; "Aerodynamic Drag of Bluff Body Shapes Characteristic of Hatch-Back Cars," *SAE Congress and Exposition*, Society of Automotive Engineers, Detroit, MI, March 1978, Paper 780267.

21. Maull, D. J.; "The Drag of Slant-Based Bodies of Revolution," *Aeronautical Journal*, Vol. 84, No. 833, June 1980, pp. 164-166.

22. Xia, X. J., and Bearman, P. W.; "An Experimental Investigation of the Wake of an Axisymmetric Body with a Slanted Base," *Aeronautical Quarterly*, Vol. 43, Feb. 1983, pp.24-45.

23. Britcher, C. P., and Alcorn, C. W.; "Intererence-Free Measurements of the Subsonic Aerodynamics of Slanted-Base Ogive Cylinders", *AIAA Journal,* Vol. 29, No. 4, April 1991, pp. 520-525.

24. Britcher, C. P., Alcorn, C. W., Kilgore, W. A.; "Subsonic Sting Interference on the Aerodynamic Characteristics of a Family of Slanted-Base Ogive-Cylinders", *NASA CR, Report No. 4299*, June 1991,66 pp.

25. Britcher, C. P., Kilgore, W. A., Alcorn, C. W.; "Subsonic Sting Interference on the Drag of a Family of Slanted-Base Ogive-Cylinders", *AIAA 7th Applied Aerodynamics Conference*, Seattle, WA, July 1989, Paper no. 89-2206, pp. 389-397.

26. Alcorn, C. W.; "An Experimental Investigation of the Aerodynamic Characteristics of Slanted Base Ogive Cylinders Using Magnetic Suspension Technology", *Masters Thesis*, Dept. of Mechanical Engineering and Mechanics, Old Dominion Univ., Norfolk VA, 1988.

27. Johnson, W. G., and Dress, D. A.; "The 13-inch Magnetic Suspension and Balance System Wind Tunnel," *NASA TM-4090*, Jan. 1989.

28. Tcheng, P., and Schott, T. D.; "A Miniature Infared Pressure Telemetry System," *Proceedings of the 34th International Instrumentation Symposium,* Alburquerque, NM, May 1988, pp. 407-416.

29. von Kármán, T.; Aerodynamics, 1st ed., McGraw Hill, New York, 1963, pp. 67-70.

30. Schlichting, H.; Boundary Layer Theory, 7th ed., McGraw Hill, New York, 1979, pp. 28-32.

31. Tanner, M.; "Reduction of Base Drag," *Progress in Aerospace Sciences,* Vol. 16, No. 4, 1975, pp. 369-384.

32. Yule, A. J.; "Phase Scrambling Effects and Turbulence Data Analysis", *Second International Symposium on Turbulent Shear Flows,* Imperial College, London, July 1979.

33. Zaman, K. B. M. Q., Hussain, A. K. M. F.; "The Mechanics of Vortex Pairing in an Axisymmetric Mixing Layer", *Second International Symposium on Turbulent Shear Flows,* Imperial College, London, July 1979.

34. Lighthill, M. J.; "On Sound Generated Aerodynamically", *Proceedings of the Royal Society of London,* Vol. 211, 1952, pp. 564-587.

35. Eldrad, K.; "Base Pressure Fluctuations", The Journal of the Acoustical Society of America, Vol 33, No. 1 Jan. 1961.

36. Fuchs, H. V., Mercker, E., Michel, U.; "Mode Expansion of Coherent Structures in the Wake of a Circular Disk", *Second International Symposium on Turbulent Shear Flows,* Imperial College, London, July 1979.

37. Fuchs, H. V., Mercker, E., Michel, U.; "Large-Scale Coherent Structures in the Wake of Axisymmetric Bodies", *Journal of Fluid Mechanics (1979),* Vol. 93, part 1, pp. 185-207.

38. Wille, R.; "Beiträge zur Phänomenologie der Freistrahlen", Zeitschrift für Flugwissenschaften, Vol. 11, No. 6, 1963, pp. 222-233.

39. Perry, A. E., Lim, T. T.; "Coherent Structures in Coflowing Jets and Wakes", *Journal of Fluid Mechanics,* Vol. 88, pp. 451-464.

40. Taneda, S.; "Visual Observation of the Flow Past a Sphere at Reynolds Numbers between 10^4 and 10^6", *Journal of Fluid Mechanics,* Vol. 85, 1978, pp. 187-192.

41. Achenbach, E.; " Vortex Shedding from Spheres", *Journal of Fluid Mechanics,* Vol. 62, 1974, pp. 209-221.

42. Roshko, A.; "Structure of Turbulent Shear Flows", *AIAA Journal,* Vol. 14, No. 10, Oct. 1976, pp. 1349-1357.

43. Koochesfahani, M.M., and Dimotakis, P.E.; "Effects of a Downstream Disturbance on the Structure of a Turbulent Plane Mixing Layer" *AIAA Journal,* Vol. 27, No. 2, Feb. 1989, pp. 161-166.

44. Korczak, K. Z., and Wessel, R. A.; "Mixing Control in a Plane Shear Layer", *AIAA Journal*, Vol. 27, No. 12, Dec. 1989, pp. 1744-1751.

45. Batt, R. G.; "Some Measurements on the Effect of Tripping the Two-Dimensional Shear Layer", *AIAA Journal*, Vol. 13, No. 2, Feb. 1975, pp. 245-246.

46. Bradshaw, P. "The Effects of Initial Conditions on the Development of a Free Shear Layer", *Journal of Fluid Mechanics*, Vol. 23, 1966, pp. 225-236.

47. Calvert, J. R.; "Experiments on the Low-Speed Flow Past Cones", *Journal of Fluid Mechanics (1967)*, Vol. 27, part 2, pp. 273-289.

48. Roberts, J. B.; "Coherence Measurements in an Axisymmetric Wake", *AIAA Journal*, Vol. 11, No. 11, Nov. 1973, pp. 1569-1571.

49. Kiya, M., et. al.; "Turbulence Properties of an Axisymmetric Separation and Reattaching Flow", *AIAA Journal*, Vol. 29, No. 6., June. 1991, pp. 936-941.

50. Sedney, R.; "A Flow Model for the Effect of a Slanted Base on Drag," *Aerodynamics of Transportation, ASME Symposium*, Niagara Falls, June 1979.

51. Ward, G. N.; Linearized Theory of Steady High-Speed Flow, Cambridge University Press, 1955.

52. Roshko, A., and Lau, J. C.; "Some Observations on Transition and Reattachment of a Free Shear Layer in Incompressible Flow", *Proc. Heat Transfer and Fluid Mech. Inst.*, Stanford University Press, 1965.

53. Wassan, A. R.; "Review of Recent Developements in Turbulent Supersonic Base Flow", *AIAA Journal*, No. 3, June 1965, pp. 1135-1138.

54. Gadd, G. E., Holder, D. W., and Regan, J. D.; "Base Pressure in Supersonic Flow", *Aeronautical Research Council CP 271*, March 1955.

55. Chapman, D. R.; "Laminar Mixing of a Compressible Fluid", *NACA Report*, No. 958, 1950.

56. Korst, H. H.; "A Theory for Base Pressures in Transonic and Supersonic Flow", *Journal of Applied Mechanics*, Vol. 23, Dec. 1956.

57. Tanner, M.; "Theoretical Prediction of Base Pressure for Steady Base Flow", *Progress in Aerospace Sciences*, Vol. 14, 1973, pp. 177-225.

58. McDonald, H.; "The Turbulent Supersonic Base Pressure Problem", *Aeronautical Quarterly*, Vol. 17, May 1966, pp. 105-126.

59. Germain, P.; "Recent Evolution in Problems and Methods in Aerodynamics", *Journal of the Royal Aeronautical Society*, Vol. 71, No. 682, Oct. 1967, pp. 673-691.

60. Stratford, B. S.; "The Prediction of Separation of the Turbulent Boundary Layer", *Journal of Fluid Mechanics*, Vol. 5, 1959, pp. 1-16.

61. Cebeci, T., Mosinskis, G. J., and Smith, M. O.; "Calculation of Separation Points in Incompressible Turbulent Flows", *Journal of Aircraft*, Vol. 9, No. 9, Sept. 1972, pp. 618-624.

62. Head, M. R.: "Entrainment in the Turbulent Boundary Layer", *Aeronuatical Research Council*, Rep. R and M3152, 1960.

63. Chu, J., Young, A. D.; "Measurements in Separating Two-Dimensional Turbulent Boundary Layers" *AGARD Conference Proceedings on Flow Separation,* No. 168, May. 1975.

64. Sirieix, M.; "Décollment Turbulent en Écoulement Bidimensional"; *AGARD Conference Proceedings on Flow Separation,* No. 168, May. 1975.

65. Kooi, J. W.; "Experiment on Transonic Shock-Wave Boundary Layer Interaction", *AGARD Conference Proceedings on Flow Separation,* No. 168, May. 1975.

66. Lueptow, R.N.: "Turbulent Boundary Layer on a Cylinder in Axial Flow", *AIAA Journal*, Vol. 28, No. 10, Oct. 1990, pp. 1705-1706.

67. Stratford, B. S.; "An Experiment of Zero Pressure Gradient Flow", *Journal of Fluid Mechanics,* Vol. 5, 1959, pp. 17-35.

68. van Ingen, J. L.; "On the Calculation of Laminar Separation Bubbles in Two-Dimensional Incompressible Flow" *AGARD Conference Proceedings on Flow Separation,* No. 168, May. 1975.

69. Wortmann, F. X.; "Über den Ablösewinkel Laminarer Ablöseblasen" *DLR-FB-74-62*, 1974.

70. Wolfe, W. P. and Oberkampf, W. L.; "SANDRAG-A Computer Program for Predicting Drag of Bodies of Revolution at Zero Angle of Attack in Incompressible Flow", *SAND85-0515*, Apr. 1985, Sandia National Laboratories.

71. Bennocci, C., Olivari, D.; "The Equations of Turbulent Motion", *VKI Course Note No. 137*, Oct. 1988.

72. Smol'yakov, A. V., Tkachenko, V. M.; The Measurement of Turbulent Fluctuations, Springer-Verlag, New York, 1983.

73. Hunt, J. C. R.; "An Introduction via Vorticity Dynamics and Statistical Theory", *VKI Lecture Series 1989-03*, Feb. 1989.

74. Mollo-Christensen, E.; "Jet Noise and Shear Flow Instability Seen from an Experimenter's Viewpoint", *Journal of Applied Mechanics*, Vol. 34, 1967, pp. 1-7.

75. Fuchs, H. V.; "Resolution of Turbulent Jet Pressure into Azimuthal Components", *AGARD-CP-131*, Paper 27, 1973.

76. Michalke, A.; "An Expansion Scheme for the Noise from Circular Jets", *Zeitschrift für Flugwissenshaften*, Vol. 20, 1972, pp. 229-237.

77. Hardin, J. C., Pope, D. S.; "Ring Vortex/Cylinder Sound Production Revisited", *AIAA Journal*, Vol. 26, No. 10, Oct. 1988, pp. 1163-1167.

78. Bearman, P. W.; "On Vortex Street Wakes", *Journal of Fluid Mechanics* Vol. 28, 1966, pp. 625-641.

79. Roshko, A.; "On the Wake and Drag of Bluff Bodies", *Journal of the Aeronautical Sciences,* Feb. 1955, pp.124-132.

80. Stephens, T.; "Design, Construction, and Evaluation of a Magnetic Suspension and Balance System for Wind Tunnels", MIT TR-136, also NASA CR-66903, Nov. 1969.

81. Covert, E. E., Finston, M., Vlajinac, M., Stephens, T.; "Magnetic Balance and Suspension Systems for Use with Wind Tunnels", *Progress in Aerospace Sciences*, Vol. 14, 1973.

82. Schott, T., et. al.; "Present Status of the MIT/NASA Langley 6-Inch MSBS", *International Symposium on Magnetic Suspension Technology,* Hampton VA, Aug. 1991.

83. Britcher, C. P., Alcorn, C. W.; "Aerodynamic Tests with the NASA Langley/MIT 6-Inch Magnetic Suspension and Balance System", Final Report for Grant No. NAS1-18581, Task Assignment 130, 1992.

84. Sargianos, N. P.; "Calibration of the Old Dominion University Low-Speed Wind Tunnel", *Masters Thesis,* Dept. of Mechanical Engineering and Mechanics, Old Dominion Univ., Norfolk VA, 1986.

85. Herriot, J. G.; "Blockage Corrections for Three-Dimensional Flow Closed Throat Wind Tunnels with the Consideration of the Effect of Compressibility", *NACA Report 995*, 1950.

86. "Blockage Corrections for Bluff Bodies in Confined Flows", *EDSU-80024*, Nov. 1980.

87. Batchelor, G. K.; "Interference of Wings, Bodies, and Airscrews in a Closed Octagonal Section", *Report ACA-5 (Australia)*, Mar. 1944.

88. Garner, H. C., Rogers, E. W. E., Acum, W. E. A., and Maskell, E. C.; "Subsonic Wind Tunnel Wall Corrections", *AGARDograph 109,* Oct. 1966.

89. Alcorn, C.W.; Britcher, C.P.; "The Influence of the Boundary Layer on the Subsonic Near-Wake of a Family of Bluff Bodies," AIAA 93-0525, 31st Aerospace Sciences Meeting, Jan. 1993.

90. Fluid Dynamics International, Inc. "FIDAP: Vols.1-4", 1991.

91. Hinze, J. O.; TURBULENCE: An Introduction to its Mechanism and Theory McGraw Hill, New York, 1959.

92. Devenport, W. J., Sutton, E. P.; "Near-Wall Behovior of Separated and Reattaching Flows", *AIAA Journal*, Vol. 29, No. 1, Jan 1991, pp. 25-31.

Appendix A: WIND TUNNEL TEST SECTION CALIBRATIONS

A.3 Test Section Dynamic Pressure vs. ΔP_{CONT} (4′×3′ Low-Speed Facility)

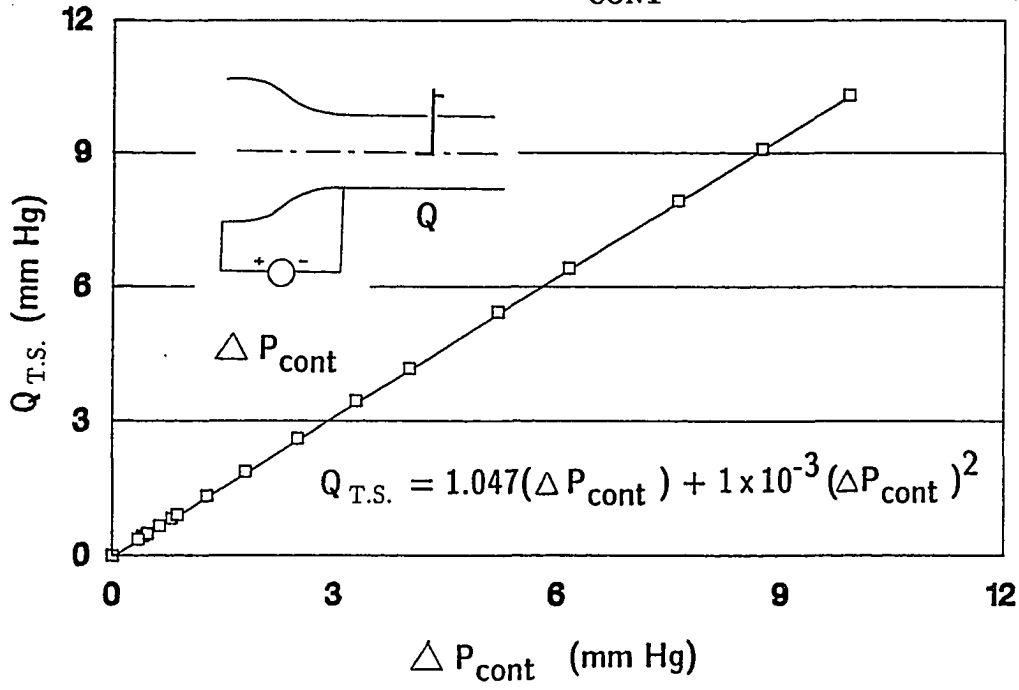

A.4 Static Pressure Drop Along Test Section (4′×3′ Low-Speed Facility)

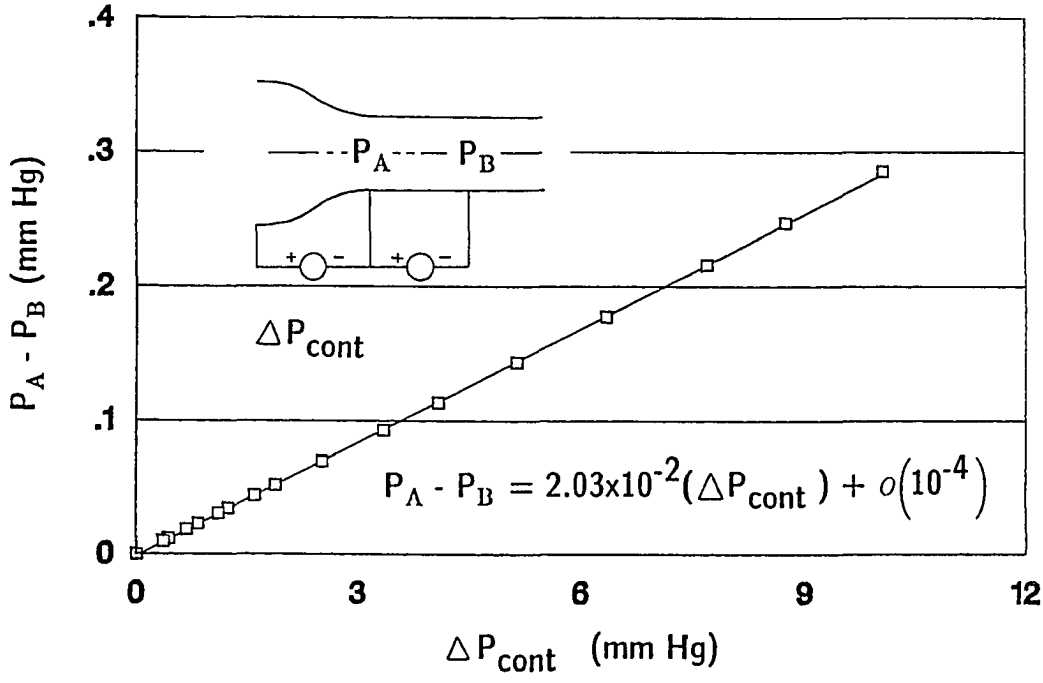

A.1 Test Section Calibration (NASA Langley 6-Inch MSBS)

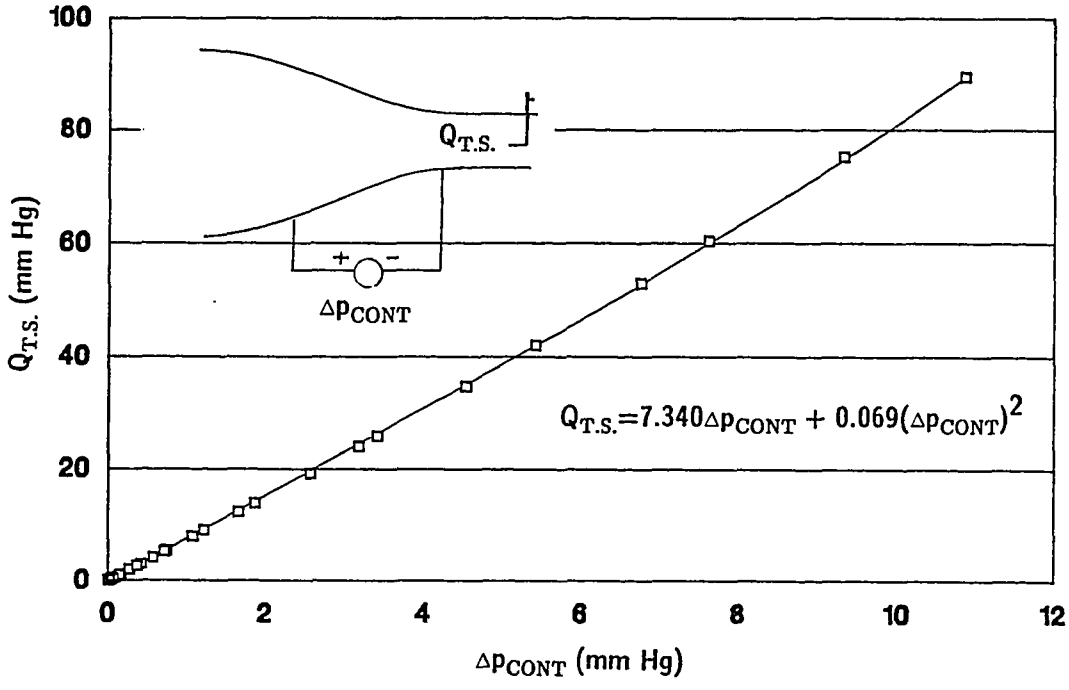

A.2 Turbulence Intensity (ODU 4′ x 3′ Low-Speed Wind Tunnel)

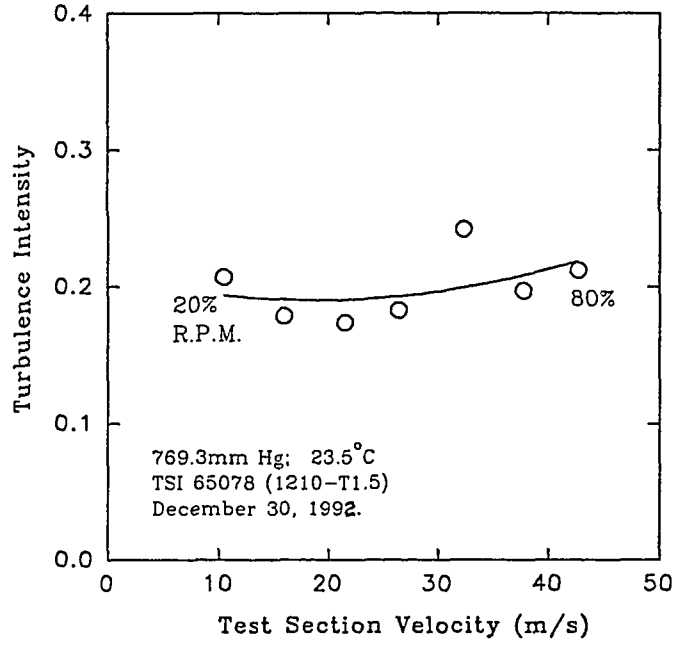

Appendix B: DATA ACQUISITION SOFTWARE PROGRAM for PRESSURE MEASUREMENTS

```
10 CLS
20  CLEAR ,60000! : IBINIT1=60000! : IBINIT2=IBINIT1+3 : BLOAD "bib.m",IBINIT1
30 CALL IBINIT1(IBFIND,IBTRG,IBCLR,IBPCT,IBSIC,IBLOC,IBPPC,IBBNA,
IBONL, IBRSC, IBSRE,IBRSV,IBPAD,IBSAD,IBIST,IBDMA,IBEOS,IBTMO,
IBEOT,IBRDF,IBWRTF,IBTRAP)
40  CALL IBINIT2(IBGTS,IBCAC,IBWAIT,IBPOKE,IBWRT, IBWRTA,IBCMD,
IBCMDA,IBRD,IBRDA,IBSTOP,IBRPP,IBRSP,IBDIAG,IBXTRC,IBRDI,IBWRTI,IBRDIA,
IBWRTIA,IBSTA%,IBERR%,IBCNT%)
50 TC0 = .10086091#: TC1 = 25727.94369#: TC2 = -767345.8295#
60 TC3 = 78025595.81#: TC4 = -9247486589#: TC5 = 6.97688E+11
70 TC6 = -2.66192E+13: TC7 = 3.94078E+14: TC8 = 0: TC9 = 0
80 DIM SCH(40)
90 TXT1$ = " PORT#   "
100 TXT2$ = "PAMB    "
110 TXT3$ = "TAMB     "
120 TXT4$ = "DPCONT     "
130 TXT5$ = "PBASE   "
135 TXT6$ = " "
140 INPUT "ENTER FILENAME: ",F$
150 OPEN "O", #1, "a:"+F$+".DAT
155 PRINT#1, TXT1$; TXT2$; TXT3$; TXT4$; TXT5$
160 CLS
170 DEV$ = "HP3497A"
180 CALL IBFIND(DEV$,HP3497A%)
190 COM00$ = "'SL1'"       'DISABLES HP3497A KEYBOARD
200 COM01$ = "'SL0'"       'ENABLES HP3497A KEYBOARD
```

```
210 COM0$ = "'SD0'"        'TURNS OFF DISPLAY
220 COM1$ = "'SA'"         'SOUNDS SYSTEM ALARM
230 COM2$ = "'AC 20'"      'CLOSE ANALOG CHANNEL # 20
240 CALL IBWRT(HP3497A%,COM0$)
250 CLS
260 INPUT "ENTER ATM PRESSURE (mmHg): ",P
270 INPUT "ENTER PORT NUMBER: ",PORT
280 LOCATE 10,20 : PRINT "HIT SPACEBAR TO TAKE DATA OR E TO END"
290 PRINT
300 K$ = INKEY$
310 IF K$ = "E" THEN GOTO 670
320 IF K$ = " " THEN GOTO 420
330 DAT$ = SPACE$(13)
340 CHAN$ = SPACE$(4)
345 FOR Z = 22 TO 23
350 CHAN$ = STR$(Z)
360 MID$(COM2$,4,4) = CHAN$
370 CALL IBWRT(HP3497A%,COM2$)
380 CALL IBRD(HP3497A%,DAT$)
390 SCH(Z) = VAL(DAT$)
395 NEXT Z
400 LOCATE 12,27: PRINT "DP ACROSS DIFFUSER ";SCH(22)
408 LOCATE 13,27: PRINT "DP ACROSS TEST SECTION ";SCH(23)
410 GOTO 300
420 CLS
430 LOCATE 12,30 : PRINT "NOW TAKING DATA"
440 DAT$ = SPACE$(13)
```

```
450 CHAN$ = SPACE$(4)
455 AAT = 0 : AA22 = 0 :AA23 = 0
460 DE = 20 : JMAX = 4 : IMAX = 80
470 ISTART = 1 : IEND = DE
480 FOR J = 1 TO JMAX
490 SCH(22)= 0
500 SCH(23) = 0
510 FOR I = ISTART TO IEND
520 FOR K = 22 TO 23
530 CHAN$ = STR$(K)
540 MID$(COM2$,4,4) = CHAN$
550 CALL IBWRT(HP3497A%,COM2$)
560 CALL IBRD(HP3497A%,DAT$)
570 SCH(K) = SCH(K) + VAL(DAT$)
580 NEXT K
590 NEXT I
600 GOSUB 680
605 AAT = AAT + TDK
606 AA22 = AA22 + SCH(22)/DE
607 AA23 = AA23 + SCH(23)/DE
610 PRINT#1, USING "  ##.    ###.##    ##.##    ###.####    ###.####
";PORT; P; TDK; SCH(22)/DE ; SCH(23)/DE
620 ISTART = IEND + 1
630 IEND = IEND + DE
640 NEXT J
645 PRINT#1, TXT6$
646 PRINT#1, USING "  ##.    ###.##    ##.##    ###.####    ###.####
```

```
";PORT; P; AAT/JMAX; AA22/JMAX; AA23/JMAX
647 PRINT#1, TXT6$
648 PRINT#1, TXT6$
649 PRINT#1, TXT1$; TXT2$; TXT3$; TXT4$; TXT5$
650 CLS
660 GOTO 260
670 CLOSE :CLS :END
680 ' Thermocouple voltage to temperature subroutine
690 ' ----------------------------------------------
700 '_______ Type " T "_________
710 ' tc0 = 0.100860910 : tc1 = 25727.94369 : tc2 = -767345.8295
720 ' tc3 = 78025595.81 : tc4 = -9247486589 : tc5 = 6.97688E+11
730 ' tc6 = -2.66192E+13 : tc7 = 394078E+14 : tc8 = 0 : tc9 = 0
740 DAT$ = SPACE$(13)
750 CHAN$ = SPACE$(4)
760 CHAN$ = STR$(18)
770 MID$(COM2$,4,4) = CHAN$
780 CALL IBWRT(HP3497A%,COM2$)
790 CALL IBRD(HP3497A%,DAT$)
800 SCH(18) = VAL(DAT$)
810 TDK =TC0 + TC1 * SCH(18) + TC2 * SCH(18) ^ 2 + TC3 * SCH(18) ^ 3 + TC4 *
SCH(18) ^ 4 + TC5 * SCH(18) ^ 5 + TC6 * SCH(18) ^ 6 + TC7 * SCH(18) ^ 7 + TC8 *
SCH(18) ^ 8 + TC9 * SCH(18) ^ 9
820 RETURN
```

Appendix C: Drawings of Slanted-Base Bluff Body Model (ODU)

NOSE-PIECE

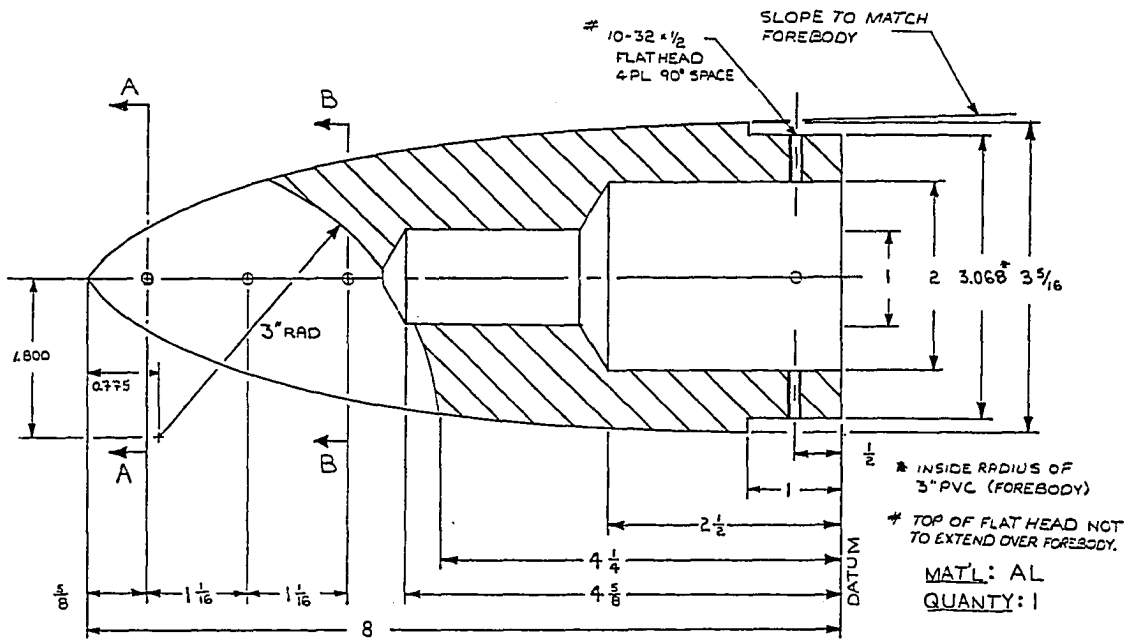

NOSE-PIECE

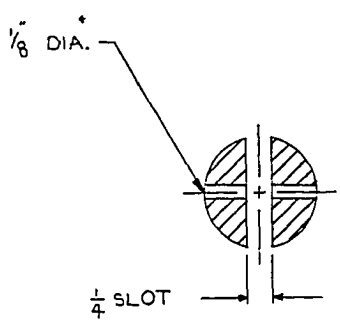

SECTION A-A

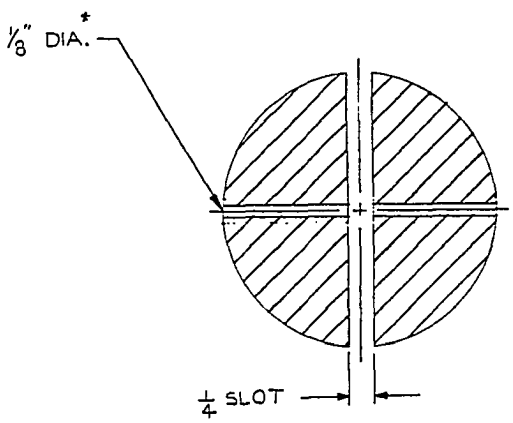

SECTION B-B

* TO HOUSE DRILL ROD

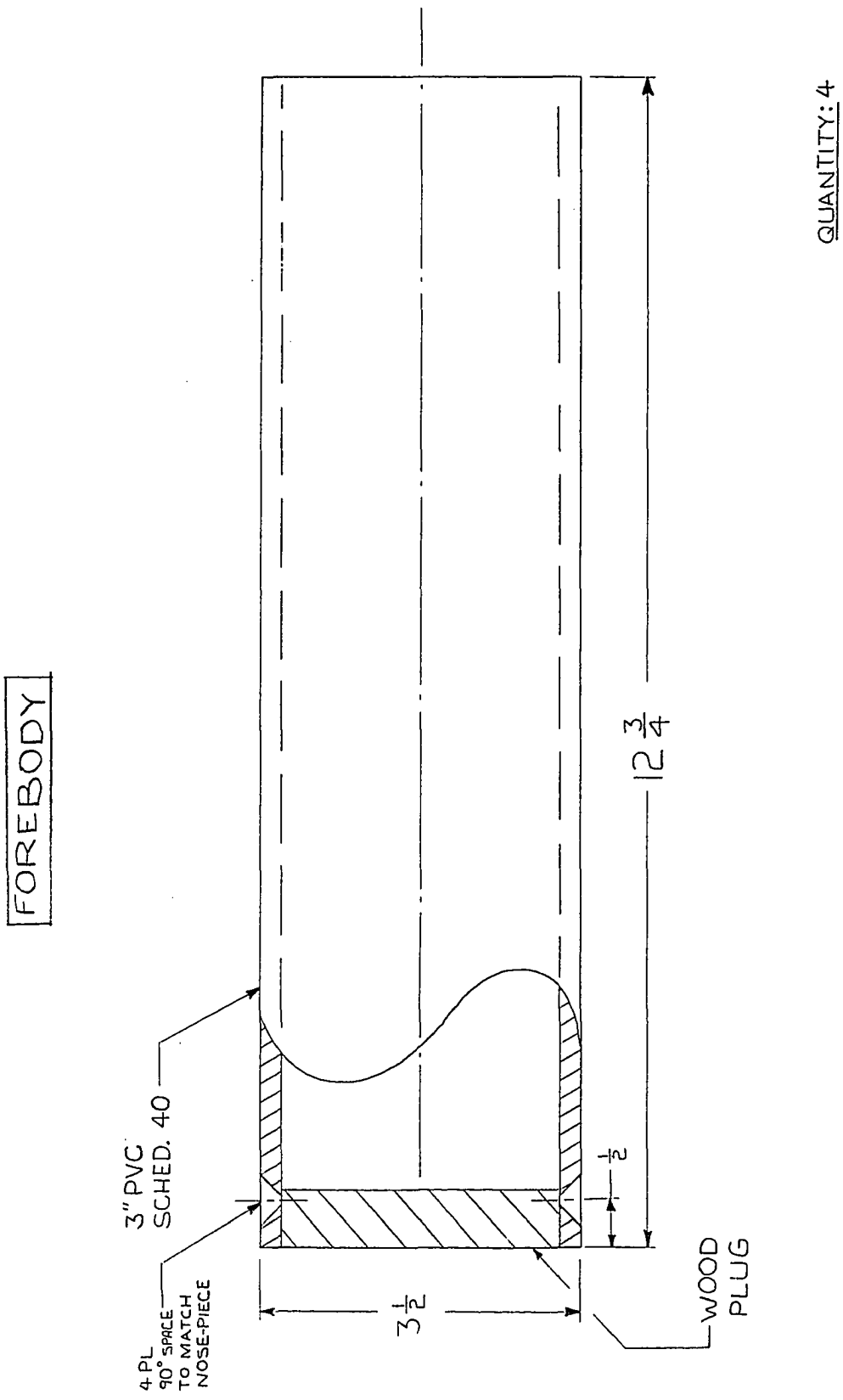

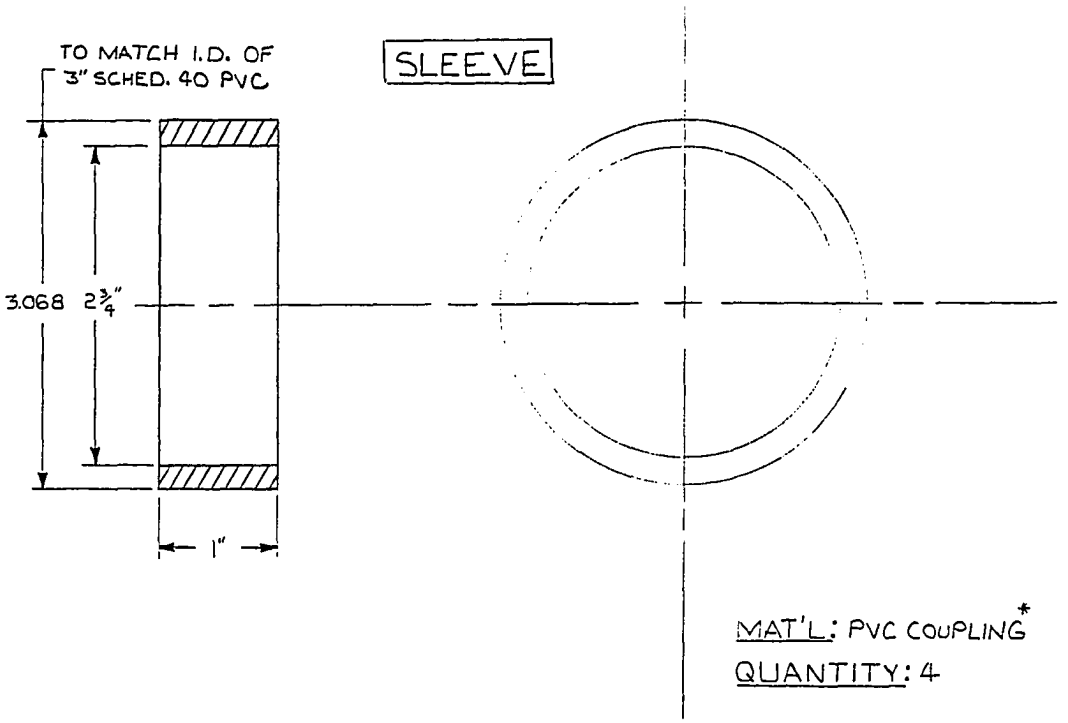

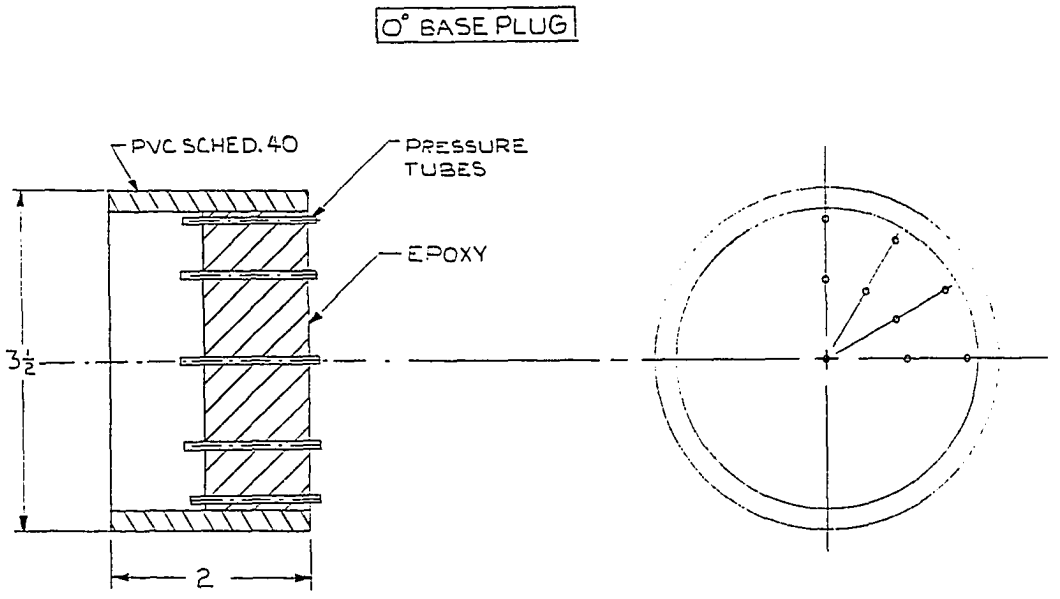

SLANTED BASE PLUG

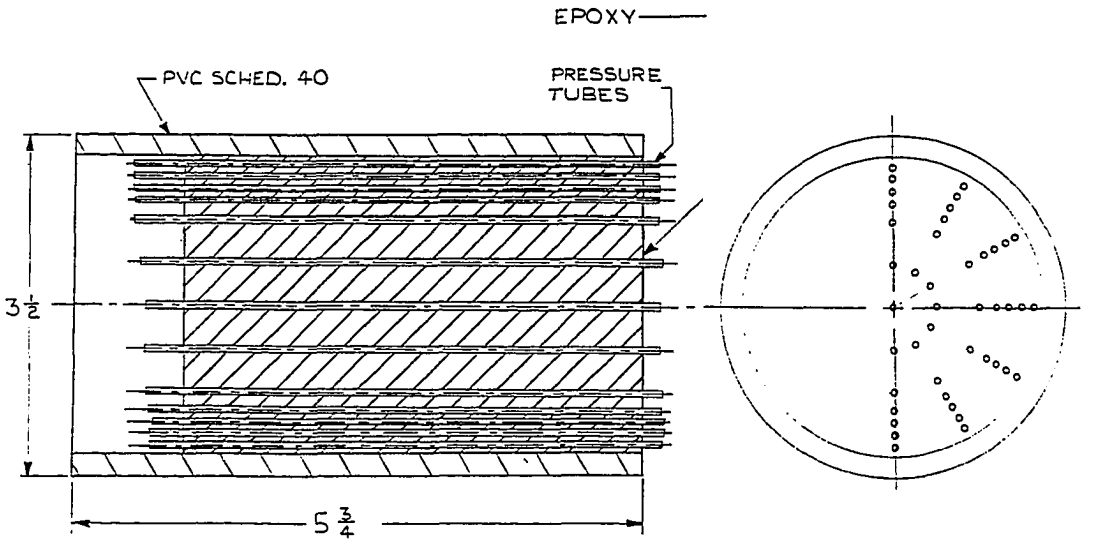

QUANTITY SUPPLIED: 3

0° BASE

① TAPER FOREBODY & BASE PLUG AS SHOWN

② CUT BASE PLUG PERPENDICULAR TO SURFACE AS SHOWN.

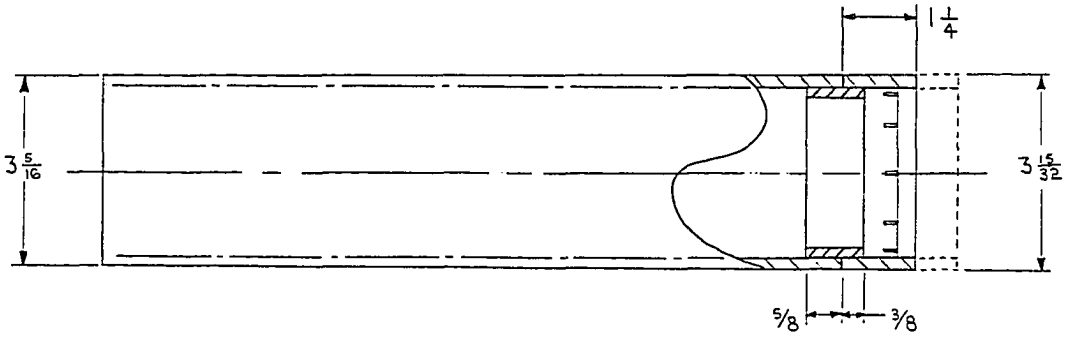

ASSEMBLY OF FOREBODY AND BASE *

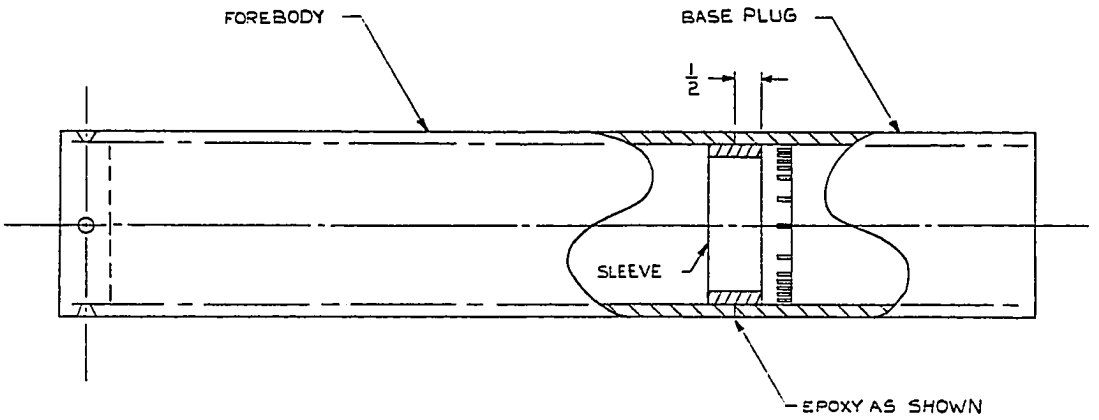

SLANTED BASES

① TAPER FOREBODY & BASE PLUG AS SHOWN.

② CUT BASE PLUG TO SPECIFIED ANGLE.

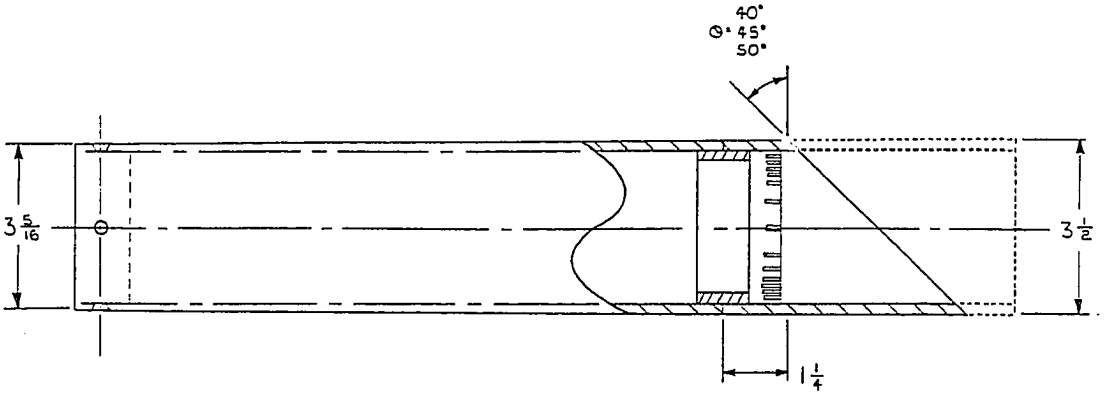

STRUT

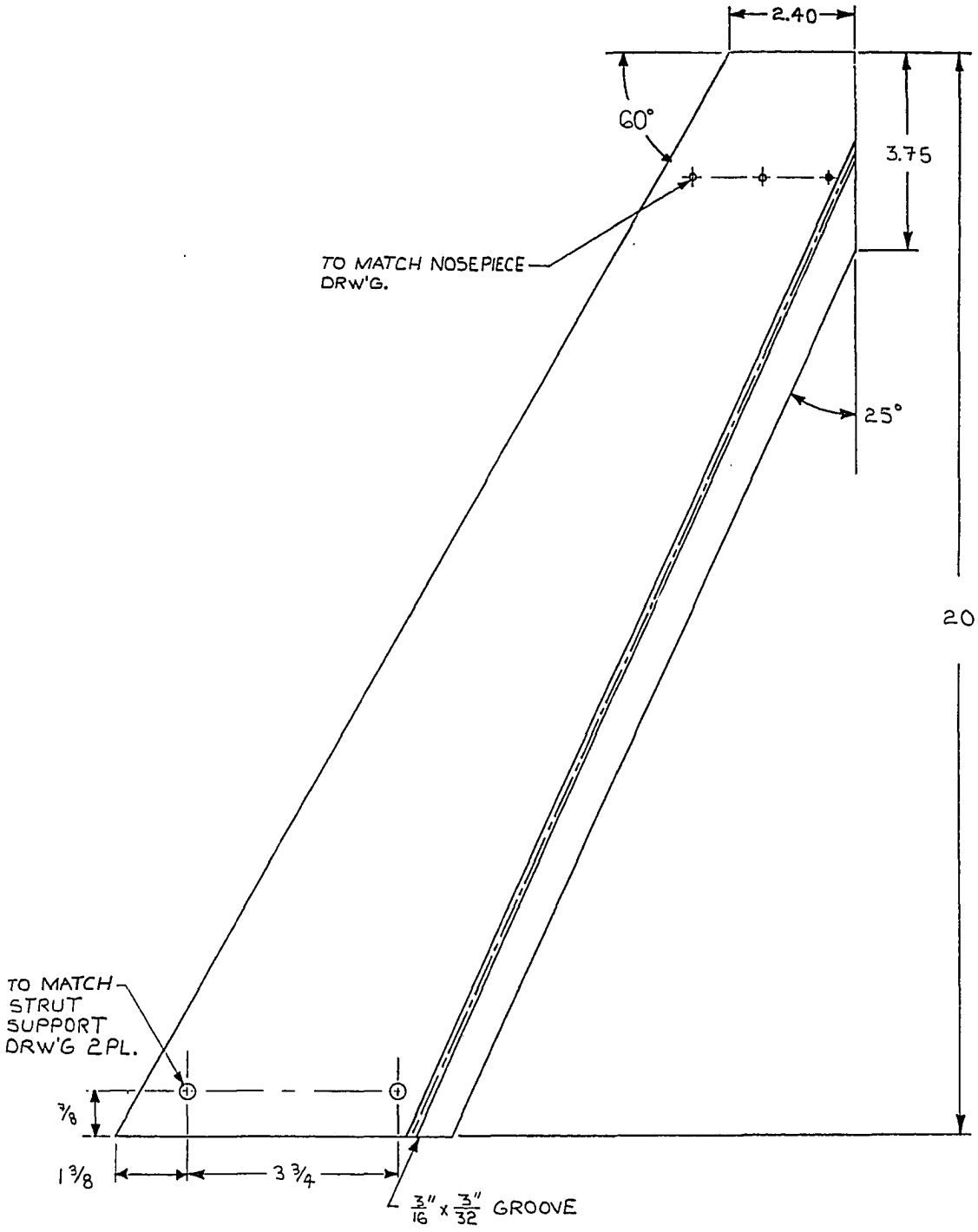

BASE PLATE

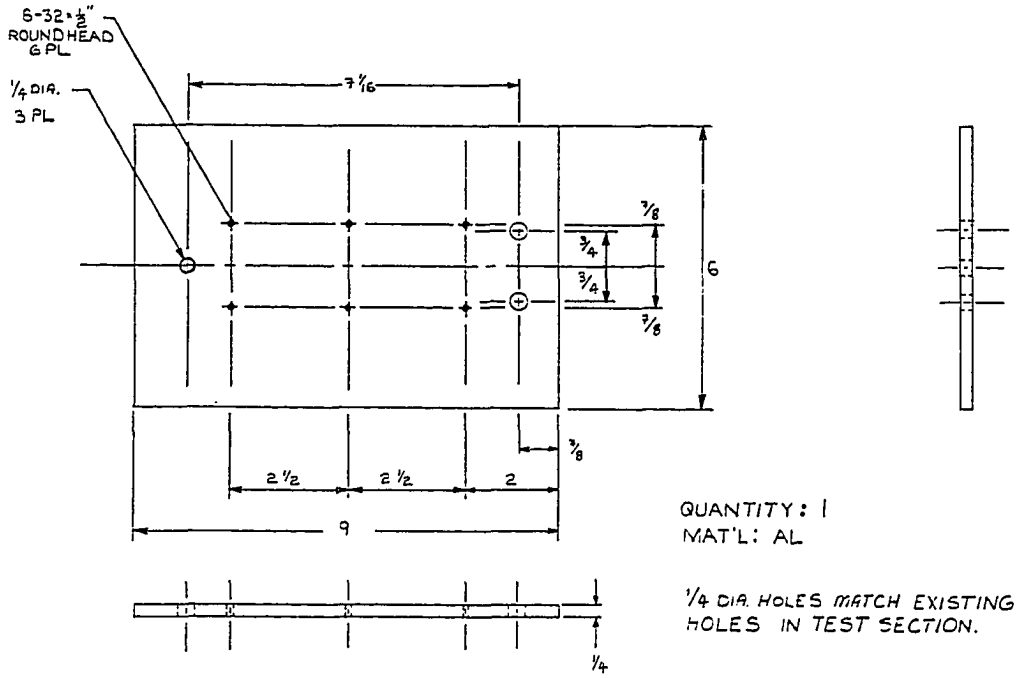

QUANTITY: 1
MAT'L: AL

1/4 DIA HOLES MATCH EXISTING HOLES IN TEST SECTION.

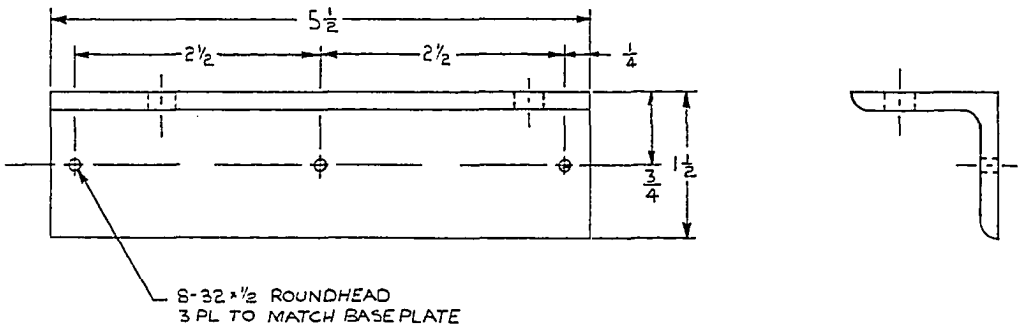

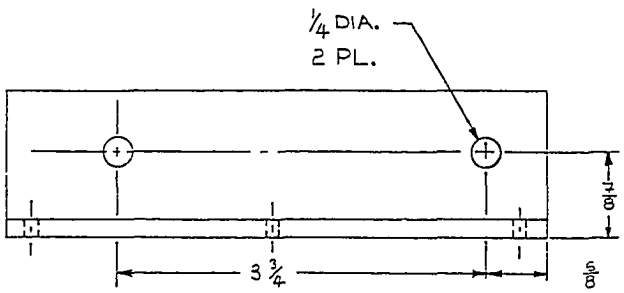

STRUT SUPPORT

QUANTITY: 2
MAT'L: AL

STRUT

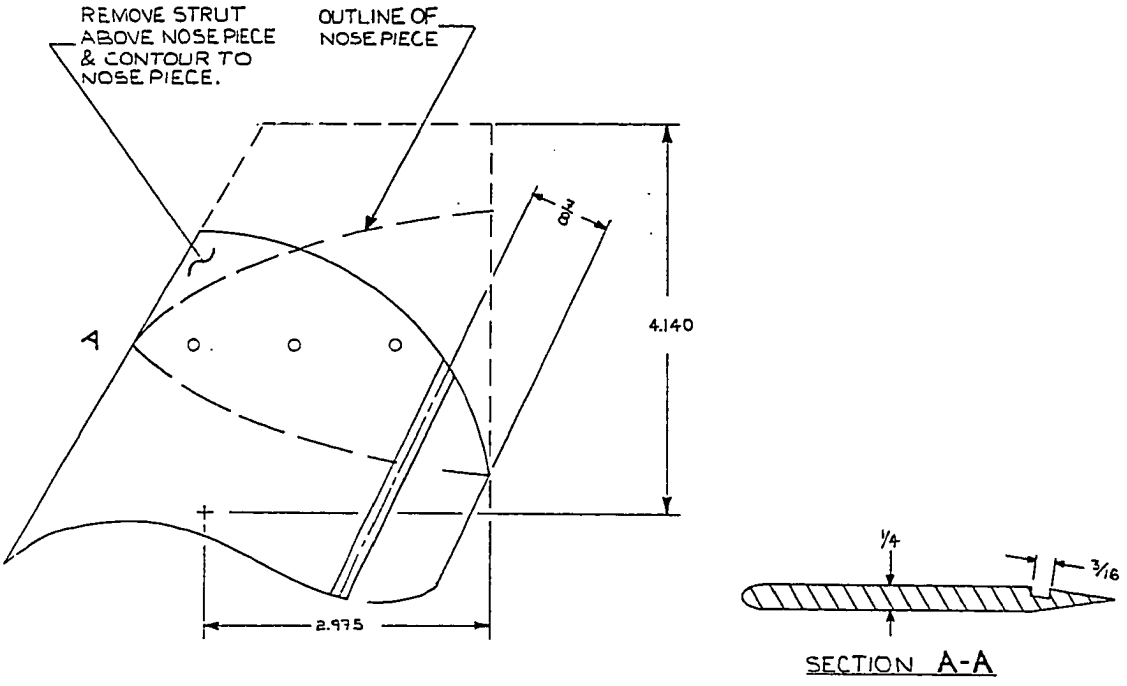

Appendix D: GOVERNING EQUATIONS: BLUFF BODY FLOWS

D.1 Reynolds Averaged Navier-Stokes Equations

(Steady, Incompressible, no Body Forces)

$$\frac{\partial \overline{U}_i}{\partial x_j} = -\frac{1}{\rho}\frac{\partial \overline{P}}{\partial x_i} + \frac{\partial}{\partial x_j}\left\{ \nu \frac{\partial \overline{U}_i}{\partial x_j} - \overline{u}_i \overline{u}_j \right\}$$

U_i = Mean Velocity Component
u_i = Fluctuating Velocity Component
ρ = Density
ν = Kinematic Viscosity

D.2 Transport Equations for Dissipation and Turbulent Kinetic Energy

(Steady, Incompressible)

$$\kappa = \frac{1}{2} u_i u_i$$

$$\epsilon = \nu \frac{\partial u_i}{\partial x_j}\frac{\partial u_i}{\partial x_j}$$

$$\frac{\partial \overline{U}_j \epsilon}{\partial x_j} = c_1 \nu_t \frac{\epsilon}{\kappa}\frac{\partial \overline{U}_i}{\partial x_j}\left\{ \frac{\partial \overline{U}_i}{\partial x_j} + \frac{\partial \overline{U}_j}{\partial x_i} \right\} + \frac{\partial}{\partial x_j}\left\{ \frac{\nu_t}{\sigma_\epsilon}\frac{\partial \epsilon}{\partial x_j} \right\} - c_2 \frac{\epsilon^2}{\kappa}$$

$$\frac{\partial \overline{U}_j \kappa}{\partial x_j} = \nu_t \frac{\partial \overline{U}_i}{\partial x_j}\left\{ \frac{\partial \overline{U}_i}{\partial x_j} + \frac{\partial \overline{U}_j}{\partial x_i} \right\} + \frac{\partial}{\partial x_j}\left\{ \frac{\nu_t}{\sigma_\kappa}\frac{\partial \kappa}{\partial x_j} \right\} - \epsilon$$

$$\nu_t = c_\mu \frac{\kappa^2}{\epsilon}$$

$$c_\mu = 0.09 \quad c_1 = 1.44 \quad c_2 = 1.92 \quad \sigma_\kappa = 1.0 \quad \sigma_\epsilon = 1.3$$

D.3 Universal Near-Wall Flow Profiles

$$u^+ = \frac{(u\text{-}u_W)}{u_*} = f_u(y_u{}^+) \; ; \quad y_u{}^+ = \frac{\rho u_* \delta}{\mu}$$

$$u_* = \left(\frac{\tau_W}{\rho}\right)^{\frac{1}{2}} = \text{friction velocity}$$

w = wall

δ = distance from wall

D.3.1 For $y_u^+ < 5$ (Viscous Sublayer)

$$u^+ = y_u^+$$

D.3.2 For $y_u^+ > 30$ (Fully Turbulent Region)

$$u^+ = \frac{1}{0.41}\ln(9 \cdot y_u^+)$$

D.3.3 For $5 > y_u^+ > 30$ (Fully Turbulent Region)

$$u^+ = \frac{1}{0.41}\ln(1 + 0.4 \cdot y_u^+) + 7.8\left\{1 - \exp\left(-\frac{y_u^+}{11}\right) - \frac{y_u^+}{11}\exp(-0.33\ y_u^+)\right\}$$

D.4 Turbulent Viscosity in Near-Wall Region

$$\mu_t = \rho l_m^2 \sqrt{\left\{\left(\frac{\partial u_i}{\partial x_j} + \frac{\partial u_j}{\partial x_i}\right) \cdot \frac{\partial u_i}{\partial x_j}\right\}}$$

μ_t = turbulent viscosity

$$l_m = \kappa\delta\left\{1 - \exp\left(-\frac{y_u^+}{26}\right)\right\} = \text{van Driest mixing length}$$

$$y_u^+ = \frac{\rho(c_\mu^{\frac{1}{2}}\kappa)^{\frac{1}{2}}\delta}{\mu}$$

Appendix E: FINITE ELEMENT (FIDAP) PREDICTIONS

A finite element fluid dynamic package (FIDAP) was used to simulate the steady, incompressible, turbulent, near-wake behind axisymmetric and two-dimensional slanted-base bluff bodies [90]. The governing equations applicable to this type of flow are presented in Appendix D. The coarseness of the finite element grid and the steady flow assumption prevent realistic comparisons to experimental results. Two objectives of the simulation were:

1.) To test the usefulness of a coarse finite element grid, and to test the assumption of steady flow in determining the wake stagnation point.

2.) To verify slanted-base wake stagnation point trends as a function of slant-angle as represented in Fig. 4.10.

The FIDAP program was run on a Sun 4/50.

E.1 *Computational Models*

A typical grid for the axisymmetric bluff body used in this study is given in Fig. E.1. The length-to-diameter ratio of the model was 6:1. Smaller grid spacing is used in regions where velocity gradients are known to be substantial, such as near the forebody and trailing edge of the model, as well as within the boundary layer and separated shear layer. The upper and lower bounds of the grid are 5 diameters from the model centerline. A breakdown of the node distribution for a typical axisymmetric grid is given below:

Boundary Layer =	450
Free Shear Layer =	300
Recirculation Region =	150
Outer Region =	1300
Upstream of Model =	250
Total =	2450

The validity of the two-dimensional slanted-base model of Fig. 4.10 was studied using the computational grids shown in Figs. E.2-E.3. The forebody is eliminated in this model to isolate the effects of the slanted-base, to lower computer time, and reduce memory requirements. Unfortunately, these simplifications were at the sacrifice of the boundary layer growth on the forebody. It is believed that a sufficiently long centerbody can minimize this effect. It is also shown in Figs. E.2 and E.3 that two grid types are necessary within the near-wake region, depending on the slant-angle. Figure E.2 is now referred to as a "separated" grid, while Fig. E.3 is referred to as an "attached" grid. A topological requirement of FIDAP [90] is that interior angles of quadrilateral regions must be in the range of $90^{\circ} \pm 60^{\circ}$, therefore, slant-angles greater than 60° cannot be represented by an "attached" grid.

Boundary Layer =	230
Free Shear Layer =	450
Recirculation Region =	275
Outer Region =	1625
Total =	2580

E.2 *Boundary Conditions*

A constant inflow boundary condition, $\frac{u}{U_{\infty}} = 1$, was imposed for both axisymmetric and two-dimensional models. Values for the turbulent kinetic energy and dissipation were also imposed at the inflow and are discussed in the following section. A constant velocity of $\frac{u}{U_{\infty}} = 1$ was imposed at the upper and lower bounds of the grid. At the outflow boundary no velocity boundary conditions are explicitly imposed. Similarly, turbulent kinetic energy and dissipation are not specified at the outflow. The no-slip condition is imposed along the model boundary as is the no-penetration condition. In addition,

rotational symmetry was imposed on the near-wake centerline of the axisymmetric model.

E.3 *Turbulence Modeling*

A two-equation high Reynolds number κ-ϵ turbulence model can be incorporated by FIDAP, and is used in the current study [90]. Transport equations for the turbulent kinetic energy, κ, and the viscous dissipation, ϵ, are given in Appendix D. A number of empirical coefficients are contained in the transport equations. Suggested values are also given in Appendix D which are valid for isothermal flows with no mass transfer [90].

The major disadvantage of the high Reynolds number κ-ϵ model incorporated in FIDAP is that it cannot be used in the near-wall region where turbulence levels are low. In the near-wall region, van Driest's mixing length approach [91] is incorporated to model turbulent diffusivities of momentum and mass [90]. Mean flow variables in this region are modeled using universal law-of-the-wall profiles. The near-wall region is considered to be a one-element thick region adjacent to the wall. It is suggested that the height of the elements adjacent to the wall be located outside the viscous and transitional sublayers. For this reason, law-of-the-wall profiles are not ideally suited for near-wall flows with significant departure from local one-dimensionality [90]. For example, the near-wall mean flow velocities of separated and reattaching flows have been determined not to obey the law-of-the-wall, and cannot be correlated outside the linear sublayer using the friction velocity [92]. This must be considered in the analysis of the predicted results.

E.4 *Solution Method*

A fixed-point iteration procedure (Successive Substitution) is chosen as the solution method. This method is known to converge slowly, however, convergence can occur over a wide range of Reynolds numbers. Successive substitution has also been shown to be amiable to the highly non-linear nature of the κ-ϵ model [90]. FIDAP results are presented with steady experimental measurements in Chapter 7. The solution is first order accurate.

E.5 *Wake Stagnation Point Results*

Wake stagnation point locations for the 0° (axisymmetric) slanted-base bluff body are shown in Fig. E.4. Boundary layer transition is fixed at the leading edge of the centerbody. A good correlation between experimental and predicted locations was obtained, with FIDAP results only slightly underpredicting the wake stagnation point location. A proper comparison could not be obtained for $Re_D = 60{,}000$ because the grit particle size was apparently too small to trip the boundary layer at the leading edge of the centerbody in experiments. No systematic variation in the predicted wake stagnation point location with Re_D could be determined.

An attempt was made to correlate experimentally determined wake stagnation point locations for slanted-base bluff bodies with the two-dimensional prediction models described in Chapter 4. Predicted results were found to be as much as twice the distances measured in experiments. Vector plots of the predicted near-wake region, which show predicted wake stagnation point locations, are presented in Fig. E.5. The difference between predicted and experimental results is related to the neglect of side-flow entrainment, which would draw the wake stagnation point closer to the base.

It was determined that a good correlation existed between experimental and predicted results if wake stagnation point locations were determined relative to the 0° base model. These measurements are presented in Fig. E.6. Furthermore, predictions show a deflection of the wake stagnation point towards the trailing edge of the base as indicated in Fig. E.5, which is in agreement with the smoke flow visualization photos of Fig. 7.5 and the slanted-base flow model presented in Fig. 4.10. Experimental measurements for slant-angles greater than 45° were not obtained since base flow reattachment occurred for these bases. Predicted reattachment for the two-dimensional cases occurred for higher slant-angles ($\psi > 55°$) due to the wake stagnation point being located much further into the wake as compared to experimental values. It is shown for the lower slant-angles that both experimental and predicted values move further within the wake as the slant-angle is increased. This trend does not continue to the higher slant-angles as the movement of the wake stagnation point is shown to slow considerably.

Predictions show a pronounced effect of rounding the base leading edge for the 55° base model, as shown in Fig. E.7. For sharp-edged separation, base flow reattachment does not occur, however, slightly rounding the trailing edge of the centerbody is shown to delay separation. An attached flow is present over a portion of the base. This is in agreement with Hucho [18] who determined that separation can occur either at the leading or trailing edge of a slanted rear-window, depending on the curvature of the roof's trailing edge. The effect of rounding the leading edge corner of a lower angle slanted-base is shown in Fig. E.8. The adverse pressure gradient required for attached base flow is too great and the flow is shown to separate on the fairing, however, the wake stagnation point is shown to shift towards the base as compared to the case of a sharp-edged separation.

A significant Reynolds number effect on predicted wake stagnation point locations could not be determined for the lower angle slanted-bases for either sharp-edged separation or for rounded base leading edges. This is shown in Fig. E.9. If the 55° base corner is rounded, then a significant effect is present as shown in Fig. E.10. Separation is delayed with increasing Reynolds number consistent with an increase in momentum within the boundary layer.

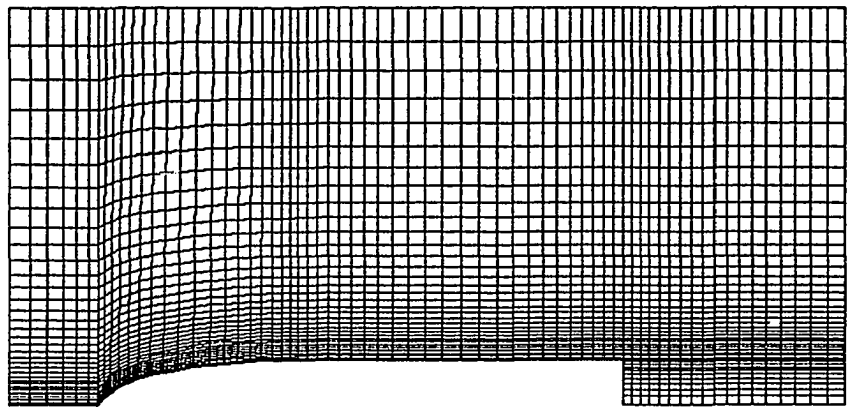

E.1 FIDAP Grid: Axisymmetric Bluff Body

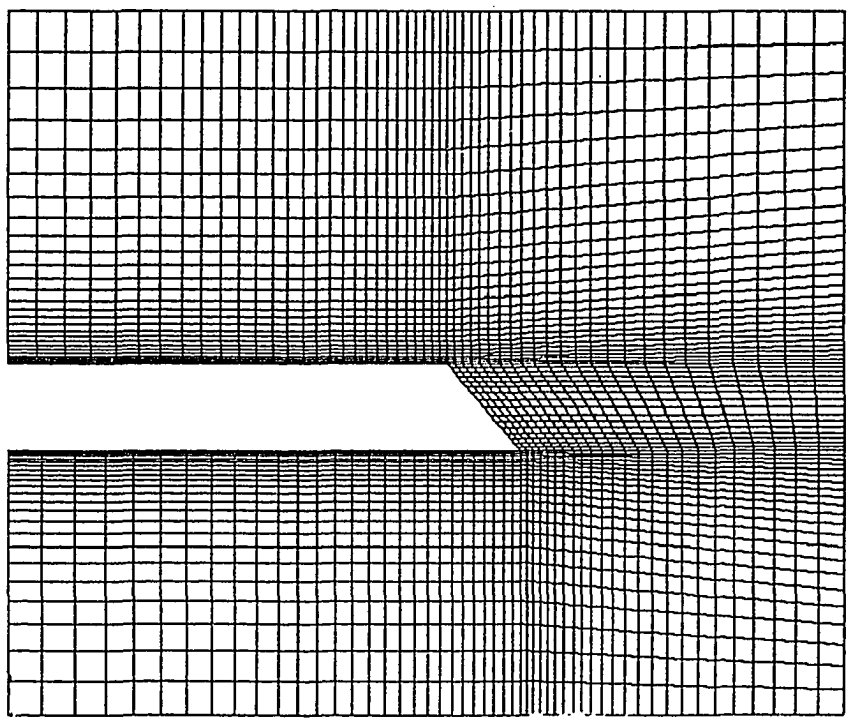

E.2 "Separated" FIDAP Grid: Slanted-Base Bluff Body

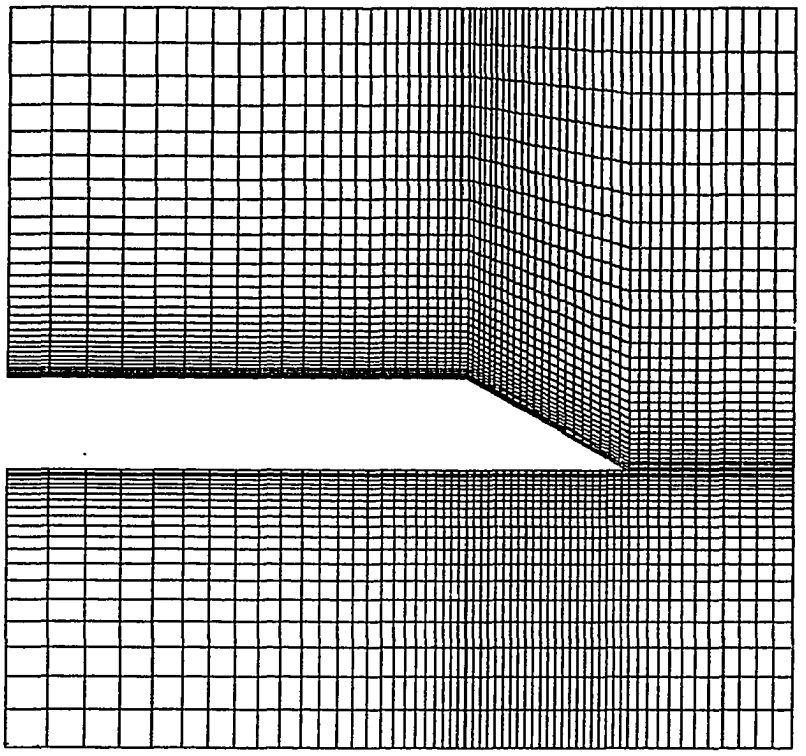

E.3 "Attached" FIDAP Grid: Slanted-Base Bluff Body

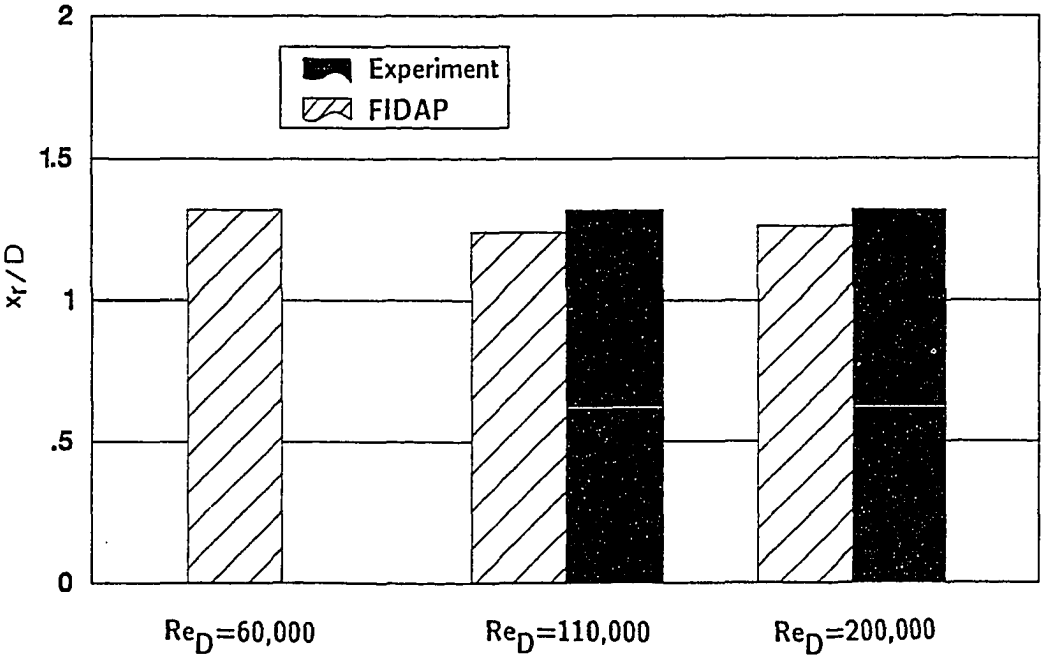

E.4 Wake Stagnation Point Locations: 0° Base

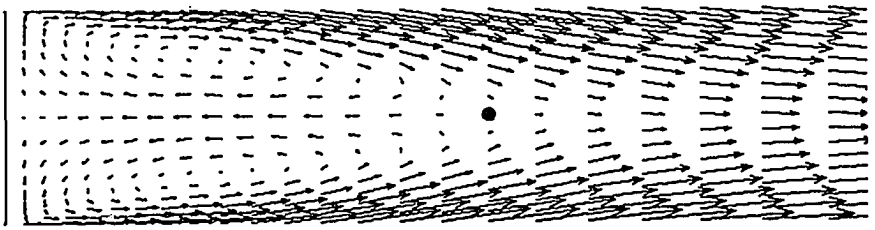

a) 0° Base $x_r/D = 2.24$ (FIDAP); x_r/D=1.25 (Experiment)

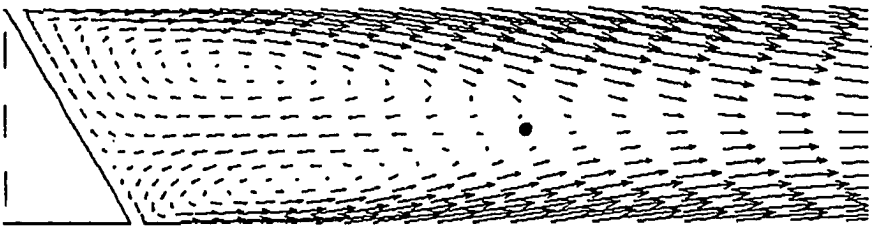

b) 30° Base $x_r/D = 2.41$ (FIDAP)

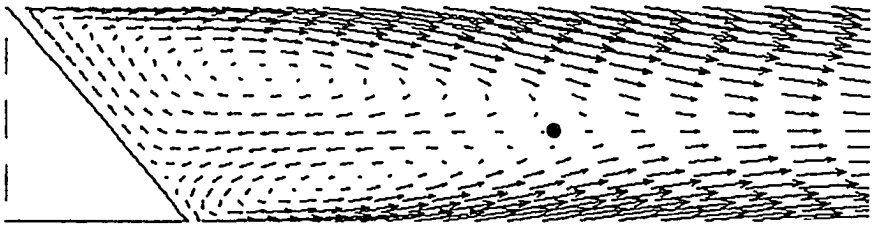

c) 40° Base $x_r/D = 2.55$ (FIDAP); x_r/D=1.48 (Experiment)

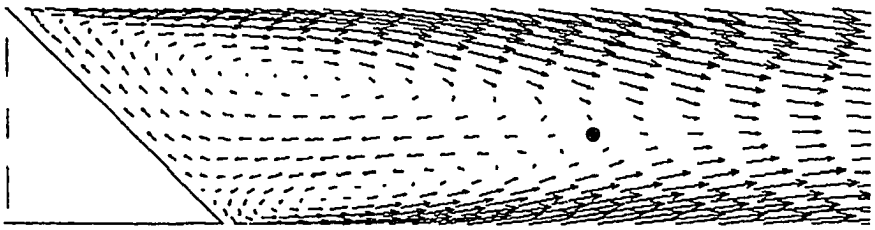

d) 45° Base $x_r/D = 2.70$ (FIDAP); x_r/D=1.48 (Experiment)

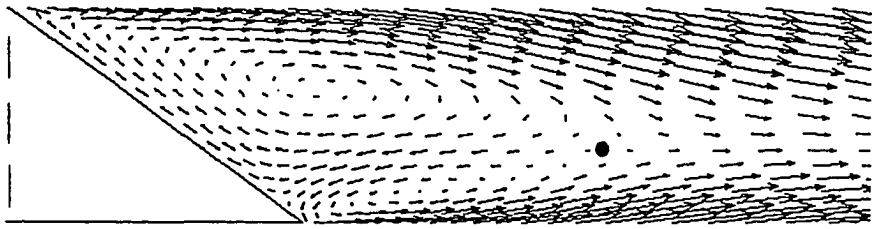

e) 55° Base $x_r/D = 2.76$ (FIDAP)

E.5 Predicted Wake Stagnation Point Locations (FIDAP)

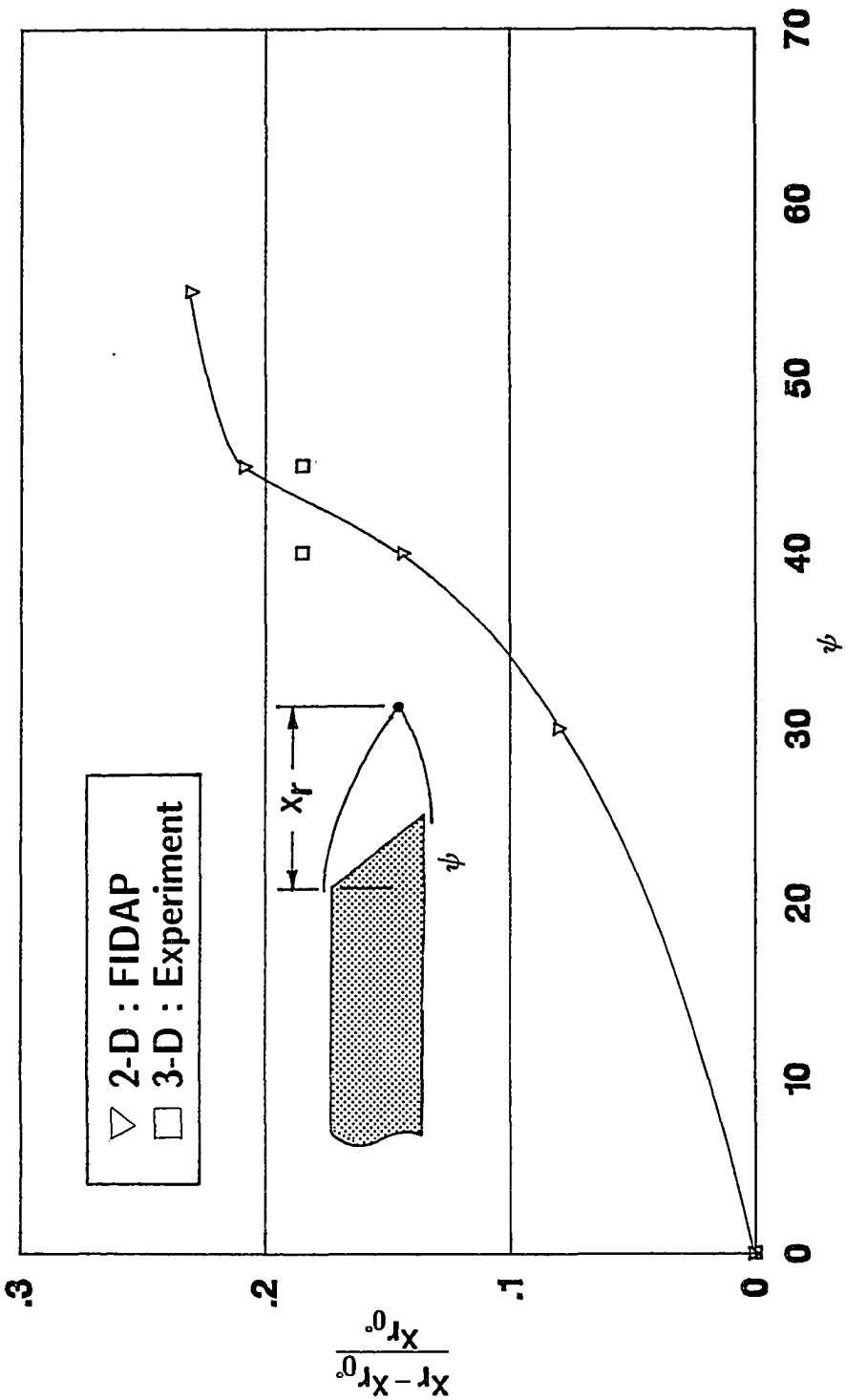

E.6 Predicted Wake Stagnation Point Locations (FIDAP)

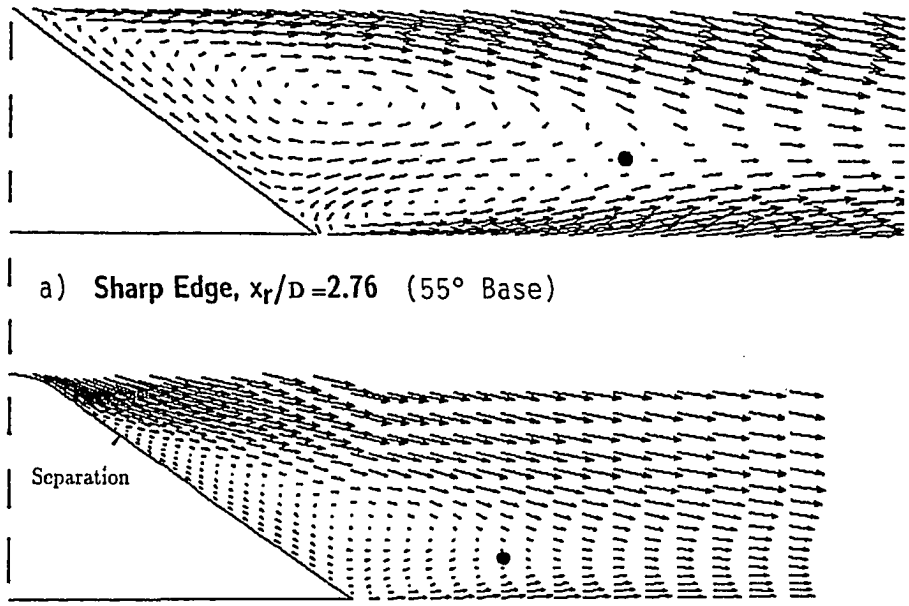

a) **Sharp Edge, $x_r/D = 2.76$** (55° Base)

b) **Rounded Corner, $x_r/D = 2.22$** (55° Base)

E.7 Predicted Effect of Rounding Corner: High Slant-Angle Bases

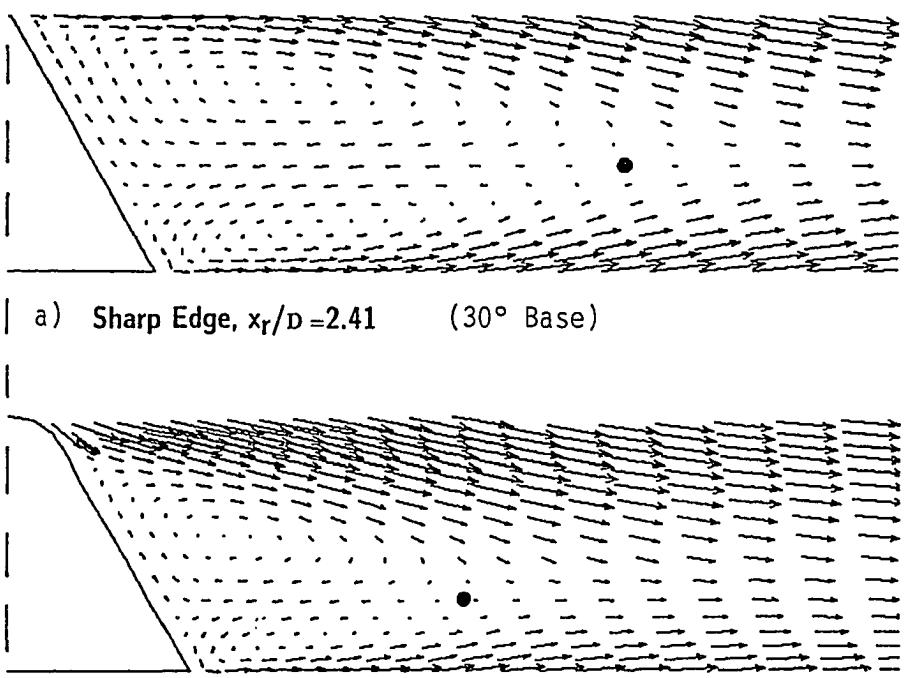

a) **Sharp Edge, $x_r/D = 2.41$** (30° Base)

b) **Rounded Corner, $x_r/D = 1.80$** (30° Base)

E.8 Predicted Effect of Rounding Corner: Low Slant-Angle Bases

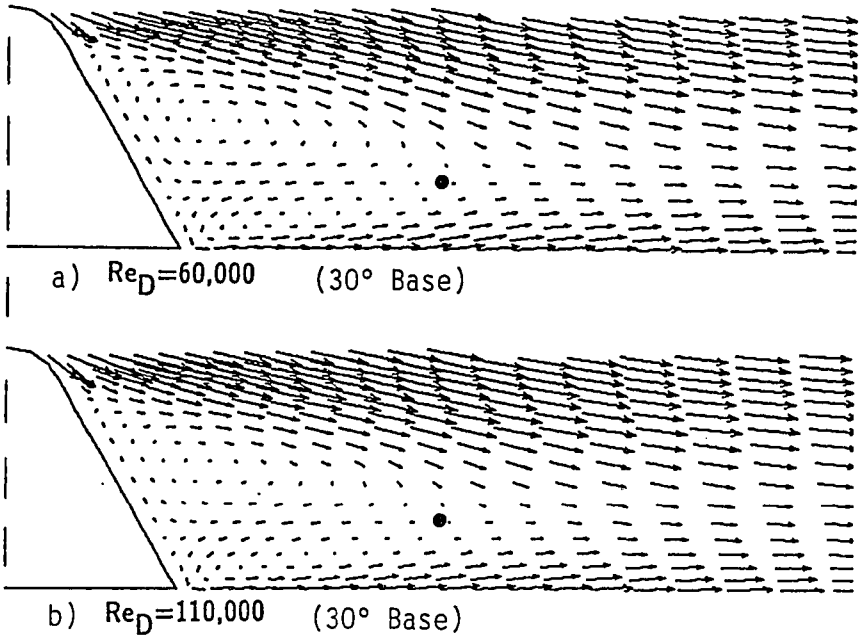

E.9 Predicted Reynolds Number Effect: Low Slant-Angle Bases

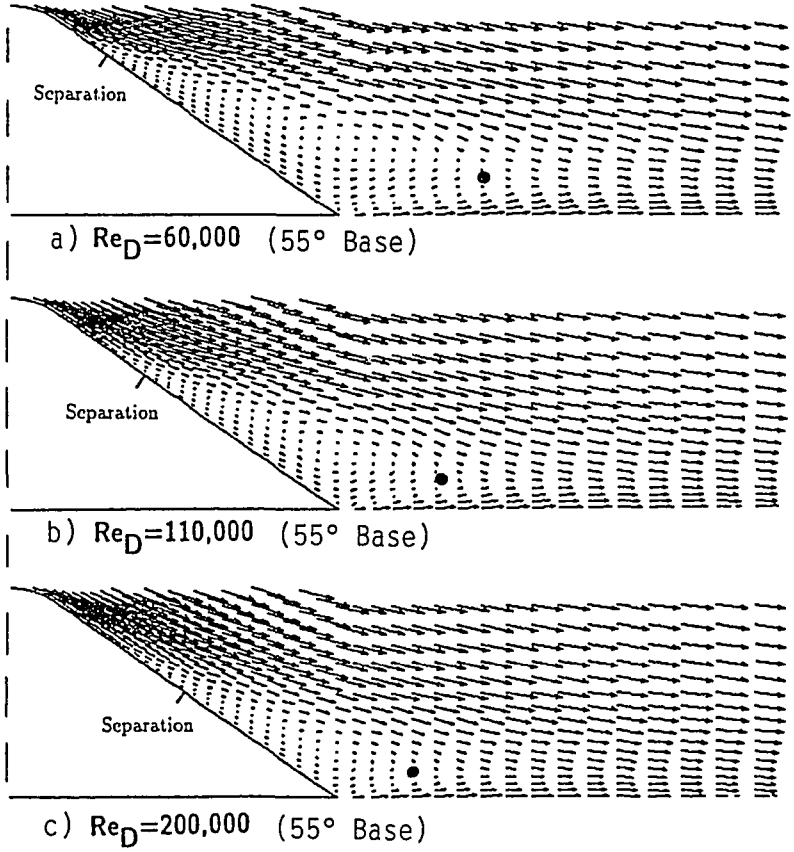

E.10 Predicted Reynolds Number Effect: High Slant-Angle Bases